

In quest of improved nanomechanical sensitivity at larger damping and applications
in ambient conditions

by

Swapan Kumar Roy

A thesis submitted in partial fulfillment of the requirements for the degree of

Doctor of Philosophy

Department of Physics
University of Alberta

© Swapan Kumar Roy, 2019

Abstract

In the current state-of-the-art, a wide variety of devices, from computer clocks to smartphone accelerometers and from pressure gauges to atomic force microscope sensors, rely on mechanical resonators, either in microscale or nanoscale. Nanoscale mechanical resonators have even more potential than microscale by offering unprecedented sensitivity through weighing a single proton (10^{-24} g) or by measuring aN (10^{-18} N) force or μ K temperature. The smaller size of nanometric mechanical resonators allows high sensitivity to their environment; ensuring excellent frequency stability, through high resonance frequency with a higher quality factor, Q , takes the best advantage of this sensitivity. At the same time, their smaller dimension makes these more susceptible to environmental fluctuations, such as thermomechanical (TM) noise, and to energy dissipation, which degrades the Q at atmospheric pressure. The amplitude of TM noise sets a limit to the frequency stability via limiting the signal to noise ratio (SNR). This limit on SNR happens to improve (decrease) as Q is lowered at a rate of $Q^{1/2}$. Meanwhile, nonlinearity practically limits the maximum signal and also causes SNR to improve as Q is lowered with signal proportional to $Q^{-1/2}$. By definition, SNR is the ratio of amplitude at the onset of nonlinearity to the TM noise peak. As a consequence, in widely accepted Robins' picture, frequency stability improves inversely with $Q \times SNR$ and motivates nanomechanical sensor operations mostly at high vacuum to get better performance via high- Q by resolving TM noise.

The negative effect on the stability of early appearance of nonlinearity in high- Q mechanical resonators is underappreciated by researchers and the mantra that the better the Q , the better the frequency stability is well known. Interestingly, if the SNR can be improved at the same rate that Q is degraded, then mass sensitivity can be maintained despite lower Q conditions. Amongst excellent demonstrations of high- Q NEMS sensors to date, such interplay between Q and SNR is not well

studied, despite importance not only for fundamental studies but also for practical applications. This thesis shows that the high displacement sensitivity of a nano-optomechanical (NOMS) transduction scheme ensures that mass sensing is generally occurring with only fundamental limitations to the stability. Put another way, NOMS transduction tends to resolve thermomechanical noise at orders of magnitude above the instrumentation noise background. Frequency stability measurements by phase-locked loop and open loop method validate Robins' picture by attaining the same level of stability at different Q . We test experimental results, both in the analytical and numerical frameworks, and provide a full model to unfold different fundamental noise sources existing in the system and noise suppression effects in phase-locked loop Allan-deviation experiments. Phase-locked loop experiments show increasing noise signal suppression with damping due to loop bandwidth artifacts. Surprisingly, open-loop experiments also show some improvement of mechanical sensor performance with increasing damping, which is attributed to reduced frequency-fluctuation noise in resonance through improved temperature fluctuation noise level via heat conduction by air molecules at atmospheric pressure. We confirm these findings by demonstrating better temperature resolution in atmosphere than in vacuum.

For temperature sensing experiments, we study the temperature dependent properties of the optical ring and NEMS to develop NOMS thermometry. Our thermometry results reveal the existence of nanoscale heat transfer issue for the NEMS that results in very high $0.7 \text{ MWm}^{-2}\text{K}^{-1}$ heat transfer coefficient in atmosphere for the doubly clamped beam resonator and agrees well with COMSOL multiphysics simulations.

We further apply the obtained frequency stability at atmospheric pressure by integrating the NOMS system with a commercial gas-chromatography. The designed, integrated GC-NOMS gas sensor demonstrates 1 ag ($1 \times 10^{-18} \text{ g}$) mass resolution, even at truncated SNR of the mechanical resonator, by detecting GC separated toluene and xylene in a mixture. The retention time of toluene and xylene are identical both in NEMS and FID and asserts the success of GC-NOMS integration in ambient condition. The obtained ambient ag mass resolution is comparable to that predicted by Robins' formula at $100 \mu\text{Torr}$ even though the Q of 29 at 760 Torr is $\approx 300\times$ lower than that at $100 \mu\text{Torr}$. Such an intriguing mass resolving capacity by the GC-NOMS in atmosphere is a baby step for future generations of portable GC-MS in ambient air.

To my late mother

Acknowledgements

First and foremost, I would like to thank my advisor Professor Wayne K. Hiebert. It is his guidance and supports, which enable me to develop the necessary experimental and analytical skills to succeed in this research. His mentorship was not only limited to academic advances but also significantly helpful in developing extracurricular advancements. His serenity in allowing me to discuss and to study random topics is highly appreciated.

I want to show my deepest gratitude to Prof. John Beamish and Prof. Richard Marchand, for their helpful advice during my early grad life before joining Hiebert group. I would also like to thank Prof Beamish and John Davis for years of insightful discussions and invaluable feedback on my Ph.D. research. Many thanks to Prof Mark Freeman for his advice to widen knowledge during the weekly Journal Club with his group.

This research work has been started with the on-chip devices designed by former grad student of Hiebert's group Dr. Vincent T. K. Sauer. I would like to thank Dr. Sauer for offering his help-no matter what experimental or analytical difficulties I have faced. I am also thankful to my fellow Ph.D. student Dr. Jocelyn Bachmann in troubleshooting experiments at the beginning of my program. I want to thank Mike Xia for his training on GC. Also, I would like to thank my co-worker, Dr. Anandaram Venkatsubranium, for his contributions to extending GC-NOMS project.

I want to thank Chittagong University of Engineering and Technology (CUET), Bangladesh for providing me the study-leave for this Ph.D.; I am grateful to all of my colleagues from Department of Physics, CUET for their supports and encouragements.

Lastly, I would like to thank all my friends and lab mates who stuck by me for years and made the burden of grad school lighter. Moreover, to my lovely wife Jayanti and our only son Om: your supports and sacrifices have accomplished this research project.

Abbreviations

ag	Attogram
BW	Bandwidth
CB	Cantilever beam
CNT	Carbon nanotube
Da	Dalton
DCB	Doubly clamped beam
DR	Dynamic range
DSB	Double side band
FID	Flame ionization detector
FM	Frequency modulation
FFM	Flicker frequency modulation
FOM	Figure of merit
FPM	Flicker phase modulation
GC	Gas chromatography
GC-MS	Gas chromatography-mass spectrometry
GC-NOMS	Gas chromatography-nanooptomechanical systems
HF2	Model name of Zurich Instrument lock-in amplifier (high-frequency 2)
HF2LI	Model name of Zurich Instrument lock-in amplifier (high-frequency 2 lock-in)
IR	Infrared

LETI Laboratoire d'électronique et de technologie de l'information

LOD Limit of detection

MEMS Micro electromechanical systems

NCO Numerically controlled oscillator

NEMS Nano electromechanical systems

NOMS Nano optomechanical systems

PLL Phase locked loop

PLLBW Phase locked loop bandwidth

PM Phase modulation

PID Proportional Integral Derivative

PM Phase modulation

Q Quality factor

QCM Quartz crystal microbalance

RH Relative humidity

RWFM Random walk frequency modulation

SSB Single side band

SNR Signal to noise ratio

TOF-MS Time of flight mass spectrometry

VOC Volatile organic compounds

WFM White frequency modulation

WPM White phase modulation

yg Yoctogram

zg Zeptogram

Contents

Abstract	ii
Acknowledgments	v
Abbreviations	vi
Contents	viii
List of Figures	xii
List of Tables	xv
1 INTRODUCTION	1
1.1 MEMS to NEMS	1
1.2 Principle of nanomechanical resonant sensing	2
1.3 Review of NEMS mass sensing	5
1.3.1 Rise of Nanomechanical mass spectrometry	7
1.3.2 Nanomechanical gas sensing	8
1.4 Goal of the thesis	10
1.5 Motivation and Research issues	10
1.5.1 The device	11
1.5.2 Research problem: effect of Q on sensor performance	11
1.5.3 An approach to mitigating the damping effect in mechanical sensor performance	12
1.6 Thesis organization	13
2 Fundamentals of Nanomechanical resonant sensors	17
2.1 Introduction	17
2.2 Fundamentals of nanomechanical motion	19
2.2.1 Mechanical body model	19
2.2.2 Simple damped harmonic model	20
2.2.3 Actuation	20
2.2.4 Thermal noise driven motion	21
2.2.5 Quality factor changes with air pressure	21
2.2.6 Nanomechanical sensitivity by mechanical body model	21

2.3	Readout of nanomechanical motion	22
2.3.1	Fundamentals of optomechanical readout	24
2.4	Experiments	27
2.4.1	Device fabrications	27
2.4.2	Experimental setup	28
2.5	Experimental results and discussions on thermal noise measurements	29
2.5.1	Thermomechanical noise detection	29
2.5.2	Effect of pressure on the resonance properties of the doubly clamped beam	33
2.5.3	Evolution of thermal noise floor with pressure	38
2.6	Conclusions	39
3	Enhancing dynamic range of mechanical resonators through larger damping	40
3.1	Introduction	40
3.2	Duffing behavior of nanomechanical motion	42
3.3	Experiments	44
3.3.1	Determination of onset of nonlinearity	45
3.4	Results and discussion	47
3.5	Conclusions	49
4	Theory of frequency stability	50
4.1	Introduction	50
4.2	Frequency Stability	53
4.2.1	Frequency and phase noise characterization	53
4.3	Time domain stability: definition of Allan Deviation	57
4.4	Robins' phase noise analysis	58
4.4.1	Relation between phase and frequency noise of resonator . . .	62
4.5	Derivation of Allan deviation from frequency noise density of resonator	66
4.6	Conclusion	67
5	Improving mechanical sensor performance through larger damping	68
5.1	Introduction	68
5.2	Experiments	70
5.2.1	Lock-in amplifier and PLL details	70
5.3	Results and discussion	72
5.3.1	Frequency fluctuation measurements (Allan deviation) by phase locked loop experiments	72

5.3.2	Open loop measurements	82
5.3.3	Can damping really improve frequency stability of a mechanical resonator?	89
5.4	Conclusion	90
6	Proof of concept: Measured temperature resolution is better at larger damping	92
6.1	Introduction	92
6.2	Fundamentals of NOMS thermometry	95
6.2.1	Theory of microring thermometry	95
6.2.2	Theory of nanomechanical thermometry	96
6.2.3	Principle NOMS thermometry	97
6.3	Experiments	98
6.4	Results and discussion	99
6.4.1	Static measurements for temperature calibration	99
6.4.2	Dynamic temperature measurements	101
6.4.3	Nanoscale heat transfer	105
6.4.4	Notes on PLL measurements' fidelity	112
6.4.5	Temperature noise suppression at higher pressure	113
6.4.6	Application of damping improved stability: temperature sensing	115
6.5	Conclusions	116
7	Nanomechanical gas sensing in ambient by integrating NOMS with gas-chromatography	117
7.1	Introduction	117
7.2	Gas chromatography	118
7.2.1	Principle of GC	120
7.3	GC-NOMS integration	122
7.4	Experiments	123
7.5	Results and discussion	124
7.5.1	Limit of detection (LOD) of nanomechanical gas detector at the GC end	127
7.6	Conclusion	128
8	Conclusions and Remarks	130
8.1	Summary	130
8.2	Original contributions of this thesis	132
8.3	Conclusions	133

Bibliography	135
Appendices	151
A Chapter 2	151
A.1 Mechanical body model	151
A.2 Simple damped harmonic model	156
A.2.1 Frequency response	159
A.2.2 Effective parameters	161
A.3 Thermal noise driven motion	162
A.4 Quality factor	166
A.5 NEMS damping in air	168
A.6 Background noise floor	170
A.7 Squeeze film effects	170
A.8 Fundamentals of optomechanical interaction in a Febry-perot cavity .	171
B Chapter 3	174
B.1 Notes on dynamic ranges measurements	174
B.1.1 Acoustic interference during piezoactuation	174
B.1.2 Non-linearity onset: modification at high pressure	176
B.1.3 A note on high drive powers	179
B.1.4 A note on comparing different drive levels	179
B.1.5 Notes on optomechanics	180
B.1.6 Acoustic interference, nonlinearity, and revisiting Figure 3.3 .	183
C Chapter 5	185
C.1 Allan deviation due to readout imprecisions	185
C.2 Phase noise behavior with damping in <i>Science</i> is equivalent to open loop behavior	187
C.3 Further verification of open loop frequency fluctuations	188
C.4 Notes on PLL measurements	188
D Chapter 6	193
D.1 Numerical evaluation of h and underlying thermal physics	193

List of Figures

1.1	Concept of frequency shift sensing.	3
1.2	Effect of mass loading on nanomechanical resonator	4
1.3	Nanomechanical mass sensing chronology: from attogram to yoctogram resolutions.	6
1.4	The concept of maximizing linear dynamic range.	13
2.1	Schematic view of a typical inertial piezoshaker actuation setup.	20
2.2	Exemplary illustrations of nanomechanical motion detection through evanescent wave coupling.	24
2.3	Measured optical transmission and its first derivative at 15 Torr.	26
2.4	Annotated SEM image of the nano-optomechanical system device.	27
2.5	Schematic of experimental setup.	28
2.6	Displacement noise of the doubly clamped silicon beam.	30
2.7	Measured quality factor variations of the DCB as a function of pressure.	33
2.8	Resonance frequency shift with pressure.	35
2.9	Measured thermomechanical noise amplitude as a function of pressure for 1 Hz measurement bandwidth.	38
3.1	A representative plot for determining critical drive power.	45
3.2	Evolution of onset of nonlinearity with increasing damping or decreasing Q	46
3.3	Dynamic range is pressure dependent.	47
3.4	The product of $Q \times SNR$ is constant in the Duffing limited regime.	48
4.1	Phase (single side band) and frequency noise density model.	56
4.2	Schematic of Allan deviation vs. averaging time plot	58
4.3	Robins' analysis: displacement noise transforms to phase noise.	60
4.4	Conceptual diagram of the force noise translating to phase noise.	62
5.1	Schematic of Phase locked loop.	71

5.2	A representative PLL transfer function obtained from Zurich instrument HF2.	72
5.3	Phase-locked loop Allan deviation falls (improves) with falling Q for a measurement bandwidth.	73
5.4	Allan deviation at 2 ms sampling time vs. Q.	74
5.5	Illustration of frequency noise density of a NEMS shaped by PLL parameters (for 500 Hz PLLBW) at different damping conditions. . .	77
5.6	Schematic view of frequency and time domain stability shaped by PLL transfer function.	78
5.7	Numerically integrated Allan deviations as a function of damping, bandwidths and DR in phase-locked loop measurements.	81
5.8	Effect of different magnitude drift in Allan deviation simulations at 760 Torr.	82
5.9	Thermomechanical noise limited phase and frequency noise density of nanomechanical resonator in open loop experiments as a function of damping.	83
5.10	Measured Allan deviations at different pressure regimes and various driving powers with 1 KHz demodulation bandwidth.	85
5.11	Directly measured open loop frequency noise density as a function of damping dependent DR	86
5.12	Quadrature representations of open loop frequency noise measurements.	88
5.13	Open loop Allan deviation results for 1 ms averaging time.	90
6.1	Schematic illustration of NOMS thermometry and nanoscale heat transfer.	97
6.2	Representative plots for determining for ring and NEMS temperature sensitivity.	99
6.3	An illustration of the change in wavelength and resonance frequency with time during step changes on and off in temperature.	101
6.4	Simultaneous dynamic temperature measurements by optical ring and nanomechanical DCB.	102
6.5	Signature of nanoscale heat transfer by NOMS thermometry.	104
6.6	Calculated and simulated heat transfer coefficient as a function of air pressure.	108
6.7	Fidelity check for PLL performance.	111
6.8	A photo of the front-view of the measurement chamber.	112
6.9	Measured temperature resolutions at different pressures.	113
6.10	NEMS Thermometry	114

6.11	Observed limit of temperature change detection at different damping.	115
7.1	Basic features and principle of gas chromatography.	120
7.2	Schematic of designed integrated GC-NOMS gas sensor for the ambient condition.	121
7.3	Snapshot of the experimental setup.	122
7.4	An exemplary real-time ambient condition gas chromatogram from integrated GC-NOMS gas detector after injecting Sample 1 into the injection port of gas chromatography.	125
7.5	Normalized response of FID and nanomechanical gas sensor in the integrated GC-NOMS system in ambient.	126
A.1	Schematic representation of a beam under transverse load.	152
A.2	Transfer function of a damped mechanical resonator.	159
A.3	Schematic of typical optomechanical interaction.	172
B.1	Acoustic interference during piezoactuation.	176
B.2	Optical resonance at 26 Torr.	177
B.3	Calibration procedures for removing the Joule heating effect in determining high-pressure critical drive.	178
B.4	Optomechanical spring effect in the device.	181
B.5	Evolution of nonlinearity with increasing drive power.	183
C.1	Noise power behaviour with respect to damping can be proportional, constant, inversely proportional, and inversely quadratic.	187
C.2	Measured Allan deviations at different pressure regimes and various driving powers with 1 KHz demodulation bandwidth in another series of experiments.	188
C.3	Normalized Frequency response due to a phase step in Phase locked transient frequency output at different damping.	189
C.4	An instantaneous change in frequency of DCB nanomechanical resonator due to heat adsorption/desorption after irradiating 1064 nm laser at different pressures.	191
C.5	Schematic view of transient frequency shift measurement at low Q condition when an event occurs faster than PLL time constant.	192
D.1	Heat transfer coefficients from COMSOL simulations at high and low vacuum.	193
D.2	Heat transfer coefficients from COMSOL simulations at 61 Torr.	194

List of Tables

5.1	P and I parameters from HF2 lock-in PLL advisor for 500 Hz experiments shown in Figure 5.3.	76
6.1	Measured ring and NOMS temperature sensitivity at different pressures	100
6.2	Temperature change measured by ring and NEMS in the NOMS from Figure 6.4 and corresponding measurement uncertainties.	103
6.3	h at different pressures.	109
7.1	Concentrations of VOC analytes in each samples	124
A.1	Power law of quality factor as a function of air pressure.	169

Chapter 1

INTRODUCTION

1.1 MEMS to NEMS

Modern civilization uses electromechanical devices in many aspects of daily life. These devices are actuators which use electromagnetic effects to generate motion. Almost all moving actuators around us are electromechanical, such as generators to create electricity or electric motors to transform electricity into mechanical work. A smaller version of these devices is known as Micro-electromechanical systems (MEMS) with a characteristic length of less than 1 mm but more than $1\ \mu\text{m}$. It is Richard P. Feynman, who envisioned smaller electric motors in his legendary speech, “There’s Plenty of Room at the bottom”, in 1959. Now, over a half-century after his famous talk, many of his ideas on miniaturization are a reality. Nowadays we use something which contains a MEMS device in it every day. For examples, smartphones in our palm have an accelerometer which is a MEMS; automobile industries use MEMS as an acceleration sensor for releasing airbags, and so on [1, 2].

With the advent of micro/nanofabrication techniques, the size of MEMS reduces to nanometers and is named Nano-electromechanical systems (NEMS) and opens exciting avenues for new generation smart sensors with unprecedented sensitivity. Whatever the MEMS or NEMS, the tiny mechanical element resonantly vibrates when subjected to an external stimulus, even in the presence of omnipresent thermal noise force and thus is named a nanomechanical resonator. Any change in the environment viz. temperature, force, magnetic state, mass, etc. changes the resonance properties such as resonance frequency, phase, and amplitude of the vibration. Among resonant properties variations due to change in surrounding environments, resonance frequency shift can be measured accurately. At present, most NEMS sensors rely on frequency shift measurement because it can quantify the amount of measurand of interest directly which depends on device size and its mechanical properties as well as the properties

of materials by which the device is made. The extraordinary sensitivity demonstrated by NEMS owes itself to its smaller dimensions that results in very high resonance frequency and quality factor. Now, nanomechanical mass sensing has reached single proton level, [3, 4] enabling NEMS gas chromatography, [5, 6] and mass spectrometry [7, 8, 9]. Force sensing has produced single-spin magnetic resonance force microscopy [10]. Torque resonance magnetometry has been revisited [11] with applications in spintronics and magnetic skyrmions. The mechanical quantum ground state has even become accessible [12, 13, 14] and used for absolute thermometry [15].

It is the minuscule size of tiny NEMS that often enables superior performance with thought-provoking applications mentioned above. For example, a smaller device mass allows detecting a smaller change in mass. Most significant nanomechanical sensing research so far uses high vacuum operations to ensure high quality factor (Q) of the device. General perceptions, as well as practical experiences, have ingrained the notion that higher Q ensures better nanomechanical sensitivity than low Q operations. Conversely, required high vacuum operations for NEMS sensing is not only costly but also not preferable, particularly for gas sensing or for portability of the sensing device. Thus, the desired high Q operations of NEMS imposes a practical limit for ambient condition sensing. This thesis mainly aims to address NEMS operations in lower Q conditions (e.g., at atmospheric pressure and room temperature) to develop an ambient condition ultrasensitive gas sensor that can be applied in, e.g., gas chromatography. In the current dissertation, we are able to show that poorer- Q operations of a nanomechanical resonator can induce better sensitivity than at high vacuum, which is completely contradictory to the conventional wisdom of nanomechanical sensor research. A version of findings are published in *Science* [16]. The success of the present study can be a baby step for future generation portable gas chromatography-mass spectrometry (GC-MS) instruments with a large range of applications in detection of trace biomarkers, breath analysis, environmental monitoring, and security screening.

1.2 Principle of nanomechanical resonant sensing

The resonance frequency, Ω_0 of mechanical beam resonators is proportional to l^{-2} , (*cf.* Chapter 2),

$$\Omega_0 = \sqrt{\frac{k}{M_{\text{eff}}}} \propto l^{-2}, \quad (1.1)$$

where l is the length of the device, k is the spring constant, and M_{eff} (*cf.* A.2.2) is the effective mass of the device. Therefore, reducing the length by an order of magnitude

results in resonance frequency improvement by two orders of magnitude.

The ability of smaller NEMS sensors to detect physical quantities like mass, force, temperature, and pressure is closely related to their resonance frequency. Any change in device mass, temperature, experienced force, etc. changes the mechanical property of the device and thus changes the resonance frequency, which accounts for the quantity to be measured. A conceptual frequency shift of a NEMS device due to change in its environment is shown below:

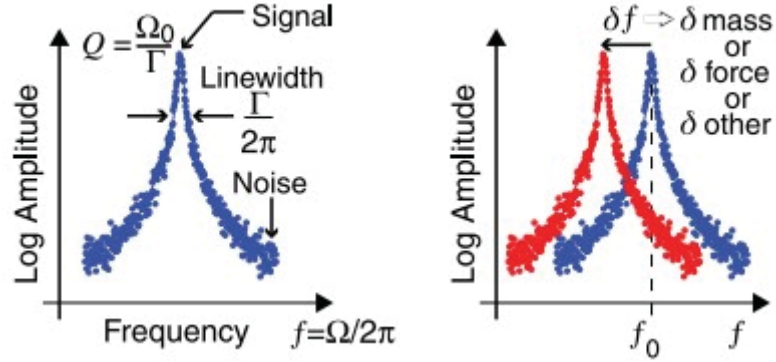


Figure 1.1: **Concept of frequency shift sensing:** A mechanical resonance is perturbed by the change in mass or force, resulting in a frequency shift. At a first approximation, the minimum detectable shift improves with sharper linewidth (i.e., lower damping, Q^{-1}) and higher signal to noise ratio (SNR) as per Robins' formula. From [16]. Reprinted with permission from AAAS.

Nanomechanical mass sensing

The schematic frequency shift measurement, in Figure 1.1 helps to determine the loaded mass when mass deposition causes a permanent change in device mass. However, in the case of real-time mass loading by a particle or molecule landing as in the schematic Figure 1.2a or adsorption of gas molecules, a phase-locked loop (PLL) measurement conveniently measures any temporal shift in resonance (Figure 1.2b). A differentiation of resonance frequency (equation 1.1) with respect to mass projects a change in device mass (*cf.* Chapter 2),

$$\delta m = 2M_{\text{eff}} \times \frac{\delta f}{f_0}. \quad (1.2)$$

Equation 1.2 manifests that detectable mass, δm will be minimum for the lowest device mass (M_{eff}), the highest resonance frequency (f_0) with the best possible minimum frequency fluctuations, δf . NEMS devices, by their name, inherently offer smaller mass and higher resonance frequency. Maintaining frequency fluctuations δf to a minimum

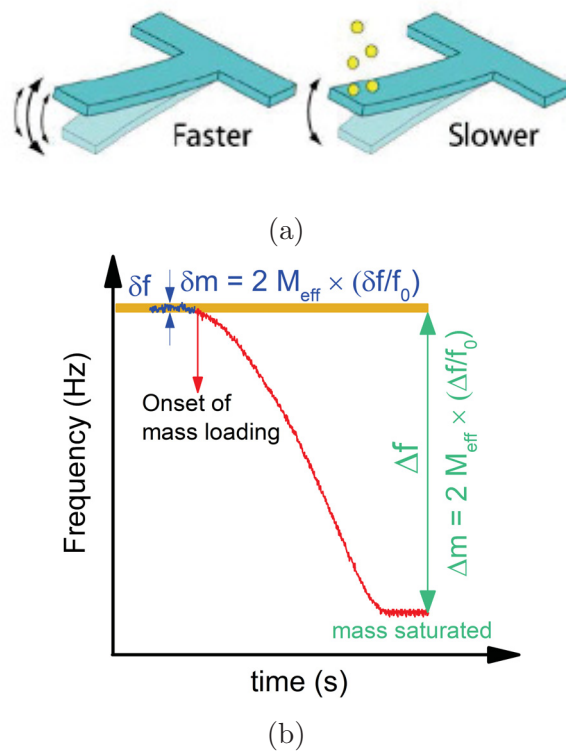


Figure 1.2: **Effect of mass loading on nanomechanical resonator** : a) An artistic view of the resonance frequency reduction due to loaded analytes on a cantilever surface. b) Conceptual illustration of mass estimation by real-time frequency shift monitoring through PLL measurements. Blue data represents device frequency fluctuations, δf before mass loading occurs, it determines the attainable mass resolutions, δm , by the device. Red data displays temporal frequency shift due to mass accumulation on to the device surface. By measuring the total frequency shift (Δf) loaded mass (Δm) onto the device surface can easily be estimated. These equations are valid only when loaded mass is minimal compared to the device mass, M_{eff} and assumes any effect on the spring constant is negligible.

is an extraordinary experimental challenge that incorporates various experimental conditions such as transduction and detection efficiency of nanomechanical motions, conditions of experiments, measurements schemes, and other related issues regarding experiments. The quantity, normalized frequency fluctuation, $\delta f/f_0$ is investigated intensively because statistical approaches of random fluctuations in the time domain are convenient to interpret different sources that cause the random frequency fluctuation δf . These fluctuations sources are collectively known as noise. And the normalized frequency fluctuation $\delta f/f_0$ is known as Allan deviation, σ_A after the name of David Allan [17]. Physically, σ_A estimates the deviations of frequency at any instant from the nominal resonance frequency and thus it is a measure of frequency stability

of mechanical resonators. Since device geometry constrains its mass, (M_{eff}), the other quantity, σ_A in the equation 1.2, is a crucial figure of merit (FOM) for any mechanical sensor which should be the lowest for the best sensor. Enormous theoretical and experimental works have been accomplished by different research groups across the globe to push the frequency stability to its ultimate value. The expression for frequency stability deduced by different authors came to similar relations with the device resonance properties whatever the device geometry [18, 19, 20, 21, 22]. It gives an estimation of the frequency stability based on the resonant quality factor, Q , and the comparison of noise energy to motional energy. The formula can be written as follows:

$$\left\langle \frac{\delta f}{f} \right\rangle \sim \frac{1}{2Q} \frac{1}{SNR} = \frac{1}{2Q} 10^{-DR/20}, \quad (1.3)$$

where SNR (signal to noise ratio) is the ratio of driven motional amplitude to equivalent noise amplitude on resonance

$$SNR = \frac{a_{\text{driven}}}{a_{\text{noise}}}, \quad (1.4)$$

and the dynamic range DR is the power level associated with this SNR . The quantity, $\delta f/f_0$, i.e., the frequency resolutions, not only limit the mass resolution but also limit resolutions of other physical quantities (like force, temperature, pressure, etc.) to be measured. The Q factor in the denominator of Equation 1.3 has led researchers to pursue high Q for better resolution [23, 24, 25].

1.3 Review of NEMS mass sensing

In the last two decades, an impressive evolution of nanomechanical mass sensing experiments is fuelled by downscaling the device size. Figure 1.3 summarizes some of the motivating mass sensing experiments of the last years. Roukes group from Caltech is pioneering in nanomechanical mass sensing for years. In 2004, Ekinici *et al.* [26] detected 40 ag (1 ag = 10^{-18} g) gold nanoparticles by exposing a SiC doubly clamped beam (DCB) resonator at 32.8 MHz frequency with a quality factor 3000. This work is a first NEMS-based real-time monitoring of mass deposition. In 2006 Yang *et al.* [27] repeated the experiment to detect 100 zg (1 zg = 10^{-21} g) mass at 133 MHz after cooling the device at 37K with a quality factor of 5000. They obtained a 7 zg mass resolution. One year later, Li *et al.* [28] from the same group developed high-frequency cantilever beam (CB) from SiC for ambient condition gas sensing. The best CB of this work in ambient condition has a quality factor of 400 at 127 MHz resonance frequency. This device demonstrates multiple gas sensing through chemisorption with a minimally resolved mass of 1 ag. In the year of 2008, another intriguing work was

reported by X. L. Feng *et al.* [29] on a SiC DCB NEMS embedded within a feedback circuit which developed a self-sustaining oscillator. In that work, they obtained a 50 zg mass resolution by operating the device at cryogenic temperature to attain a quality factor 2500 while the resonance frequency was 428 MHz. All these examples stated so far have fabricated nanomechanical resonators by a top-down approach.

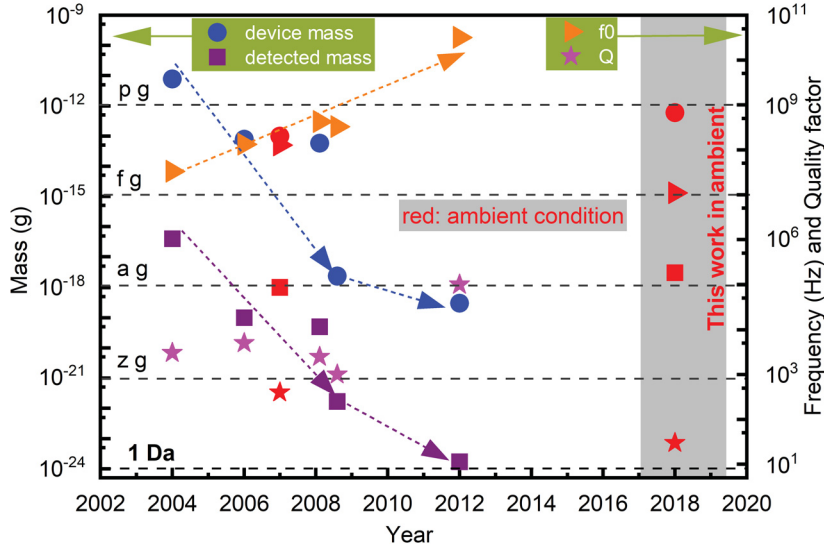


Figure 1.3: **Nanomechanical mass sensing chronology: from attogram to yoctogram resolutions:** Among substantial mass sensing experiments, only a few are chronologically plotted here from [3, 26, 27, 28, 29, 30]. Device mass and detected mass are plotted in the left axis. The right axis corresponds to respective resonance frequencies (f_0) and Q s. Only the red symbols represent ambient measurements, including the results from the current dissertation in 2018 [16]. All other experiments are in a high vacuum, even at the cryogenic condition to ensure high- Q mass sensing operations. The mid-2008 and 2012 devices are fabricated CNT by a bottom-up approach. Others use a top-down approach. The chronology demonstrates that smaller devices can attain higher frequency and better resolutions. Mass detection down to Dalton resolutions approaches at a logarithmic rate. 2018 results from this thesis challenge the sequential trend; it shows the possibility to have better mass resolutions at lower- Q situations, even with moderately small device resonated at MHz frequency range.

The race for attaining lower mass resolution shows significant interest with bottom-up devices such as a carbon nanotube (CNT). The hollow structure of CNTs results in a lower mass than top-down devices by a few orders of magnitude and frequency at GHz range and thus CNT can lower the mass resolution down to atomic resolutions. K. Jensen *et al.* [30] measured a doubly clamped CNT resonated at 328 MHz that featured a quality factor of 1000 at high vacuum. Their mass sensing experiment was compared to a reference QCM to gain zg scale mass detection. Bachtold group [3]

achieved the record mass sensing to date by weighing at single proton level (mass of a proton is $\sim 1 \text{ yg} = 10^{-24} \text{ g}$) with another CNT in 2012. Authors cooled the device down to 58 K to ensure a high quality factor of 100000, while the CNT was resonated at 32 GHz. Except for the reference [28] most successful mass sensing experiments were done under extreme environmental conditions such as ultrahigh vacuum and cryogenic temperature. Authors used such an idealized condition to reduce damping (energy dissipation) which is known to degrade the device Q factor, and thus the mass sensitivity. It is interesting to see in Figure 1.3 that the detected mass from the current work measured by a top-down DCB beam resonated in ambient at 11 MHz with a quality factor 29 only, is comparable to that of Mo Li *et al.* [28] for ambient gas sensing by a cantilever of smaller mass. Frequency and quality factor in ref. [28] are higher by orders of magnitude than the current DCB. This incredible mass sensitivity observed in this thesis raises a question, would damping enhance the nanomechanical sensor performance? Gradually, this dissertation will unveil the story of this success.

1.3.1 Rise of Nanomechanical mass spectrometry

The extraordinary mass resolution demonstrated by NEMS is comparable to the extensively used mass spectrometer (MS) in analytical laboratories. Nowadays, MS is a versatile technique for determining chemical compositions across different areas such as chemistry, biology, medicine, materials science, surface physics, geology, and so on. MS determines the mass of molecules by measuring mass to charge ratio, which requires ionization of the molecules with known charge. Therefore, it needs an ionization chamber with a high vacuum condition that results in a bench top nonportable laboratory technique. Inspired by the efficacy of nanomechanical mass sensor for weighing neutral molecules, Hiebert and his co-workers [9] from Roukes group demonstrated a NEMS-based mass spectrometer for the first time of this kind. They have used a $1.7 \mu\text{m}$ long and 120 nm wide SiC DCB beam. For facilitating mass sensing, authors built up an MS setup by using an electrospray ionization source and hexapole focusing which can project single biomolecules such as albumin (66 kDa) and beta-amylase (200 kDa) on the resonating DCB. The device was cooled at 40K with zg mass resolutions. The frequency jumps due to mass adsorption was tracked by PLL acquisition method.

This first setup for NEMS-MS is a significant step because it demonstrated that nanomechanical resonators are not only a practical alternative of typical time of flight mass spectrometer but also potential for future generation on-chip mass spectrometry. However, the remaining challenge is to determine the mass of the loaded molecule

directly, because, frequency shift by molecule landing not only depends on molecular mass but also on its landing position. Since the position of the molecule could not be known, authors adopted a statistical approach, which is time-consuming. In quest of improved NEMS-MS Hanay, *et al.* [7] from the same group and Olcum *et al.* [31] from Scott Manalis group used multimode mass sensing to determine the position of the loaded mass. Around the same first quarter of 2015, Sebastien Hentz group from LETI, France built up a set up which comprises conventional time of flight MS (TOF-MS) [8] and NEMS-MS which can compare the charge insensitive mass measurement by NEMS to the charge sensitive conventional TOF-MS and demonstrated single particle mass spectrometry in 2018 [32]. In November 2018 Hentz group improve their NEMS-MS by detecting charge neutral virus capsid above 100 MDa mass [33], but in high vacuum. In the evolution of NEMS-MS, high vacuum environment restricts portability and widespread applications. For bringing up this technology in our everyday life, we need a low-cost portable NEMS-MS, which requires ambient condition operations.

1.3.2 Nanomechanical gas sensing

Resonance frequency shift due to adsorption induced mass change makes nanomechanical resonators attractive for gas sensing with potential applications in gas molecule detection for security screening, health, and environmental monitoring. There are growing needs for developing a fast, sensitive, reliable, and portable gas sensing at low cost; this can be a niche that could be offered by NEMS technology. Interaction of gas molecules with a solid structure occurs either via physisorption or chemisorption. The primary challenge of gas sensing is to accommodate gas loading on to the minuscule device surface. Most of the early mechanical gas sensing experiments [34, 35, 36, 37, 38] in MEMS domain have been implemented by physisorption and/or chemisorption where a resonator was exposed to the environment containing a single chemical species rather than multiple species. To overcome gas landing issue researchers find alternatives by enhancing gas adsorption mechanism using chemically active device surface. A functional layer deposited on the device surface improves gas sorption process as well as provides selectivity for specific gas compounds. As in reference [28], Roukes and coworkers used cantilever beams for chemical detection, which is also listed in Figure 1.3. In this work, they demonstrated that a smaller cantilever with high resonance frequency could have a higher quality factor ($Q = 400$) in the air. For enhancing the affinity of gaseous 1,1-difluoroethane ($C_2H_4F_2$) molecules, authors modified the device surface using a thin film of polymethyl methacrylate (PMMA). Results from these experiments enable nanomechanical label-free and specific detection of 1,1-difluoroethane

molecules at the attogram level.

1.3.2.1 GC-NEMS

Despite the potential of NEMS mass sensors as a gas detector, until now, there are no clear demonstrations of these as a universal gas detector. For selective gas detection, these need some specific coating that is not always favorable for multiple gas detection at the same time. To solve the selectivity issue, gas chromatography can be a viable alternative. Gas chromatography is very well known for separating individual gaseous components from a mixture depending on boiling point or retention time of individual gas components. Thus, it can be an alternative selective component for polymer coating on the device surface. On the other hand, if a bare NEMS can detect separated gas, then adding NEMS at the GC detector can reduce the cost and extra steps for the coating process. Hence, integrating a NEMS mass sensor at the GC end will open a possibility to a future generation (portable) GC-MS. Unfortunately, successful experiments on GC-NEMS integrations are rare in literature [5, 6].

One drawback to conventional GC-MS is that its expense and specialized basis limits its application [39]. Progress in micro-GC fabrications and their commercial uses are now well established [40, 41], as an example, the 490 Micro-GC of Agilent (agilent.com) (California, US-CA) is commercially available. However, portable GCs have carved a recent market niche [42], but performance is limited, and detectors are the least sensitive kinds, these instruments often drop or simplify the chromatography. Innovations in detection, particularly those that lead to miniaturization while preserving (or improving) functionality, have extraordinary potential: on-site monitoring for food and chemical industries, in-situ environmental monitoring, point-of-care diagnostics in health care, and routine chemical analysis would all benefit significantly from sophisticated portable GC-MS. Exceptional mass sensitivity and faster response make NEMS devices perfect for the faster output of the GC column. Two works reported from Roukes group have begun to apply polymer coated NEMS to GC sensing [6, 43]. However, this coating was chosen to be very specific for a particular application (explosive detection). Two NEMS device with different functionalized polymer layers have been used to detect a dozen chemical compounds in the gas phase. Depending on the affinity of gaseous compounds to the polymer, they could not detect some chemicals such as toluene and octane due to comparatively smaller partition coefficients. Coated NEMS array at the GC end are in focus of LETI, France for years [44]. For universal detection, coatings with similar responses to many different compounds will be crucial. Gas adsorption capabilities of native silicon oxide is well known in surface chemistry [45, 46]. In 2016, this thesis applied uncoated NEMS in ambient as GC detector [5] by

integrating current NOMS (Nano optomechanical systems) system with a commercial Agilent 5890 gas chromatography.

There is more room to develop a methodology for gas transferring from the GC column to NEMS sensors, gas adsorptions, and packaging. Besides these, one fundamental issue is how to maintain exceptional nanomechanical sensitivity at ambient condition gas sensing. All referred NEMS ambient condition gas sensing measurements in the current sections are affected by resolution loss due to damping, which is inescapable. As a consequence, most exciting nanomechanical sensing can be found in high vacuum condition, which poses a limit for portable NEMS sensing.

1.4 Goal of the thesis

After reviewing nanomechanical mass sensing experiments, it can be inferred that large damping in ambient condition imposes a practical and fundamental barrier in sensing experiments. This thesis aims to achieve a vacuum level nanomechanical sensitivity at atmospheric pressure and room temperature. The ultimate goal of this Ph.D. project is to design experiments for integrating a nanomechanical resonator at the output of gas chromatography for ambient condition gas sensing with vacuum compatible mass sensitivity.

1.5 Motivation and Research issues

In section 1.2, while discussing the principle of nanomechanical resonant sensing, we have seen that effective mass and frequency resolution of the device must be minimized to attain a high sensitivity (*cf.* equation 1.3). The current state-of-the-art of nanofabrication is routinely used to fabricate smaller devices precisely to achieve high frequency. Efficient transduction of these nanoscale resonators is challenging not only from the fundamental point of view but also from specific requirements of their applications [47]. Recent progress in nano-optomechanics significantly improves the transduction and detection efficacy of small nanomechanical motion. In the light of optomechanics, the motion of tiny NEMS can be detected and manipulated optically rather than electrically, which shifts the acronym, NEMS to NOMS. Our group expertise in designing nanophotonic measurement systems [48] and fabricating NOMS to study optomechanics [49, 50, 51, 52, 53, 54] allows the ability to track mechanical motion with femtometer precision. This sensitivity level allows easily achieving thermal noise measurements in a wide variety of conditions (high Q or low Q) and device size regimes [50]. Optomechanical transduction of these devices

has recently been shown very promising for conserving intrinsic dynamic range (DR) while size down scaling [55]. Further, the design freedom to tune optomechanical coupling strength allows full control over the linear operation range of the transduction. Together, these attributes make optomechanical readout perfectly suited for accessing the full intrinsic DR of NEMS devices. By measuring an intrinsic dynamic range of a single device across different Q , i.e., by changing air pressure from high vacuum to atmospheric pressure it is possible to test the frequency stability relation given by the equation 1.3.

1.5.1 The device

As a testing bed for this thesis, a similar typed device as to the one described in reference [50] has been selected. The device under test is a nanomechanical doubly clamped beam which is side coupled to a racetrack resonator optical cavity in all-pass configurations. Details of nanoptomechanical transductions and devices are outlined in Chapter 2. DCB beams ($9.75\ \mu\text{m} \times 220\ \text{nm} \times 160\ \text{nm}$) and the racetrack resonators are $160\ \text{nm}$ apart. So, it can be assumed that any gas/mass loading on the nanomechanical DCB can have a negligible effect on the optical cavity to maintain optomechanics invariant.

1.5.2 Research problem: effect of Q on sensor performance

So far, we have discussed the advantages of smaller devices as sensors. Conversely, the minuscule size of nanomechanical resonators makes them more vulnerable to noise that results in poor quality factor (Q) by energy dissipation to the surrounding bath. The quality factor is the inverse of damping and indicates how sharp the resonance is in frequency. Referring to equation 1.3, Q has been used as a proxy metric for frequency stability that leads researchers to fabricate devices with a Q as high as possible [24] or to reduce damping by using extremely low pressure for device operations. However, damping or energy dissipation is unpreventable irrespective of pressure. At lower pressures, dissipation is lower and vice versa. Philosophically speaking, an infinite Q , i.e., the absence of any dissipation, could never produce a sensor as the ability to excite or read the resonance would become vanishingly small. So, for practical realization of a resonant sensor, of course, we need a sort of finite dissipation. Surprisingly, an appropriate trade-off between mechanical sensitivity and quality factor is until now obscure. Any method that can provide any means to achieve significant improvement in nanomechanical sensitivity at lower Q condition can pave the way for a new horizon for ambient condition NEMS sensors. As an example, to be successful at the goal

of the thesis in developing a GC-NOMS gas sensor at atmosphere, any improvement of mechanical sensitivity will be potentially noteworthy, let alone the experimental challenges of loading gaseous molecules on the nanoscale device surface. For this purpose, one may revisit the relations between damping and mechanical sensing performance manifested by its frequency stability.

1.5.3 An approach to mitigating the damping effect in mechanical sensor performance

A version of the following discussion was published in [16]. Exquisite NEMS sensitivity is enabled through ultra-small mass or stiffness combined with precise resonant frequency determination. This allows perturbations to that frequency (such as mass or force) to be probed (see Figure 1.1). Robins' formula [18], articulated in the atomic force microscope (AFM) community by Rugar [19] and in NEMS by Roukes [20, 21], forms the basis for force and mass sensitivity analyses. It gives an estimation of the frequency stability based on the resonant quality factor, Q , and the comparison of noise energy to motional energy (see equation 1.3). Consequently, in accounting mechanical sensor performance, Q only provides half the contribution; the other half comes from how large the resonance signal is compared to the noise (SNR).

Interestingly, researchers primarily focus on achieving higher Q for better resolutions [23, 24, 25]. Whereas, strategies for SNR improvement have been scarcer [56], with almost no consideration given to the relationships between Q and SNR . There is an implicit assumption that Q will also benefit the signal fidelity. Figure 1.4 presents a DR response to changing Q from this traditional view. An extrinsic noise floor (e.g., readout amplifier) sets a noise that does not change with Q . Drive power is also assumed to be unchanged, resulting in amplitude loss with damping, and shrinking DR for lower Q .

There is, however, a case when $SNR \propto 1/Q$ that results in no sensitivity dependence on Q . This is not a special case. In fact, it is the general case if the DR is properly maximized. When instrument noise is negligible (Figure 1.4, right), lower- Q resonances reveal fundamentally lower intrinsic noise floor peaks (e.g., thermomechanical noise). The intrinsic upper end of the dynamic range is associated with the end of the linear response. The wider linewidth of a lower- Q resonance tolerates more nonlinearity and extends this linear range to larger amplitude. Combined, the two effects give $10^{-DR/20} \propto Q$.

This peculiar observation implies that frequency fluctuation noise, δf should not depend on Q in the case when thermomechanical noise is well resolved, and amplitude

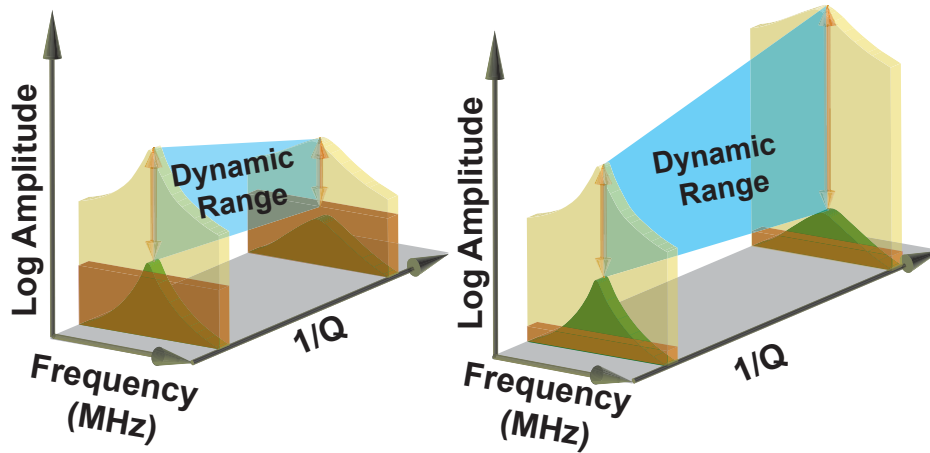


Figure 1.4: **The concept of maximizing linear dynamic range: Left: Traditional View.** The dynamic range DR (arrows) extends from the noise floor to the driven resonance peak (beige Lorentzian-peak shape). The instrumentation noise floor (brown rectangle) often obscures the thermomechanical noise floor (green Lorentzian-peak shape). Decreasing Q leads to a loss in system DR . **Right: Maximized DR case.** Well-resolved thermomechanical noise leads to a drop in noise peak value during increased damping; simultaneously, the upper end of the linear range becomes higher as nonlinearity onsets at a higher amplitude. System DR grows on both ends with falling Q . From [16]. Reprinted with permission from AAAS.

can be driven to nonlinearity. If true, the model provides a pathway to completely mitigate sensitivity loss due to low Q . Evading sensitivity loss due to larger damping can be an exciting property of lower- Q devices. This is an exciting prospect with wide-ranging implications for (frequency modulated) scanning probe microscopy, mass sensing and biosensing, and inertial and timing MEMS (gyroscopes [57], accelerometers [58], and crystal oscillators [59]). Such an exciting property of low Q mechanical sensor is until now experimentally unexplored with their sensing operation at the optimum dynamic range as a function of damping.

1.6 Thesis organization

In developing an integrated gas chromatography-NOMS gas sensor at atmospheric pressure and room temperature it is a priority to attain maximum mass sensitivity (minimum frequency stability for the device under test) in ambient conditions. With this goal, the thesis can have three parts. First, by considering the proposed approach of measuring intrinsic DR as a function of Q , measured frequency stability must be tested systematically from high vacuum to atmosphere. If stability improves with lowering Q , then it needs to be verified by sensing a physical quantity, which will be

the second step of the thesis. Finally, in the last phase, the experimental design of transferring separated gas from GC towards NOMS will be demonstrated through VOC detection on bare silicon nanomechanical resonator.

Chapter 2 embodies a brief theoretical background on nanomechanics in the light of continuum mechanics. It provides analytical treatments in details for specific resonance properties of interests for this thesis to elucidate advantages of the smaller dimension of nanomechanical resonators in sensing applications through continuum mechanics. Thus, the critical figure of merit (FOM), frequency stability, often referred to as Allan deviation, is deduced for characterizing any nano/mechanical sensor. Since nanomechanical frequency stability is ultimately limited by thermal motion, a concise description of the thermal motion of a resonator is discussed along with the driven linear mechanical motion. This chapter describes how the fundamental challenge of detecting infinitesimal thermal displacement of nanomechanical resonators is resolved precisely by placing an optical cavity adjacent to the movable mechanical beam: thus the system gets its name as NOMS. Section 2.4 introduces the experimental techniques used in this Ph.D. project for detecting nanomechanical motion and resonant characterizations. Finally, the experimental results of TM noise at different damping conditions, i.e., at different pressure for a DCB beam is presented and discussed. Resonance frequency drop at atmospheric pressure is attributed to the moisture adsorption from ambient humidity.

Chapter 3 discusses the details of driven response measurements just after the TM noise measurements at each pressure. Experimental results of this chapter demonstrate that DR of the mechanical resonator enhances with damping. It establishes what is hypothesized in section 1.5.3, that the term $Q \times SNR$ can have constant value for changing Q when the device is driven at the onset of nonlinearity for each Q .

Chapter 4 gives a detailed review of frequency stability theory and measurements issues. A comprehensive description of noise processes is provided here. In this chapter, we revisit Robins' phase noise analysis to figure out the role of damping on mechanical sensor performance. We confirm Robins' model and equation 1.3 and shed light on a common misunderstanding in the NEMS community about how phase noise translates to frequency noise.

Chapter 5 demonstrates experimentally measured frequency stability improves with damping both in the phase-locked loop (PLL) and open loop measurements, but these two methods improve stability by different principles. PLL has an inherent artifact on noise suppression by its gain factor. We analytically investigate details of noise shaping by PLL as well as open loop and compare with simulations. Interestingly, despite the artifact, PLL time constant agrees well with a measured time constant,

once loop shaping is accounted for, and validates the fidelity of PLL measurements for slow enough changes. In contrast to PLL, open loop measurements free from artifact are used to probe actual noise characteristics of NEMS. At low pressure (high- Q regime), the resonator has excess noise over thermal noise due to ubiquitous frequency-fluctuation noise in resonance, which gradually improves with damping to reach frequency stability down to the thermal limit at atmosphere. This chapter concludes that improved temperature fluctuations at larger damping suppress excess noise to get TM noise stability. Thus, not in Robins' theory, but for a real NEMS sensor, damping improves mechanical sensor performance. Within the Duffing limited regime, results in this chapter attests Robins' model by attaining same frequency stability because of the constant $Q \times SNR$ at different pressures.

Chapter 6 explores the temperature dependent properties of the optical ring and NEMS in the nano optomechanical systems. A modification in temperature shifts both optical ring resonance and NEMS resonance simultaneously and allows us to develop on-chip nanoptomechanical systems thermometry. The development of NOMS thermometry has two-fold implications in the current dissertation. Firstly, NOMS thermometry provides a way to directly observe the heat transfer process in nanoscale by comparing instantaneous ring and NEMS temperature at any instant. Such hybrid thermometry is unique by its nature to demonstrate nanoscale heat transfer for the first time without any reference thermometer in experiments. This secondary thermometry established in this chapter can have applications in biomedical applications and IR detections. Secondly, NOMS thermometry allows us to create a known temperature change on the chip, track the PLL response, and to compare the frequency shift with the predicted value. Thus temperature measurements in this chapter is a fidelity test of PLL experiments as well as to verify measured temperature resolutions are improved at atmosphere compared to in vacuum.

Chapter 7 presents the design of the proposed GC-NOMS gas sensor in ambient condition. Here, we have splitted inlets of Agilent 5890 gas-chromatography equally towards FID detector and NOMS detector by a temperature controlled gas transfer line from the splitter. Similar length of GC capillary from the splitter to FID and NOMS ensure a simultaneous gas loading on both detectors. FID provides conventional GC peaks for analytes with a characteristic retention time of each species of molecules. PLL tracked DCB in the NOMS provides a resonant frequency shift due to gas loading with the same retention time. The measured mass resolutions in ambient attains a value similar to that of high vacuum which demonstrates the ultimate success of the goal of this thesis. Such an ambient condition GC-NOMS gas sensor is a baby step for future generations GC-NOMS as a GC-MS.

Finally, Chapter 8 will summarize the content of this thesis in conjunction with the hypothesis and evaluate to which extent the objectives of the thesis have been reached through the original contributions. For optimum use of improved mechanical sensor performance in ambient, some future directions will be presented.

Chapter 2

Fundamentals of Nanomechanical resonant sensors

2.1 Introduction

A mechanical resonator with one of its dimension less than one micrometer is referred to as a nanomechanical resonator. Typically, such a system is actuated and detected by electrical means and thus named as nanoelectromechanical systems (NEMS). Along with device geometry, resonance frequency(f_0), stiffness (k), and the quality factor (Q) are three crucial parameters of a nanomechanical resonator. All of these parameters directly depend on the mechanical properties and energy losses of the nanomechanical resonators. Because of their infinitesimal dimensions, a suitable readout efficiency of NEMS's smaller displacements is an a priori requirement along with suitable actuation techniques. Recent progress in integrating a nanomechanical element to an optical cavity demonstrates excellent readout competence compared to electrical detection [50]. Thus, the terminology of NEMS nowadays can take the form of nano-optomechanical systems (NOMS). In this Ph.D. project, I have performed experiments with a NOMS device where the mechanical element is a doubly clamped beam (DCB) and adjacent to a racetrack optical cavity for improved readout ability. Whatever the system is either NEMS or NOMS, the sensing operation of this class of devices is based on tracking the motion of mechanical structure affected by the measurand of interest. Hence, detail of underlying principles of nanomechanical motion and resonance properties is essential to characterizing the figure of merits (FOM) of any nanomechanical sensors.

Nanomechanical structures are continuum mechanical structures. This chapter develops the theoretical foundation of nanomechanical motion based on the continuum mechanics and simple harmonic model to define required vibration properties which characterize a nanomechanical sensor. The first approach is a mechanical body model

by the standard elastic theory of continuum mechanics that explains the deformation of the oscillating mechanical structure. Thus, this model successfully elucidates mechanical effects on resonance properties of a mechanical body by defining its resonance frequency, stiffness, mode shape, *etc.* In the second approach, the mechanical resonator is treated as a 2nd order spring-mass system. Thus, the nanomechanical motion can be explained by simple harmonic oscillations, which allows us to understand various non-mechanical influences like damping on the motion of the beam. These approaches will lead us to determine the power spectral density of nanomechanical vibrations due to thermal motion. For developing a practical resonating gas sensor, it is essential to know how resonance frequency shifts due to the added mass. A mathematical treatment shows that the mass sensitivity of nanomechanical sensors is a purely mechanical effect.

After developing essentials of nanomechanical motion, a brief introduction on device actuation and detection is provided followed by experimental approaches involved in this thesis. Thermomechanical (TM) noise spectra measurements from high vacuum to atmosphere are not only important for determining the lower limit of DR for the thesis hypothesis but also significant for nanomechanical displacement calibration. This chapter shows the detailed thermal noise calibration method and estimation of background noise in the system. Often in this thesis, the term ‘thermal noise’ will be used as a stand for ‘thermomechanical (TM) noise’.

Discussions on thermomechanical (TM) noise measurements of a nanoscale doubly clamped beam at different pressures illuminate evolution of the quality factor (Q), the resonance frequency (f_0) and TM noise amplitude (a_{th}) as a function of air pressure [60, 61, 62, 63, 64, 65]. Experimental results show that evolution of Q satisfies existing power-law by air damping model but the resonance frequency, f_0 does not. Investigations on resonance frequency shift with air pressure reveal that water adsorptions on to the bare Si device surface [66, 67] from ambient humidity likely causes excess frequency shift from the air mass loading model [65, 68]. This short investigation gives an example usage of the mass sensing equations developed in the chapter, while highlighting NOMS incredible sensitivity level.

Frequency shift due to water adsorption has been utilized for developing humidity sensors by larger MEMS devices [36, 69, 70, 71, 72, 73] and in the NEMS domain [74]. All these works changed humidity in a controlled way to measure mechanical frequency shift due to moisture adsorption. As a matter of fact, despite extensive studies on different aspects of mechanical sensors including air pressure variations, investigations on ambient humidity on the resonance frequency of those devices are scarce, possibly due to diverse nature of water chemistry on the silicon surface [66, 67].

By an uncontrolled experiments, Hamed *et al.* [75] observed that adsorption from ambient air and native oxide formation on a freshly released cantilever took a few days to be saturated. Authors estimated adsorbed mass of water contaminations by comparing resonance frequency in air to that of high vacuum. Evolutions of the adsorbed water layer structure on silicon or native oxides as a function of relative humidity is an ongoing subject of various theoretical and experimental approaches for years, especially in the realm of surface chemistry [66, 67]. Quantifying the grown water layer thickness and mass of the water molecules are potentially relevant in the field of nanotechnology, e.g., during nanofabrication, bio-sensing, and environment monitoring. Not only the adsorbed vapor mass but also the number of water layer(s) grown on the device surface is determined here from TM noise spectra experiments. Adsorbed mass of vapor from ambient humidity ($RH = 40\%$) is calculated as 0.5% of device effective mass which corresponds to ~ 2 monolayers of water layer formation onto the device surface. Observed mass sensing capability without chemical functionalization is impressive in the context of the thesis goal for designing integrated GC-NOMS gas sensor in ambient by an uncoated NOMS. Discussions in section 2.4.2, 2.5.1, 2.5.1.1, A.6, and A.7 are from the published journal in Ref. [16].

2.2 Fundamentals of nanomechanical motion

2.2.1 Mechanical body model

For designing and modelling of a nanomechanical resonator, a theoretical understanding of its vibrations is necessary for correct interpretation of experimental data. Mechanical properties of nanomechanical resonators are often described by the Euler-Bernoulli theory for elastic deformations of solids. This dissertation considers two geometries *viz.* a doubly clamped beam (DCB) and a cantilever (CB). Results in the 4th order differential equation with solutions of modal shape, eigen frequencies and spring constants of beam during vibration are presented in Appendix A.1. As example, the first modal frequency of DCB is:

$$\Omega_1 = 6.466 \frac{t}{l^2} \sqrt{\frac{E}{\rho}}, \quad (2.1)$$

and the spring constant for a load force at the beam center is:

$$k = \frac{F}{u_{\max}} = \frac{32Ewt^3}{l^3}. \quad (2.2)$$

In the above equations, l , w , and t are the length, width and thickness of DCB respectively. E is the modulus of elasticity, and ρ is the density of device materials.

2.2.2 Simple damped harmonic model

The Euler-Bernoulli model can be turned into a simple, damped harmonic oscillator lumped element by adding a damping term, a force term, and integrating over the mode shape [76]. We show details in Appendix A.2. From this, amplitude and phase functional forms are:

$$a_0 = \frac{F_0}{M \sqrt{(\Omega_0^2 - \Omega^2)^2 + (\Gamma\Omega)^2}}; \quad (2.3)$$

$$\phi = \tan^{-1} \left(\frac{\Gamma\Omega}{(\Omega_0^2 - \Omega^2)} \right). \quad (2.4)$$

The derivative of phase and frequency can be shown to be A.2.1

$$\frac{\partial\phi}{\partial\Omega} = -\frac{2}{\Gamma} = -\frac{2Q}{\Omega_0}. \quad (2.5)$$

This relation is very important for understanding the translation of phase noise to frequency noise (see Chapter 4) and for working with the key figure of merit (FOM) of $\left| \frac{\partial f}{f_0} \right| = \left| \frac{\partial\phi}{2Q} \right|$.

2.2.3 Actuation

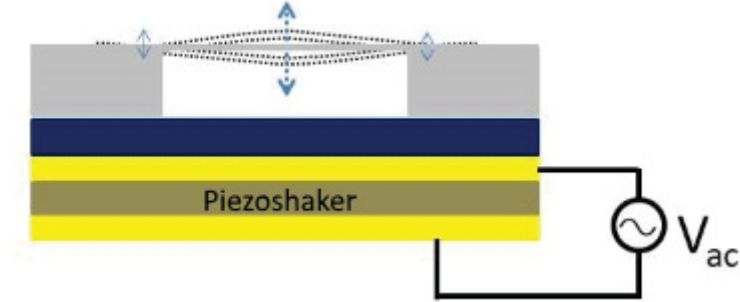


Figure 2.1: **Schematic view of a typical inertial piezoshaker actuation setup.** The applied voltage to the piezo induces the motion on the entire chip containing a doubly clamped beam (DCB). In the moving frame of the DCB chip, any periodic internal force acting on DCB center of the mass drives it into the motion. The range of the displacement at the midpoint of DCB is its resonance amplitude described in equation A.42. Small arrows on two sides indicate the effect of the bulk acoustic wave on DCB motion which will be discussed in Chapter 3.

As seen from the equation A.42, the maximum displacement of a linear resonator with a constant drive is proportional to Q , a figure of merit of the device which quantifies the damping, loss of energy by nonconservative forces. Hence to keep the oscillations sustained or to detect this displacement, we need to provide some external

excitations. Actuation techniques of nanomechanical devices are in principle limited to only a few, such as piezoelectric, electrostatic, thermal, magnetic, and recently adopted optical actuation techniques [53]. Each of these has its advantages or disadvantages. An excellent review of different aspects of various actuation techniques along with many detection techniques can be found in a recent review [77] and the references therein. Among those, piezoelectric actuation has two forms: piezoelectrical properties used by a macroscopic piezo shaker provides inertial actuation and direct piezoelectric actuation which often uses an integrated micro-or nanoscale piezoelectric actuator. We follow the usual practice in piezo drive in which the chip containing vibrating elements like NEMS (see Fig. 2.1) is glued to the top of a piezo shaker. When the piezo shaker is subjected to the driving voltage, it physically shakes the chip containing NEMS devices. Generally speaking, we use a shear piezo shaker which gives motions parallel to the chip plane.

2.2.4 Thermal noise driven motion

A force noise can be added to the simple damped harmonic equation of motion of section 2.2.2. Using an auto correlation function, the equipartition theorem and the fluctuation-dissipation theorem, the thermomechanical noise in the system can be derived as in Appendix A.3 to give nanomechanical displacement noise spectral density

$$S_x^{\text{th}}(\Omega) = \frac{4k_B T \Omega_0}{MQ[(\Omega_0^2 - \Omega^2)^2 + (\frac{\Omega_0}{Q}\Omega)^2]}, \quad (2.6)$$

with peak value at resonance frequency

$$S_x^{\text{th}}(\Omega_0) = \frac{4k_B T Q}{M\Omega_0^3} \text{ m}^2 \text{ Hz}^{-1}. \quad (2.7)$$

2.2.5 Quality factor changes with air pressure

Definition of Q and how to measure Q is discussed in appendix A.4. How air pressure affects Q , based on what value the Knudsen number (K_n) has, is covered there as well. For our purpose, Q vs. P should have dependence like $Q \sim P^0$ in vacuum, then $Q \sim P^{-1}$ in molecular flow regime, then $Q \sim P^{-1/2}$ in transitions and viscous flow regimes.

2.2.6 Nanomechanical sensitivity by mechanical body model

Rearranging the equation 2.1, resonance frequency of a nanomechanical resonator regarding device effective mass (M_{eff} , cf. A.2.2) can be found as

$$\Omega = \lambda_n^2 \left(\frac{EI}{M_{\text{eff}} l^3} \right)^{1/2}, \quad (2.8)$$

where, λ_n is a constant.

The derivative of the resonance frequency with respect to mass, M gives

$$\frac{d\Omega}{dM} = -\frac{1}{2} \frac{(EI)^{1/2}}{l^{3/2}} M_{\text{eff}}^{-3/2}. \quad (2.9)$$

By dividing equation 2.9 by equation 2.8, change in frequency due to a mass change is found inversely proportional to device mass or

$$\frac{\frac{d\Omega}{dM}}{\Omega} = -\frac{1}{2M_{\text{eff}}}. \quad (2.10)$$

If the mass change is minimal, i.e., $dM \ll M_{\text{eff}}$, we may write, $dM \approx \delta m$ and assume that the spring constant of the mode which depends on device geometry and elastic properties remains unaffected. Then the corresponding change in resonance frequency, $\delta\Omega$ by the equation 2.10 is.

$$\delta\Omega = -\frac{\delta M}{2M_{\text{eff}}}\Omega. \quad (2.11)$$

For fundamental mode, $\Omega_0 = 2\pi f_0$. Hence, minimum resolvable mass by a nanomechanical resonator can be written in terms of linear frequency as

$$\delta m = -2M_{\text{eff}} \frac{\delta f}{f_0}. \quad (2.12)$$

2.3 Readout of nanomechanical motion

From discussions above we have seen that operation of a nanomechanical resonator relies on the motion of the tiny solid element such as a cantilever or a doubly clamped beam (as in the current work), and, is modeled as a one-dimensional damped harmonic oscillator under a time-dependent driving force $F(t)$. Typically, resonance properties of such nanomechanical motion can be realized through electrical actuation and detection, and the resonator is referred to as NEMS. Hence, efficient transduction mechanisms are essential for NEMS operation and applications. An input transducer or the actuator converts an electrical or optical signal into the driving force to generate the motion. On the other hand, the mechanical motion is converted into a detectable electrical modulation signal by the output transducer, which can be named as the detector or motion (displacement) sensor. For typical NEMS operations, both transductions efficacy must be sensitive enough to transduce force and infinitesimal displacement

noise density above the readout noise. In the current work, we have used piezo actuation, which is found useful to drive the device harder to attain the upper end of the dynamic range (DR). In section 2.2.4 we have seen that even in the absence of any driving signal nanoscale mechanical motion appears resonantly due to thermal force noise around $\text{pm Hz}^{-1/2}$. Such TM noise amplitude characterizes the bottom of the DR . Hence, detection of infinitesimal nanomechanical oscillation due to thermal noise is required for practical realization of a nanomechanical resonant sensor. So, effective transduction of thermomechanical displacement noise is a vital factor which limits further development and widespread implementation of nanomechanical sensors, especially at an ambient condition where TM noise amplitude diminishes due to enhanced damping. A variety of NEMS actuation and detection techniques in the electronic domain have been adopted including capacitive [78, 79, 80], piezoelectric [81, 82], piezoresistive [28, 83, 84], electrothermal [85] along with free space optics [86, 87, 88] and cavity optomechanics [89, 90, 91, 92, 49, 93]. A comprehensive discussion of different techniques can be found elsewhere [47]. Electrical readout techniques have a disadvantage as these need to be developed for a specific system with specific requirements and not transferable to a different geometry or materials.

To overcome such drawbacks in the readout, conventional free space optics [94, 95] demonstrates high displacement sensitivity but is not suitable for a device smaller than the diffraction limit. Not only the constraints in device size, but free space optics also are not efficient enough in high-frequency operations [96]. Among different optical techniques reviewed in Ref. [93, 47, 54] cavity optomechanics is treated as an efficient technique for reading out and controlling of mechanical motion through recirculated optical photons inside the cavity, and thus electrical domain NEMS devices are now often known as NOMS. NOMS devices have emerged as an excellent option for overcoming drawbacks of efficient transduction of nanomechanical motion by demonstrating unprecedented displacement sensitivity around 10^{-18} m [97, 98]. On-chip optical cavities in the system improve transduction efficacy as photons contained within the cavities interact multiple times with the nanomechanical devices before dissipations [54]. Device operations in the optical near-field eliminate size constraint imposed by the diffraction limit. Also, the optical detection scheme of nanomechanical displacements by NOMS is neither frequency nor bandwidth limited, which allows suitable access for high-frequency operations while leaving piezo actuation efficacy retained.

2.3.1 Fundamentals of optomechanical readout

This section is devoted to explaining the potential of cavity optomechanics in detecting small mechanical motion displayed by a nanomechanical resonator. Admittedly, only the fundamentals of optomechanics in NEMS motion detection will be discussed, and details are skipped.

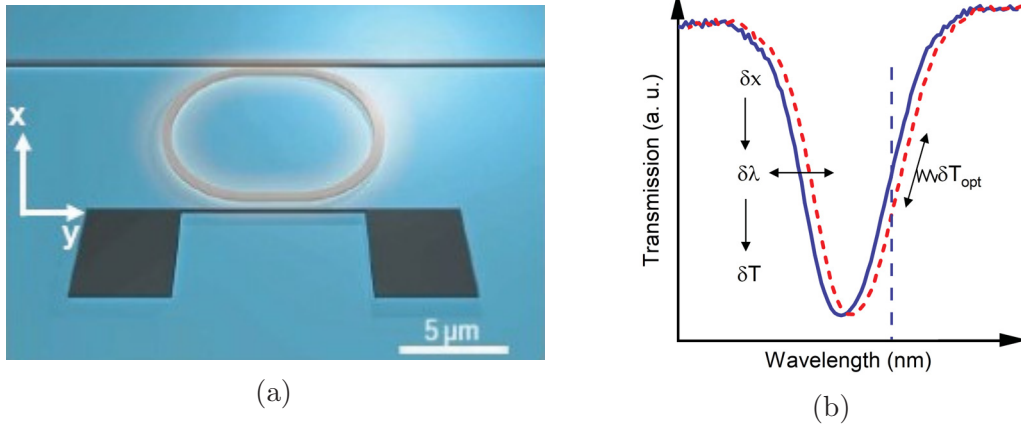


Figure 2.2: **Illustrations of nanomechanical motion detection through evanescent wave coupling.** a) Cartoon of a NOMS chip with a waveguide bus (top), racetrack optical resonator (middle), and mechanically resonant doubly clamped beam (bottom). The in-plane motion of the DCB is along the x-axis and changes the gap between ring and DCB to alter the optical resonance in the ring. b) Concept of the optical cavity resonance shift caused by mechanical beam motion. Oscillation in displacement δx of the mechanical beam modulates the optical resonance wavelength $\delta \lambda$ which, when probe light is situated on the side slope of the cavity, transduces to transmission modulation $\delta T_{\text{optical}}$. a.u., arbitrary units. From [16]. Reprinted with permission from AAAS.

Cavity optomechanics, as its name suggests, is the description of the interaction of a mechanical resonator coupled to the light inside an optical cavity. With the advent of micro- and nanofabrication a variety of different optomechanical systems has been implemented such as Fabry-Perot cavities [99, 100, 101, 102, 103, 104], whispering gallery mode resonator [105, 106], photonic crystals [107], and near field coupling [50, 108]. The principle of mechanical displacement detection through optomechanics is straightforward. Mechanical motion modifies the cavity's resonance condition and thus the intensity of circulated light inside the cavity. A fast photodetector can easily track this intensity change to register the corresponding nanomechanical displacement. Either by radiation pressure on an exposed surface or by optical gradient forces due to an evanescent coupling between light waves, optical forces can be generated which can displace a physical entity.

In our lab, we are investigating near-field optomechanics to improve mechanical sensor performance to develop future generation ambient conditioned mass spectrometer. How optical resonance condition can alter by mechanical displacement in an optomechanical system is described in A.8 for a generic Fabry-Perot cavity, and details of the theory of displacement transduction of NOMS in Figure 2.2 are described in previously published work [54]. The study [54] from our group established that near-field optical transduction of nanomechanical motion in on-chip NOMS as in the schematic 2.2 (a) shows higher responsivity than free space interferometry. Throughout my Ph.D. research, I have characterized similar devices. Here, change in the position of DCB in the evanescent optical field near the racetrack alter the index of refraction and the cavity resonance. The coupled waveguide to the racetrack is made between two grating couplers; one is input and another for throughput. Sitting on the maximum slope (which corresponds to the maximum detection sensitivity) of one of the optical resonances as in 2.2 (b) a photodetector records the mechanical displacement. The mechanical beam is made external to facilitate its mask-less release process and also, so it does not modify the physical properties of the optical ring. At the same time, it can be assumed that any gas flowing over the DCB beam will not interrupt the optical transmission. This device is made specially for gas sensing.

Readout linearity

The goal of the thesis is to drive the device at a large amplitude closer to the onset of Duffing nonlinearity. Presence of other nonlinearity can contradict the research hypothesis of improved DR with decreasing Q . So, it is necessary to check the readout linearity in experiments. An optomechanical system described in Figure 2.2 uses optical resonance shift proportional to mechanical displacement to perform the optomechanical transduction. The strength of the optomechanical transduction depends on the gap between the optical ring and the mechanical resonator. Evanescent optical field exponentially decreases with increasing gap and results in poor optomechanical coupling [50] or vice versa. Consequently, larger nanomechanical displacements can linearly enhance the coupling by reducing the gap from the adjacent ring, which results in a cavity shift. Such a cavity shift also moves the probe power (T) from the probe wavelength (λ) set at the largest slope (where, $dT/d\lambda = 0$, as in Figure 2.3) into nonlinear zone of the optical resonance where linear approximation (proportional shift of cavity with mechanical displacement) does not exist. This phenomenon is known as readout nonlinearity of an optomechanical system.

The strength of the optomechanical transduction is formulated by the light angular

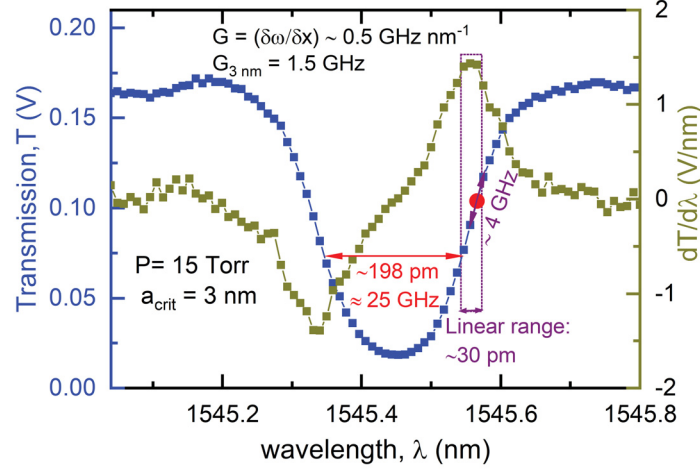


Figure 2.3: **Measured optical transmission and its first derivative $dT/d\lambda$ at 15 Torr.** The measured optical resonance (blue) has FWHM around 198 pm \approx 25GHz corresponds to a optical quality factor, $Q_{\text{opt}} \sim 7800$. The red data point in the optical resonance has a maximum slope (dark green). The violet rectangle shows that the linear approximation spans for a range of 30 pm equivalent to 4 GHz optical cavity shift. For a 3 nm mechanical displacement expected cavity shift ± 1.5 GHz is certainly within linear readout regime.

frequency ($\omega = c/\lambda$, where, $c = 3 \times 10^8 \text{ ms}^{-1}$ is the speed of light) shift per unit displacement of the mechanical resonator and known as optomechanical coupling factor, $G = (\delta\omega/\delta x)$. In the Appendices B.1.5, an exemplary calculation of G for a similar NOMS has been shown for a 120 nm gap. The experimental value, $G \sim 2.83 \text{ rad GHz nm}^{-1}$ agrees well with theory. In chapter 3, we will show that we can reach Duffing onset at medium pressures, such as at 15 Torr. The critical amplitude at 15 Torr is ~ 3 nm, which is the largest in Figure 3.3. It should be noted that the DCB used in the main text of the thesis is 160 nm away from the microring and G is expected to be lower than $2.83 \text{ rad GHz nm}^{-1}$.

For a quick check of readout linearity, we can consider the measured value of $G/2\pi \sim 0.5 \text{ GHz nm}^{-1}$ from the Appendix that results in ~ 1.5 GHz cavity shift by 3 nm mechanical displacement, and can be compared to equivalent optical frequency shift ~ 4 GHz from the probe wavelength in optical transmission measured at 15 Torr, illustrated in the Figure 2.3. These results indicate that for a maximum driven amplitude before the Duffing nonlinearity, experiments in the current dissertation is not affected by readout nonlinearity.

2.4 Experiments

2.4.1 Device fabrications

Former Ph.D. student from our group Dr. Vincent T. K. Sauer has designed the device for fabrications. Dr. Sauer has discussed the detail of fabrications and optomechanical characterizations in his Ph.D. thesis [109] which are also available in published works [48, 49, 50, 51, 52, 53]. In this dissertation, I have used similar devices from the same fabrication batch. So, in the context of the thesis, I have skipped those fabrication and optomechanical aspects studied by Dr. Sauer.

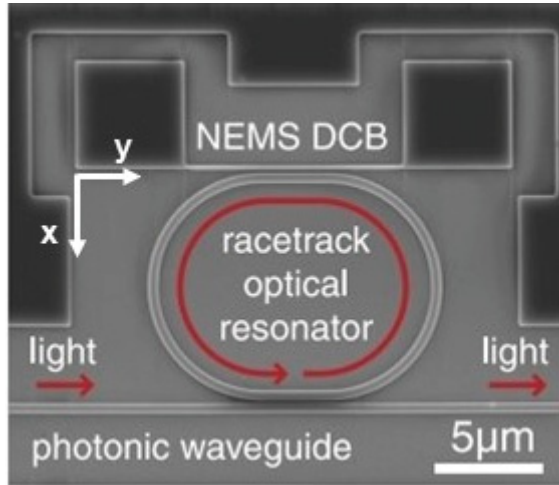


Figure 2.4: **Annotated SEM image of the nano-optomechanical system device.** A mechanically released doubly clamped beam (NEMS) is adjacent to a racetrack optical cavity and bus photonic waveguide, all patterned in 220 nm thick silicon-on-insulator. Device is 160 nm apart from the optical ring with dimensions $9.75\ \mu\text{m} \times 160\ \text{nm} \times 220\ \text{nm}$.

A racetrack resonator optical cavity structure is used to detect the nanomechanical motion of the doubly-clamped beam [50]. A photonic foundry (IMEC) fabricates the 220 nm silicon-on-insulator devices, and NEMS devices are released by post-processing at the University of Alberta Nanofab. The NEMS is designed to be narrower than the waveguides, facilitating a maskless release step wherein the NEMS is released without releasing the photonic elements. The NEMS is coupled laterally to the photonic elements and is contained in the same device layer. Further description of the fabrication can be found in [50, 109]. An SEM picture of the primary device used in this work is shown in Figure 2.4.

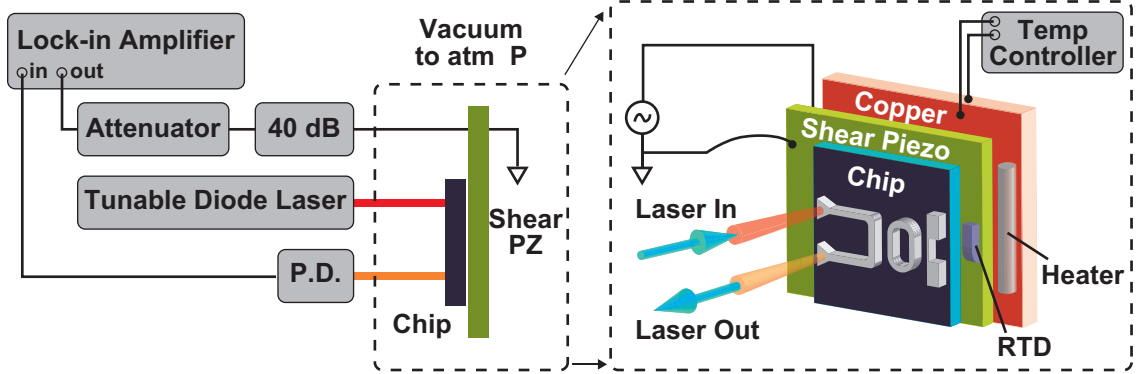


Figure 2.5: **Schematic of experimental setup.** The right panel depicts a graphical arrangement of a NOMS device on a Silicon chip surface mounted on the top of the piezo shaker (green slab) followed by further mounting on a copper plate which facilitates a thermal contact to the base of the pressure controlling chamber. The heater on top of copper is controlled by the temperature controller via the temperature sensor (RTD) placed on the top surface of the piezo and just a few mm away from the chip edge. The left panel is the arrangement of detection and measurement unit where a Zurich instrument HF2 lock-in is the heart of nanomechanical vibration characterizations. The 40 dB box represents a Minicircuits LZY-22+ power amplifier, through which a maximum power of 45 dBm is available. In experiments, drive power is generally limited to 36 dBm before the shear piezo starts to heat substantially and shift the optomechanical resonance. From [16]. Reprinted with permission from AAAS.

2.4.2 Experimental setup

The nano-optomechanical system used in the thesis is shown in Figure 2.4, along with the principle of detection in Figure 2.2 (b). The doubly clamped beam mechanical resonance is detected using an all-pass implementation of a racetrack resonator optical cavity. Light couples from a silicon strip waveguide to circulate in a race-track optical cavity resonator. In-plane displacement of the doubly clamped beam mechanical resonator modifies the local index of refraction of the racetrack, which changes the optical resonance wavelength. With the probe light parked on the side of the cavity, mechanical vibration is transduced to modulation of the optical transmission. Multiple passes of the light contribute to the excellent displacement sensitivity. A comparatively lower finesse (around ~ 70 , see B.1.5) and weaker optomechanical coupling along with smaller mechanical displacement (for a maximum ~ 3 nm driven amplitude in Figure 3.3 in the next chapter for 15 Torr) provide linear transduction to the upper end of the dynamic range (also see Figure B.5).

A Santec TSL-510 fiber-coupled tunable diode laser (TDL) is used to probe the device. To achieve the largest displacement sensitivity, the measurement wavelength

is detuned from the optical cavity center by approximately half the cavity linewidth. For both thermomechanical and driven signals, the power modulation of the detuned probe which is caused by the mechanical beam motion is measured using a Zurich Instruments HF2LI lock-in amplifier (LIA). The LIA provides the drive voltage sent to the shear-mode piezo (Noliac CSAP03) which is used to mechanically drive the DCBs in the wafer plane. A power amplifier (Minicircuits LZY-22+) is used to achieve higher drive when required. The NOMS chip is mounted on the piezo shaker with thermal conductive silver epoxy. The piezo is placed on top of a copper plate with an attached resistive heater and platinum resistance thermometer (RTD) (both placed roughly as drawn in Figure 2.5) which are operated using a PID controller (Cryo-con Model 24C). The device is placed in a vacuum chamber, and light from the TDL is coupled from free space through the chamber’s optical window and into the nanophotonic circuits using optical grating couplers. The chamber is pumped to below 1×10^{-4} Torr, and a bleed valve is used to raise the pressure in the chamber to change the damping in the system. Like the Allan deviation measurements, the DCB is implemented into a phase-locked loop (PLL) using the Zurich’s built-in PLL module to track any shift in resonance frequency due to temperature change made by the resistive heater.

2.5 Experimental results and discussions on thermal noise measurements

2.5.1 Thermomechanical noise detection

Resolving TM noise from high vacuum to atmosphere is not only crucial for gas sensing, but also it is fundamentally vital to test the effect of pressure on the intrinsic dynamic range (DR) of the device. The ultimate goal of this Ph.D. project is to test the evolution of DR as a function of pressure so that an optimum mass sensitivity can be achieved with the proposed GC-NOMS gas sensor. With this aim, we examined the Brownian motion of the same NOMS device for a wide range of pressures ranging from $\geq 100 \mu$ Torr to 760 Torr at room temperature in order to measure resonance properties such as resonance frequency, $\Omega/2\pi$ and loaded quality factor, Q . This method has the benefit of keeping all other parameters that could affect the result precisely identical. Following figures shows the measured displacement noise $S_x^{1/2}$ (*cf.* section 2.2.4) in an example doubly clamped beam, measured in a vacuum where Q is high and at atmospheric pressure where Q is low. As per convention, values for S_x are calibrated from voltage signals (S_V) by assuming the peak noise relation (derived via equipartition theorem, see appendix A.3) of equation 2.7.

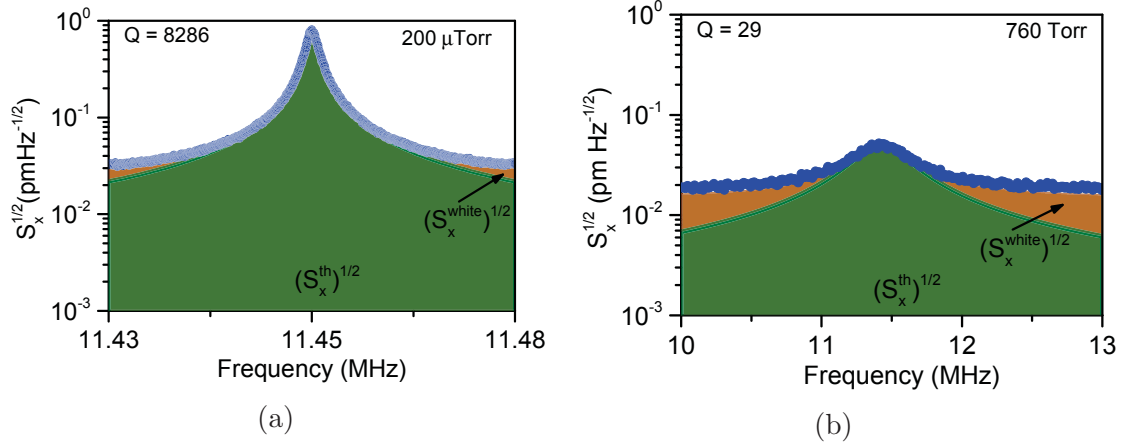


Figure 2.6: **Displacement noise $S_x^{1/2}$ (blue circles) of the doubly clamped silicon beam ($9.75\ \mu\text{m} \times 180\ \text{nm} \times 220\ \text{nm}$) shown in Figure 2.4.** (a) is at high Q measured in a vacuum; b) is at low Q measured at atmospheric pressure. The green fit $(S_x^{\text{th}})^{1/2}$ is resolved out of the orange (white-noise) background $(S_x^{\text{white}})^{1/2}$ near resonance. The peak noise value is suppressed at lower Q . From [16]. Reprinted with permission from AAAS.

In both cases, the noise is dominated by the thermomechanical term near resonance, flattening to a white background far from resonance. The relatively large peak at high- Q sharply juts out of the background, dominating for 30 kHz, which is about 20 linewidths. The suppressed low- Q peak also still reaches out of the background for about 1.5 linewidths (600 kHz). These data show that our system reaches the bottom end of the full dynamic range for at least 30 kHz measurement bandwidth. Of particular note is how the noise floor a_{th} diminishes as the pressure increases (and Q decreases). This is consistent with equation 2.7 which confirms that a_{th} is proportional to $Q^{+1/2}$ and can be conceptually understood in the following way. The area under the thermomechanical resonance curve is conserved for a given temperature (in proportion to $k_B T$; note that, k is used in this manuscript for spring constant and k_B is for Boltzmann constant.); as the width of the curve increases (Q decreases), the peak value must fall in order to compensate. The reduction in Q from high vacuum to 760 Torr is about a factor of 286. We thus expect a drop in peak height by about $17\times$, and this is what is observed. ¹

¹Note that atmospheric pressure at Edmonton City, Alberta, Canada, is around 700 Torr (https://edmonton.weatherstats.ca/charts/pressure_station-hourly.html),. Throughout the thesis, we quote pressure at 760 Torr as a colloquial reference to atmospheric pressure. The chamber was not over pressurized. Rather, when 760 Torr is listed in the thesis, it refers to atmospheric pressure, which in the case of the Edmonton taken measurements, is about 700 Torr.

2.5.1.1 Thermomechanical noise calibration

Accurately determining the displacement noise floor (*cf.* Fig. 2.6 and Eqn. 2.7) is crucial for the analysis in this work. We follow the standard established method for thermomechanical noise calibration [110, 111] which is nicely detailed in [112]. A summary of the procedure appears below.

The voltage noise power spectral density (S_V in $V^2\text{Hz}^{-1}$) of the photodetector output, if peak shaped (as in Fig. 2.6), can be assumed to be the sum of thermomechanical noise and a white background (due to instrumentation noise)

$$S_V(\Omega) = S_V^{\text{th}}(\Omega) + S_V^{\text{white}}(\Omega). \quad (2.13)$$

By comparing the measured noise to theoretically expected displacement noise spectral density S_x in m^2Hz^{-1} , we can calibrate the system responsivity \mathfrak{R} in Vm^{-1} . We measure S_V using a Zurich instrument HF2 lock-in amplifier in zoomFFT mode up to 78 Torr and by an Agilent 8593E spectrum analyzer from 120 – 760 Torr (the latter being better suited to larger frequency spans) while holding temperature constant at 298 K. Measured peaks and quality factors (Q) are used in the calibration. What is needed is a theoretical functional form for $S_x = S_x^{\text{th}} + S_x^{\text{white}}$. This is derived (see Appendix A.3) via equipartition theorem resulting from the Langevin (random thermal) [113] force acting on the resonating normal mode and is given by

$$S_x^{\text{th}}(\Omega) = \frac{S_F^{\text{th}}(\Omega)}{M_{\text{eff}}^2} \frac{1}{(\Omega_0^2 - \Omega^2)^2 + (\Gamma\Omega)^2} = \frac{S_F^{\text{th}}(\Omega)}{M_{\text{eff}}^2} \frac{1}{((\Omega_0 - \Omega)(\Omega_0 + \Omega))^2 + (\frac{\Omega_0}{Q}\Omega)^2}, \quad (2.14)$$

where, $S_F^{\text{th}} = (4k_B T M_{\text{eff}} \Omega_0)/Q$ in N^2Hz^{-1} is the thermal force spectral density acting on the nanoscale resonator. Here, k_B , M_{eff} , $\Omega_0/2\pi$, Q and, $\Gamma/2\pi = \Omega_0/(2\pi \times Q)$ are Boltzmann constant, effective mass, resonance frequency, quality factor and linewidth of the DCB resonator. At $\Omega = \Omega_0$ equation 2.14 reduces to

$$S_x^{\text{th}}(\Omega_0) = \frac{4k_B T Q}{M_{\text{eff}} \Omega_0^3} \text{m}^2\text{Hz}^{-1}. \quad (2.15)$$

Thus the r.m.s displacement peak of the power spectral density in absence of any background noise can be found as (in a 1 Hz bandwidth)

$$a_{\text{th}} = \sqrt{S_x^{\text{th}}(\Omega_0)} \text{m Hz}^{-\frac{1}{2}} \times 1 \text{Hz}^{\frac{1}{2}} = \sqrt{\frac{4k_B T Q}{M_{\text{eff}} \Omega_0^3}} \text{m}. \quad (2.16)$$

If $|\Omega_0 - \Omega| \ll \Omega_0$, then the displacement spectral density curve described in equation 2.14 can be reduced with approximations $(\Omega_0 - \Omega)(\Omega_0 + \Omega) \cong 2\Omega_0(\Omega_0 - \Omega)$ and

$\Omega_0\Omega/Q \cong \Omega_0\Omega_0/Q$ as below

$$S_x^{\text{th}}(\Omega) = \frac{S_F^{\text{th}}(\Omega)}{M_{\text{eff}}^2} \frac{1}{4\Omega_0^2(\Omega_0 - \Omega)^2 + (\frac{\Omega_0}{Q}\Omega_0)^2} = \frac{1}{\Omega_0^2} \frac{S_F^{\text{th}}(\Omega)}{M_{\text{eff}}^2} \frac{1}{4(\Omega_0 - \Omega)^2 + (\frac{\Omega_0}{Q})^2}. \quad (2.17)$$

Equation 2.17 is a Lorentzian function to which a white background can be added

$$S_x(\Omega) = S_x^{\text{th}}(\Omega) + S_x^{\text{white}}(\Omega). \quad (2.18)$$

By fitting the voltage noise to a Lorentzian with background (directly comparing equation 2.13 with equations 2.17 and 2.18), the calibration of S_x to S_V is naturally achieved.

2.5.1.2 Calculation of displacement responsivity, $\Re \text{Vm}^{-1}$

A Lorentzian curve fit was performed for measured $S_V \text{V}^2\text{Hz}^{-1}$ at each pressure to obtain the resonance frequency, f_0 and mechanical quality factor, Q and the background S_V^{white} . The peak height of this measured spectral density can be calculated as

$$S_{V_{\text{pk}}}^{\text{th}} = S_V(\Omega_0) - S_V^{\text{white}} \text{ in } \text{V}^2\text{Hz}^{-1}. \quad (2.19)$$

Now, substituting the measured f_0 and Q from Lorentzian fit into equation 2.15 gives displacement power spectral density $S_x^{\text{th}}(\Omega_0)$ in m^2Hz^{-1} of the resonator vibration at its resonance frequency and depends on damping induced by the chosen pressure. Defining $S_{x_{\text{pk}}}^{\text{th}}$ as

$$S_{x_{\text{pk}}}^{\text{th}} = S_x(\Omega_0) - S_x^{\text{white}} \text{ in } \text{m}^2\text{Hz}^{-1}, \quad (2.20)$$

means that $\sqrt{S_{x_{\text{pk}}}^{\text{th}}}$ in $\text{m Hz}^{-\frac{1}{2}}$ must be equal to the measured peak height, $\sqrt{S_{V_{\text{pk}}}^{\text{th}}}$ in $\text{V Hz}^{-\frac{1}{2}}$ of voltage spectral density given by equation 2.19. Thus, measured voltage in experiments can easily be converted into displacement by obtaining the conversion factor, \Re as below

$$\Re \text{Vm}^{-1} = \frac{\sqrt{S_{V_{\text{pk}}}^{\text{th}}} \text{ V Hz}^{-\frac{1}{2}}}{\sqrt{S_{x_{\text{pk}}}^{\text{th}}} \text{ m Hz}^{-\frac{1}{2}}}. \quad (2.21)$$

Figure 2.6 uses this method to calibrate the vertical axis and it is used to convert all measured driven amplitude in voltage into displacement throughout the thesis. ²

²This responsivity calibration only works when amplitudes are in the linear regime.

2.5.2 Effect of pressure on the resonance properties of the doubly clamped beam

2.5.2.1 Quality factor variation with pressure

The quality factor of a mechanical resonator is inverse of damping (*cf.* simple harmonic equations A.26 - A.28) and describes the sharpness of resonance peak (*cf.* Figure A.2a) and is detailed in Appendices A.2 to A.4. Physically it is the ratio of stored energy to the dissipated energy in a cycle (equation A.65). Effect of pressure on the measured quality factor is reviewed based on existing literature and formulated in Table 1 to compare experimental results in Figure 2.7.

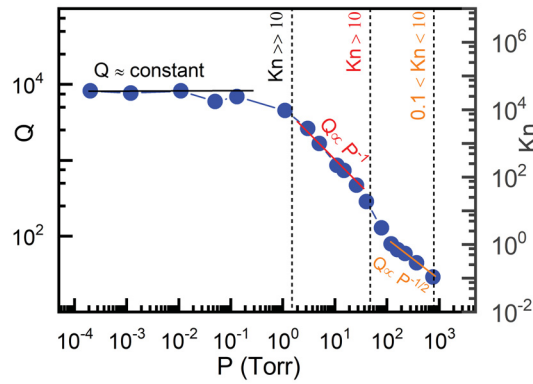


Figure 2.7: **Measured quality factor variations of the DCB as a function of pressure.** Lorentzian fitting for measured TM noise data at each pressure gives the corresponding Q . The right axis is the Knudsen number calculated by equation A.66. Measured data shows a typical Q vs. P relation with the power law, $Q \propto P^r$; where, $r = 0, -1, -0.5$ for intrinsic, FMF and viscous regime respectively.

Pressure dependence of quality factor is illustrated in Figure 2.7. It follows the well-recognized power law, $Q \propto P^r$, discussed in appendix A.5 [62]. This power law is derived from the gas rarefaction effect characterized by Knudsen number, K_n . K_n is the ratio of air mean free path and the characteristic device dimension. Based on the K_n the $Q \propto P^r$ relation is tabulated in table A.1 to compare experimental Q s in the Figure 2.7. It is evident that with increasing pressure, the gradual entrance of air molecules into the chamber slowly enhances the coupling between the NOMS device and its surroundings to introduce substantial air damping.

Measured Q s from TM noise spectra at different pressures divides the full pressure range into three well-known regimes which inform us of dominating damping mechanism in each regime. From high vacuum to 1 Torr (where, $K_n \gg 10$), Q is almost constant with pressure and suggests that intrinsic resonator losses dominate within this pressure range. At moderately low pressures (up to 40 Torr) Q decreases inversely with P

because of momentum exchange by noninteracting air molecules. From the calculated K_n we can see our device (geometry) hardly arrive at the continuum regime at 760 Torr. From the plot, the transition and slip regime dominate from 78 to 760 Torr where Q scales with $P^{-0.5}$. These two regimes are collectively known as viscous regime [60, 61].

Besides air damping discussed so far, drag force damping and squeeze film damping should not be neglected at 760 Torr. At higher pressures, fluid flow between the moving structure and a fixed substrate can be squeezed which is known as squeeze film damping and a significant one among different fluid damping, if it exists. Another source of damping is the damping due to drag force. Airflow at the top of resonator causes the drag force damping which is a significant fluid damping in case of larger gaps [114]. For narrow gap (which is the present case), loss due to drag force is negligible compared to squeeze film damping. Appendix A.7 shows squeeze film damping should also be relatively small in our system.

2.5.2.2 Effect of air pressure and humidity on the resonance frequency

So far we have discussed how loaded Q changes with pressure. Any variation in Q also shifts the resonance frequency as

$$f_d = f_0 \sqrt{1 - \frac{1}{4Q^2}} \quad (2.22)$$

where, f_0 is the measured intrinsic resonance frequency at the vacuum, f_d is the measured damped resonance frequency at pressure with quality factor Q , and drops by the factor $\sqrt{1 - \frac{1}{4Q^2}}$. In classical mechanics, an oscillator can remain in rest, which is a contrast to quantum mechanics. A quantum oscillator is always in motion. The small residual motion at absolute zero temperature is known as the zero-point fluctuation x_{zpf} and corresponding energy is called the zero-point energy. With the aid of equipartition theorem (see section A.3) we can compare the energy of quantum oscillator and mode energy of a thermally driven oscillator at room temperature: $E = \hbar\Omega_0 n = k_B T = (1/2)M_{\text{eff}}\Omega_0^2 = (1/2)ka_{\text{th}}^2$, where, \hbar is the reduced Plank constant. If the room temperature (298 K in this thesis) resonance frequency, $\Omega_0 = 2\pi f_0$ is measured we can estimate number of quanta in the mechanical mode by solving the equation. For the DCB under test we have, $f_0 \approx 11.45$ MHz which corresponds to 540.6 k quanta in the fundamental mode by $n = k_B T / \hbar\Omega_0$. Due to such a large number of quanta in the fundamental mode, we can ignore ground state contribution to the NEMS energies.

In viscous regime, i.e., at higher pressures, the air mass effect is simply proportional to the product of mass and acceleration of the air molecules on the mechanical beam

surface. A vibrating mechanical body pushes away air molecules around it. Damping effect due to loaded air molecules onto the device surface shifts the intrinsic resonance frequency by an amount [65, 68]

$$\Delta f = \frac{\pi f_0 R^3}{3M_{\text{eff}} R_0 T} \left(M_a P + \frac{9}{4R} \sqrt{\frac{\mu R_0 T M_a P}{\pi f_0}} \right), \quad (2.23)$$

where, Δf is the frequency shift due to air mass loading onto the device surface, R is the radius of the hypothetical sphere equals the width of the vibrating mechanical structure, M_{eff} is the effective mass of the device, $R_0 = 8.317 \text{ J mole}^{-1} \text{ K}^{-1}$ is the gas constant, T is the absolute temperature, $M_a = 0.029 \text{ kg mole}^{-1}$ is the molar mass of air, $\mu = 1.85 \times 10^{-5} \text{ kg ms}^{-1}$ is the viscosity of air, and P is the measurement pressure.

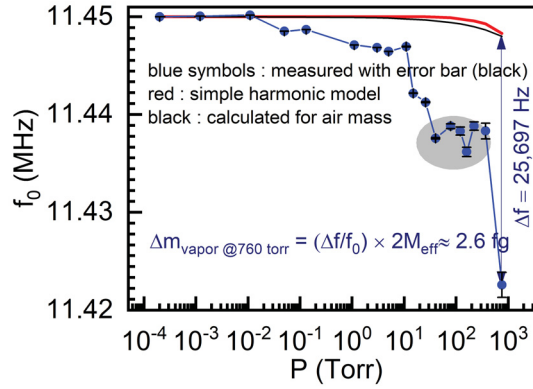


Figure 2.8: **Resonance frequency (f_0) shift with pressure.** f_0 at different air pressures are extracted at the same time of Q extractions from Lorentzian fit of TM noise spectra. So, both f_0 and Q are subjected to similar experimental conditions at each measurement pressure. A slight discrepancy between fitted data by equation 2.22 (red) and 2.24 (black) is evident for air mass. Surprisingly, experimental data with increasing pressures move away from air mass loading predictions (equation 2.23). The sharp fall in resonance frequency at atmosphere attributes to ambient moisture adsorption. Shaded area indicates that somehow, the amount of ambient vapor at these pressures are quite similar. Since we did not perform any systematic change in humidity conditions, any conclusions on vapor contents will be misleading except 760 Torr. Lorentzian fitting of TM noise data provides errors (black bars on the measured data symbols) in resonance frequency measurement, which are reasonably satisfactory at lower pressures. At 760 Torr broad peak with small height may cause a significant error (1281 Hz) in resonance frequency extraction, which is only $\sim 5\%$ of total shift (25,697 Hz) due to vapor adsorption. In other way, these error bars on resonance frequency imply that measured frequency shift, Δf has too many significant digits.

Damped resonance frequency at different pressures due to air mass loading can be

calculated by Equation 2.23

$$f_d = f_0 - \Delta f. \quad (2.24)$$

Authors [115] approximated the cantilever as a row of spheres with radius R in modeling equation 2.23. Nanomechanical sensor communities often use this equation to measure molar mass of unknown gas, e.g. [68]. Equation 2.22 and 2.23 are valid when air pressure is the dominant damping mechanism, although slight discrepancies between these two models are not surprising [65]. The following figure compares the measured and theoretically predicted resonance frequencies with pressure.

In the Figure 2.8 both calculated fitting lines by equation 2.22 (red) and 2.24 are in good agreement with each other at lower pressures with an exception at higher pressures. Air mass loading causes additional small frequency shifts at higher pressures, which agrees with the observations made in the ref. [65]. However, measured resonance frequency after 50 mTorr declines progressively from fitting, and at atmospheric pressure, it drops a maximum by $\sim 0.2\%$ of measured frequency at high vacuum. We attribute such resonance frequency drops different from air mass loading predictions to moisture (or vapor molecules) adsorption from ambient air. At 760 Torr,³ observed resonance shift, Δf , between air mass loading predictions and measured frequency is ~ 26 kHz, which corresponds to loaded mass, $\Delta m = (\Delta f/f_0)M_{\text{eff}} = 2.63^{-15}$ g. Following [96], the DCB geometry ($9.75 \mu\text{m} \times 220 \text{ nm} \times 160 \text{ nm}$) provides an effective mass is $M_{\text{eff}} = 0.735M_{\text{total}} = 587.7 \text{ fg}$. $1 \text{ fg} = 10^{-15} \text{ g}$. Hence, the loaded mass is approximately 0.5% of the device effective mass and corresponds to few monolayers of vapor on the device surface shown below.

Estimating monolayer formation

The mass loading results discussed here involves the creation of one or more monolayers of water at the top of the device surface. A monolayer can be considered as a thin film with a thickness of water molecule's size. The average diameter of the water molecule is 0.275 nm which can be considered as the thickness or height (t) of the monolayer. Now the volume of the monolayer at the top of the device surface can be estimated as, $V_{\text{monolayer}} \approx \text{Device Surface area} \times \text{thickness of grown water layer (t)} = 5.90 \times 10^6 \text{ nm}^3$. By approximating the shape of a water molecule as a cylinder with height d and radius, $r = d/2$, we can estimate the volume of a single water molecule as, $V_{\text{molecule}} \approx t \times \pi r_{\text{molecule}}^2 = 0.01633 \text{ nm}^3$. Now, the number of water molecules, N_m , which can exist in the approximated monolayer can be calculated from the volume of

³We note that this hypothesis could be confirmed by bleeding 0% humidity air into the chamber rather than ambient air, however, in this dissertation, we did not perform such measurements.

monolayer and the volume of a molecule.

$$N_m = \frac{V_{\text{monolayer}}}{V_{\text{molecule}}}. \quad (2.25)$$

After plugging in estimated volumes into equation 2.25, we have 36.1×10^6 water molecules in the monolayer corresponds to a loaded mass, $36.1 \times 10^6 \times 2.99 \times 10^{-23} \text{g} = 1.08 \text{ fg}$; the mass of a single water molecule is $2.99 \times 10^{-23} \text{g}$. Compared to experimental results (2.63 fg) it is clear that multiple layers have formed at the device surface and the number of layers is ~ 2 .

For a specified relative humidity, water layer thickness (t) can also be theoretically estimated as below [69]

$$t^3 = \frac{M_w \alpha}{\rho k_B T \ln(RH^{-1})}, \quad (2.26)$$

where, $M_w = 2.99 \times 10^{-23} \text{g}$ is the molecular mass of water, $\alpha = 2 \times 10^{-19} \text{ J}$ is the coefficient related to interatomic strength, $\rho = 997 \text{ kgm}^{-3}$ is the density of water, $k_B = 1.38 \times 10^{-23} \text{ JK}^{-1}$, the constant temperature (T) during experiment is 298 K, and $RH = 40\%$ is relative humidity of lab, which results in 1.16 nm water layer thickness due to vapor adsorption that corresponds to 4 monolayers which is $1.6\times$ higher than experimental values. Such a discrepancy in the theoretical and experimental values also observed in ref. [69] due to uncertainties in the constants involved. Making any conclusion on the discrepancy with the theory is confusing because of disparities in vapor adsorption mechanisms on silicon/silicon oxide surface. David B. Asay and Seong H. Kim [66] have investigated adsorbed water layer on hydrophilic silicon oxide by changing relative humidity from 0 – 100%. Their investigations revealed that depending on the level of humidity, the structure of water layers are different. Within 0 – 30% relative humidity (RH), 3 water layers were found which grow slowly for 30 – 60% RH with additional one layer. X. Wang *et al.* [67] studied ambient molecular water accumulation on silica surfaces with interferometric optical balance which results in variations in water layer thickness from picometers up to nanometers. In the context of the thesis water chemistry is not our goal. So we skip this investigation for future work. However, it is impressive to see the affinity and sensitivity of the device to vapor molecules around it. These findings of frequency shift due to vapor adsorption establish the NOMS system as a potential candidate for ambient gas sensing, which is our ultimate goal.

2.5.2.3 Notes on experimental condition

While experimenting, for each pressure, TM noise measurements discussed in this chapter, driven frequency responses in Chapter 3, Allan deviation measurements in

Chapter 5 were done in a single sitting and took almost a day. At pressures higher than 1 Torr chamber was evacuated overnight for the next measurements. By this way, measurements were performed up to 760 Torr. Also, we did not control the humidity condition precisely. We relied on the central humidity control of the entire building, which maintains 40% relative humidity. So, ambient conditions in the intermediate pressure regimes are skipped for the discussion. However, the effect of humidity, as well as the pressure on each higher pressure data accounts for local environments on the day of experiments. As an example, before 760 Torr measurements, device chamber was pumped down to high vacuum overnight to remove possible residual gases. The next morning, the pressure was being controlled slowly to reach 760 Torr. So, one can expect TM noise measurements at the atmosphere contains information about the relative humidity at the time of experiments. Here, we have compared frequency shift at 760 Torr with water formation calculation.

2.5.3 Evolution of thermal noise floor with pressure

For ambient gas sensing, we propose to study DR as a function of damping to maximize device sensitivity. TM noise peak (a_{th}) defines the bottom level of intrinsic DR . Hence, we are particularly interested in studying the evolution of experimental thermomechanical (th) noise amplitudes, a_{th} on resonance as a function of extrinsic Q . In the Figure 2.9, a_{th} (equation 2.15) are displayed as a function of measurement pressures. The noise floor, a_{th} diminishes as the pressure increases. This behavior

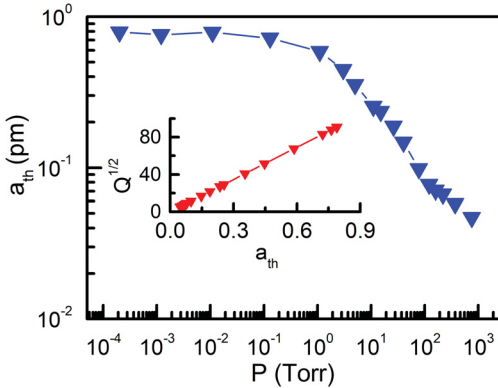


Figure 2.9: **Measured thermomechanical noise amplitude as a function of pressure for 1 Hz measurement bandwidth.** TM noise amplitude diminishes with pressure as increasing air molecules introduce more damping on nanomechanical motion. The behavior is exactly similar to that of Q vs P because $a_{th} \propto Q^{1/2}$ as in inset. Note that 1 Hz bandwidth is used for simplifying theories. For experiments one need to use measurement bandwidth.

confirms half of our hypothesis: that the noise limiting factor from vacuum to atmosphere is likely due to thermomechanical noise and is proportional to $Q^{1/2}$. The next chapter will explore the top end of the dynamic range and answer if $SNR \sim Q^{-1}$.

2.6 Conclusions

The focus of this chapter was to explore characteristics of nanomechanical motion analytically for driven and undriven cases and to compare with experimental results. We have shown that nanomechanical mass sensitivity is a purely mechanical effect. The measured Q agrees well with the theory. The resonance frequency measurements with pressures show a clear deviation from the air mass loading effect likely due to vapor adsorption from ambient humid condition. The calculated vapor mass from the frequency shift is close to existing theoretical predictions and supported by reported surface chemistry experiments. For practical realizations of any nanoscale resonator, accurate calibration is crucial. Thermomechanical calibration procedures described in this chapter is found accurate to calibrate the experimental TM noise signal in voltage for the entire pressure regime. Dependence of thermal noise amplitude on quality factor ensures the bottom end of the intrinsic dynamic range at different pressures agree with theory. Thus the DCB beam characterized in this chapter is not only an ideal test element to study the DR behavior with damping but also vapor adsorption results make it a potential candidate for ambient condition gas sensing without any surface coating.

Chapter 3

Enhancing dynamic range of mechanical resonators through larger damping

3.1 Introduction

A complete quantitative characterization and understanding of the dynamics of mechanical resonators is crucial for exploring potentials of better sensor performance. Generally, these resonators are treated as linear resonators, and simple harmonic approximation can adequately explain the dynamics of motion described in the previous chapter. In case of a simple harmonic oscillator, the force acting on it is linear, i.e., vibration amplitude grows linearly with increasing driving force. However, nonlinearities are commonly come across in NEMS devices and manifest themselves in the harmonic equation of motion, as a force proportional to the cube of the displacement. Such nonlinearity is commonly known as a Duffing nonlinearity [116]. In a Duffing resonator, above a specific driving amplitude, the amplitude response becomes a multivalued function of frequency where hysteresis appears due to discontinuity in amplitude-frequency relation in the response, [117, 118, 119, 120, 121, 122, 123] and is the characteristic of nonlinear oscillations. The corresponding driving power is known as critical driving power, and the amplitude referred to as critical amplitude, a_c . For linear operations of NEMS sensors, the device must be driven just below a_c [20, 21, 22, 120]. With down-scaling device dimensions, such nonlinearity onsets earlier and limits the dynamic range, DR [120] of the device that reduces the sensitivity (*cf.* see equation 1.3 in Chapter 1).

The term, DR , compares the largest value to the smallest one of any quantity or a system. In the NEMS domain, the linear dynamic range is an established concept to describe the linear behavior of nanomechanical motion. The origin of DR concept stems

from amplifier studies to express the range of input power where the amplifier behaves linearly and adopted by Roukes and coworkers for NEMS domain [20, 21, 22, 120]. The noise power generated by an amplifier determines the bottom end of the DR and the input power level at which 1 dB compression occurs characterizes the upper end of DR . Correspondingly, the intrinsic dynamic range of a nanomechanical resonator compares the driving power at the onset of nonlinearity to the thermal noise power and is explicitly defined by Postma *et al.* [120] as below

$$DR = 20 \log \frac{0.745 a_c}{a_{th}}, \quad (3.1)$$

where, a_c and a_{th} are the amplitude at the onset of nonlinearity and thermomechanical noise peak.

DR is also expressed as the ratio of maximum driving power to noise power, i.e. as signal to noise ratio, $SNR = a_{driven}/a_{noise}$. If the thermal noise is resolved and the maximum driven amplitude can reach the onset of nonlinearity then

$$SNR = \frac{a_c}{a_{th}}. \quad (3.2)$$

Thermal noise peak at resonance (*cf.* equation 2.16) changes with square root of damping, i.e., $a_{th} \propto Q^{1/2}$ (*cf.* equation 2.16). On the other side, as will be shown in this chapter, critical amplitude equation (3.6 or 3.7) is inversely proportional to damping, i.e., $a_c \propto Q^{-1/2}$. Hence, functional form of SNR in equation 3.1 or 3.2 demonstrates an improvement with increasing damping by, $SNR \propto Q^{-1}$.

This full intrinsic DR has seldom been accessed in state-of-the-art sized NEMS devices of sub-micron cross-sectional dimensions and few micron lengths. In such devices, while the upper end of the DR is often accessible, typically, the noise floor is set by instrumentation noise levels [20, 21] (*cf.* see left panel of Figure 1.4 in Chapter 1). Traditionally, these levels remain unchanged during device size down-scaling or changes in Q -factor and pose a severe problem to transducing small, low- Q NEMS mechanical resonances. As hypothesized in 1.5.3 (*cf.* see right panel of Figure 1.4), this problem is obviated when transducing with optomechanics for resolving intrinsic TM noise, the bottom end of the DR . To maximize DR , innovations in experimental techniques have been demonstrated [124, 125, 126] by overcoming the early onset of high- Q nanomechanical resonators, but why not use damping itself to improve DR ?

Q dependence on the onset of Duffing nonlinearity and thermal noise of NEMS resonator suggests that a device in lower Q conditions can have better dynamic range than higher Q conditions. Surprisingly, this fundamental issue: substantial damping (lower- Q) effect on the intrinsic DR is not thoroughly tested in the realm of

NEMS before this dissertation. Improving DR through damping has received growing attention in the community since 2014 as several different groups started to become aware of and articulate the concept [22, 55, 127, 128, 129, 130]. Some of the following works may have been operating at intrinsic maximum dynamic range and some reports also tap into nonlinear regimes for improving nanomechanical sensor performance [5, 6, 21, 22, 27, 28, 120]. Since 2014, from experimental results of this thesis, we reported a dynamic range improvement of mechanical resonators through larger damping in different conferences, such as, [55, 131, 132, 133, 134, 135, 136, 137, 138] and published a full-fledged article in June 2018 [16].

Results and discussions, and appendices of the current chapter are parts of our research article in *Science* [16]. This chapter will demonstrate the DR enhancement through damping and its impact on the sensor performance by testing the frequency stability relation. In the introductory chapter, we have proposed to measure optimum DR at each pressure for mitigating the lower- Q issue on the sensor performance. Hence, an accurate measurement of a_c is essential for determining the intrinsic DR . Studying the evolution of DR as a function of damping (Q) is the heart of the current dissertation. Despite widely accepted higher- Q operation for nanomechanical resonators, this chapter will show how a NEMS device can have higher DR at higher pressures to explore an exciting avenue for NEMS lower- Q operations that maintain stability. However, for practical realization of nanomechanical resonant sensor atmospheric pressure is the optimum pressure that causes lowest- Q operation in this dissertation.

3.2 Duffing behavior of nanomechanical motion

The harmonic approximation is the simplest of the practical resonators in NEMS class and valid only for small driven amplitude. When the resonator is driven to a large amplitude, it will enter into nonlinear oscillations. Rewriting equation A.28 for an external sinusoidal or harmonic force $F_0 \cos \Omega t$ for small amplitude a , we have

$$M_{\text{eff}} \frac{d^2 a}{dt^2} + M_{\text{eff}} \Omega_0^2 a + \Gamma \frac{da}{dt} = F_0 \cos \Omega t, \quad (3.3)$$

here, F_0 scales the magnitude of the periodic force with frequency Ω and we assume that F_0 is constant within driving frequency span of measurement (see appendices B.1.1, and B.1.6).

When we increase the drive, amplitude grows proportionally to drive power. At some point, it can be driven into the nonlinear regime which is characteristics of the Duffing oscillator. Introducing the Duffing term αa^3 and nonlinear damping term ηa^3

equation 3.3 can be written for cubic nonlinearity as

$$M_{\text{eff}} \frac{d^2 a}{dt^2} + M_{\text{eff}} \Omega_0^2 a + \Gamma \frac{da}{dt} + \alpha a^3 + \eta a^2 \frac{da}{dt} = F_0 \cos \Omega t, \quad (3.4)$$

where, α is the Duffing parameter or cubic spring constant and η is the coefficient of nonlinear damping that increases with the amplitude of oscillation.

A solution of this equation by Ron Lifshitz and M. C. Cross [118] provides the quadratic relation between the maximum frequency Ω_{max} and the oscillation amplitude a_0 as follows

$$\Omega_{\text{max}} = \Omega_0 + \frac{3}{8} \frac{\alpha}{M_{\text{eff}} \Omega_0} a_0^2, \quad (3.5)$$

where Ω_0 is the linear response peak frequency at small excitation, (where the system nonlinearity is negligible) and a_0 is the amplitude that depends on frequency (Ω). Equation 3.5 explains why the resonance frequency shifts with increasing amplitude at resonance. For, $\alpha > 0$ frequency shifts to a larger value corresponding to the oscillations on a more tensioned beam and is called spring stiffening. If $\alpha < 0$, the frequency shifts to a smaller value that indicates a less tensioned beam, and is called spring softening. When the driving power is high enough to produce a large amplitude, frequency response deviates from usual Lorentzian line shape with the subsequential development of hysteresis. The corresponding amplitude is known as critical amplitude.

Above critical amplitude, the vibrating mechanical element experiences various nonlinearities in its restoring force, e.g., elongation of the beam, defects in clamping, material nonlinearity, existence of any force gradient in the system due to detection or actuation or even thermal gradient. In the current work, we have characterized a nano-scale beam clamped at both ends, so at large vibration, it is natural for a DCB beam to suffer from a change in its length that produces additional tension. Consequently, in our DCB resonators, strain induced tension, and geometrical nonlinearity occurs. The critical amplitude a_c occurs when the frequency solution to the Duffing equation just starts to be multivalued (*i.e.* the bifurcation point) and is characterized by a section of infinite slope and the start of hysteresis in frequency sweeps (that is, the first appearing saddle node of the equation [117]). It is important to note that this critical amplitude arises purely from the Duffing analysis and does not depend on the nature of the nonlinearity (whether caused by geometry, gradient forces, tension, or other sources). Mathematically, it relates to the backbone of the family of increasing drive resonance curves and the fact that peak amplitude vs. frequency follows a square root dependence. As a general relationship, it applies equally well to cantilevers, doubly-clamped beams or any other geometry.

In Postma *et al.* [120] the expression for critical amplitude, a_c is given as (when considering no residual tension in the DCB resonator)

$$a_c = \Omega_0 \frac{L^2}{\pi^2} \sqrt{\frac{\rho\sqrt{3}}{EQ}}, \quad (3.6)$$

where, Ω_0 is the resonance frequency of the DCB resonator with a length L . ρ and E are the density and Young's modulus of the material. Here, Q is the measured quality factor of the resonator. In a doubly clamped beam with a residual tension [120], T_0 , the onset of nonlinearity is as below

$$a_c = \frac{2}{\sqrt[4]{3}} \sqrt{\frac{1}{Q} \left(\frac{d^2}{3} + \frac{T_0 L^2}{\pi^2 E t d} \right)}. \quad (3.7)$$

Here, t is the thickness and d is the width of the beam in the direction of motion. The second term within the bracket corresponds to resonance frequency. From equation 3.6 or 3.7 one can tell that a_c (upper end of the *DR*) increases with increasing damping (decreasing Q) for a particular device geometry. The fact that a_c is proportional to $Q^{-1/2}$ ultimately arises from equation 3.5. Intuitively, it can be understood in the following way. At a given amplitude, the intrinsic nonlinearity causes a defined frequency shift enough to tilt the resonance shape for a narrow linewidth while still being hidden by a wider one.

3.3 Experiments

A racetrack resonator optical cavity structure is used to detect the nanomechanical motion of the doubly-clamped beam. The NEMS (DCB beam) is coupled laterally to the photonic elements and are contained in the same device layer. Details of the experimental setup and device are described in section 2.4. A shear piezo actuating the chip drives the device, and the device is interrogated using a free-space confocal lens system to couple light to on-chip grating couplers [48]. NEMS motions are transduced by their interaction with the evanescent field of the light in the optical racetrack. Essentially, NEMS motion modulates the wavelength of the optical cavity resonance. Setting a probe wavelength on the steep side slope of an optical resonance translates that modulation into optical transmission power modulation (*cf.* Figure 2.2 (b)). This optical power modulation is read out by the photodiode to ultimately give a voltage modulation that is directly proportional to the NEMS displacement. Measured voltage signals are converted into corresponding displacement signal through the thermal calibration procedures described in section 2.5.1.1.

3.3.1 Determination of onset of nonlinearity

Accurately determining the onset of nonlinearity is important for defining the upper cutoff of the dynamic range. In this section, we describe the calibration of onset of nonlinearity in the doubly clamped beams. The driving power is applied to the piezo shaker by the 50 ohm output of an rf amplifier with gain relative to the lock-in output of +38.3 dB. The piezo motion is difficult to calibrate since the amount of power reflection is frequency dependent; however, the motion is linear with drive voltage (*cf.* Figure B.5) and the reflection is constant at a given frequency. This allows sweeping the drive voltage while on resonance to locate the 1 dB power compression amplitude, a_{crit} , of the DCB response, just before the onset of nonlinearity. Here, driving voltage refers to the voltage output from the amplifier and can also be quoted as a drive power in dBm assuming the standard 50 ohm conversion. Figure 3.1 (a) shows a representative plot for determining critical drive power. The blue open circles are measured DCB response on resonance, and the red solid line is the 1 dB compression line, computed by making a linear fit to the data near zero drive and then applying 1 dB reduction in power (1/2 dB reduction in voltage) to the line slope. This allows locating the 1 dB compression amplitude, a_{crit} , and critical drive, V_{crit} , at the intersection of the line with the data.

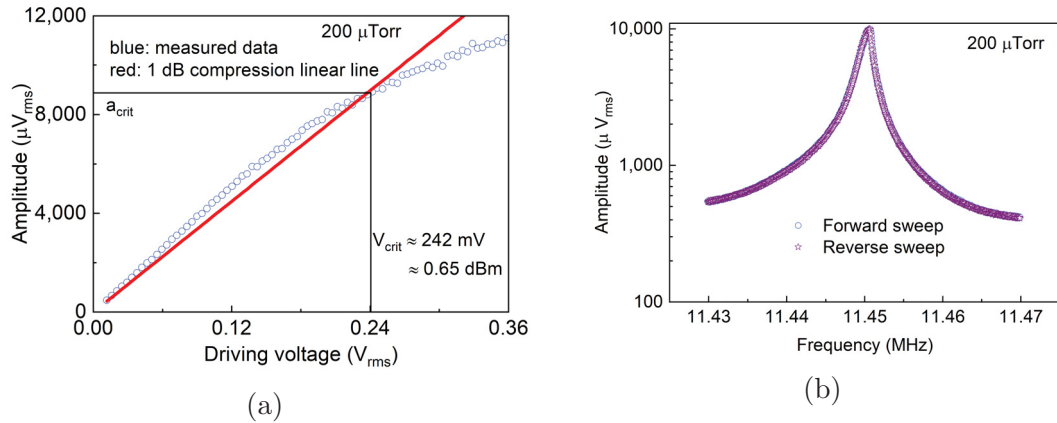


Figure 3.1: **(a): A representative plot for determining critical amplitude, a_{crit} .** a_{crit} and V_{crit} are defined from where the 1 dB compression line crosses the measured data. **(b): Forward and reverse sweeps at critical drive power.** Forward and reverse sweeps at the critical drive voltage of 242 mV show the distinctive slight-leaning curve-shape corresponding to 1 dB compression critical amplitude. There is no hysteresis as this is still below the bifurcation amplitude (a_c) and Lorentzian fit measured Q values are the same at a_c as for TM noise. From [16]. Reprinted with permission from AAAS.

A forward and reverse frequency sweep at critical drive (*cf.* Figure 3.2 (b)) confirms

that the resonance shape is just starting to tilt and hysteresis has not yet set in. The Q -factor also remains similar to that measured in the thermomechanical noise. The absence of hysteresis and similar Q values at the driven response compared to in-driven Q indicates that the device can be operated at the maximum linear amplitude. Strictly speaking, we define $a_{\text{crit}} = 0.745a_c$ to correspond with the theoretical amplitude for 1 dB of compression, and define it as the practical end of the linear range [120].

All experimental a_{crit} , from high vacuum to atmospheric pressure are compared to corresponding theoretical values given by equation 3.6 and 3.7 (with and without tension) and plotted together with experimental values in Figure 3.2. From a comparison between experimental and analytical values in the Figure 3.2 it can be inferred that the DCB beam used is subjected to geometrical nonlinearity. Also, the difference between two equations is seen to be negligible.

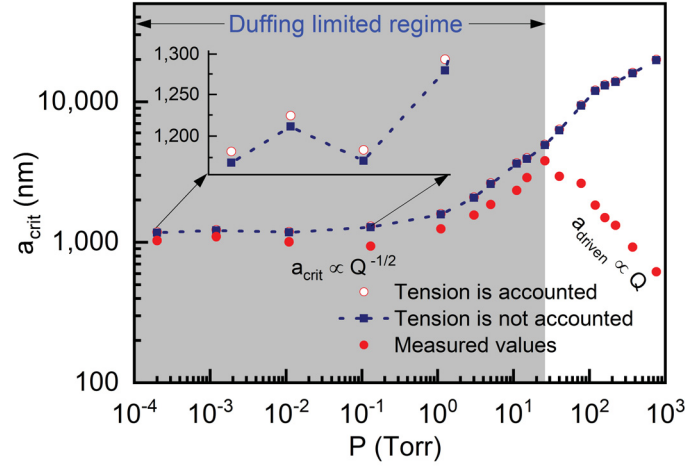


Figure 3.2: **Evolution of onset of nonlinearity with increasing damping or decreasing Q .** The theoretical amplitude of nonlinearity is only negligibly changed by accounting for tension or not. Measured critical amplitudes follow fairly close to theoretical ones in the Duffing limited regime, and $a_{\text{crit}} \sim Q^{-1/2}$. When drive power can no longer be increased, $a_{\text{driven}} \sim Q$ as expected. From [16]. Reprinted with permission from AAAS.

A gradual fall of a_{crit} with increasing pressure after 30 Torr is attributed to saturation of available driving power from the power amplifier. Within the drive saturated region (from 40-760 Torr in Figure 3.2) the device was driven with a constant driving power of 36 dBm. Because of increased damping (decreased Q), the driven amplitude at this constant drive falls inversely with measured Q .

3.4 Results and discussion

In Chapter 2, we confirmed that the noise displacement amplitude a_{th} is proportional to $Q^{+1/2}$ (equation 2.16) and that we have displacement resolution able to measure the noise in our NOMS for all pressures up to atmospheric. In the previous section, we established that a_{crit} is proportional to $Q^{-1/2}$ (equation 3.6) in the Duffing limited pressure regime (up to 26 Torr in this device). When the full dynamic range is accessed, we can equate a_{noise} to a_{th} and a_{driven} to a_{crit} and equations 2.16, 3.6 and 3.2 combine to produce SNR theoretically proportional to $1/Q$.

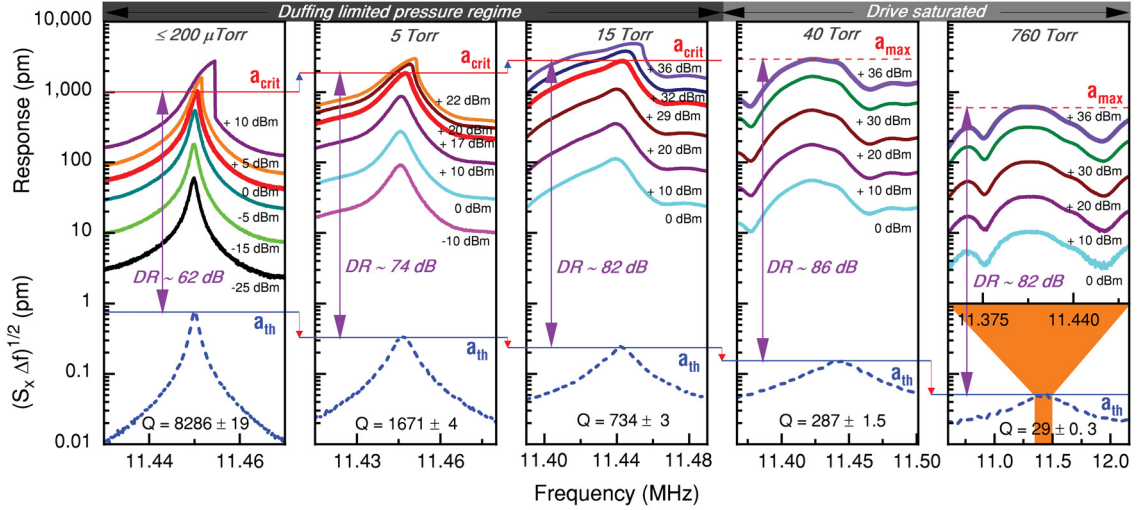


Figure 3.3: **Dynamic range is pressure dependent.** Dashed lines (blue) are measured thermomechanical noise frequency curves presented in a 1 Hz bandwidth; a_{th} is their peak value which falls with increasing pressure. Filled symbols are driven response frequency curves for various drive powers; a_{crit} (thicker, red) grows with increasing pressure in the Duffing limited pressure regime. The 760 Torr driven frequency axis is zoomed in with respect to the thermomechanical noise at the same pressure. From [16]. Reprinted with permission from AAAS.

To test SNR behavior we measure properties of the same doubly-clamped beam at different pressures (thus different extrinsic quality factors) from vacuum to atmospheric pressure. This approach keeps all parameters except for Q identical. Results are presented in Figure 3.3 with frequency sweeps for five representative pressures. At each pressure, the thermomechanical noise is plotted for a 1 Hz bandwidth along with the driven root mean square amplitude response for varying drive power. Marked in thick red are traces for the drive power corresponding to Duffing critical amplitude (up to 15 Torr) and in thick purple for the maximum driving power available (40 and 760 Torr). For 15 Torr pressures and up, the driven resonance line-shape is distorted. This is not due to nonlinearity (note the conserved response shape and see Figure B.5),

rather, the resonance has broadened to the point where piezo drive efficiency is no longer a constant function of frequency [139]; the distorted features are related to bulk acoustic resonances in the piezo-chip system. This distortion carries no information about the NEMS beam resonance (see [139], Section B.1.1, and Figure B.1). The first

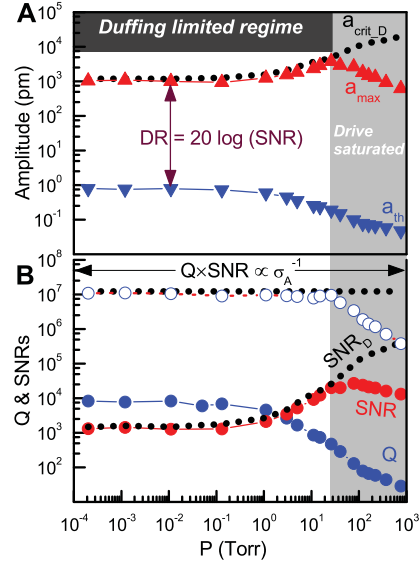


Figure 3.4: **The product of $Q \times SNR$ is constant in the Duffing limited regime.** (a) Peak frequency curve amplitude response vs pressure: $a_{\text{crit,D}}$ is the theoretical Duffing amplitude defined by equation 3.6, a_{max} is the measured peak amplitude, and a_{th} is the thermomechanical peak amplitude. DR is the dynamic range which grows with pressure. (b) Quality factor (Q) and signal-to-noise ratio (SNR) vs pressure: SNR_D is $a_{\text{crit,D}}/a_{\text{th}}$ and SNR is $a_{\text{max}}/a_{\text{th}}$. From [16]. Reprinted with permission from AAAS.

thing to note in Figure 3.3 is that the peak of the noise floor a_{th} diminishes as the pressure increases and generally follows $a_{\text{th}} \propto Q^{1/2}$ (cf. equation 2.16). For the upper end of DR , within the Duffing limited pressure regime, a_{crit} is increasing in proportion to $Q^{-1/2}$, as predicted by equation 3.6. Accounting for both effects, $SNR \propto 1/Q$ up to 15 Torr pressure. At 40 Torr and up, we no longer have enough drive power to reach the Duffing critical amplitude and no longer take advantage of the full intrinsic DR of the system. Nonetheless, we note that dynamic range is still higher at atmospheric pressure than in vacuum.

Figure 3.4 plots the peak amplitudes a_{crit} and a_{max} , the thermal amplitude a_{th} , quality factor Q , signal-to-noise ratio SNR , and product of $Q \times SNR$ as a function of pressure. We can clearly see that $Q \times SNR$ is conserved within the Duffing limited regime. According to Robins' picture (equation 1.3), the frequency fluctuations in our system should be independent of Q up to 15 Torr.

3.5 Conclusions

This chapter has made important advances in engineering nanomechanical resonators for their optimum linear operations as a function of damping. Enhancement of intrinsic dynamic range with increasing damping leads to an intuitive experimental success by maintaining the term $Q \times SNR$ as a constant irrespective of damping. This success is not surprising, because it is explained by existing theoretical frameworks with an impressive conclusion that it is possible to have a vacuum compatible frequency stability by NEMS resonators at atmosphere pressure if the full intrinsic dynamic range is accessible. As we have shown that $Q \times SNR$ is conserved in the Duffing regime, it remains to test the relation in frequency stability measurements. First, the next chapter is dedicated to understanding the perspective of $Q \times SNR$ conservation in the theory of frequency stability of mechanical resonators.

Chapter 4

Theory of frequency stability

4.1 Introduction

For deploying a nanomechanical resonator in sensing applications, we need to interrogate the sensor by using electronics to determine its resonance properties. A resonant sensor combined with electronic components creates an oscillator and can be referred to as resonant sensor oscillator. The output of such oscillator is the resonance frequency of the mechanical resonator, which is modulated by the measurand of interest during resonant sensing. Unfortunately, the frequency and amplitude of any such resonant sensor oscillator is not constant in time but fluctuates. A variety of physical processes which are not under control can affect the resonance properties of resonant sensors in a complicated way. As a result, the amplitude, frequency or phase of any resonator irregularly fluctuates in a way that in general, such fluctuations, cannot be represented by an analytic function of time. These unwanted fluctuations in resonance properties are commonly referred to as noise or jitter and need statistical treatments for exploring their behavior. Frequency stability of a resonator is a measure of the degree to which the oscillating signal maintains the same level of frequency over time. It is established [19, 20, 21, 22, 140] that among different noise processes, thermomechanical noise of a resonant sensor often determines the minimum detectable change in frequency (frequency resolutions or stability) and hence the minimum detectable mass, force, temperature, etc. i.e., the sensor resolution. Therefore it is invaluable to have clarification on how the properties of both the resonators and electronics in the measurement system affect frequency noise. Since frequency resolution translates into sensor resolution, it is essential to be able to estimate it analytically.

In this dissertation, we are dealing with nanomechanical resonators for ambient condition gas sensing. Mass sensitivity of these devices is a pure mechanical effect and limited by its frequency resolution, $\left\langle \frac{\delta f}{f} \right\rangle$ (see section 2.2.6 of chapter 2). For a

mechanical sensor, this quantity, $\left\langle \frac{\delta f}{f} \right\rangle$ is a measure of its frequency stability, where $\langle \rangle$ represents the statistical average of $\delta f/f$. Commonly, a goal is to improve this stability down to its thermal limit because thermal noise induces an incoherent nanomechanical motion with random amplitude and phase [20, 21, 127, 141]. In quest of determining the frequency stability of MEMS and NEMS, studies were begun by Vig and Kim in 1999 [141] through the phase noise analysis of these devices. Later Cleland and Roukes in 2002 [20] investigated different sources of noise to estimate their impact on a single crystal silicon doubly clamped beam. These authors used Robins' approach [18] in developing a self-containing formalism to estimate the frequency stability. Two years later, from the same partnership, Ekinici *et al.* [21] followed a similar approach to derive the widely accepted DR formula that is ultimately limited by the device thermal noise. A Phase locked loop (PLL) was used to interrogate the device for obtaining the following equation

$$\sigma_A(\tau) = \left\langle \frac{\delta f}{f} \right\rangle \sim \frac{1}{2Q} \frac{1}{SNR} \frac{1}{\sqrt{\tau}} = \left(\Delta f \frac{\Omega_0}{Q} \right)^{1/2} 10^{-DR/20}, \quad (4.1)$$

where $\sigma_A(\tau)$ is the time domain representation of frequency stability and is known as Allan deviation, the measurement bandwidth Δf is related with averaging time τ by $\Delta f = 1/2\pi\tau$ and, Q is the quality factor defined by the linewidth Γ at resonance frequency Ω , $Q = \Omega/\Gamma$. DR is the maximum linear dynamic range. Ekinici *et al.* [21] defined DR as the ratio of maximum driven energy ($E_c = M_{\text{eff}}\Omega_0^2 a_c^2$) to the thermal energy ($k_B T$) as $DR = 10 \log(E_c/k_B T)$, where a_c is the maximum linear amplitude at the onset of nonlinearity, k_B is the Boltzman constant. One year later, Postma *et al.* [120] from the same group rederived DR in terms of ratio of driven amplitude at the onset (where, 1 dB compressions occurs for an amplitude $0.745a_c$) to displacement spectral density of thermomechanical noise at Ω_0 , $S_a^{\text{th}}(\Omega_0)$ by $DR \sim 20 \log(0.745a_c/S_a^{\text{th}}(\Omega_0))$. In the last chapter we have measured 1 dB compression. So, we define intrinsic dynamic range as, $DR = 20 \log(a_{\text{crit}}/a_{\text{th}}) = 20 \log(SNR)$. Note that Postma's and our DR are slightly different than Ekinici's DR due to the former referencing thermal amplitude on resonance and the latter referencing average thermal energy. The relationship between the two versions of DR is defined later in the chapter in equation 4.26.

Equation 4.1 contains an important relationship: the frequency stability dependence on sampling time τ . The log-log slope of σ vs. τ is $-1/2$ in this equation. This relationship is well-known and known to correspond with a white frequency noise (such as thermomechanical noise). A slope of 0 would correspond to $\frac{1}{f}$ flicker noise while a slope of -1 would correspond to white phase noise (*cf.* Figure 4.2).

In the last chapter, we studied the Duffing behavior of a nanoscale doubly clamped beam. Our experimental results nicely show that a Duffing resonator preserves a constant $Q \times SNR$ at different damping conditions. The consequence of such constant $Q \times SNR$ directly translates into similar frequency stability of the DCB resonator at different damping by the equation above. In pursuit of improved sensitivity, many efforts have been devoted experimentally and theoretically to attain the fundamental limit of frequency stability of NEMS devices. In practice, even with a maximum DR , nanomechanical resonators presently operate far away from the thermal limit. Collaborative research works by M. Sansa *et al.* [22] thoroughly reviewed available data based on the DR formula showing a tendency to be higher than the thermal limit by few orders of magnitudes. These authors postulated that omnipresent frequency fluctuation noise in all nanomechanical resonators imposed extra noise which prevents reaching the TM noise limited stability. This flicker frequency fluctuation noise, in fact, restricts Allan deviation from improving with larger SNR and appears at τ^0 slope in an Allan deviation plot. Another work by Gavartin *et al.* [127] demonstrated a closed loop operation within the linear regime of the Duffing oscillator. They used one mode of resonance to stabilize the limit of frequency stability of another mode down to the TM noise limit and developed a model for externally driven closed loop operation. Results of this work recommend a τ^{-1} slope instead of $\tau^{-1/2}$ when the measurement takes place for a PLL BW less than the linewidth Γ which is similar to our recent observation [16]. In ref. [16] we have shown that low- Q operation of NEMS devices has considerable immunity from frequency fluctuation noise. We found a flat band regime ($\Delta f < \Gamma/2\pi$) where Allan deviation even goes below the limit predicted by the Robins' formula (equation 4.1) with the τ^{-1} trend similar to [127]. However, these findings raised a critical question on the nature of noise due to the τ^{-1} slope in the Allan deviation plot. Since thermomechanical induced frequency noise is white, it should produce $\tau^{-1/2}$ slope unless it is somehow acting like white phase noise.

In this chapter, we provide the theoretical framework needed for understanding phase noise processes in resonant measurement systems and their translations into frequency stability, including the definitions of the colours of noise and Allan variance. We derive Robins' formula for the case of thermomechanical noise. We provide clarification on the flatband model [16] arising from this derivation and the flaw in the conceptual framing of that model, while noting the historical context of this conceptual flaw in the NEMS community. We discuss the phase locked loop used in our experiments and adopt the PLL transfer function from Demir and Hanay [142] to confirm Robins' model. The framework in this chapter contributes to a better understanding of NEMS frequency stability while also providing the formalism for

interpreting experimental results on mechanical sensor stability in the rest of the thesis. Sections 4.3, and some of 4.4 in the chapter are from published journal [16].

4.2 Frequency Stability

Phase and frequency of any resonator are directly related to each other because frequency is the phase changing with time. Derivatives and integrals relate these: the derivatives of phase is the frequency. As a consequence phase noise and frequency noise are corollaries of same noise sources. Once we know one we will have the other. Different noise processes that exist in the system can corrupt the nominal frequency causing it to fluctuate. Minimizing the effect of these noise processes is a measure of frequency stability which can be examined both in the time domain and frequency domain depending on users' choice and applications. For resonant sensing, we are interested in time domain stability, i.e., in Allan deviation. However, often Allan deviation plots alone are not sufficient enough to understand noise processes without frequency domain models. In the frequency domain, noises are represented by the spectral density. Before establishing an analytical model of Allan deviation, it is useful to review the spectral density of phase and frequency in a resonant measurement system.

4.2.1 Frequency and phase noise characterization

4.2.1.1 General definition of instantaneous frequency

The output signal from a real oscillator can be expressed as follows that permits to study the random phase and frequency fluctuations [143]

$$a(t) = [A_0 + \epsilon(t)] \sin(\Omega_0 t + \Delta\phi(t)), \quad (4.2)$$

where, A_0 is the nominal signal amplitude, $\Omega_0 = 2\pi f_0$ is the nominal signal frequency, $\epsilon(t)$ is the instantaneous amplitude fluctuations and $\Delta\phi(t)$ is the instantaneous phase fluctuations is the random process of interest.

Now the instantaneous frequency of the signal 4.2 is given by

$$f(t) = \frac{d}{dt} \frac{1}{2\pi} (\sin(2\pi f_0 t + \Delta\phi(t))) = f_0 + \frac{1}{2\pi} \frac{d\Delta\phi(t)}{dt}, \quad (4.3)$$

where,

$$\Delta f(t) = \frac{1}{2\pi} \frac{d\Delta\phi(t)}{dt} \equiv f(t) - f_0. \quad (4.4)$$

Equation 4.4 is the time derivative of $\Delta\phi(t)$ what is the instantaneous frequency deviation from the nominal frequency f_0 and is referred as frequency noise. Transforming this equation into Fourier frequency domain one obtains:

$$\Delta f(f_m) = f_m \Delta\phi(f_m), \quad (4.5)$$

where f_m is the offset frequency which will be expressed simply by f in this thesis.

It should be noted that the statistical process for characterizing the phase and frequency stability is only valid when the instantaneous fluctuations are small compared to their nominal value, i.e.,

$$\frac{\epsilon(t)}{A_0} \ll 1 \text{ and } \frac{d\phi}{dt} \ll 2\pi f_0. \quad (4.6)$$

Generally, it is assumed that fluctuations in amplitude and phase are orthogonal to each other. Thus, no amplitude noise are transferred into phase noise and vice versa. It is useful to define the dimensionless frequency fluctuations as follows

$$y(t) = \frac{\Delta f}{f_0}. \quad (4.7)$$

From these time-dependent expressions, two sets of parameters are used to characterize the oscillators *viz.*

- the spectral density of phase and frequency fluctuations in the Fourier frequency domain.
- the variance of average frequency fluctuations (which leads to Allan deviation) in the time domain

4.2.1.2 Frequency domain spectral densities

By neglecting any disturbance in amplitude, it is common to express the double sideband spectral density (DSB) of phase noise in the following form [144]:

$$S_{\phi\phi}(f) = \frac{\Delta\phi^2}{BW} \frac{\text{rad}^2}{\text{Hz}}, \quad (4.8)$$

which describes the phase noise power in a defined bandwidth BW . In Phase noise discussion, it is assumed that the bandwidth is normalized to 1 Hz. For $\Delta\phi \ll 1$, the assumption of single sideband (SSB) phase noise is valid for half of the DSB. Also, it is common to define the short-term frequency stability of an oscillator by the spectral density of frequency fluctuations which describes the energy distribution as a

continuous function. It is expressed in units of frequency variance per unit bandwidth as follows

$$S_{\Delta f}(f) = \frac{\Delta f^2}{BW} \frac{\text{Hz}^2}{\text{Hz}}. \quad (4.9)$$

In the Fourier frequency domain, one-sided spectral densities characterize respective phase and frequency fluctuations which are related by the simple law according to equation 4.5:

$$S_{\Delta f}(f) = f^2 S_{\phi}(f), \quad (4.10)$$

which corresponds to the time derivative relationship between the phase and frequency fluctuations. Similarly for dimensionless frequency fluctuations we can write

$$S_y(f) = \frac{f^2}{f_0^2} S_{\phi}(f), \quad (4.11)$$

where $f = \omega/2\pi$ is the Fourier frequency.

Spectral densities above (or the autocorrelation function which is the inverse of Fourier transform) contains maximum information about Gaussian stationary random process [143].

4.2.1.3 Types of phase and frequency fluctuation spectral densities

There are five basic spectral densities of instantaneous phase fluctuations which are related to frequency fluctuation densities either by equation 4.10 or 4.11. Several articles can be found (see [145] and the references therein) which have considered theoretical and experimental results to show that a power law model can describe spectral densities of random noise that can vary as a power of f . Power law for $S_y(f)$ can be written as

$$S_y(f) = \sum_{\alpha=-2}^{\alpha=2} h_{\alpha} f^{\alpha} \quad \text{for } 0 < f < f_h, \quad (4.12)$$

where, f_h is the upper cut-off frequency. Each term in the equation 4.12 is related to a given noise process which can be further classified between in-loop and outside the oscillator loop. Five different noise processes are shortly described below and illustrated in schematics in Figure 4.1.

In-loop phase noise spectral density:

1. Random walk FM (f^{-4}): It is usually close to the carrier. This spectral density results from oscillator's physical environments such as temperature, mechanical shock, vibration or any other environmental effect that may cause random shifts in resonance frequency. Usually, it is challenging to measure random walk frequency modulation (RWFM) noise.

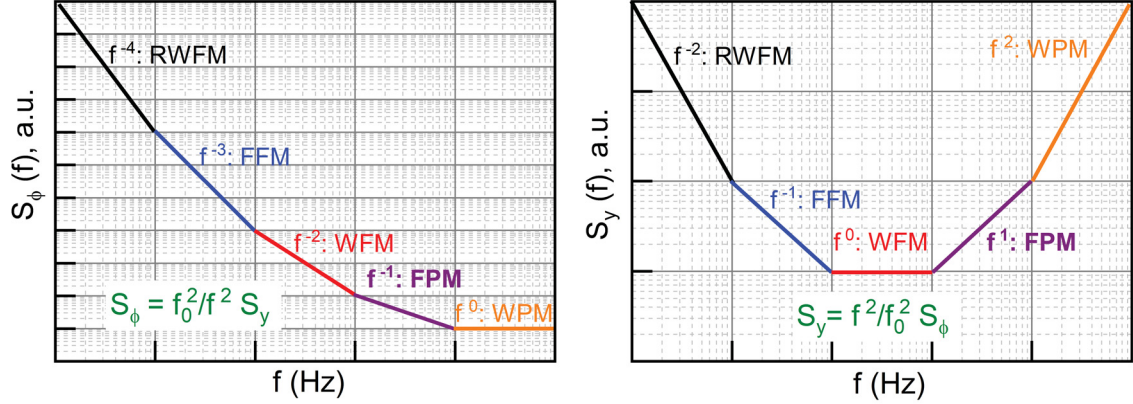


Figure 4.1: **Phase (single side band) and frequency noise density model.** Left: Spectral density of phase noise from commonly occurred noise sources in resonant sensing. Right: The same color sketches respective frequency noise densities. Advanced instrumentations help by suppressing RWFM, FPM and WPM noises. We are interested in WFM and FFM only which comes from the mechanical resonator.

2. Flicker frequency noise (f^{-3}): The physical origin of this noise is not fully understood. It is thought to be related to the physical resonance mechanism of an active oscillator or the environmental properties or the design or active electronics in the measurement system. This noise is common in high-Q oscillators.
3. White FM (f^{-2}): This spectral density results from white noise source like thermal noise within the oscillator loop. Sometimes it is called internal additive noise.

Phase noise spectral density outside the loop:

4. Flicker PM (f^{-1}): This results from the noise outside the oscillator loop added by noisy electronics. Good quality instruments can suppress Flicker PM significantly.
5. White PM (f^0): This broadband noise probably has the same origin as Flicker PM(f^{-1}). Most modern electronics can keep it at a negligible level. It is often referred to as additive external noise.

The derivation of $S_y(f)$ to understand the frequency noise of the mechanical or electronic oscillators represents a branch of today's research in physics and engineering, and a good overview of the theory is available in textbooks such as Ref. [146]. Frequency noise density information can be qualitatively used to understand the noise process, but its time-domain transformation is more useful for quantitative and easier identifications of the existing noise processes. The theory of $S_y(f)$ is thoroughly

revised, and the application of the theory for NEMS is mostly developed in [21, 20]. In the next section, we will mention how frequency domain stability transforms into time domain stability.

4.3 Time domain stability: definition of Allan Deviation

Allan deviation, σ_y , is defined as the square root of the Allan variance, σ_y^2 ,

$$\sigma_y(\tau) = \sqrt{\sigma_y^2(\tau)} = \sqrt{\frac{1}{2} \langle (\bar{y}_{n+1} - \bar{y}_n)^2 \rangle}. \quad (4.13)$$

τ is the observation period and \bar{y}_n is the n th fractional frequency average over the observation time. The relationship between close-in frequency or phase noise and Allan variance (worked out primarily at NIST in the 1960s and 70s [147]) integrates the noise with a transfer function $H(f, \tau)$ as below

$$\sigma_y^2(\tau) = 2 \int_0^{f_H} S_y(f) \frac{\sin^4(\pi\tau f)}{(\pi\tau f)^2} df, \quad (4.14)$$

where

$$S_y(f) \equiv \frac{f^2}{\nu^2} S\phi(f), \quad \text{in which } f = \omega/(2\pi) \text{ and } \nu = \Omega/(2\pi).$$

and the transfer function is

$$H(f, \tau) \equiv \frac{\sin^4(\pi\tau f)}{(\pi\tau f)^2}.$$

For $S_y(f)$ exhibiting power law behaviour there are known power law solutions to equation 4.14:

$$\sigma_y^2(\tau) = \begin{cases} Af^2 S_y(f) \tau^1 & \text{for } S_y(f) \sim f^{-2}; (S\phi(f) \sim f^{-4}) \\ Bf^1 S_y(f) \tau^0 & \text{for } S_y(f) \sim f^{-1}; (S\phi(f) \sim f^{-3}) \\ Cf^0 S_y(f) \tau^{-1} & \text{for } S_y(f) \sim f^0; (S\phi(f) \sim f^{-2}) \\ Df^{-1} S_y(f) \tau^{-2} & \text{for } S_y(f) \sim f^1; (S\phi(f) \sim f^{-1}) \\ Ef^{-2} S_y(f) \tau^{-2} & \text{for } S_y(f) \sim f^2; (S\phi(f) \sim f^0) \end{cases} \quad (4.15)$$

where

$$A = 4\pi^2/6$$

$$B = 2 \ln 2$$

$$C = 1/2$$

$$D = 1.038 + 3 \ln(2\pi f_H \tau_0)/(4\pi^2)$$

$$E = 3f_H/(4\pi^2)$$

Allan variance equation defined in 4.15 treats various power-law noise types distinctly, conveniently allows to identify them and estimate their strength. Square-root of the Allan variance is the Allan deviation, which is the metric of frequency stability. The appearance of five basic noise processes in Allan deviation measurements is schematically shown in the next figure.

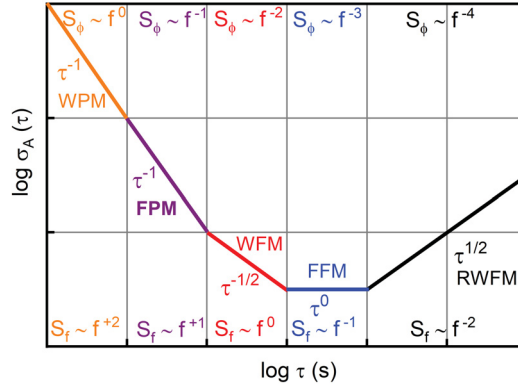


Figure 4.2: **Schematic of Allan deviation vs. averaging time plot:** σ_A vs. τ plot can separate five basic noise processes in a system more distinctly for characteristic time span in the τ axis. It can not separate WPM and FPM noise. However, it is hard to see WPM and FPM in experiments. τ^0 region establishes the noise floor, which is characteristics for FFM noise of the resonator. The corner between WFM and FFM is of our interest

4.4 Robins' phase noise analysis

Consider a driven resonator (NEMS), driven by another source or even driven into self-oscillation. The NEMS fundamental noise can be expressed as phase noise in the NEMS device by comparing the energy of the noise to the driven energy. This approach is known as Robins' analysis of phase noise [18]. Here, we use it to express the thermomechanical noise in NEMS.

The white force noise, due to thermal energy which is normalized to give $1/2 k_B T$ after the integration over a mechanical mode resonance as stated by the equipartition

theorem, is defined as follows:

$$S_F^{\text{th}}(\Omega) = 4M\Gamma k_B T. \quad (4.16)$$

This force noise is shaped into a Lorentzian displacement noise by the mechanical susceptibility, χ , of the mechanical resonator (i.e. the mechanical transfer function):

$$S_x^{\text{th}} = \chi^2 S_F^{\text{th}}, \quad (4.17)$$

where

$$\chi^2(\Omega) = \frac{1}{M(\Omega_0^2 - \Omega^2 - i\Gamma\Omega)}. \quad (4.18)$$

Above, $\Gamma = \Omega/Q$ where Q is the mechanical quality factor, Γ is the resonant linewidth (i.e. damping), and M is the effective mass of the mechanical resonant mode.

That displacement noise transforms to phase noise is the essence of a Robins' phase noise analysis. Consider the instantaneous displacement position vs time during the oscillation cycle (Figure 4.3 (a)). Noise on this displacement creates uncertainty in both the peak amplitude obtained as well as the zero-crossing. The former contributes to amplitude noise and the latter to phase noise. Using a phasor view, where a vector of amplitude length rotates in an x-y plane once per cycle, one defines X_1 and X_2 axes as amplitude and phase quadratures, respectively. Figure 4.3 (b) on the left displays a hypothetical circle of displacement noise with an average squared thermal amplitude of $\langle x_{\text{th}}^2 \rangle$. This noise circle is displaced along X_1 quadrature by the driven amplitude x_d . The average squared phase noise $\langle \Delta\phi^2 \rangle$ is in proportion to the ratio of squared displacement noise to squared driven displacement. Extrapolating from Figure 4.3, the phase noise is taken as

$$S\phi^{\text{th}}(\Omega) = \frac{1}{2} \frac{S_x^{\text{th}}}{\langle x_d^2 \rangle}. \quad (4.19)$$

The factor of 1/2 comes from the property that 1/2 the noise will be in the amplitude quadrature and 1/2 will be in the phase quadrature. Also from the figure, the average squared thermal amplitude is defined as

$$\langle x_{\text{th}}^2 \rangle = \frac{k_B T}{M\Omega_0^2}. \quad (4.20)$$

If we define f as the offset from the carrier frequency such that $\omega = 2\pi f = \Omega - \Omega_0$ we find that

$$|\chi(\Omega)|^2 = \frac{1}{(2\Omega_0\omega + \omega^2)^2 + \Gamma^2\Omega^2} \frac{1}{M^2}, \quad (4.21)$$

thus,

$$S\phi^{\text{th}}(\Omega) = \frac{1}{2} \frac{1}{(2\Omega_0\omega + \omega^2)^2 + \Gamma^2\Omega^2} \frac{4\Gamma k_B T}{M\langle x_d^2 \rangle}. \quad (4.22)$$

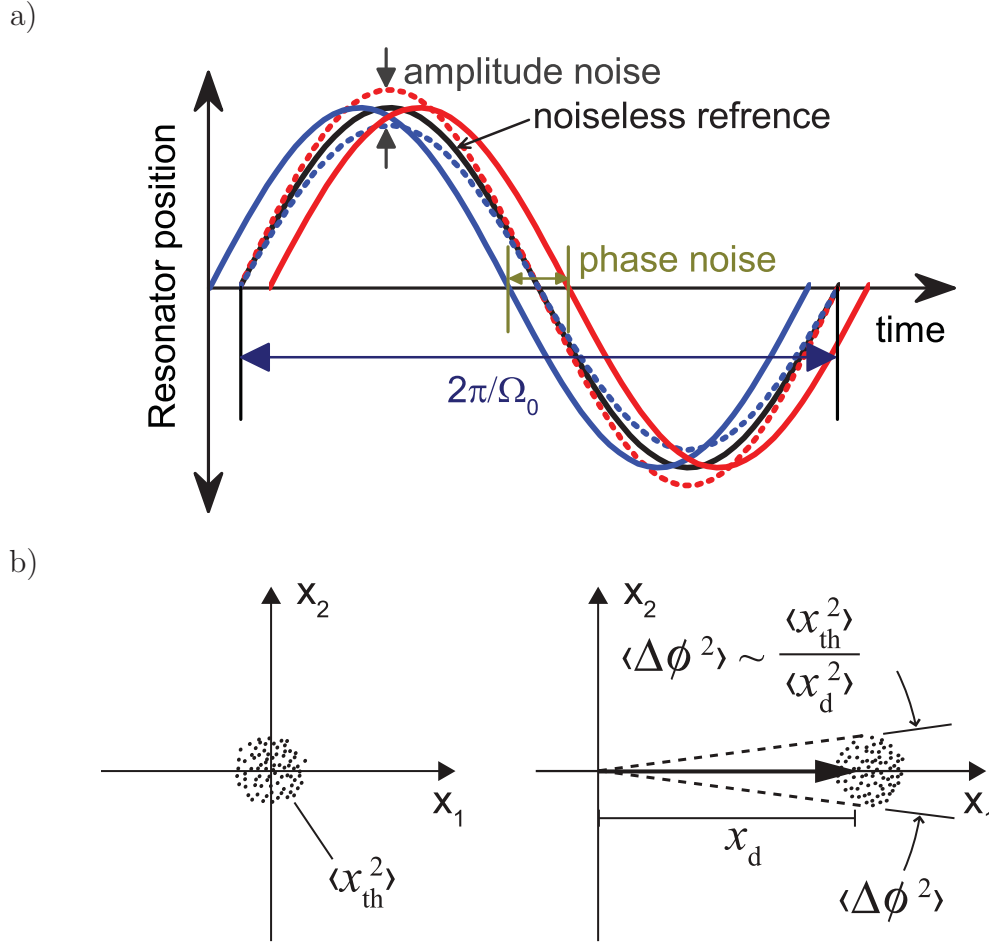


Figure 4.3: **Robins' analysis: displacement noise transforms to phase noise.** (a) **Position vs time during one oscillation cycle.** Displacement noise acts as an instantaneous background sine wave of similar frequency that adds to the black signal sine wave. If the noise is the same phase (180 degrees) as the signal, it increases (decreases) the signal amplitude as shown by the red (blue) dashed line. If the noise is 90 degrees leading (lagging) the signal phase, it decreases (increases) the zero crossing time, as shown by the blue curve (red curve). In this way, noise creates uncertainty in either or both of peak amplitude (amplitude noise) and instant of zero-crossing (phase noise), depending on the quadrature of the noise. (b) **Ratio of energies concept.** From a phasor viewpoint, amplitude X_1 and phase X_2 quadratures are defined. **Left.** Displacement noise spread at the origin with average squared amplitude $\langle x_{th}^2 \rangle$. **Right.** Same noise spread is displaced from the origin by driven amplitude x_d . The uncertainty in (average) squared phase angle $\langle \Delta\phi^2 \rangle$ is in proportion to the ratio of squared thermal to driven amplitudes. From [16]. Reprinted with permission from AAAS.

Normally, the following assumptions are made: (1) $\omega \ll \Omega_0$, and (2) $\omega \gg \Gamma$.

These simplify the derivation to result in [20, 19]

$$S\phi^{\text{th}}(\omega) \approx \frac{\langle x_{\text{th}}^2 \rangle \Gamma/2}{\langle x_{\text{d}}^2 \rangle \omega^2}. \quad (4.23)$$

However, for moderate and higher damping, and for frequencies close to the carrier, condition (2) no longer holds. Simplifying using only condition (1) we obtain

$$\begin{aligned} S\phi^{\text{th}}(\omega) &\approx \frac{1}{(2\Omega_0\omega)^2 + \Gamma^2\Omega_0^2} \frac{2\Gamma k_{\text{B}}T}{M\langle x_{\text{d}}^2 \rangle} \\ &\approx \frac{1}{(2\Omega_0)^2} \frac{1}{\omega^2 + (\Gamma/2)^2} \frac{2\Gamma k_{\text{B}}T}{M\langle x_{\text{d}}^2 \rangle} \\ S\phi^{\text{th}}(\omega) &\approx \frac{\langle x_{\text{th}}^2 \rangle}{\langle x_{\text{d}}^2 \rangle} \frac{\Gamma/2}{\omega^2 + (\Gamma/2)^2}. \end{aligned} \quad (4.24)$$

Next, if we define $a_{\text{th}}^2 \equiv S_{\text{x}}^{\text{th}}(\Omega_0)\Delta f$, where Δf is the measurement bandwidth of the S_{x}^{th} quantity

$$\begin{aligned} a_{\text{th}}^2 &= \frac{4k_{\text{B}}T}{M\Omega_0^2\Gamma}\Delta f \\ &= \frac{\langle x_{\text{th}}^2 \rangle}{\Gamma/4}\Delta f, \end{aligned} \quad (4.25)$$

we can then define

$$(SNR)^2 \equiv \frac{\langle x_{\text{d}}^2 \rangle}{a_{\text{th}}^2} = \frac{\langle x_{\text{d}}^2 \rangle \Gamma/4}{\langle x_{\text{th}}^2 \rangle \Delta f}. \quad (4.26)$$

Therefore, $S\phi^{\text{th}}(\omega)$ can finally be written as:

$$S\phi^{\text{th}}(\omega) = \frac{1}{(SNR)^2} \frac{1}{2\Delta f} \frac{(\Gamma/2)^2}{\omega^2 + (\Gamma/2)^2} \quad (4.27)$$

The shape of $S\phi^{\text{th}}(\omega)$ is thus a low pass filter with a knee at $\omega = \Gamma/2$; it can be approximated as a constant value near the carrier frequency and as a $1/\omega^2$ function far from the carrier frequency:

$$S_{\phi,\text{near}}^{\text{th}}(\omega) \sim \frac{1}{(SNR)^2} \frac{1}{2\Delta f} \quad \omega \ll (\Gamma/2) \quad (4.28)$$

$$S_{\phi,\text{far}}^{\text{th}}(\omega) \sim \frac{1}{(SNR)^2} \frac{1}{2\Delta f} \frac{(\Gamma/2)^2}{\omega^2}. \quad \omega \gg (\Gamma/2) \quad (4.29)$$

A conceptual diagram of how Langevin force noise becomes phase noise is presented in Fig. 4.4. With a caveat that will be discussed in the next section, we can use equation 4.10 to derive instantaneous frequency noise density from the instantaneous phase noise density of equation 4.28 and 4.29.

$$S_{\Delta\omega,\text{near}}^{\text{th}}(\omega) \sim \frac{1}{(SNR)^2} \frac{\omega^2}{2\Delta f} \quad \omega \ll (\Gamma/2) \quad (4.30)$$

$$S_{\Delta\omega,\text{far}}^{\text{th}}(\omega) \sim \frac{1}{(SNR)^2} \frac{(\Gamma/2)^2}{2\Delta f}. \quad \omega \gg (\Gamma/2) \quad (4.31)$$

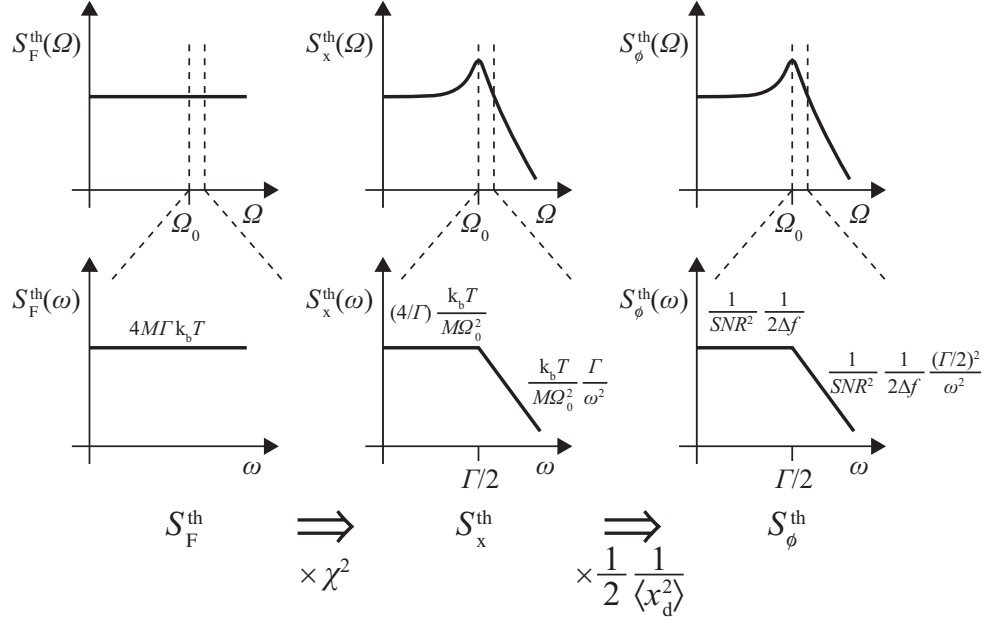


Figure 4.4: **Conceptual diagram of the force noise translating to phase noise.** White Langevin force noise S_F^{th} from the thermal bath turns into Lorentzian displacement noise S_x^{th} through the resonator's squared mechanical susceptibility χ^2 and then into phase noise through normalization by squared driven amplitude x_d^2 . As Ω zooms in to ω (top row going to bottom row), the low-pass filter nature of the Lorentzian curve is revealed. Functional values for the flat and slope regions are listed on the graph. From [16]. Reprinted with permission from AAAS.

This section has assumed that the resonator is driven by a separate clean reference frequency, so far without mentioning feedback. Equation 4.30 and 4.31 represent the analytic signal at the output of the NEMS device (as it would be measured by a frequency counter in open loop, for example) and is the basis for the flat-band model derived in [16]. However, the frequency noise level of equation 4.30 and 4.31 is not directly useful in terms of determining the ability of NEMS to perform sensing.

4.4.1 Relation between phase and frequency noise of resonator

4.4.1.1 Open loop measurements : flatband model conceptual flaw

The information provided by equation 4.30 and 4.31 is with respect to the stability of the oscillator signal that is driving the NEMS device after NEMS thermomechanical

noise has been added to that signal. However, if the goal is to define a background noise level or resonator noise level for sensing of changes in the NEMS equation of state, those fluctuations are not the appropriate choice. Essentially, the goal is not to deduce changes in instantaneous frequency to the analytic signal that exits the open loop NEMS, but rather changes in the equation of state frequency of the NEMS resonator.

A perturbation to NEMS frequency (e.g., by mass loading) will cause a shift in the phase of the NEMS that is proportional to the phase vs. frequency slope of the NEMS response function (Figure A.2b and equation 2.5 in Chapter 2):

$$\Delta\omega = \frac{\Omega_0}{2Q} \Delta\phi. \quad (4.32)$$

This condition is valid only when the resonator operates in the linear regime of its phase response, i.e., for small phase perturbations. Thus, to interrogate the noise in NEMS resonator equation of state frequency, the phase noise must be multiplied by the inverse squared phase slope [21] to get flatband ($\omega \ll (\Gamma/2)$) frequency noise spectral density

$$S_{\Delta\omega,\text{near}}^{\text{th}}(\omega) = \frac{S_{\Delta\phi,\text{near}}^{\text{th}}(\omega)}{(\frac{\delta\phi}{\delta\omega})^2} = \left(\frac{\Omega_0}{2Q}\right)^2 \times S_{\Delta\phi,\text{near}}^{\text{th}}(\omega) = \left(\frac{\Gamma}{2}\right)^2 \times S_{\Delta\phi,\text{near}}^{\text{th}}(\omega). \quad (4.33)$$

The phase noise from an open loop system can be directly measured by a lock-in amplifier and converted to NEMS equation of state frequency noise by the above multiplication. This is a common procedure [22] that we also use in this thesis. Using $\frac{\delta\phi}{\delta\omega} = \frac{\Gamma}{2}$ rather than equation 4.10, this produces equation 4.34 from equation 4.28 as below

$$S_{\Delta\omega,\text{near}}^{\text{th}}(\omega) \sim \frac{1}{(\text{SNR})^2} \frac{(\Gamma/2)^2}{2\Delta f}. \quad \omega \ll (\Gamma/2), \quad (4.34)$$

which has the same form of equation 4.31 for high- Q resonator when $\omega \gg (\Gamma/2)$. Thus frequency noise density of a resonator defined in equation 4.34 removes bandwidth approximation described in our previous publication [16].

4.4.1.2 Notes on NEMS frequency noise measurements from predecessors

Robins' original derivation [18] assumed an oscillator system (a closed loop with gain and positive feedback such that self-oscillation occurs). The same approach was taken for AFM sensing [19]. In such a system, amplification causes extreme narrowing of the linewidth [18, 19, 146], creating an effective quality factor, $Q' = (\langle a_d \rangle^2 / \langle a_{\text{th}} \rangle^2) \times Q$. Here, Q is the mechanical quality factor from TM noise spectra, a_{th} and a_d is thermal

noise and driven amplitude respectively. This effectively shrinks the flat-band region to become negligible, leaving equation 4.31 (i.e., 4.34) as the frequency noise. In the pioneering work from Cleland and Roukes [20] in 2002, however, the system had a separate signal carrier with NEMS noise sidebands (implied open loop). This was the precedent for applying equation 4.10 to an open-loop phase noise to recover a frequency noise. In this case, a high- Q assumption was made to deliver equation 4.34. That high- Q assumption was not particularly well-suited to NEMS and small bandwidths, but wound up with the correct expression for frequency noise regardless due to the high- Q assumption having the same effect as closing the loop would have had. This precedent led Gavartin et al. [127] and Roy et al. [16] to make a distinction regarding the close-in phase-noise region (i.e., the flat-band region), and correspondingly to argue for a τ^{-1} region of Allan deviation. This distinction did not take full consideration of the loop transfer function on the phase noise. In 2004, Ekinci and Roukes [21] considered NEMS in a PLL closed loop case with a generic transfer function of unity and correctly used equation 4.32 and 4.33 to arrive at a version of 4.34. More recently, Olcum et al. [31], and Demir and Hanay [142], considered explicit proportional integral (PI) PLL NEMS loop transfer functions. As discussed below, the result always returns to a version of equation 4.34. Finally, in 2012, Fong *et al.* [25] articulated a distinction between resonator frequency and instantaneous frequency to show that frequency noise translates into higher phase noise for higher Q (essentially applying equation 4.32 in reverse). They also correctly apply 4.32 to deduce meaningful (resonator) frequency noise in spite of a suggested interpretation that higher Q degrades the sensing performance.

4.4.1.3 Closed loop system

In a closed loop system, the output frequency tracks to the NEMS oscillator resonant frequency, so the conversion of instantaneous phase output to instantaneous frequency is appropriate (equation 4.10) due to the higher instantaneous phase noise.

4.4.1.3.1 Positive feedback (self-oscillation): If the system is self-oscillating, the resonator phase noise in the NEMS is amplified in the feedback loop by the well-known Leeson effect (as articulated well by Rubiola [146]). The output phase noise of the system ($S_{\psi, \text{oscillator}}(\omega)$) will take on a perfect integrator noise transfer function in comparison to the resonator open-loop phase noise ($S_{\phi, \text{open}}(\omega)$). This perfect integrator amplifies the noise that is slower than resonator bandwidth

$$S_{\psi, \text{oscillator}}(\omega) = \left[1 + \left(\frac{\Omega_0}{2Q} \right)^2 \frac{1}{\omega^2} \right] S_{\phi, \text{open}}(\omega) = \left[1 + \frac{(\Gamma/2)^2}{\omega^2} \right] S_{\phi, \text{open}}(\omega). \quad (4.35)$$

For $\omega \ll (\Gamma/2)$, the integrator perfectly cancels the low-pass filter of equation 4.27, turning it into

$$S_{\psi,\text{oscillator}}(\omega) \sim \frac{(\Gamma/2)^2}{\omega^2} \times \frac{1}{(\text{SNR})^2} \frac{1}{2\Delta f} = S_{\Delta\phi,\text{far}}^{\text{th}}(\omega). \quad (4.36)$$

The equation 4.36 is an alternative derivation of Robins' phase noise from Leeson model derived for flatband regime. Then, equation 4.10 turns into frequency noise equivalent to equation 4.34

$$S_{\omega,\text{oscillator}}(\omega) = \omega^2 S_{\psi,\text{oscillator}}(\omega) = S_{\Delta\omega,\text{Robin}}(\omega) \sim S_{\Delta\omega,\text{open}}(\omega). \quad (4.37)$$

4.4.1.3.2 Frequency locked loop or phase locked loop (negative feedback):

In addition to Ekinici *et al.* [21], references to non-NEMS literature provide similar insight. Rubiola [146] examines a test case for a discriminator stabilized frequency locked loop (which the NEMS PLL essentially is) with simple gain. The output phase noise returns a Leeson amplification close-in (as long as the gain is large) returning again to equation 4.34. More formally, with a fuller exploration of a 2nd order, proportional integral (PI), PLL NEMS loop, Demir and Hanay [142] report a phase noise transfer function as:

$$\chi_{\phi,PLL}^{\text{th}}(s) = \frac{1}{s} \frac{1}{\tau_r} \frac{(sK_p + K_i)\chi_L(s)}{s^2 + \frac{s}{\tau_r} + (sK_p + K_i)\chi_L(s)}, \quad (4.38)$$

where, $s = j\omega$ and

$\chi_{\phi,PLL}^{\text{th}}(s)$ is the transfer function for phase noise measurement

K_p is the proportional gain of PID in PLL.

K_i is the integral gain of PID in PLL.

$\chi_L(s)$ is the low-pass transfer function of the demodulator and $\chi_L(j\omega_{\text{PLL}}) \approx 1$

$\tau_r = 2Q/\Omega_0$ is the resonators intrinsic ring-down time.

Corresponding transfer function, $\chi_{\Delta\omega}^{\text{th}}(s)$ for frequency noise density can be found as

$$\chi_{\Delta\omega,PLL}^{\text{th}}(s) = \frac{1}{\tau_r} \frac{(sK_p + K_i)\chi_L(s)}{s^2 + \frac{s}{\tau_r} + (sK_p + K_i)\chi_L(s)}. \quad (4.39)$$

Now the spectral density of frequency fluctuation noise at PLL output can be written as

$$S_{\Delta\omega}^{\text{th}}(\omega) = |\chi_{\Delta\omega,PLL}^{\text{th}}(s)|^2 S_{\phi}^{\text{th}}(\omega), \quad (4.40)$$

when, $s \rightarrow 0$ this transfer function satisfies for all Q values as

$$\chi_{\Delta\omega, PLL}^{\text{th}}(s \rightarrow 0) = \frac{1}{\tau_r}. \quad (4.41)$$

Thus, the presence of $\tau_r = 2Q/\Omega_0$ in equation 4.39 is also satisfied for the condition, $\omega \ll (\Gamma/2)$ and we again have close in frequency noise, $S_{\Delta f}(f)$, from equation 4.28 by 4.40

$$S_{\Delta\omega, \text{near}}^{\text{th}}(\omega) \sim \frac{1}{(SNR)^2} \frac{1}{2\Delta f} |\chi_{\Delta\omega}^{\text{th}}(s \rightarrow 0)|^2 = \frac{1}{(SNR)^2} \frac{1}{2\Delta f} \frac{1}{\tau_r^2}, \quad \omega \ll (\Gamma/2) \quad (4.42)$$

which yields.

$$S_{\Delta\omega, \text{near}}^{\text{th}}(\omega) = S_{\Delta\omega, \text{far}}^{\text{th}}(\omega) \sim \frac{1}{(SNR)^2} \frac{1}{2\Delta f} (\Gamma/2)^2. \quad (4.43)$$

The end result is, for both near and far noise regions, the frequency noise is the same and is white (independent of omega) and is of the same form as Robins' formula. Furthermore, when SNR is proportional to Gamma in equation 4.43, they cancel, leaving a Q independent frequency noise (as discussed in chapter 3).

4.5 Derivation of Allan deviation from frequency noise density of resonator

After revisiting Robins' phase noise in the light of open and closed loop measurements, we can show how phase noise density of a mechanical resonator transforms into frequency noise density by phase-frequency relation at resonance. Whatever the Q , our analysis shows that phase perturbations by thermal displacement noise induces white frequency noise density predicted by Robins' model and theoretically valid for a wide range of measurement bandwidths. Now recalling, equation 4.34 (from the open loop) and 4.43 (from the PLL) we have the same frequency noise density given by

$$S_{\Delta\omega}^{\text{th}}(\omega) \sim \frac{1}{(SNR)^2} \frac{1}{2\Delta f} (\Gamma/2)^2,$$

which yields

$$\begin{aligned} S_y(f) &= \frac{1}{\Omega_0^2} S_{\Delta\omega} \cong \frac{1}{(SNR)^2} \frac{1}{2\Delta f} \frac{1}{(2\pi)^2 \nu^2} \left(\frac{\Gamma}{2}\right)^2 \\ &\sim \left(\frac{1}{2Q}\right)^2 \frac{1}{(SNR)^2} \frac{1}{2\Delta f}. \end{aligned} \quad (4.44)$$

This implies that, assuming $\Delta f = 1$ for the measurement bandwidth f_H ,

$$\sigma_y(\tau) = C f^0 S_y(f) \tau^{-1} = \frac{1}{4} \frac{1}{SNR} \frac{1}{Q} \frac{1}{(\tau)^{1/2}}. \quad (4.45)$$

Equation 4.45 is essentially Robins' formula (denoted with subscript "R"). For situations where $SNR \propto 1/Q$, such as when accessing full dynamic range, $\sigma_R \sim Q^0$ (no Q dependence).

4.6 Conclusion

This chapter briefly summarizes the theoretical foundations of NEMS frequency stability by considering its ultimate limit imposed by thermomechanical noise. Translation of phase noise into the frequency noise and relations with time-domain stability is described and compared to other literature benchmarks. We address some confusion in the NEMS literature, including our own, about appropriate ways to convert phase noise to frequency noise. We rederive Robins' formula for a NEMS system to find a flat-band region of f^0 phase slope near the carrier frequency with the traditional f^2 slope far from the carrier frequency. We then show that both such regions turn into white resonator frequency noise in all cases (open loop, self-oscillation, PLL or FLL) equivalent to the high- Q approximation of Robins' original formula. Ultimately, thermal noise limited frequency stability is found described efficiently by the term $Q \times SNR$ rather than the Q alone. In the next chapter, the experimental results of frequency stability will be discussed based on the theoretical foundations made in this chapter.

Chapter 5

Improving mechanical sensor performance through larger damping

5.1 Introduction

Elements of this chapter have been published in [16]. The coupling of mechanical motion to an optical cavity allows tracking the motion with femtometer precision. When using NOMS (or their electrical cousin NEMS) as a stable frequency reference, tiny force and mass changes can be distinguished by small frequency shifts. This is useful in atomic force microscopy and ultrasensitive mass measurement. For example, mass sensitivity has been shown able to resolve single molecules and has launched a prospective new paradigm of mechanical mass spectrometry. Any method to improve stability improves the performance of these sensors. If stability can be the same or better with more damping, NOMS ultrasensitivity could be deployed in a damping medium, like air or liquid, greatly enhancing their utility for use as biosensors, gas sensors or in the environment. Better stability could also benefit oscillator clock electronics which could ultimately improve technologies such as GPS.

The Q-factor (Q) is proportional to the inverse of the damping and tells how sharp the resonance is in frequency. Q has been used as a proxy metric for frequency stability. However, Q only provides half the contribution; the other half comes from how large the resonance signal is compared to noise (the signal to noise ratio (SNR)). This relationship is known as Robins' model and is described elaborately in the last chapter. While traditionally Q and SNR have been assumed to be correlated, we noted that when the resonance conditions are limited only by intrinsic factors, the SNR should be inversely proportional to Q . In this case, stability should be independent of Q , and stable performance should be maintained in a variety of damping conditions.

The goal of this chapter is to test the $Q \times SNR$ relation on the measured frequency stability of the nanometric DCB resonator coupled to an optical ring through successive experiments by phase-locked loop and open loop. Interestingly measured Allan deviation by phase-locked loop shows improved stability at larger damping, which is far better than Robins' prediction. However, we just established in chapter 4 that beating Robins' limit should not be possible. We explain the discrepancy in this chapter; a thorough inspection of existing phase-locked loop theory reveals that such improvement with damping is associated with PLL transfer functions. Here we will elaborately show how a PLL transfer function shapes the noise process in experiments. With the knowledge of noise-shaping by PLL transfer function, this chapter successfully derives analytical models of Allan deviation for shaped phase noise. We have derived and simulated models so well that they agree with experimental Allan deviation results for different PLL bandwidths. Such detailed PLL analysis explains that high-frequency noise suppression by low-pass filter integration artificially improves stability at larger damping, which is not associated with properties of the mechanical resonator. We also find that our modeled PLL rise times match experimental ones, and that the PLLs should properly track frequency changes over long time periods.

To study the intrinsic resonator behavior, open-loop experiments (free from gain artifacts as in PLL) are employed. Open loop data analysis shows that measured Allan deviations at lower pressures (higher Q) are higher than the respective thermal limit, but gradually reduce down to the thermal limit with increasing pressure. High- Q conditions produce data consistent with ubiquitous flicker fluctuations in resonance (f^{-1} noise)[22] hiding the thermal limited stability of the mechanical resonator. A significant contribution of the current thesis is the experimental evidence of gradually weaker f^{-1} noise at higher pressures (low- Q) via better temperature stability through heat conduction by air molecules which will be explored in the later chapter. Feeble flicker fluctuations at higher pressures allow TM noise limited stability at atmosphere, whereas high- Q sensor performance is higher than this limit due to the excess noise. Although damping, itself, does not lower Robins' limit, it reduces excess noise at atmosphere to attain Robins' limit, which is not accessible at high- Q conditions (at least in the current thesis). Thus the chapter title remains apropos and frequency stability grows better through damping [16] albeit indirectly. Such observations firmly say that damping can also be beneficiary for better mechanical sensor performance. Here we will unveil why and how damping can improve stability of mechanical resonator under certain conditions. Discussions in sections 5.3.1, 5.3.2.2, and 5.3.2.4 are composed from the publication [16].

5.2 Experiments

Throughout the thesis, we have used the basic experimental setup described in Chapter 2. For frequency stability measurements, the built-in phase locked loop (PLL) architecture of Zurich instrument HF2 lock-in has been used. Three series of measurements have been performed. In the first series, measurements of TM noise, driven responses, and Allan deviations for different bandwidths have been made at 17 different pressures from high vacuum to atmospheric pressure, among which *DR* results were discussed in Chapter 3. In the second series, similar experiments have been conducted for only 100 μ Torr, 5.5 Torr, 55 Torr and 760 Torr to get both open and closed loop Allan deviations. In the last series, open loop measurements within Duffing limited pressure regime for 10 mTorr, 100 mTorr, 1 Torr, 10 Torr, and 25 Torr have been carried out. It should be noted that aforementioned series of experiments was carried out for 3 different chips with exactly same configuration of device at different time.

5.2.1 Lock-in amplifier and PLL details

A phase-locked loop (PLL) is essentially a feedback control system which locks the phase and frequency output of a low noise oscillator to the phase and frequency of an input signal. In a sensing context, it can be used to stabilize and track the resonance frequency of the input signal, which carries the sensed information in its resonance frequency. Extensive applications of PLL for tracking nanomechanical vibration can be found in Ref. [148] and the references therein for atomic force microscopy. Roukes' group pioneered analog PLL use in NEMS for mass sensing [27]. Recently, Olcum *et al.* [31] gave a very detailed discussion of loop dynamics during the use of a closed loop PLL for measuring stability and mass sensitivity. We use a PLL in closed loop to track frequency shifts for the purposes of determining stability (such as for Allan deviation measurements) as well as for tracking frequency shifts caused by mass adsorbants[5] or due to temperature change (*cf.* Chapter 6). We use open loop measurements for verification of presence or absence of intrinsic frequency fluctuation noise (as in next chapter). Figure 5.1 describes our PLL circuit, which basically takes advantage of the built in functionality of the Zurich Instruments HF2LI. The NEMS as the device under test is the frequency determining element in the circuit, controlling the NCO (numerically controlled oscillator) frequency in the Zurich instrument via PID feedback. The feedback controller and the PID parameters control the PLL bandwidth via the PID gains, creating a transfer function for the error signal. Fluctuations on a faster time scale than the corner frequency of the transfer function start to become

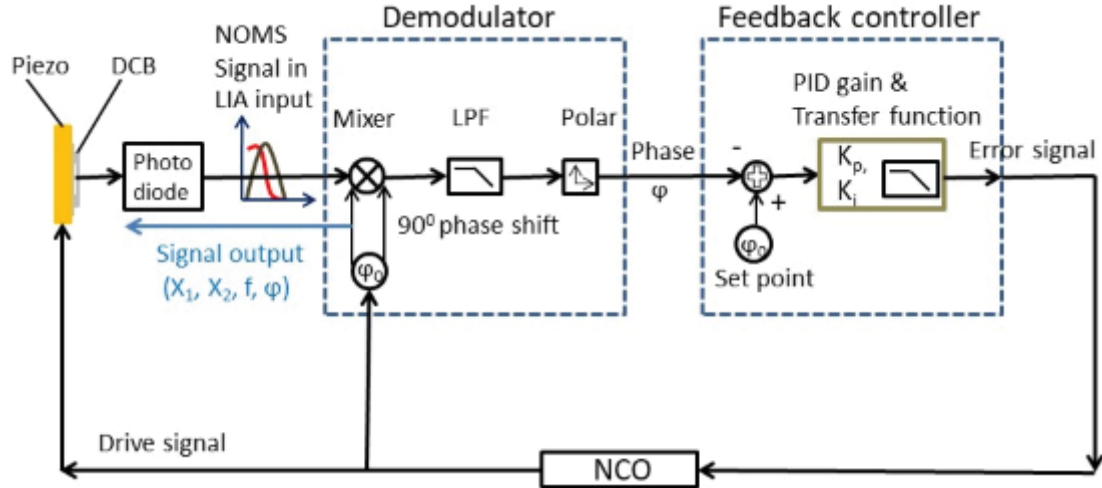


Figure 5.1: A dual-phase demodulator, a controller, and an NCO (numerically controlled oscillator) are three essential building blocks of a phase locked loop configuration inside the Zurich instrument HF2 lock-in amplifier. These three are combined to form a negative feedback loop. Within the loop, the phase detector (mixer) detects the phase difference between the incoming NOMS signal and the reference. Depending on PI gain (set by the bandwidth, D parameter is not in use) the controller regulates the NCO to achieve a vanishing phase difference, which means that the NCO frequency always adapts the NEMS frequency at a constant SNR by maintaining a -90° phase between the DUT and NEMS. Thus the lock-in output, i.e., the reference always follows the NEMS frequency depending on phase error controlled by the feedback and overlooks any error due to amplitude fluctuations. From [16]. Reprinted with permission from AAAS.

filtered out. Thus, sampling times τ shorter than the inverse of the PLL bandwidth are generally not reported. The demodulator portion of the circuit measures the instantaneous frequency and phase of the incoming signal. It has a demodulation bandwidth set by its low pass filter that is kept at 8 times the PLL bandwidth for stability reasons. For purposes of noise measurement, the PLL bandwidth is what sets the noise measurement bandwidth Δf and the high frequency integration cutoff f_H discussed in the next section.

The PID parameters are automatically calculated by the lock-in “advisor” software based on Q , center frequency, desired PLL bandwidth, locking range, and phase setpoint. The advisor computes through a numerically optimized algorithm of loop dynamics to generate a set of feedback gain parameter which tries to match the target bandwidth in its simulated second-order transfer function. Figure 5.2 shows a representative bode plot of an advisor simulated transfer function for 500 Hz PLL BW which has a 3 dB roll-off at 500 Hz and is a typical example of PLL transfer function.

We were specifically using ziControl software from Zurich Instruments in our

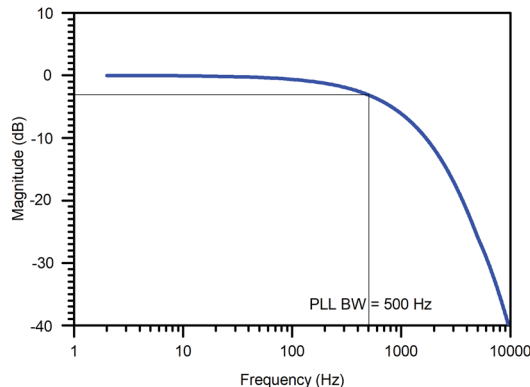


Figure 5.2: **A representative PLL transfer function obtained from Zurich instrument HF2.** Target BW is at -3 dB point in the bode plot. In case of any mismatch between set resonance parameters, a target bandwidth, and numerical modeling advisor fails to produce such bode plot with warning indications. It automatically adjusts the demodulation bandwidth to value eight times PLLBW to avoid being limited by the demodulation speed. From [16]. Reprinted with permission from AAAS.

PLL loops in this thesis. Unfortunately, certain combinations of gain parameters would produce acceptable looking bode plots (see Figure 5.2) while the actual transfer function looked markedly different. In particular, for small proportional gain setting (less than resonator linewidth) we belatedly discovered that the ziControl PLL advisor Bode plot could not be trusted ¹. More will be said about this in the following section.

5.3 Results and discussion

5.3.1 Frequency fluctuation measurements (Allan deviation) by phase locked loop experiments

With $Q \times SNR$ conserved (see Figure 3.4 in chapter 3), it is left to check the fractional frequency stability $\delta f/f$ in our device. We do this using the 2-sample Allan variance, a standard method of characterizing frequency stability [147] related to Robins' formula (see Chapter 4). The Allan deviation $\sigma(\tau)$, as the square root of the Allan variance, is an estimate of fractional frequency stability for a given time τ between frequency readings. The functional form for $\sigma(\tau)$ is

$$\sigma_R(\tau) = \frac{1}{4Q} \frac{1}{SNR} \frac{1}{\sqrt{\tau}} \quad (5.1)$$

¹We later conducted tests on a driven Qplus quartz crystal using Zurich Instrument LabOne software and HF2LI lock-in under similar loop conditions as this chapter (where proportional gain was set lower than resonator linewidth). In contrast to ziControl, changing PLL bandwidth did not change measured Allan deviation when using LabOne software. Initial indication were that the advisor Bode plots were always accurate in LabOne.

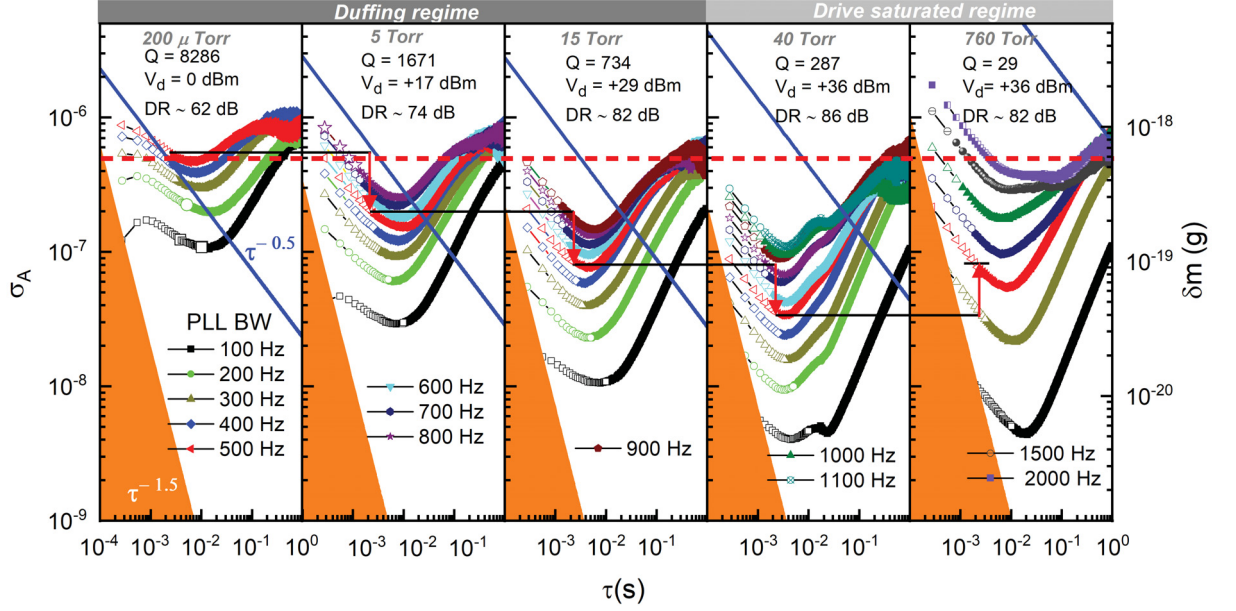


Figure 5.3: **Phase-locked loop Allan deviation falls (improves) with falling Q for a measurement bandwidth.** The figure describes Allan deviation versus sampling time at different pressures for different PLL BW. Symbols are measured data. Open symbols are measured data above bandwidth, and out of the discussion. The roll-off in measured data happens due to satisfying Nyquist criteria by the demodulation bandwidth ($8 \times$ PLLBW) and sampling frequency 3600 Hz. 500 Hz data (red plot) is considered for comparison. The solid line (blue) is a theoretical minimum from equation 5.1 while horizontal red dashed line is an imaginary line drawn for guiding the eye to show that the magnitude of $\sim QSNR^{-1}$ can be conserved at different damping. Shaded (orange) region is theoretical minimum set by instrumentation noise floor (equation C.2). Right axis represents equivalent mass resolutions from measured frequency stability by $\delta m = 2M_{\text{eff}} \sigma_A$. From [16]. Reprinted with permission from AAAS.

Figure 5.3 presents the measured Allan deviation data for our device at the five representative pressures and Q s for different PLLBWs less than the natural linewidth (Γ) along with theoretical model of Robin. Data is taken with a demodulation bandwidth of $8 \times$ PLL BW and collected while tracking frequency is the phase-locked loop (PLL) bandwidth (BW). Demodulation bandwidth represents the integration bandwidth for the noise while PLLBW sets the bound above which the PLL begins to attenuate fluctuations (effectively setting a minimum meaningful τ).

All data are well above the instrumentation noise floor contributions (equation C.2) shown by the orange shade (see Appendix section C.1). The solid blue line at each pressure represents the theoretical thermal limit set by Robins' formula (equation 5.1) for measured SNR . 500 Hz data at 200 μ Torr is close to respective thermal limit.

Hence, by equation 5.1), we may expect the same level of stability at $\tau \sim 2$ ms, at least, within the Duffing regime, as marked by the red-dashed line from left to right. Surprisingly, rather than staying constant, σ improved as the pressure increases and Q falls (up to 40 Torr pressure).

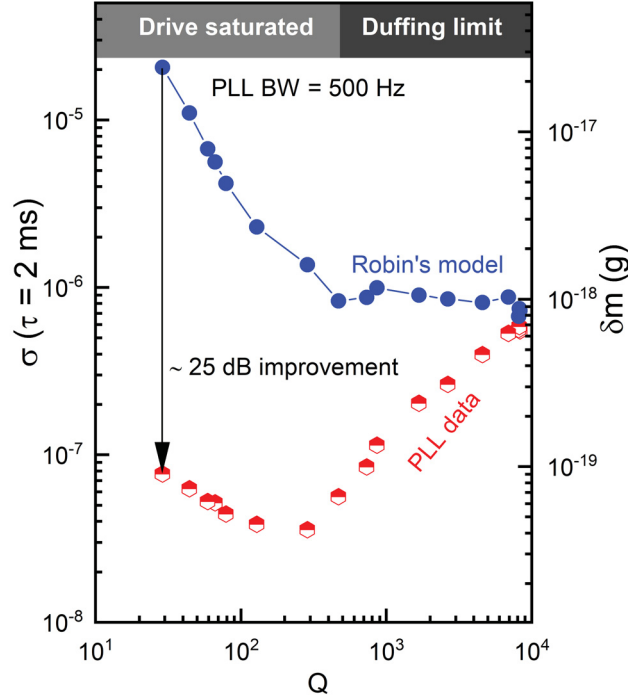


Figure 5.4: **Allan deviation at 2 ms sampling time vs. Q .** Except for high vacuum, PLL data significantly improves with Q . At 760 Torr measured data shows 25 dB improvement from theoretical limit by Robins' model. Such an improvement need further revision in interpreting time domain stability of mechanical sensor subjected to a phase-locked loop. From [16]. Reprinted with permission from AAAS.

Further, the measured data dip well below the theoretical minimum set by Robins' formalism and equation 5.1 (solid blue lines). Frequency stability, and therefore, performance, seems correlated to SNR alone although higher BW data at low pressures (5, 15, and 40 Torr) ascend towards the blue line but still far below the thermal limit. Figure 5.4 portrays the fall of measured Allan deviation with pressure and compares those to the respective thermal limit. The experimental results shown above are hard to believe. Derivation of σ_R (equation 5.1) considers only frequency fluctuations in resonance coming from TM noise which sets the ultimate limit of frequency stability. So, measured value below TM noise limit is a questionable result until proper diagnosis. In our publication in *Science* [16], we reported a flat-band model that we believed answered the question. However, as we discussed in the last chapter, the flat-band model reported in ref. [16] is conceptually wrong, although it is mathematically

accurate. So, the question remains, why such performance is better than the thermal limit. Here, we will explore the dilemma by analyzing the full model of PLL transfer function [142] developed for the similar architecture of HF2PLL block that consider effect of TM noise only.

5.3.1.1 Noise-shaping: Frequency domain stability analysis of PLL experiments

We have adopted recent phase-locked loop analysis done by Demir and Hanay [142] for HF2 PLL blocks and discussed in the last chapter. Following Ref. [142] transfer function at the PLL output has the form in case of thermomechanical noise limited operations:

$$\chi_{\Delta\omega, \text{PLL}}^{\text{th}}(s) = \frac{1}{\tau_r} \frac{(sK_p + K_i)\chi_L(s)}{s^2 + \frac{s}{\tau_r} + (sK_p + K_i)\chi_L(s)}, \quad (5.2)$$

where, $s = j\omega_{\text{mod}}$ and ω_{mod} is the offset frequency from resonance Ω_0 ; $\tau_r = \frac{2Q}{\Omega_0}$ is the intrinsic ring-down time. K_p and K_i is the proportional and integral gain parameters of the loop. ² From the proportional gain, P (Hz/degree) and Integral gain $I = \tau_i$ (s) advised by PLL adviser we calculate, $K_p = P$ in rad/s/rad, and $K_i = \frac{K_p}{I}$. All P-I parameters from 500 Hz experiments are listed in table 5.1. The transfer function, $\chi_{\Delta\omega, \text{PLL}}^{\text{th}}(s)$ is derived without considering any noise in PLL components. Hence, it is assumed that noise transfer function shaped by equation 5.2 will contain only resonator's behavior due to thermomechanical displacement noise only.

Now, the spectral density of frequency fluctuation noise at PLL output is

$$S_{\Delta\omega}^{\text{th}}(\omega) = |\chi_{\Delta\omega, \text{PLL}}^{\text{th}}(s)|^2 S_{\phi}^{\text{th}}(\omega). \quad (5.3)$$

From Chapter 4, we know the phase noise spectral density is valid for $\omega_{\text{mod}} < \Gamma$ as

$$S_{\Delta\phi}^{\text{th}}(\omega_{\text{mod}}) = \frac{1}{2} \frac{S_x^{\text{th}}}{a_{\text{driven}}^2} = \frac{1}{2} \frac{1}{(SNR)^2 \Delta f}. \quad (5.4)$$

Equation 5.3 yields

$$S_{\Delta\omega}^{\text{th}}(\omega) = |\chi_{\Delta\omega, \text{PLL}}^{\text{th}}(s)|^2 \frac{1}{2} \frac{1}{(SNR)^2 \Delta f}. \quad (5.5)$$

Equation 5.5 provides insight into how the PLL loop shapes the system noise. Figure 5.5 shows plots of $|\chi_{\Delta\omega, \text{PLL}}^{\text{th}}(s)|^2$ and $S_{\Delta\omega}^{\text{th}}(\omega)$ as a function of offset frequency according to equation 5.2 and 5.5. Part **b** of the figure presupposes a maximized

²Unfortunately, the ziControl does not output P and I parameters with the saved data. Luckily, we were able to locate all of the P and I values that were used by the advisor software through screenshots of the PLL adviser screen.

Table 5.1: P and I parameters from HF2 lock-in PLL advisor for 500 Hz experiments shown in Figure 5.3.

P (Torr)	P (Hz/degree)	I (ms)	K_p (rad.s ⁻¹ /rad)	K_i (rad.s ⁻¹ /rad.s)
100 μ	13.4	6.91	4,820	698,000
5	13.7	12.3	4,930	401,000
15	13.1	4.28	4,720	1,100,000
40	12.8	2.94	4,610	1,570,000
760	12.9	3.4	4,640	1,370,000

$SNR \propto Q^{-1}$ (Duffing assumption) and part **c** uses the experimental values of SNR . It is quickly evident that the PLL shaping is a viable explanation for measured Allan deviation results presented in Figure 5.3.

Four different frequency regions are evident in Figure 5.5. On the left plateau, region I, changes are slower than the integration time, and the loop follows the resonator frequency with high-fidelity. For the first roll-off, region II, ω/τ_r has become larger than K_i , and the loop begins losing tracking ability. Region II changes to region III when $\omega \times K_p$ equals K_i ; in Figure 5.5, this happens between 100 to 200 rad/s. In region III, the right plateau, K_p dominates over τ_r^{-1} to create a zero slope region. This zero-slope region renders a faux white frequency noise and ultimately a suppressed Allan deviation. The second roll-off, where ω/τ_r dominates, defines region IV and corresponds to the expected natural roll-off due to resonator linewidth.

In region I, $|\chi_{\Delta\omega, PLL}^{th}(s)|^2$ is inversely proportional to Q^2 and $S_{\Delta\omega}^{th}(\omega)$ is proportional to $(Q \times SNR)^{-2}$. This is the outcome expected by Robins' formula. In region III, the proportional gain K_p sets the $|\chi|$ amplitude. This gain is constant across pressures (set for a target 500 Hz loop bandwidth) and creates a faux Q , $Q' \sim \Omega_0/K_p$ that is the same for all Q conditions. Indeed, $|\chi|^2$ in this region is independent of Q (in actuality, inversely proportional to a constant Q'^2) and $S_{\Delta\omega}^{th}(\omega)$ depends only on SNR . Ultimately, this leads to a 50 dB noise suppression from region I to region III at

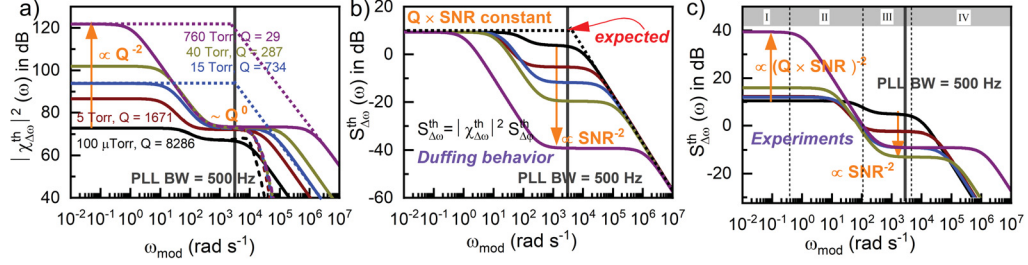


Figure 5.5: **Illustration of frequency noise density of a NEMS shaped by PLL parameters (for 500 Hz PLLBW) at different damping conditions. a)** $|\chi_{\Delta\omega,PLL}^{th}(s)|^2$ vs. ω_{mod} plot. Solid lines represent corresponding transfer function at each pressure mentioned in the plot for 500 Hz PLLBW ($\sim 3000 \text{ rad s}^{-1}$ and is indicated by the solid dark gray line from bottom to top). The dashed line represents respective transfer function for a 4th order filter used in the experiments which have a sharp cut-off at $\sim 8 \times \text{PLL BW}$. The flat dotted line (shown for 760, and 15 Torr only) is our expected PLL transfer function from the PLL advisor Bode plot. It is evident that each transfer function with a low pass filter of unit gain ($\chi_L(s) \cong 1$) has four distinct regions. In the low frequency region (around 1 rad s^{-1} and designated as Region I), transfer function is frequency independent and increases with decreasing Q . In Region II, the magnitude of it falls with frequency until the third region where the gain is constant (Region III). The roll-off of this integration region occurs faster with lower Q because of the shorter intrinsic ring down time, τ_r . Falling Transfer functions for all Q s converges around 200 rad s^{-1} to develop the Region III by the same proportional gain, K_p . $100 \mu\text{Torr}$ data is a little below this converging line. In Region III, the constant magnitude of $\chi_{\Delta\omega}^{th}(s)$ indicates white frequency noise (f^0) again and extends up to the respected $\Gamma/2$ followed by a signature of f^{-2} roll off in Region IV. **b)** Frequency noise behavior shaped by the PLL transfer function in **a)** when full DR is accessible from vacuum to atmospheric pressure. Inversely improved SNR with damping cancels the Q effect on $\chi_{\Delta\omega,PLL}^{th}(s)$ to measure the same amount of close-in frequency noise (Region I). Dotted lines represent the ideal Duffing behavior of measured frequency noise density for a given PLLBW with equal contributions from thermal noise at different damping. Q independent magnitude of $\chi_{\Delta\omega,PLL}^{th}(s)$ in the Region III drops proportionally with growing SNR at larger damping to establish reduced frequency noise at larger damping. **c)** Replica of plot **b)** for measured DR . A slightly lower measured SNR (than the calculated values in **b)** fails to establish an exact straight line in Region I for constant $Q \times SNR$. However, it fairly verifies constant $Q \times SNR$ relations for close-in frequency noise at different pressures and degrades with smaller $Q \times SNR$. In Region III, the transfer function depends on the measured SNR irrespective of measured Q and justify to consider an effective quality factor, Q' .

atmospheric pressure. This explains the 50 dB improvement in Allan variance (25 dB improvement in Allan deviation) evident in Figure 5.4.

5.3.1.2 Full model analysis

This section more explicitly covers how the frequency noise of equation 5.5 transforms into different Allan deviation in the four different regions. Figure 5.6 is a schematic presentation of the frequency domain stability and its transformation into the corresponding time domain stability when device noise is shaped by a phase-locked loop in Figure 5.5. Using equation 4.15 we can have AD expressions for different regions as

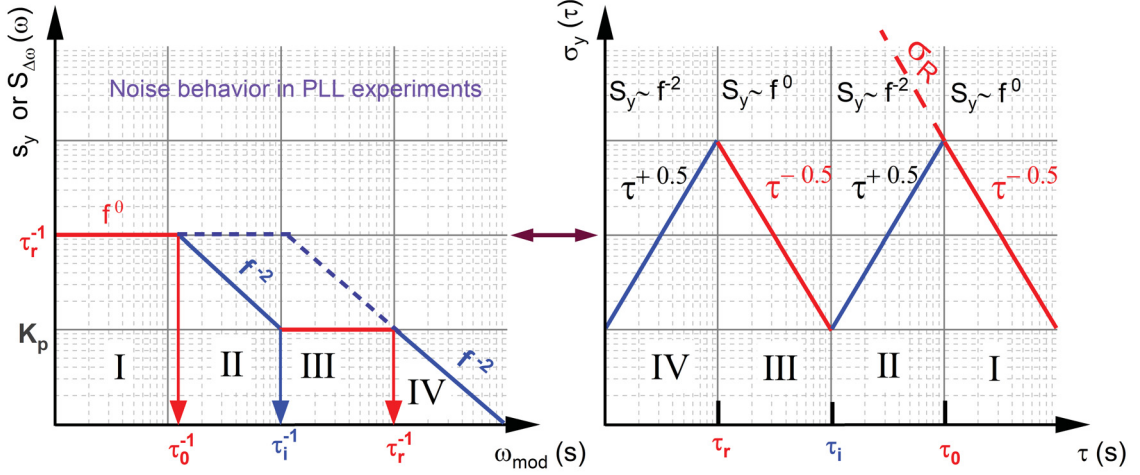


Figure 5.6: **Schematic view of frequency and time domain stability shaped by PLL transfer function.** Here, we define, $\tau_0 = K_i^{-1}\tau_r^{-1} = (\frac{K_P}{\tau_i}\tau_r)^{-1}$. **Left:** Frequency noise density shaped by PLL experiments for $\omega \ll \Gamma$ whatever the measured Q . **Right:** Shows corresponding time domain stability behavior.

follows:

Region I:

$$\begin{aligned}\sigma_y^2(\tau) &= C f^0 S_y(f) \tau^{-1} \\ &= \frac{1}{2} \frac{1}{\Omega_0^2} \frac{1}{SNR^2 2\Delta f} \frac{1}{\tau_r^2} \frac{1}{\tau}.\end{aligned}$$

Plugging $\tau_r = \frac{\Omega_0}{2Q}$ into above we have

$$\sigma_y(\tau) = \frac{1}{4} \frac{1}{Q SNR \sqrt{\Delta f}} \frac{1}{\sqrt{\tau}}. \quad (5.6)$$

Region II: By considering frequency noise close to carrier as RWFm we can write frequency noise density as follows:

$$\begin{aligned}S_y &= \frac{1}{\Omega_0^2} \frac{1}{SNR^2 2\Delta f} \left[\frac{1}{\omega} \frac{1}{\tau_r} \frac{K_p \tau_r}{\tau_i} \right]^2 \\ &= \frac{1}{\Omega_0^2} \frac{1}{SNR^2 2\Delta f} (2\pi)^{-2} f^{-2} \left(\frac{K_p}{\tau_i} \right)^2.\end{aligned}$$

So,

$$\begin{aligned}
\sigma_y^2(\tau) &= Af^2 S_y(f) \tau^1 \\
&= \frac{4\pi^2}{6} \frac{1}{\Omega_0^2} \frac{1}{SNR^2 2\Delta f} (2\pi)^{-2} f^{-2} \left(\frac{K_p}{\tau_i}\right)^2 \tau^1 \\
&= \frac{1}{6} \frac{1}{SNR^2 2\Delta f} \left(\frac{K_p}{\Omega_0 \tau_i}\right)^2 \tau,
\end{aligned}$$

which yields

$$\sigma_y(\tau) = \frac{1}{\sqrt{6}} \frac{1}{SNR} \frac{1}{\sqrt{2\Delta f}} \left(\frac{K_p}{\Omega_0 \tau_i}\right) \sqrt{\tau}. \quad (5.7)$$

Region III:

$$S_y = \frac{1}{\Omega_0^2} \frac{1}{SNR^2 2\Delta f} [f^0 K_p]^2.$$

That implies,

$$\begin{aligned}
\sigma_y^2(\tau) &= Cf^0 S_y(f) \tau^{-1} \\
&= \frac{1}{2} \frac{1}{\Omega_0^2} \frac{1}{SNR^2 2\Delta f} K_p^2 \frac{1}{\tau}.
\end{aligned}$$

Now, if we define an effective quality factor because of proportional gain of loop we may write, $Q' = \frac{\Omega_0}{K_p} = \frac{\Omega_0}{\Gamma} \frac{\Gamma}{K_p} = Q \frac{\Gamma}{K_p}$, which gives Allan variance as below

$$\begin{aligned}
\sigma_y^2(\tau) &= \frac{1}{2} \frac{1}{\Omega_0^2} \frac{1}{SNR^2} \frac{1}{2\Delta f} \frac{1}{Q'^2} \frac{1}{\tau} \\
&= \frac{1}{2} \frac{1}{Q'^2} \frac{1}{SNR^2} \frac{1}{2\Delta f} \frac{1}{\tau}.
\end{aligned}$$

Hence, thermal stability at this domain has the form

$$\sigma_y = \frac{1}{2} \frac{1}{Q'} \frac{1}{SNR} \frac{1}{\sqrt{\Delta f}} \frac{1}{\sqrt{\tau}}. \quad (5.8)$$

Region IV: In this region we have

$$S_y = \frac{1}{\Omega_0^2} \frac{1}{SNR^2 2\Delta f} \left[\frac{1}{\omega} \frac{1}{\tau_r K_p} \right]^2,$$

which gives us

$$\begin{aligned}
\sigma_y^2(\tau) &= Af^2 S_y(f) \tau^1 \\
&= \frac{4\pi^2}{6} \frac{1}{\Omega_0^2} \frac{1}{SNR^2 2\Delta f} (2\pi)^{-2} f^{-2} \left(\frac{K_p}{\tau_r}\right)^2 \tau^1 \\
&= \frac{1}{6} \frac{1}{SNR^2} \frac{1}{2\Delta f} \left(\frac{K_p}{2Q^2}\right)^2 \tau.
\end{aligned}$$

Hence, Allan deviation will be

$$\sigma_y = \frac{K_p}{\sqrt{6}} \frac{1}{2\sqrt{2}Q} \frac{1}{SNR} \frac{1}{\sqrt{\Delta f}} \sqrt{\tau}. \quad (5.9)$$

The four region analytical Allan deviations are summarized in the right panel of Figure 5.6, with $\tau^{-1/2}$ behavior in regions I and III, and $\tau^{+1/2}$ behavior in regions II and IV.

We can go even further by numerically integrating the frequency noise using the Allan variance integral definition. Now, recalling equation 4.14 we can write,

$$\sigma_y^2(\tau) = \frac{4}{\pi\tau^2} \int_0^\infty \frac{\sin(\frac{\omega\tau}{2})^4}{\omega^2} \left(\frac{1}{2\Delta f(SNR)^2} + \frac{\xi}{\omega} \right) \left(\frac{\Omega_0}{2Q} \right)^2 \left| \frac{(j\omega K_p + K_i)\omega_L^4}{((j\omega)^2 + \frac{j\omega\Omega_0}{2Q})(\omega_L + j\omega)^4 + (j\omega K_p + K_i)\omega_L^2} \right|^2 d\omega. \quad (5.10)$$

Equation 5.10 can be used to calculate the Allan deviation σ_y , which is the square root of the Allan variance σ_y^2 , including the low-pass filter term and an extra term ξ to account for flicker. We must numerically integrate over ω and plot the Allan deviation over τ in seconds. Ω_0 is the centre frequency in rad/s, Q is the quality factor, Δf is the demodulator bandwidth, SNR is the signal to noise ratio, K_p and K_i are the P and I gain constants respectively, and ω_L is the inverse of the time constant of the fourth order low-pass filter.

Numerical integration of equation 5.10 provides expected time domain stability, σ_A , assuming TM noise subjected to PLL transfer function. For experiments depicted in Figure 5.3 numerical integration was done by LabView for all measured Q , SNR , and experimental PI parameters for each bandwidth. The resultant σ_A vs. τ plots from integrations is superimposed into corresponding experimental results in Figure 5.7 by solid lines. The derivations and simulations are good enough to mimic the experimental results. For each simulated bandwidth (or gain), white frequency noise density close to the resonance frequency (Region I) stems from resonator characteristics and gives the line superimposed on σ_R , predicted by Robins' phase noise (blue line). For an averaging time, shorter than $\tau_0 = K_i^{-1}\tau_r^{-1} = (K_p/\tau_i)\tau_r^{-1}$, σ_R suffers roll-off (region II). At averaging time shorter than τ_1 white frequency noise density of constant gain region III deciphers into short-term stability with characteristic $\tau^{-1/2}$ slope until an averaging time equivalent to the demodulation bandwidth, $8 \times \text{PLL BW}$.

In the experimental data, $\tau^{-1/2}$ character in region III is not obvious for high- Q cases. In addition, the simulations lie somewhat below the experimental data. This is a sign of additional noise beyond TM noise, which we will discuss more later in the chapter. In addition, the $\tau^{+1/2}$ slope is often not well represented in the experimental data. This can be attributed to additional drift noise at longer sampling times. Long-term drift in a system changes with measurement conditions and is hard to precisely control. It can be either of flicker or RWFm colour. In order to confirm the validity of our simulations, we added drift noise to equation 5.10 in the form of a flicker by adding the constant $\frac{\xi}{\omega}$ term in equation 5.5 and reintegrating with both the

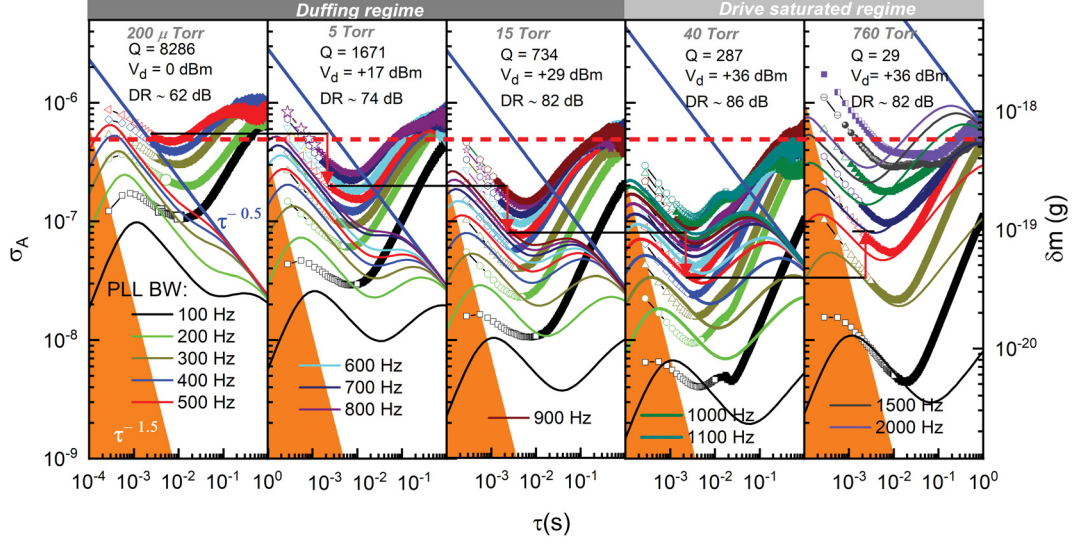


Figure 5.7: **Numerically integrated Allan deviations as a function of damping, bandwidths and DR in phase-locked loop measurements.** The figure compares numerically integrated Allan deviation (equation 5.10) to measured data presented in Figure 5.3 at different pressures for various PLLBW. Symbols are measured data. Open symbols are measured data above bandwidth, and out of the discussion. The color matched lines are corresponding theoretical plots (equation 5.10) from derived models' simulation. The roll-off σ_A in the measured data and theoretical plots has a different origin. In the theoretical plot, the roll-off designates noise shaped by the PLL transfer function at high frequency (see Figure 5.6). Satisfactory agreement between experimental and simulated data justifies the accuracy of analytical models and simulations for different noise shaped by PLL transfer function.

white frequency (thermomechanical) and the flicker frequency terms present. Results are shown in Figure 5.8 for 760 Torr pressure. Increasing the drift in comparison to the TM noise (Figure 5.8 (a)) distorts the inverted W shape of the simulated Allan deviation on the right-hand side of the shape (for longer sample times). It turns the region I dependence from $\tau^{-1/2}$ to flat (τ^0) and the region II dependence from $\tau^{+1/2}$ to τ^{+1} . In Figure 5.8 (b), the flicker term is kept constant as the gain parameters of the PLL loop (taken from the experiments) are changed. Region II slopes change from τ^{+1} to $\tau^{+1/2}$ and the minima move left as the PLL bandwidth increases. These simulated behaviors qualitatively mimic the experimental data in the 760 Torr panel of Figure 5.7 very well. With drift rounding out the analysis, the Allan deviation simulation helps confirm that PLL noise shaping is the likely culprit in pushing our experimental stability data below the Robins' limit.

In the appendix, C.4, we provide additional information on the ability of the PLL with our P and I parameters to track frequency changes. The response time of our

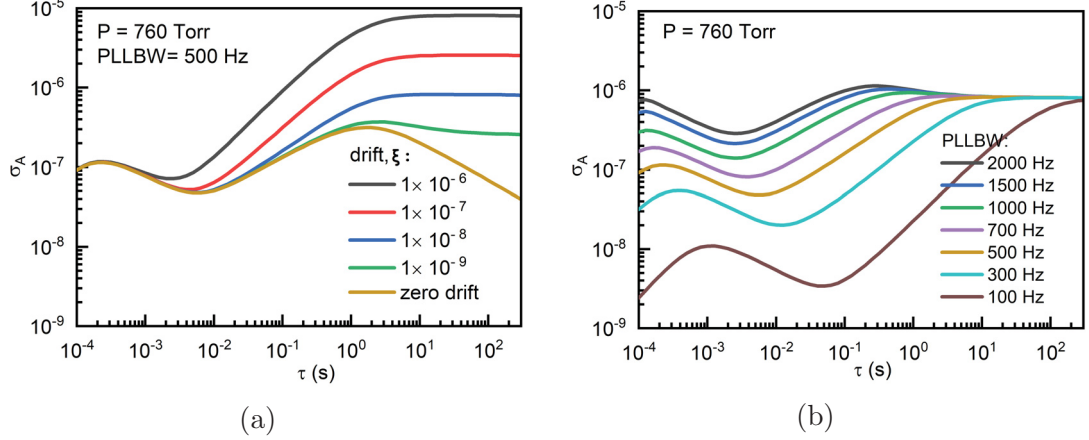


Figure 5.8: **Effect of different magnitude drift in Allan deviation simulations at 760 Torr.** **a)** Numerically integrated Allan deviations for different drift at 760 Torr by 500 Hz Bandwidth PLL parameters. Simulated results display that additional drifts do not change the short-term stability drastically, but brings the noise floor towards shorter averaging time. A significant change is observed after 1 second, where Allan deviation without drift represents resonators characteristics. **b)** An equal drift is added in simulation for different bandwidths. Higher the bandwidth faster the integration (region I in PLL transfer function extend to higher frequency). After 1 second, the effect of drift for 500 – 2000 Hz is almost the same.

oddly shaped PLL transfer functions to a phase step is simulated and compares very well with temperature step measurements. Essentially, as might be expected, the response time is limited to be of the order of τ_0 at the end of region I, with higher damping PLLs having slower response due to an earlier roll off of their region I.

It is clear that the experimental data of frequency stability that we have in closed loop is limited in its ability to interrogate the actual noise floor values due to the loop noise shaping issue. For this reason, we turn to open loop measurements to validate the conserved $Q \times SNR$ model.

5.3.2 Open loop measurements

In open loop, the frequency driving the resonator is set unchanging, and no feedback is applied to close the loop. As discussed in chapter 4, the deviation of the output analytic frequency in time is not directly reporting the NEMS stability, however, the analytic phase with time can be turned into meaningful frequency fluctuations of the NEMS using the phase slope relation $\Delta\omega = (\Omega_0/2Q)\Delta\phi = (1/\tau_T)\Delta\phi$. The collected time trace by lock-in demodulator is a simple quadrature measurement which provides a time stamp for in-phase (X_1) and the quadrature component (X_2) of amplitude to get the phase ($\tan^{-1} \frac{X_2}{X_1}$) at the set frequency. Such open-loop experiments were

performed at different driven amplitudes (SNR) within the onset of nonlinearity at several lock-in bandwidths, as well as for four measurement pressures.

5.3.2.1 Theory of open loop frequency fluctuation measurements

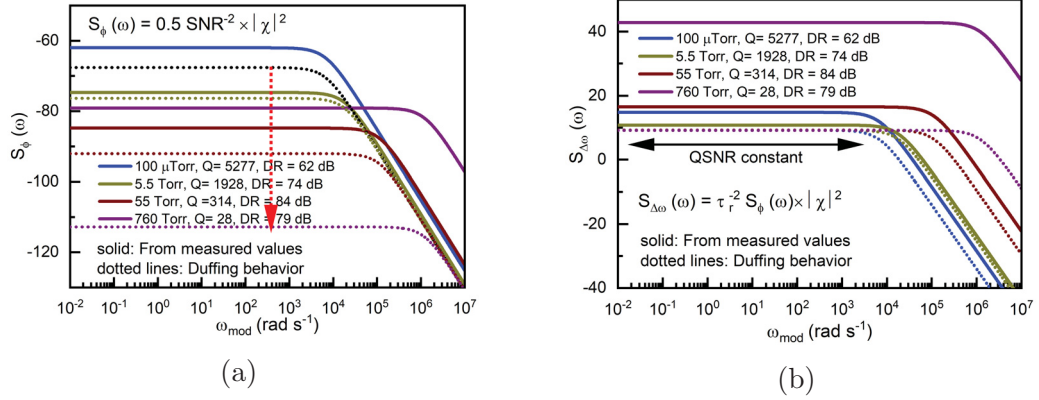


Figure 5.9: **Thermomechanical noise limited phase and frequency noise density of nanomechanical resonator in open loop experiments as a function of damping.** **a)** Phase noise behavior of mechanical resonator with damping: Dotted lines represent proportionally reduced phase noise with increasing damping when full DR is accessible. Solid lines are from measured SNR . From vacuum to 55 Torr improved SNR reduces in-band phase noise by Q^{-2} and agree with Duffing behavior of Robins' phase noise prediction. Instead of decreasing with Q , $S_\phi(\omega)$ at 760 Torr increases because driven amplitude measured is below the respective critical amplitude. All Q s are obtained from the Lorentz fit of TM noise spectra at each pressure. **b)** Illustration of frequency noise density shaped by the phase slope at resonance due to thermal displacement noise in phase: Effect of Q neutralization on $S_\phi(\omega)$ by the respective τ_r^2 provides the same amount of frequency noise within measurement bandwidth for Duffing behavior. This is the conserved $Q \times SNR$ hypothesis theorized in the thesis. Frequency noise density according to measured resonance parameters illustrated here expect the same Allan deviation curves for all pressures except 760 Torr. When full DR is not accessible, measured frequency noise is expectantly proportional to measured $QSNR$ rather than a single line as in Duffing behavior.

The theoretical transfer function of Robins' phase noise density can be written as

$$S_\phi^{\text{th}}(\omega) = |\chi(\omega)|^2 |\chi_L(\omega)|^2 \frac{1}{2} \frac{1}{SNR^2 \Delta f}, \quad (5.11)$$

and corresponding open loop NEMS frequency noise density

$$S_{\Delta\omega}^{\text{th}}(\omega) = \frac{1}{\tau_r^2} |\chi(\omega)|^2 |\chi_L(\omega)|^2 \frac{1}{2} \frac{1}{SNR^2 \Delta f}, \quad (5.12)$$

where, resonator transfer function is given by its ring-down time, τ_r

$$|\chi(j\omega)|^2 = \frac{1}{1 + (\omega\tau_r)^2}. \quad (5.13)$$

This resonator transfer function has its origin from thermal displacement noise density, $S_x^{\text{th}}(\omega)$ and its relation with phase noise density is explicitly described in [16]. The demodulator low-pass filter is written as

$$|\chi_L(j\omega)|^2 = \frac{1}{1 + (\omega\tau)^2}.$$

The relation 5.11 or 5.12 is generally satisfied for, $|\chi(0)| = |\chi_L(0)| = 1$ for base-band equivalent resonator transfer function $|\chi(j\omega)|$ [142]. By considering $|\chi_L(0)| = 1$ one can simply predict thermal limited noise phenomenon in open loop experiments from measured Q and SNR at different damping conditions.

For four different pressures, the theoretical behavior (equation 5.11 and 5.12) of phase and frequency noise by open loop experiments are portrayed in Figure 5.9. It demonstrates how thermal displacement phase noise shapes the frequency noise density of a mechanical resonator. The phase noise in Figure 5.9 is proportional to SNR^{-2} and falls with decreasing Q . When translated into frequency noise, the factor of $1/\tau_r^2$ neutralizes the Q dependence and $S_{\Delta\omega}$ is proportional to $(Q \times SNR)^{-2}$. In practice, other noise sources in the system can further limit the ultimate frequency stability imposed by intrinsic TM noise. Any deviation from the predictions in the measured noise density above will provide information about the dominant noise process in the system.

5.3.2.2 Frequency fluctuation measurements (Allan deviation) by open loop experiments

A representative open loop Allan deviation plot for the measurement conditions described in Figure 5.9 is presented in Figure 5.10. There is a reasonable signature of extra noise in the system above the thermal noise-induced phase noise.

Short-term stability at 100 μTorr , 5 and 55 Torr are not following strictly the characteristic $\tau^{-1/2}$ slope for additive thermal noise. For 100 μTorr in particular, the noise floor is not improving (reducing) with increasing SNR . This trend in an Allan deviation plot is a signature of flicker frequency noise (f^{-1}) of the resonator establishing the noise floor. The noise floor extends to longer τ at enhanced pressures. More apparent $\tau^{-1/2}$ slope with increasing pressures, as well as a better improvement in noise floor with increasing SNR at higher pressure tells that excess f^{-1} noise gradually diminishes with damping. Since $Q \times SNR$ product is similar from high vacuum to 55 Torr noise floor are expected to be similar. It is seen that measured noise floor in Figure 5.10 are very close to each other from 100 μTorr to 55 Torr, even improving with damping. Such an improvement with damping along with stronger $\tau^{-1/2}$ slope at

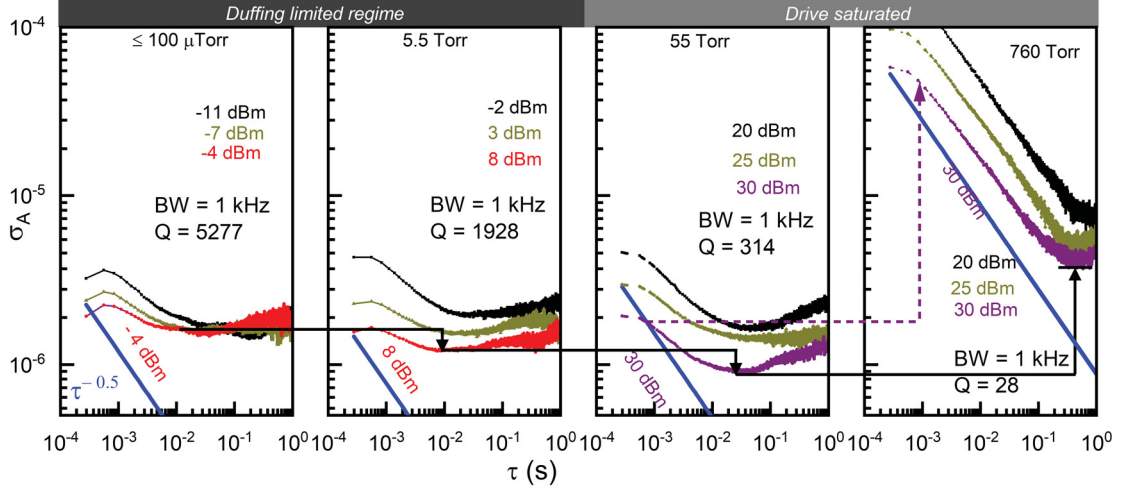


Figure 5.10: Measured Allan deviations at different pressure regimes and various driving powers with 1 KHz demodulation bandwidth. With a sampling frequency of 3600 Hz, data is collected for 20 s. 20 s is a relatively long time in comparison with ring-downtime ($\sim \frac{Q}{\Omega_0}$) of the resonators at each pressure. Blue lines are theoretical predictions of σ_R (equation 5.1) by measured Q and SNR at each pressure at the maximum drive power of each panel. Falling off in all measured AD plot below 1 ms appears because of the roll-off effect of low-pass filtering and data below 1 ms are not meaningful. Red plots are corresponding Allan deviation measured at the respective critical drive power. At 100 μ Torr short-term stability does not improve proportionately with driven amplitudes (SNR). With increasing drive, there is a gradual collapsing of white noise nature ($\tau^{-1/2}$ slope), and the noise floor (τ^0) at all three driven cases are almost similar which is characteristic of frequency fluctuation noise for long measurement time. With increasing pressures (i.e., a decrease in Q) it is evident that effect of frequency fluctuation noise (collapse of $\tau^{-1/2}$ behavior for shorter averaging time with increasing drive powers) is progressively weakening; the signature of pure additive white noise with additive $1/f$ noise becomes gradually stronger. The 760 Torr data show evidence of simple additive noise operation, free from frequency fluctuation noise signature, up to at least 0.2 s. From [16]. Reprinted with permission from AAAS.

higher pressure asserts that excess noise does not contaminate device performance as in lower pressures (higher Q). 760 Torr data shows clear evidence of thermal noise domination ($\tau^{-1/2}$ signature) with little contamination from f^{-1} noise. We attribute this to better temperature stability by air conduction (see next chapter) that weakens flicker in resonance. $S_{\Delta\omega}$ at 760 Torr is ≈ 26 dB higher than that of 55 Torr (Figure 5.9) to provide a ≈ 13 dB poorer (higher) stability than that of 55 Torr. 760 Torr Allan deviation measured at 30 dBm agrees well with frequency noise density results by showing ≈ 13 dB higher stability than 55 Torr for 1ms averaging time. Hence, measured time domain stability by open loop experiments closely follows $Q \times SNR$

trend at different damping conditions. Noise floor at 55 Torr is certainly better than that of high vacuum. Even, for truncated DR , 760 Torr noise floor is only $\sim 2.4\times$ higher than that of 100 μ Torr, whereas, Q is worse by $\sim 190\times$.

This section describes the time-domain stability of NEMS by comparing predicted frequency noise density in open-loop theory. Measured data at different damping conditions identify two noise processes intrinsic to resonator viz. white frequency noise from thermal displacement noise and flicker in resonance. An alternative picture of these noise in experiments can also be viewed qualitatively from measured frequency noise density.

5.3.2.3 Directly measured frequency noise density

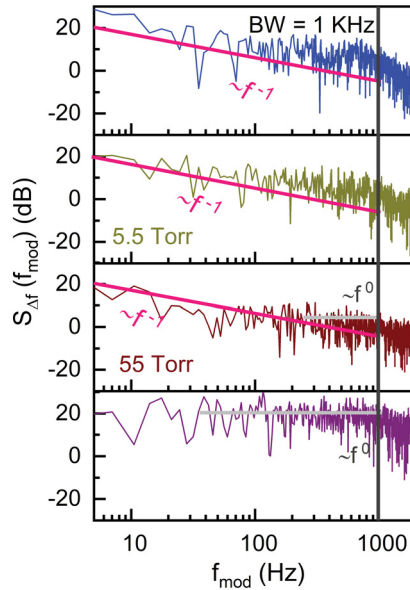


Figure 5.11: **Directly measured open loop frequency noise density as a function of damping dependent DR .** In open loop, after 1000 Hz, observed roll-off represents the low-pass filter characteristics. An approximate f^{-1} slope (pink line) at 100 μ Torr and 5 Torr shows flicker is the dominating noise. Like Allan deviations flicker noise effect gradually weakens with damping and at 760 Torr noise is almost white (by thermal displacement noise) for the entire frequency span and indicated by a light gray horizontal line (f^0).

Using the same open loop data as in Figure 5.10, we present directly measured frequency noise as a function of pressure in Figure 5.11. These data do seem to qualitatively agree with theoretical frequency noise spectral density discussed in Figure 5.9 as well as measured Allan deviation results Figure 5.10. Data was taken with sampling frequency of 3600 Hz and measurement BW of 1 kHz. A fast Fourier

transform by Welch method was run to get measured spectral densities of frequency noise, $S_{\Delta f}(f_{\text{mod}})$ for 1024 data points. 1024 data point corresponds to 300 ms time trace of frequency fluctuations for each case.

The slopes of the noise close-in gradually change from f^{-1} to f^0 character with increasing pressure. This is consistent with frequency flicker gradually reducing below thermomechanical white noise level. In the next section we will give quadrature representations of open loop measurements to study the evolution of f^{-1} noise seen in this series of experiments.

5.3.2.4 Notes on frequency fluctuation noise

The frequency stability of the nanomechanical resonator in this work reaches closely to its predicted thermodynamic limit 5.10. It appears to maintain the thermodynamic limit at short duration τ at higher pressure (while for longer τ , other noise sources begin to dominate). The presented results are in contrast to the 2016 nature nanotechnology study reported by M. Sansa *et al.* [22]. The group reviewed 25 different published works on measured frequency stability of nanomechanical resonators with different designs and sizes and found that none of those devices can attain the experimental stability down to the thermal noise limit by DR formula (equation 5.1). Their study revealed that along with additive thermal noise another source of extra phase noise exists in NEMS class of devices which is parametric and is known as “frequency fluctuation noise”: intrinsic fluctuations in resonance frequency over time that are independent of thermal bath and drive effects. They find this noise to have a flicker behavior following a f^{-1} power law and giving flat temporal Allan deviation response. This extra noise source is independent of the signal to noise ratio. As a consequence, the stability of the device cannot be improved with increasing SNR , and applications of DR formula becomes invalid (see Figure 3 in [22]). The most obvious sign of frequency fluctuation noise is thus a plateau in the Allan deviation where increasing drive power does not further reduce the deviation. In Figure 5.10, it is evident that parametric frequency fluctuation noise for sampling times longer than 20 ms dominates on frequency noise measurements in high Q regime for the silicon NOMS device in this work. The 5.5 and 55 Torr data do not show domination by frequency fluctuations, though neither is their behavior fully consistent with additive noise alone. For 760 Torr, there is only a little hint of frequency fluctuation noise (near 1 s).

To confirm these findings, we plot both standard deviations and histograms of the phase quadrature as a function of drive power in Figure 5.12. These data are for the full 20-second datasets, so they incorporate behavior from all averaging times τ . Vacuum data show growth in the standard deviation of the phase quadrature (X_2)

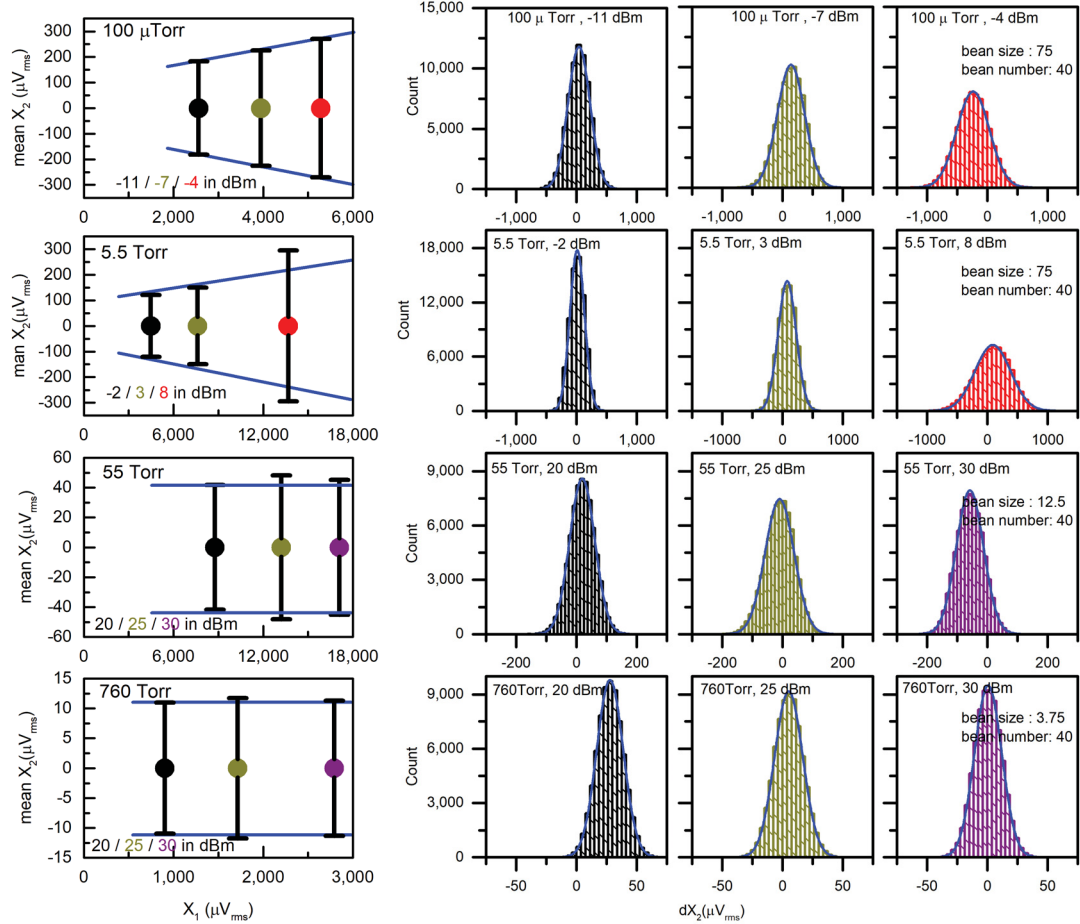


Figure 5.12: **Left: Quadrature representation of the same data used in Figure 5.10 to calculate Allan deviations.** The in-phase-quadrature (X_1) at each data set is rotated in order to make the mean phase zero so that data can be centered at zero and at the same time, the amplitude of oscillations (in μ V) can be plotted along the horizontal axis. Consequently, phase information (X_2 in μ V)) can be set along the vertical axis. Mean phase for each dataset is forced to zero to show the variation of phase quadrature noise by the standard deviation (black bars) of X_2 data with respect to driven amplitude, X_1). Blue lines are guides to the eye. For lower pressure and lower damping (higher Q), phase quadrature noise increases with driven amplitude - a signature of frequency fluctuation noise; this is in contrast to 760 Torr data at higher damping where phase quadrature noise is constant with driven amplitude. **Right: Histograms of the phase quadrature values.** The blue line at each histogram is a normal fit for each set. Widening and shortening of the histograms at higher drives confirm the presence of excess frequency fluctuation noise for higher Q . Width and height are constant for 760 Torr showing that frequency fluctuation is negligible at atmospheric pressure. From [16]. Reprinted with permission from AAAS.

fluctuations with drive power, another signature of frequency fluctuation being the primary noise source. In the atmospheric pressure case, phase quadrature deviations

remain the same with respect to driven amplitudes. Intermediate pressures show some effect of a noise source that is not diminished with drive power (such as frequency fluctuations). In all cases, the phase angle lines do not converge at zero drive, so frequency fluctuation noise is never the sole noise source. The histograms support similar conclusions. With increasing drive power, the histograms shorten and widen for the two lower pressures, and remain constant for atmospheric pressure. 55 Torr histograms reflect almost similar behavior as by 760 Torr data, but Allan deviation plots at different driving power do not exactly proportionally decrease with driving amplitude, which is an indication of excess noise over thermal noise at this pressure.

From the Allan deviation data, we can infer that the frequency fluctuation noise is only kicking in for longer averaging times. This would be consistent with the noise source being temperature fluctuations of the DCB, especially considering our very large temperature coefficients with frequency. As such, this effect might be partially mitigated at atmospheric pressure by the much larger heat transfer coefficient with the surrounding air (see next chapter). From next chapter experiments, open-loop Allan deviation results (see Figure C.2 in Appendix) from low to atmospheric pressures show similar improvement of $\tau^{-1/2}$ with increasing air pressure as observed in Figure 5.10, and confirms our findings.

5.3.3 Can damping really improve frequency stability of a mechanical resonator?

For the linear operation of a mechanical resonator, noise sets the ultimate limit by Robins' model. This model tells us that $\sigma_R \propto (Q \times SNR)^{-1}$. This thesis hypothesized to attain the intrinsic DR to have a constant $Q \times SNR$, which would provide the same level of stability irrespective of damping conditions (Q). So, damping by itself, can not improve mechanical sensor performance. However, experimental evidence of this chapter recommend that damping indirectly can suppress excess noise of a resonator. Experimental results identify such excess noise as a flicker in resonance frequency (f^{-1} noise), which is intrinsic to nanomechanical resonators. We experimentally demonstrate that such excess noise gradually diminishes with damping. In the next chapter we will discuss that the presence of air molecules at larger damping (higher pressure) more quickly thermalize the NEMS with surrounding bath than for lower damping experiments. As a consequence, temperature fluctuations effect on NEMS is weaker at higher pressure which leads to suppression of f^{-1} noise [22]. Thus, in Figure 5.10 the noise floor of the device improves with damping as excess noise impact gradually weakens. So, yes, damping can facilitate improved mechanical sensor

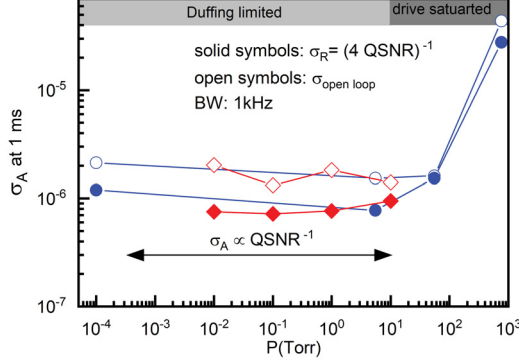


Figure 5.13: **Open loop Allan deviation results for 1 ms averaging time.** σ_A for 1 ms averaging time are taken from open loop Allan deviations shown in Figure 5.10 from series 2 and from series 3 (not shown in detail) experiments. Open loop σ_A vs. P results presented here illustrates that measured sensor performance within Duffing limited regime is close to thermal noise limited sensor performance with decreasing Q . Contribution from excess f^{-1} noise worsens device stability by 1 dB only. Gradually weaker f^{-1} noise with damping benefits sensor performance to attain thermal limited stability at 10 Torr. Within Drive saturated regime, 55 Torr data is identical to that of theory by measured $QSNR$. 760 Torr data is also close to the theoretical value. Measured σ_A at 760 Torr is a little higher than the theory. This discrepancy is not due to f^{-1} noise, which is almost absent at 760 Torr.

performance when devices possess enough linear SNR .

In all series of experiments, we noticed that open-loop Allan deviation for an averaging time, $\tau \sim (1/BW)$ are close to Robins' prediction for a measured SNR . σ_A for 1 ms averaging time from 1 kHz open-loop experiments are plotted in Figure 5.13 against pressure to show that Allan deviation of a mechanical sensor does closely follow measured $Q \times SNR$ at different damping (Q), and matches it at high pressure.

Finally, it can be concluded that damping enables the attainment of frequency stability of a mechanical resonator down to TM noise limit by reducing excess noise in the system. So, better mechanical sensor performance at larger damping is actually true when the damping facilitate flicker noise suppression.

5.4 Conclusion

This chapter demystifies frequency stability measurements of a nanomechanical resonator down to its ultimate limit imposed by inevitable thermomechanical noise. Two methods viz. phase-locked loop and open loop resonant tracking are explored. Both methods rely on phase frequency relation (slope) at resonance. Detailed analysis, as well as experimental results on phase and frequency noise, show how phase

noise improves with damping and transforms into Robins' model of frequency noise. Frequency resolution could be independent of Q in the Robins' picture, which has been hinted at [22, 127], but not tested, and not widely appreciated in the NEMS community. Verification of constant $Q \times SNR$ (in chapter 3) and its implementation in Allan deviation measurements is an important development with implications in NEMS, AFM, and other fields. A systematic inspection of PLL transfer function on frequency fluctuation measurements makes it possible to derive new models for PLL based measurements. These models are found adequate to interpret measured Allan deviation, which can be a reference for NEMS, AFM communities, or others.

Experiments in this chapter reveal another side-benefit of low Q . Intrinsic resonator frequency fluctuation noise [22, 24, 25, 127, 149, 150] is found to be suppressed with damping. Sansa *et al.* [22] recently noted this noise as ubiquitous in preventing NEMS from reaching thermal limits though Gavartin *et al.* [127] were able to mitigate it with sophisticated force feedback. At atmosphere, better thermal equilibrium by air conduction may reduce temperature fluctuation for suppressing flicker in resonance.

However, choosing an appropriate BW and measurement mode according to the experimental requirements is user-defined. For gas sensing, we need better frequency resolutions suitable for gas landing to resolve the minute amount of gaseous molecules detected by the DCB NEMS. Since a PLL indirectly tracks the resonance frequency of the DUT, it must be tested by a known amount of measurand of interest. To deliver a known amount of gas on to nanoscale DCB surface is an extraordinary experimental challenge which requires special experimental arrangements. However, inducing temperature change is a comprehensive means because of uses of temperature controller in our experimental chapter. By inducing a known amount of temperature change, we have checked the improved stability at larger damping (*cf.* next chapter) as well as the efficiency of PLL tracking to measure the corresponding shift. In the next chapter, we will discuss the detail of nanoptomechanical thermometry developed in the current thesis.

Chapter 6

Proof of concept: Measured temperature resolution is better at larger damping

6.1 Introduction

Accurate temperature sensing and measurements is a fundamental objective of many scientific experiments and technological applications. For instance, temperature dependent resonance frequency of NEMS imposes isothermal conditions for precise sensing of other measurands of interest like mass, force, *etc.* by limiting the temperature-induced frequency shift. More importantly, temperature fluctuations in the thermal bath is known to contaminate TM noise limited operations of NEMS by flicker in resonance as in [22] and discussed in the previous chapter. Due to the temperature dependence of resonance properties, M/NEMS are routinely studied as thermometers. For instance, bi-material cantilevers are widely used as micro-calorimeter through measuring the deflection by heat (e.g., infrared radiation) induced stress due to thermal mismatch of the device surface [151, 152, 153]. Resonant frequency shift temperature sensors are also available in the realm of M/NEMS [154, 155, 156]. Nanomechanical photothermal sensing has potential in single-molecule imaging[157]. Often a reference temperature sensor is used in parallel to nanomechanical thermometry for calibrating NEMS thermometer [158, 159, 160] that introduces additional experimental challenges. Recently, the effect of temperature fluctuation in the noise process of NEMS is revisited for fundamental study [161]. On the other side, using optical ring resonators in photonic thermometry is an increasingly growing technique [162, 163]. Optomechanical thermometry [15, 164] has just started its journey as a hybrid temperature sensor relies on the frequency-temperature behavior of mechanical elements. Though many reports separately describe either ring or nanomechanical thermometry, a simultaneous

application of NOMS thermometry is still unexplored.

The NOMS in this thesis includes a high-quality optical cavity: a microring optical resonator coupled to a nanoscale mechanical resonator. The mechanical element is a double clamped beam. Here, the motion of the mechanical resonator is imparted onto the optical field circulating the cavity, and this enhances the displacement sensitivity of nanomechanical motion. Both the optical ring and DCB NEMS in the integrated NOMS structure are susceptible to environmental fluctuations, and so, both can be used as temperature sensors. A small temperature change on the device surface simultaneously changes the resonance wavelength, λ_0 of the optical ring and the resonance frequency, f_0 of the NEMS. λ_0 changes with temperature mainly due to the thermo-optic effect of silicon [165]. Quantities such as the elastic modulus and the thermal expansion coefficient of silicon determine the resonance frequency of NEMS, which depends on temperature strongly [155, 156, 166]. By using a PID controlled heater, we can modify the chip surface temperature and test both the NEMS and ring as thermometers. An effective calibration of these temperature sensors against each other can be used to develop orthogonal on-chip thermometry, called nano-optomechanical systems (NOMS) thermometry.

By definition, thermometry is a technique that measures temperature to study different aspects of heat-related phenomenon. Conventional thermometry like resistance thermometry has limitations on making measurements at the sub-micron scale, for example, temperature mapping of microcircuits [167, 168], microfluids [169, 170], and intracellular temperature fluctuations [171, 172]. From a biomedical perspective, precise information of relative temperature change of a living cell is necessary for cancer detection as cancer cells have higher temperature relative to healthy tissues due to the increased metabolic activity [172, 173]. The temperature of living cells changes during every cellular activity, such as enzyme reaction, cell divisions, and modifications in metabolite activity, *etc.* [174]. Thus precise measurements of the relative steady state, as well as transient temperature gradients in biological systems and or chemical reactions [175, 176] potentially demand nanoscale thermometry. NOMS thermometry can be a potential non contact thermometer in various nanotechnology where two built-in thermometers, NEMS and optical ring, can be calibrated to each other and thus be redundant reference thermometers in applications. Interestingly, many thermodynamic properties distinctly change at the nanoscale, while other new ones arise [177, 178, 179]. Thus, nanoscale thermometry requires a new paradigm in their use.

From a statistical point of view, temperature is related to the average kinetic energy of carriers (e.g., molecules, electrons, photons and, phonons) in the substance.

Statistically, if the ensembles of particles are not in equilibrium, then distributions above need to restore the equilibrium by considering different collision or scattering processes of particles among themselves or to surrounding particles. Consequently, the mean free path (l_{mfp}) of the respective carriers and its relaxation time (τ_{relax}) turn into the fundamental parameters which characterize the heat transfer mechanism [177, 178, 179, 180]. The downscaling trend of NEMS close to the mean free path of air opens new thermal physics of nanoscale heat transfer for their use in atmosphere [156, 181]. Recently, Chun Cheng *et al.* in [181] established that the heat transfer coefficient is too high at nanoscale solid-gas interface to detect a small temperature change. Nanoscale heat transfer is till now an extraordinary experimental challenge [179] which need to be properly addressed in the current thesis before applying NOMS for ambient condition gas sensing.

The decisive goal of this project is to integrate the NOMS resonator with a commercial gas-chromatography for ambient condition gas sensing by the nanomechanical DCB in NOMS. Calibrating NEMS performance as a mass/gas sensor is experimentally challenging by loading a known amount of tiny mass around 10^{-18} g onto the nanoscale DCB resonator. Alternatively, it is easy to load a known amount of temperature change in NOMS to compare the frequency shift tracked by the PLL to the predicted value. Thus, the reliability of PLL resonance tracking by temperature sensing can be valid for gas sensing also.

In the previous chapter, we have revealed that nanomechanical frequency stability can be improved down to respective thermal limit at larger damping. Substantial damping reduces the effect of excess noise like f^{-1} noise of resonator for improving mechanical sensor performance. We assumed that the reason behind weakening frequency fluctuations with damping could be attributed to reduced temperature fluctuations in ambient through conductive heat transport via air molecules. In this chapter, we provide evidence for this assertion. We show that conductive heat transfer via air is the primary channel for nanoscale heat transfer at atmospheric pressure solid-gas interface. This channel at the nanoscale can provide improved stability at larger damping. Appendix C.4 demonstrates that PLL at different damping condition can respond according to theoretically predicted PLL time constant. We concluded that PLL measurement at a longer time scale should not affect resultant frequency shift made by any event.

Hence, the goal of this chapter is to establish the principle of NOMS thermometry followed by a verification of phase lock loop performance in tracking the resonance frequency shift by a known amount of temperature. To do this, we have run a temperature sensing experiments from vacuum to atmospheric pressure. At the same

time, these experiments allow us to study the effect of nanoscale heat transfer with increasing air pressure. Sections 6.2.1 -6.2.2.1, and 6.4.1 are discussed in the publication [16].

6.2 Fundamentals of NOMS thermometry

6.2.1 Theory of microring thermometry

Details of device configuration and principle have been described in detail [50]. A change in temperature ΔT will shift ring properties via thermal expansion of silicon and oxide and via thermo-optic coefficient (TOC) of Si, $\alpha_{\text{nSi}} = 2 \times 10^{-4} \text{ K}^{-1}$ [163]. The latter is the dominant effect. This will give a temperature responsivity $S_{\lambda,T} \equiv \frac{d\lambda_0}{dT}$ that can be theoretically approximated by

$$S_{\lambda,T} \cong \frac{\lambda_0 \alpha_{\text{nSi}}}{n_{\text{Si}}}, \quad (6.1)$$

which gives approximately 80 pm/K for 1550 nm light [165].

In our system, we use the probe sitting on the side of the optical resonance to transduce $\Delta\lambda$ due to temperature change into ΔT_r , the change in transmission, through the slope responsivity, $\mathfrak{R}_\lambda \equiv dT_r/d\lambda$. This gives, finally

$$\Delta T_{\text{ring}} = \frac{\Delta\lambda_0}{S_{\lambda,T}} = \frac{\Delta T_r}{\mathfrak{R}_\lambda \times S_{\lambda,T}}. \quad (6.2)$$

Both $S_{\lambda,T}$ and \mathfrak{R}_λ can be measured experimentally. $S_{\lambda,T}$ is calibrated by setting known temperature changes into the PID temperature controller and extracting $\Delta\lambda_0$ values from static temperature wavelength sweeps. \mathfrak{R}_λ is observed directly from wavelength sweep slope at the probe point. ¹

¹The ring thermometry described above is valid for linear optical resonance. With large input laser power, thermometry could become more complicated because of additional redshift (increase in resonance wavelength) by self-heating. Input light, circulating in the optical ring causes redshift of the cavity by self-heating effect due to free carrier absorption [182] which can also cause optical non-linearity and non-symmetric optical resonance line-shapes. Authors of [182] extensively studied self-heating effect on a silicon microring by changing input optical power to model the dynamics of self-heating. In our work (*cf.* left plot of Figure 6.2), self-heating effects and optical nonlinearity are small and optical resonances are essentially symmetric in all cases. For example, visually inspecting Figure 2.3, we can infer that asymmetry (the shift of the dip away from being center of the shape) must be at least smaller than about 2% of the linewidth, i.e., less than 4 pm. This implies that (at ring temperature sensitivity of 80 pm/K) the heating difference between on resonance and off is no more than 1/20th of a kelvin. We, therefore, take intracavity heating from the photons to be negligible for further discussion.

6.2.2 Theory of nanomechanical thermometry

The fundamental flexural mode eigenfrequency of a straight doubly clamped beam (without residual tension) made of homogeneous material is [20]

$$f_0 = 1.027 \frac{t}{l^2} \sqrt{\frac{E}{\rho}}, \quad (6.3)$$

where, t and l are the thickness and the length of the beam, E and ρ are the elastic moduli and density of the material. For a beam with residual tension such as compressive stress σ_i , the frequency modifies to [154]

$$f_{\sigma_i} = f_0 \sqrt{1 - \frac{0.295\sigma_i l^2}{Et^2}}. \quad (6.4)$$

All quantities on the R.H.S. of equations 6.3 and 6.4 change with temperature. As a consequence, the resonance frequency of nanomechanical resonators strongly depends on temperature. This f - T relationship is referred to as the temperature coefficient of resonant frequency, $TCRF$, [156] which is the ratio of temperature sensitivity ($S_{f,T} = df/dT$) to its resonance frequency, f_0 . i.e.

$$TCRF = \frac{1}{f_0} \frac{df}{dT} = \frac{1}{f_0} S_{f,T}. \quad (6.5)$$

$S_{f,T}$ can be measured experimentally by identifying f_0 from thermomechanical noise spectra taken at different set temperatures. Thus measured temperature from temperature induced frequency shift of PLL data can be found as

$$\Delta T_{\text{NEMS}} = \frac{\Delta f}{S_{f,T}}. \quad (6.6)$$

6.2.2.1 Estimating $TCRF$ from Si properties

Substituting differentiation of equation 6.3 with respect to temperature into equation 6.5 we have,

$$TCRF = \frac{1}{f_0} \frac{df}{dT} = \frac{1}{2E} \frac{dE}{dT} - \frac{1}{2\rho} \frac{d\rho}{dT} - \alpha, \quad (6.7)$$

where, $(1/E)(dE/dT) = \beta$ is the temperature coefficient of Young modulus, $(1/\rho)(d\rho/dT) = \gamma$ is the thermal coefficient of density, and $(1/l)(dl/dT) = \alpha$ is the thermal expansion coefficient. According to [183], for pure silicon β is not a well defined parameter and found in the range of $-113 \text{ ppm K}^{-1} \geq \beta \geq -55 \text{ ppm K}^{-1}$, $\gamma = -13 \text{ ppm K}^{-1}$ and $\alpha = 3 \text{ ppm K}^{-1}$. Using these values in equation 6.7 we have intrinsic $TCRF$ of pure silicon made resonator between -56 ppm K^{-1} to -27 ppm K^{-1} that includes measured values. Despite temperature dependence of elastic modulus, density, and geometric dimension the $f - T$ relation of silicon resonator can be affected by stress also [154].

6.2.3 Principle NOMS thermometry

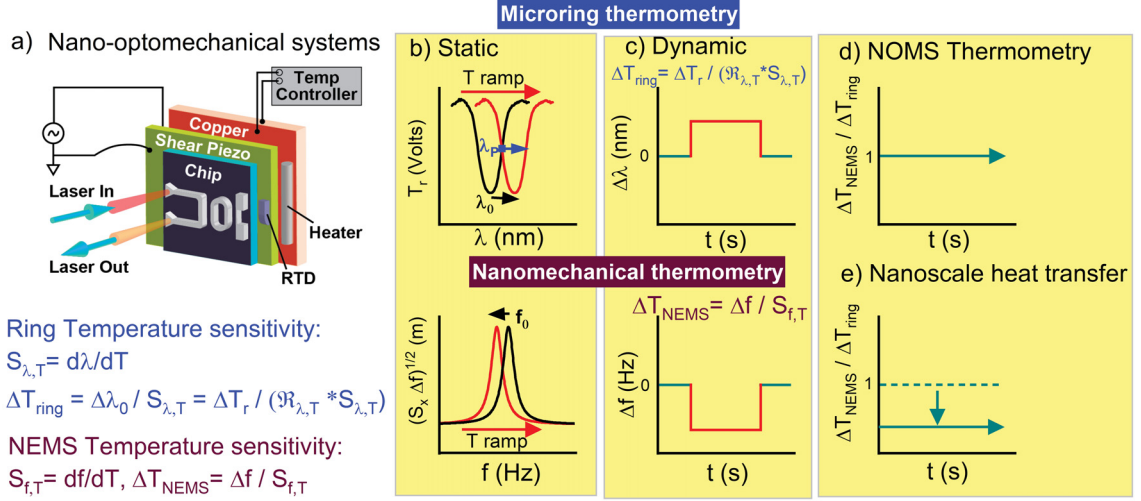


Figure 6.1: **Schematic illustration of NOMS thermometry and nanoscale heat transfer.** **a)** Cartoon of on-chip NOMS glued on the top of a piezo shaker that is placed on Cu plate. The resistive heater on a Cu plate induces heat on the system through the PID controller. RTD sensor placed on the piezo is a few mm away from the silicon chip. In a separate experiment, we found that temperature tracked by the RTD and calibrated microring are the same. Thus simultaneously tracked relative temperature change by the ring and PLL NEMS can introduce the concept of nano-optomechanical thermometry. **b)** Static thermometry for temperature calibration: According to the theory, optical resonance increases with increasing temperature in contrast to the thermo-mechanical resonance. By measuring optical and mechanical resonance at different temperature we can have $S_{\lambda,T}$ and $S_{f,T}$ from measured wavelength/frequency *vs.* temperature plot. **c)** Dynamic thermometry: Top sketch shows a redshift of resonance wavelength with increasing temperature. The bottom shows resonance frequency reduces with increasing temperature for nanomechanical resonator. Measured $S_{\lambda,T}$ converts transient wavelength into transient temperature in microring thermometry. The bottom panel shows simultaneously recorded temperature by NEMS frequency tracking by PLL. **d)** In the absence of heat loss by NEMS both ring and NEMS track the same temperature. **e)** If there is intrinsic nanoscale heat transfer, then NEMS will measure less surface temperature change than macroscopic ring governed by related heat transfer mechanism.

From the above discussion, we have seen that both the optical ring and nanomechanical DCB resonator are sensitive to temperature. Any relative change in device surface temperature must change the optical resonance (proportional to probe power) and resonance frequency simultaneously. If the wavelength sensitivity of the ring ($S_{\lambda,T}$) and the frequency sensitivity of the NEMS resonator ($S_{f,T}$) is precisely known then relative temperature measured by the ring and NEMS in a NOMS system must be

same. Such simultaneous measurement of same temperature change by two inherently built-in temperature sensor in NOMS system can be referred to as nano-optomechanical thermometry. The governing equation of NOMS thermometry can be described as follows

$$\Delta T_{\text{ring}} = \Delta T_{\text{NEMS}}. \quad (6.8)$$

The condition above is valid only for an equilibrium temperature of a NOMS system when both the ring and NEMS are measuring the same temperature. The on-chip microring is in thermal contact with the bulk surface; thus, the heat transport mechanism of the ring and surface should be identical. On the other hand, the released mechanical DCB resonator is exposed to air (or vacuum) on most of its surface, so the heat transfer mechanism for the NEMS thermometer may differ distinctly from the microring [179]. According to the study [181], air molecules around the NEMS may cause a substantial heat transfer coefficient through heat conduction by air to make NEMS cooler than the ring during transient temperature increase. Hence nano-optomechanical thermometry across pressures is incomplete without considering nanoscale heat transfer. The schematic in Figure 6.1 explains the different features of NOMS thermometry in this work.

6.3 Experiments

In order to measure temperature by a NOMS system, at first, we need to know the $S_{\lambda,T}$ and $S_{f,T}$ to convert relative wavelength and frequency shift into a corresponding temperature change. Accurate determination of $S_{\lambda,T}$ and $S_{f,T}$ depends on the precise measurements of optical and mechanical resonance spectra at a stable equilibrium temperature of the entire system. It is possible only when the system is at a constant temperature for each measurement. We have ensured such a stable temperature by (1 K or 2 K steps from room temperature) in all measurement by a PID temperature controller. To make sure that PID controlled temperature is stable, we waited at least for 15 minutes at each temperature before starting any measurement. Such a long waiting time allows the chip surface and surrounding bath to establish a constant equilibrium temperature. This waiting time is not only for static thermometry, it is also important for dynamic thermometry to measure a temperature change in the system (chip plus the surroundings) at a constant temperature. See section 4.2 in Chapter 2 for details of the experimental setup. Such measurements for determining $S_{\lambda,T}$ and $S_{f,T}$ can be referred as static measurements. The PID controller made the transient temperature change for changing temperature by 0.1 to 0.4 K, the corresponding relative frequency change is recorded by HF2 PLL, and a built-in LabView program

tracks the change in optical transmission at probe wavelength: this is referred as dynamic temperature measurements.

6.4 Results and discussion

6.4.1 Static measurements for temperature calibration

An example of the calibration of ring ($S_{\lambda,T}$) and NEMS ($S_{f,T}$) temperature responsivity is given in Figure 6.2 for 3 Torr pressure. Increasing temperature causes a red shift in optical ring wavelength and a decrease in the resonance frequency. Measurements of temperature sensitivities (by both ring and NEMS) at different pressures are shown in Table 6.1. The slight drop in sensitivity with increasing pressure may be due to the surface not fully reaching the temperature change set by the PID and measured by the Pt RTD at the copper base due to increased heat transfer coefficient of the higher pressure air. Both surface sensors show a consistent measurement.

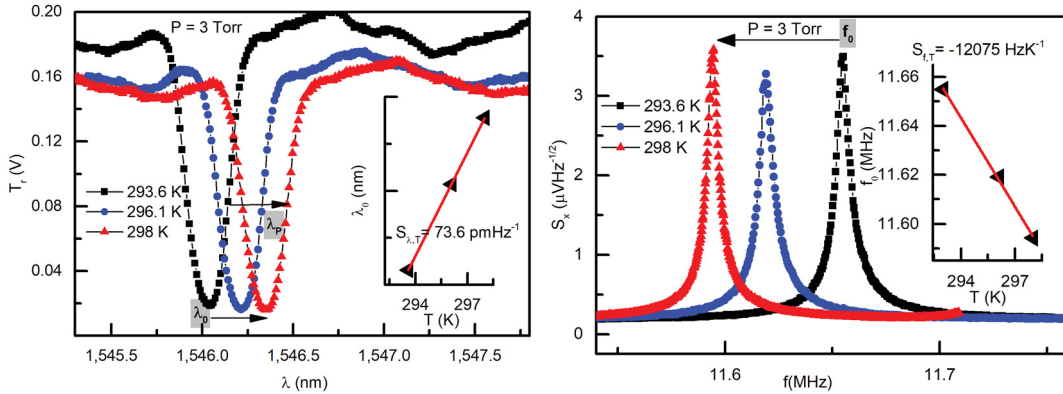


Figure 6.2: **Representative plots for determining $S_{\lambda,T}$ and $S_{f,T}$.** These are found from the linear temperature dependence of resonance wavelength of the optical ring (left) and the resonance frequency of the NOMS (right). From [16]. Reprinted with permission from AAAS.

The temperature sensitivity of the optical ring, at around 70 to 80 pm/K, is consistent with the literature [165]. The TCRF of the NOMS in this device ranges from -1050 to -1270 ppm/K, which is an order of magnitude larger than expected from materials properties alone. In another chip, the values ranged from -140 to -340 ppm/K. This discrepancy can be explained by the residual tension within the NEMS doubly clamped beams [184]. Changes to the temperature can have a much larger effect on the resonant frequency through modifying this tension [154, 156] than the material properties.

6.4.1.1 Origin of higher $TCRF$ in NEMS doubly clamped beams

From the beam geometry, $t = 160$ nm, $l = 9.75$ μ m and materials values, $E = 170$ GPa, $\rho = 2330$ kgm^{-3} , so the expected resonance frequency of the device from equation 6.3 can be found as 14.8 MHz. Measured frequency is quite different at 11.8 MHz. This is likely an indication of residual compressive stress. Rearranging equation 6.4 we have

$$\sigma_i = 3.4E \frac{f_0^2 - f_{\sigma_i}^2}{f_0^2} \frac{t^2}{l^2}, \quad (6.9)$$

which allows estimating the residual compressive stress as 57 MPa. If the beam is heated, the compressive stress will change, ultimately changing the frequency. The total stress can be set as an initial stress plus a thermal induced stress.

Table 6.1: Measured ring and NOMS temperature sensitivity at different pressures

P(Torr)	Ring sensitivity $S_{\lambda,T} = \frac{d\lambda}{dT} [pmK^{-1}]$	NEMS sensitivity $S_{f,T} = \frac{df}{dT} [(kHz)K^{-1}]$	TCRF $\frac{1}{f_0} \frac{df}{dT} \times 10^6 [ppm]$
100 μ	81 ± 5	-14.7 ± 0.2	-1269 ± 19
3	73.6 ± 0.3	-12.1 ± 0.4	-1041 ± 35
61	76.1 ± 1.4	-13.4 ± 0.2	-1156 ± 13
760	70.5 ± 2.5	-12.1 ± 0.6	-1046 ± 54

$$\sigma = \sigma_i + \sigma_t = \sigma_i - \alpha_1 E \Delta T, \quad (6.10)$$

where α_1 is the thermal expansion coefficient. This gives a temperature coefficient of thermal stress due to initial strain

$$\alpha_\sigma = \frac{1}{\sigma_i} \frac{d\sigma}{dT} \approx \frac{\sigma - \sigma_i}{\sigma_i dT} = \frac{-\alpha_1 E}{\sigma_i}. \quad (6.11)$$

After substituting in values we find, $\alpha_\sigma = -7780$ ppmK⁻¹. Inomata *et al.*[156] deduce the analytical expression for temperature coefficient of resonance frequency, $TCRF$

for a stressed double clamped beam as follows

$$TCRF = \frac{1}{2}\alpha_E - \alpha_1 - \frac{1}{2}\alpha_\rho + \frac{1}{2} \frac{0.295\epsilon \frac{l^2}{t^2}}{1 + 0.295\epsilon \frac{l^2}{t^2}} \alpha_\sigma, \quad (6.12)$$

where α_E , α_ρ , and α_σ are the temperature coefficients of Young's modulus, density, and thermal stress, respectively. Also, α_1 is the thermal expansion coefficient, ϵ is the initial strain (calculated value of 334×10^{-6} for the device in the current work), and l and t are the device length and flexure-direction thickness, respectively. Plugging values for our device into equation 6.12 we find a $TCRF = -1078 \text{ ppm K}^{-1}$ which is in good agreement with our experimental results (around $1100 - 1200 \text{ ppm K}^{-1}$) displayed in Table 6.1.

6.4.2 Dynamic temperature measurements

An example of dynamic temperature measurements is given in Fig. 6.3 measured at 3 Torr for 1 kHz PLL bandwidth. Both temperature sensors show a similar transient response with temperature change. Similar experiments as those shown in Figure 6.3 were performed at high vacuum, 61 and 760 Torr also. The temperature was maintained at 298 K for each experiment through the PID controller. For transient temperature measurements the set temperature for the measurement pressure, $\leq 100 \mu$, 3, 61 and 760 Torr were 0.1, 0.3, 0.3 and 0.3 K above 298 K respectively. Results from ring and NEMS detectors were converted into relative temperature changes and are presented in the Figure 6.4.

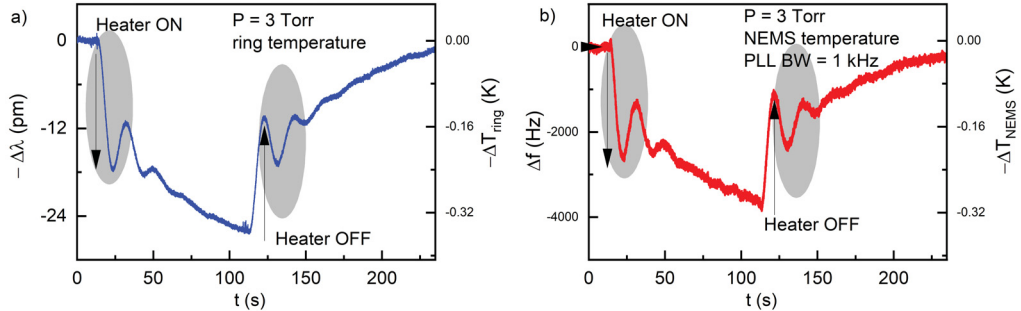


Figure 6.3: **An illustration of the change in a) wavelength and b) resonance frequency with time during step changes on and off in temperature.** A PID controlled heater steps from 298 K to 298.3 K followed by a cooling step back to 298 K. The ring data in panel (a) and NEMS data in panel (b) were measured simultaneously during the same heating and cooling cycle. The largest temperature difference measured (just when the heater was turned off to return at 298 K) by the ring is ≈ 0.34 K and by the NEMS is ≈ 0.32 K. The shaded areas highlight overshoot of the PID temperature control loop.

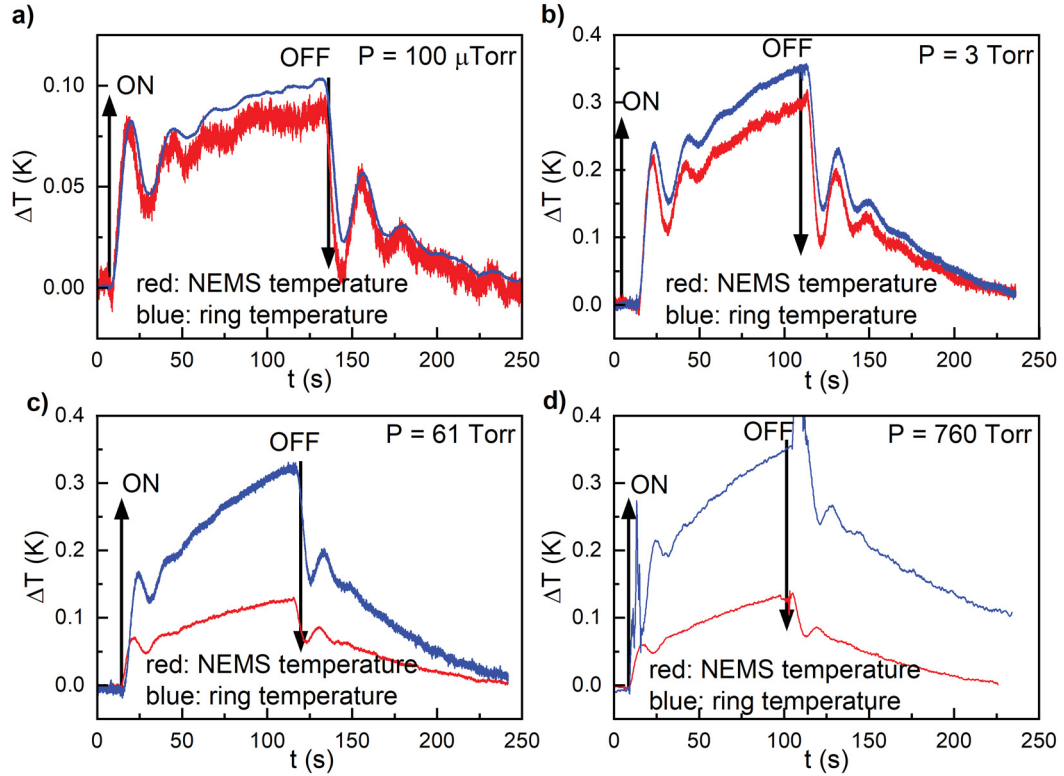


Figure 6.4: **Simultaneous dynamic temperature measurements by optical ring and nanomechanical DCB.** Measured transient temperature tracking by the DUT at low-pressure regime, (a) and (b), and high- pressure regime, (c) and (d). By sitting on the probe wavelength, temporal optical transmission shift due to temperature change is recorded by LabView. Frequency shift is simultaneously recorded by PLL at the driven amplitude. Differences in measured relative temperature change in the low-pressure regime are due to the measurement uncertainty: 6.4% at $\leq 100 \mu$ Torr, and 1.9% for 3 Torr. Whereas, $\sim 61\%$ discrepancies between the ring and NEMS temperature at higher pressures (Figure c) and d)) are significant compared to measurement uncertainty. Such discrepancies between ring and NEMS temperature is due to the extremely high nanoscale heat transfer coefficient at high pressure. Spikes at 760 Torr are artifacts from transients in optical coupled power due to setting temperature manually at the front panel of the PID controller.

Dynamic temperature measurements in Figure 6.4 show two features: First, temperature measured at low pressures by the ring and NEMS agree with each other (within measurement uncertainty estimated in section 6.4.2.1), but two higher pressure (61 and 760 Torr) experiments show a significant difference by 61%. Naturally, such huge discrepancy calls into question the accuracy of PLL frequency shift measurement at low- Q conditions. Later, we will confirm the underlying theory of this discrepancy (large heat transfer in the air), which is free from PLL artifact and verify by extensive experiments and numerical solutions. A second noteworthy item in the figure is the

substantial reduction in noise on the NOMS signal at the two highest pressures. We suspect this phenomenon also relates to the larger heat transfer in air by way of mitigating temperature fluctuation noise.

6.4.2.1 Error in dynamic measurements

The measurement uncertainty for a temperature change measured from the wavelength shift or frequency shift at a given time can be assumed to arise from the error from the linear slope fit in f vs. T and λ vs. T plots obtained during static experiments. Corresponding error in ΔT_{NEMS} and ΔT_{ring} are also evaluated. For a quantity $z = y/x$ the standard error can be estimated as [185]

$$\delta z = |z| \sqrt{\left(\frac{\delta x}{x}\right)^2 + \left(\frac{\delta y}{y}\right)^2}. \quad (6.13)$$

Table 6.2: Temperature change measured by ring and NEMS in the NOMS from Figure 6.4 and corresponding measurement uncertainties.

P (Torr)	$\Delta T_{\text{ring}}(K)$	$\delta \Delta T_{\text{ring}}\%$	$\Delta T_{\text{NEMS}}(K)$	$\delta \Delta T_{\text{NEMS}}\%$	$\frac{\Delta T_{\text{ring}} - \Delta T_{\text{NEMS}}}{\Delta T_{\text{ring}}} \times 100\%$
100 μ	0.102	6.2	0.095	1.5	6.5
3	0.341	1.5	0.322	1.8	1.9
61	0.330	1.8	0.129	1.2	61
760	0.350	3.4	0.134	5.1	62

During temperature conversion, we have chosen wavelength (transmission) and frequency shift ($\Delta\lambda$ or Δf) at the instant when PID is turned off and for simplicity assume that there is no error in the corresponding $\Delta\lambda$ or Δf . Hence comparing equation 6.13 to 6.2 we can write error in ring temperature as, $z = \Delta T_{\text{ring}}$, i.e., $\delta z = \delta \Delta T_{\text{ring}}$, and, $y = \Delta\lambda$ is assumed error less, hence, $\delta y = 0$. Error lies in determination of $x = S_{\lambda,T}$ by the slope of linear fit, $\delta x = \delta S_{\lambda,T}$. Plugging corresponding values from experiments into equation 6.13 we can estimate the error in ring temperature

$\delta\Delta T_{\text{ring}}$. Similar arguments can be made for also, $\delta\Delta T_{\text{NEMS}}$. Errors in temperature measurements shown in the Figure 6.4 are tabulated into the Table 6.2 and compared in the Figure 6.5 From Figure 6.4, it is evident that at low pressures, temperature induced frequency shift accurately measure transient temperature change within measurement uncertainty, 6.4% at $\leq 100 \mu\text{Torr}$ and 1.9% for 3 Torr. However, 61 Torr and 760 Torr experiments show $\sim 61\%$ inconsistency from temperature measured by the ring.

6.4.2.2 Discrepancy between ring and NOMS temperature at high pressure

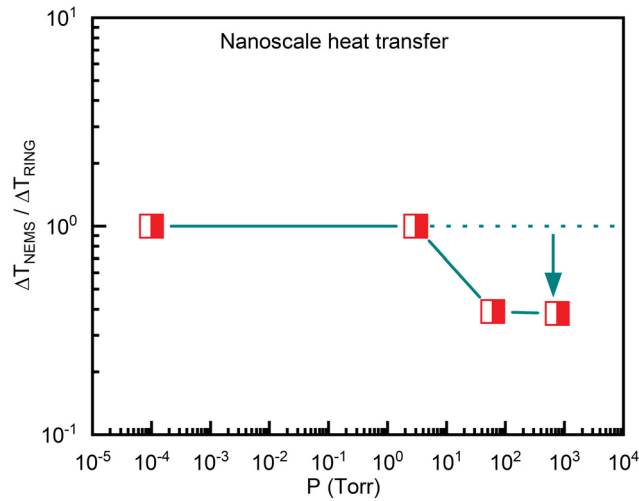


Figure 6.5: **Signature of nanoscale heat transfer by NOMS thermometry: The nanoscale mechanical resonator feels less temperature than the adjacent optical ring in a NOMS system at a same temperature ramp.** Due to the good thermal clamping of optical microring on the Si-chip surface, materials for thermal transport, it can track the actual surface temperature. Presence of air molecules at higher pressure around the tiny DCB resonator causes extra heat dissipation by air conduction which results in lower temperature change sensing by NEMS than the actual chip surface.

From Figure 6.5, it is evident that up to 3 Torr both ring and nanomechanical temperature sensors track the same temperature within acceptable experimental errors. At higher pressures, NEMS detects $\sim 2.6\times$ less temperature change well beyond the range of experimental errors. Thus breaks down the principle we have proposed in section 6.2.3 for nano-optomechanical thermometry ,i.e., $\Delta T_{\text{ring}} = \Delta T_{\text{NEMS}}$. Rather, the principle of nanoscale heat transfer could explain the discrepancy as follows. The microring has good thermal clamping to the chip surface and heat transport via conduction to the substrate can be assumed to dominate for the ring. On the other

hand, due to the nanometric size of DCB, and the fact that almost its whole surface is accessible to air, it can feel extra heat dissipation in the presence of air which needs systematic investigations. In the following, we will estimate the nanoscale heat transfer coefficients for DCB resonator to understand the underlying theory of additional heat loss at higher pressure.

6.4.3 Nanoscale heat transfer

Heat transfer across the macroscopic solid-gas interface is well understood where adequate experimental data and empirical formulas are available. Commonly used resistance thermometers or thermocouples at macroscale are not applicable in experimenting heat transfer coefficient at nanoscale solid-gas interface. Thus, a quantitative experimental determination of nanoscale heat transfer coefficient is always challenging and requires some non-contact thermometry. In previous sections, we have developed a novel approach of nano-optomechanical thermometry where a mechanically rigid optical ring is coupled to a movable doubly clamped beam released from the surface. We found that the optical temperature agrees well with expected predictions across the entire pressure regime in both static and dynamic measurements. Conversely, high-pressure responses of nanomechanical DCB resonator to surface temperature is significantly lower than theoretical predictions. This section will address this discrepancy by looking to the physics of enhanced heat transfer at higher pressure.

6.4.3.1 Review on nanoscale heat transfer

Significant research efforts in recent years are dedicated to understanding the thermal transport mechanism in sub-micron scale solids. Classical heat transport theory is found inadequate in explaining heat transfer at nanoscale [177, 178, 179, 181]. Different experimental and computational methods have been implemented by different research groups to understand the thermal transport at nanoscale [179]. Record high thermal conductivity (6600 W mK^{-1}) for a carbon nanotube was calculated by Berber *et al.* [186]. Besides increased thermal conductivity, reduced thermal conductivity measured for silicon nanowire beyond current theoretical predictions [187] was also seen. S. Neogi *et al.* [188] showed that surface topology and chemical impurities could reduce the thermal conductivity of the ultrathin silicon membrane by 25 times compared with bulk crystalline solid. As dimensions shrink heat transfer mechanism from hot solid to surrounding environments is also interesting, and little is known at the sub-micron scale. Classical heat transfer theory severely changes while accounting heat transport for a nanoscale solid surface to the surrounding air or gas interface [181].

Variation in fluid density or external fluid flow around the hot solid body is known as a bulk flow that causes convective heat transfer at a macroscopic solid-gas interface. At higher temperature, the convective heat transfer coefficient diminishes, it depends weakly on temperature. Convective heat transfer coefficient also depends on pressure because molecular density varies with pressure. From kinetic theory of gases, another mode of heat transfer can be seen due to molecular conduction or diffusion of air molecules at the boundary layer next to the solid [189], whereas, the thermal conductivity of air is proportional to density, mean free path and mean velocity of air molecules and specific heat of constant volume. For a constant specific heat, the mean velocity becomes a decisive factor in determining thermal conduction of air. On the other hand, the mean free path changes inversely, and density changes directly with pressure. Consequently, thermal conductivity is independent of pressure or density and is proportional to the square root of temperature. Hence it is reasonable to consider the joint effect of molecular conduction and advection in determining the dependency of pressure and temperature on heat transfer coefficient.

A theoretical approach [190] showed that natural convection at the microscale is insignificant because of too little buoyancy, the driving force for natural convection, and suggests that larger surface to volume ratio has a stronger impact on heat transfer coefficient [191]. In general, the bulk heat transfer coefficient of gas is accepted for a range of $10-25 \text{ Wm}^{-2}\text{K}^{-1}$. Literature value of nanoscale heat transfer coefficient in the presence of air found to vary from 100 to $7000 \text{ Wm}^{-2}\text{K}^{-1}$ [192], even higher, around $0.1 \text{ MWm}^{-2}\text{K}^{-1}$, from experiments by thin-film evaporative cooling MEMS, [193], and at carbon nanotube-air interface by molecular dynamic simulation [194]. Laser thermography experiments [181] on a suspended VO_2 nanowire in the air challenged the classical description of heat dissipations at the nanowire-air interface. Precisely, their results obey an analytical model based on Dickins' geometry [195] that shows strong pressure dependence of heat transfer coefficient above 10 Torr and significantly higher at lower pressures. Experimentally observed values are in good agreement with the analytical results and obtained heat transfer coefficient at atmospheric pressure is around $0.01 \text{ MWm}^{-2}\text{K}^{-1}$.

The degree of variation ($100 - 10^6 \text{ Wm}^{-2}\text{K}^{-1}$) in the literature suggests that nanoscale heat transport mechanism at solid-air interface need more study. On-chip thermometry, like NOMS thermometry in this chapter, provides an excellent opportunity to understand the underlying mechanism. In the following, we evaluate and model higher pressure nanoscale heat transfer explain the observations in Figure 6.5. To the best of our knowledge, heat transfer measurements by two orthogonal thermometers on a single sensor, like NOMS thermometer in this thesis are the first

report.

6.4.3.2 Evaluation of nanoscale heat transfer coefficient, h

For investigating the discrepancy in simultaneous relative temperature measurements by the optical ring and NEMS at higher pressures, heat transfer coefficients are evaluated analytically as well as by COMSOL Multiphysics simulations.

Analytical evaluation of h and underlying thermal physics: The optical ring in the NOMS is clamped to the silicon surface on one entire side, whereas the NEMS device is only clamped at two points with almost all surfaces exposed to surrounding air. Estimating heat transfer coefficient of the NEMS device due to natural convection is nontrivial since it can be changed dramatically from one system to another depending on the operating environment, sample mounting conditions, etc. Here we are going to estimate the heat transfer coefficient of the DCB geometry as a function of pressure following Dickins approach [195] that considers heat dissipation by air thermal conductivity.

In 1934 B.G Dickins [195] considered a long hot wire of diameter D which is suspended along the axis of a cold cylinder of radius R full of gas at pressure P . Both solids are concentric. The goal of the study was to understand and to measure the thermal conductivity of surrounding gas around the hot wire. Heat loss due to convection was not accounted for in experimental design. Estimated radiation loss was negligible. The author derived the heat transfer coefficient, h around the hot wire which was adopted by Cheng Chun *et al.*[181] in 2011 for suspended silicon nanowire as below

$$h(P, D) = \frac{\gamma \kappa_{\text{air}}}{D \ln\left(\frac{R}{D}\right) + \frac{c}{P}\left(\frac{D}{R} + 1\right)}, \quad (6.14)$$

where, $D = 2wt/(w+t)$ is the characteristic dimension of the NEMS and is proportional to the volume-to-surface ratio. According to kinetic theory of gas heat transfer regimes at solid-air interface are separated into three regions depending on Knudsen number, K_n which is proportional to the mean free path of air molecules (l_{mfp}) and inverse to D . For air, $l_{\text{mfp}} = 0.225k_{\text{B}}T/d_{\text{air}}^2P = c/P$, which accounts for the evolution of h as function of pressure (P). κ_{air} is the thermal conductivity of air, and numerical factor γ accounts the difference between experimental structure and Dickins geometry.

Equation 6.14 is valid only when $R \geq D$. In the present work, the substrate is the heat source for the DCB, and both clamping ends of the DCB are at the same temperature as the substrate, i.e., at the temperature measured by optical ring

during dynamic measurements. So DCB subjected to heat transport via anchor is not rejecting any heat to the closest silicon surface. Heat dissipation is taking place only due to surrounding air molecules. The choice of the value of the R effectively sets the transition from molecular free regime to viscous flow regime. It also sets a cap for the value of h in the viscous flow regime; however, due to natural \log , the h is not very sensitive to the choice of R . We try three value of R of $100 \mu\text{m}$, $10 \mu\text{m}$, and $1.3 \mu\text{m}$ to calculate the analytical model. The value is chosen to most closely match the value of h obtained in COMSOL at atmospheric pressure (see next section). The calculated values of h and K_n as a function of pressure is depicted in the Figure 6.6 (a). Figure 6.6 (b) shows the simulation results for atmospheric pressure.

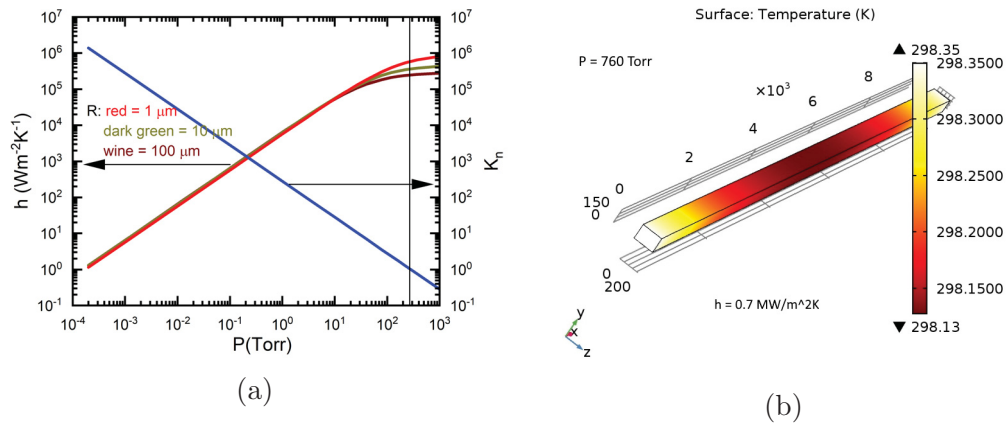


Figure 6.6: **Calculated and simulated heat transfer coefficient as a function of air pressure.** a) Calculated heat transfer coefficient from equation 6.14 as a function of pressure P (red plot along the left axis). Blue plot is Knudsen number along with the right axis. With increasing air pressure (decreasing K_n) h improves linearly up to the transition pressure around 270Torr, shown by the line. After the transition pressure presence of enough air molecules for heat dissipation through conduction rather than convection initiates a quasi-thermal equilibrium which makes h almost independent of pressure. b) 760 Torr Comsol simulation result for DCB geometry $9.75 \mu\text{m} \times 220 \text{nm} \times 160 \text{nm}$. The temperature at both ends is at same elevated by the PID controller heater 0.3K from equilibrium temperature of the entire system at 298K . During simulation, the h value is increasing gradually for the best match of the simulated temperature at the middle of DCB around 0.13K (see table 6.2). Simulated value of $0.7 \text{MWm}^{-2}\text{K}^{-1}$ is in good agreement with that of Figure (a).

When $K_n \gg 1$, i.e., $l_{mfp} \gg D$ then $h \propto P$ and independent of D in equation 6.14. This pressure regime is known as molecular flow regime where multiple collisions between air molecules cannot be expected because of low molecular density. In this regime, all molecules can carry away heat by single collisions to the hot surface. Therefore, h is proportional to the frequency of molecular collisions i.e., $h \propto P$ which

is illustrated in Figure 6.6 (a) up to $K_n \approx 1$ which occurs at 270 Torr. At this transition pressure, inter-collision between air molecules themselves have the same rate as the collisions between air-DCB surface. After this transition pressure, device enters the fluidic flow regime where $l_{mfp} \ll D$ and $K_n \ll 1$. In this condition, higher pressures h are insensitive to P and strongly depend on D , i.e., the size of the heated device. After 270Torr, we can see a flat h vs. P relation which corresponds with the regime of thermal conduction independent of pressure in viscous flow.

Numerical evaluation of h and underlying physics To verify the analytical treatments on experimental results, we have performed COMSOL Multiphysics heat transfer simulation for experimental conditions at each measurement pressure for various numerical value of h . Our simulation results indicate that the heat dissipation mechanism for nanoscale DCB resonator depends on air pressure as argued in Dickins' approach. Using numerical h values based on the analytical model at the various pressures results are in good agreement and tabulated in the following table.

Table 6.3: h at different pressures.

P (Torr)	analytical h ($\text{MWm}^{-2}\text{K}^{-1}$)	Numerical h ($\text{MWm}^{-2}\text{K}^{-1}$)
100 μ Torr	1×10^{-6}	1×10^{-5}
3	0.017	0.017
61	0.3	0.6
760	0.7	0.7

From Table 6.3 with measured difference in temperature sensing (table 6.2) between ring and NEMS it can inferred that for $h \leq 0.017 \text{ MWm}^{-2}\text{K}^{-1}$, i.e., up to 3 Torr, air conductivity is insignificant, COMSOL considers $h = 10 \text{ Wm}^{-2}\text{K}^{-1}$ for convective heat dissipation which would be negligible. Hence, observed discrepancies between measured temperature by ring and NEMS (see Figure 6.5) is consistent with a conductive dissipation channel made by air molecules at 61 and 760 Torr.

It is worth mentioning that h at 61 Torr that is needed in COMSOL to produce the observed NEMS measurement is slightly higher than that from Dickin’s model. We are not following the exact Dickins’ geometry where air molecules inside the hypothetical cold cylinder are at the same lower temperature. In our experimental structure, the top edge of the DCB satisfies the Dickins’ geometry condition. The thin air film between the bottom edge of the DCB and the substrate can be assumed at a higher temperature than the DCB; similar conditions are valid for the side walls where heat transfer can occur from the hot substrate to cold DCB. These conditions are not accounted in equation 6.14, which may account for the difference. However, modified Dickins’ model can qualitatively explain the heat dissipation issues at higher pressure measurements. For $0.6 \leq h \leq 0.7 \text{ MWm}^{-2}\text{K}^{-1}$ we can see the same amount of heat dissipation from 61 – 760 Torr which agrees well with literature values reviewed so far.

6.4.3.3 Correction factor for nanoscale heat transfer

Efficacy of thermometry is essential for reliable temperature measurements. NEMS thermometry in ambient may result in incorrect conclusions about the surface temperature without proper knowledge on nanoscale heat transfer. The recent trend of using nanometric thermometry at various applications demands appropriate determinations of the loss factor due to nanoscale heat transfer to account for the actual temperature in experiments. Recently, Inomata *et al.* [156] observed the nanoscale heat transfer issue for a doubly clamped beam resonator while tracking temperature modifications by a single brown fat cell (BFC). To know the actual measured temperature by the NEMS, the authors needed thermometric analysis with the aid of a separate temperature sensor for estimating the loss factor. NEMS thermometry, developed in this chapter is unique in this manner in that we do not need any extra temperature sensor. It has an inherent exquisite feature for monitoring the local temperature with the knowledge of the difference between the local chip surface and air temperature provided by on-chip dual temperature sensor readings. The ratio of actual surface temperature (ring temperature) to that measured by NEMS estimates the loss factor due to conductive heat loss by air molecules in ambient as below

$$c_h = \frac{\Delta T_{\text{ring}}}{\Delta T_{\text{NEMS}}}. \quad (6.15)$$

From Figure 6.5 we have $c_h \approx 2.6$ for 61 and 760 Torr. Hence the actual surface temperature measured by NEMS will be

$$\Delta T_{\text{NEMS-true}} = \frac{\Delta f}{S_{f,T}} \times c_h = \frac{\Delta f}{S_{f,T}} \times \frac{T_{\text{ring}}}{T_{\text{NEMS}}}. \quad (6.16)$$

Hence, integrated optical ring adjacent to a NEMS device does not only enhance the displacement sensitivity to resolve thermomechanical noise across the entire pressure regime, but also it can accurately predict the surface temperature more reliably than an air-moderated NEMS device at higher pressure. Two thermometers, optical ring, and NEMS are orthogonal to each other by their characteristic response to surface temperature variations.

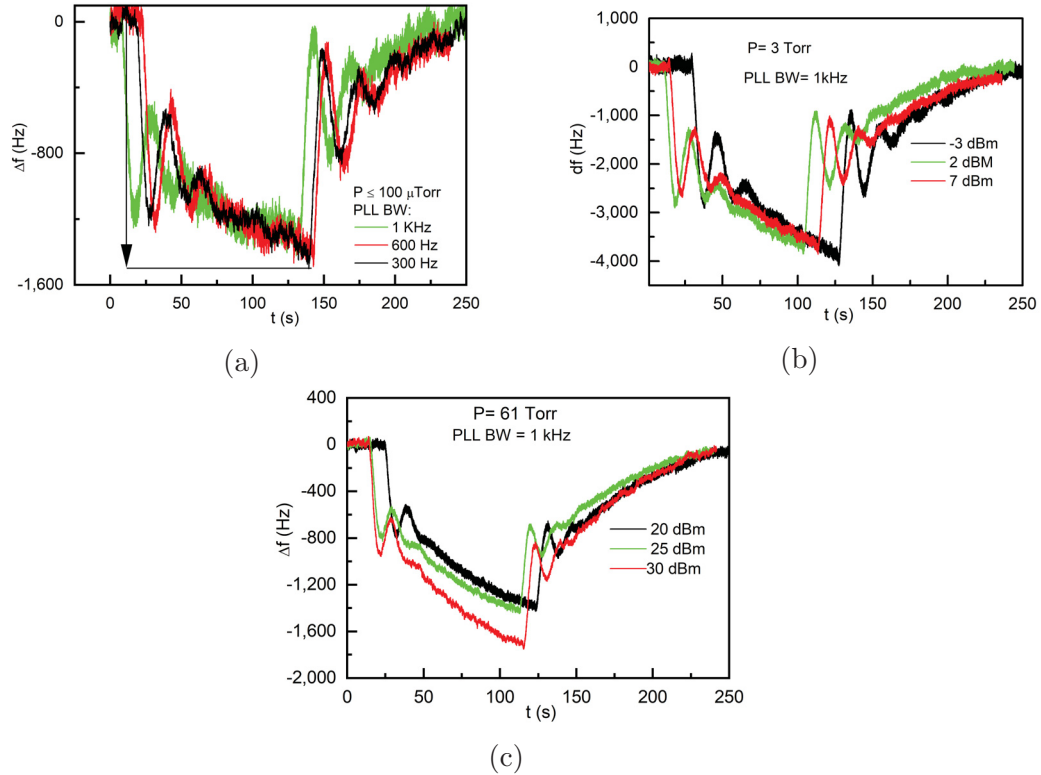


Figure 6.7: **Fidelity check for PLL performance:** All figures represent the frequency shift in experiments during dynamic temperature measurements. In all data, time zero is arbitrary. **Low-pressure regime:** **a)** The figure represents frequency evolution during 0.1 K temperature change at a pressure $\leq 100 \mu\text{Torr}$ for different PLLBW. All measurements are also equivalent to measured ring temperature. It is clear that in all experiments BW is reducing the frequency fluctuations only, not the frequency shift amplitude. **b)** Similar to $\leq 100 \mu\text{Torr}$ experiments 3 Torr experiments at different driving amplitude (SNR) also follow the ring temperature. **High-pressure regime:** **c)** A representative plot for 61 Torr is presented here for different drive power. The frequency shift measured is equivalent to ring temperature after the correction factor c_h . Similar to 3 Torr, 61 Torr also demonstrate that higher driving power improves temperature resolutions (frequency fluctuations). The temperature change step for 30 dBm drive is likely slightly larger due to a change in the piezo shaker heating during the course of measurement.

6.4.4 Notes on PLL measurements' fidelity

For any sensor, the reliability of measurements is important. We already showed in Figure C.4 and Figure C.5 that our PLL at longer time scale was not missing information in tracking frequency shifts at the lowest- Q operation. This section will demonstrate more experimental evidence of the fidelity of the long-term PLL frequency shift measurements as a function of bandwidth and SNR of the NEMS. Figure 6.7 demonstrates that neither the bandwidth nor the SNR affects the total frequency shift made by a known temperature change. In particular, the changing bandwidth should correspond with varying levels of signal suppression (as per chapter 5) but only for the signal of high enough bandwidth. The temperature change steps shown here are slow enough that all three PLL bandwidth produce the same signal (Figure 6.7 (a)). Similarly, changing the SNR produces identical frequency shift measurements (Figure 6.7 (b)). At both lower pressures, NEMS temperature change matches that of the ring.



Figure 6.8: **A photo of the front-view of the measurement chamber.** The chip is glued by Ag epoxy on the piezo surface. RTD sensor close to chip also glued by the same epoxy on the piezo. The piezo shaker containing the chip and RTD sensor was further glued on a copper plate. The resistive heater is placed on the copper by epoxy.

At higher pressure, c_h , the correction factor is introduced in order to match the 61 Torr NEMS frequency shift to the ring measured shift (Figure 6.7 (c)). We note that the +30 dBm drive case shows a slightly higher responsivity. We postulate that this arises due to changing power coming from the piezo shaker. At this high drive

power, the piezo is a substantial heat source. The shift in resonance frequency is large enough that the piezo efficiency changes and the piezo heat output changes. Since the PID sensor of temperature controller sits on the piezo, the PID call for power is slightly different in the +30 dBm case, and the NEMS temperature change is also actually different, and accurately represented by the data. Figure 6.8 now shows a picture of the chip inside the chamber with labeled heater and Pt RTD sensor.

6.4.5 Temperature noise suppression at higher pressure

Measured temperature resolution is related to the frequency stability as follows

$$\sigma_{\delta T} = \frac{\sigma_A \times f_0}{S_{f,T}}. \quad (6.17)$$

From dynamic NEMS thermometry presented in Figure 6.4, we use 5 seconds of the

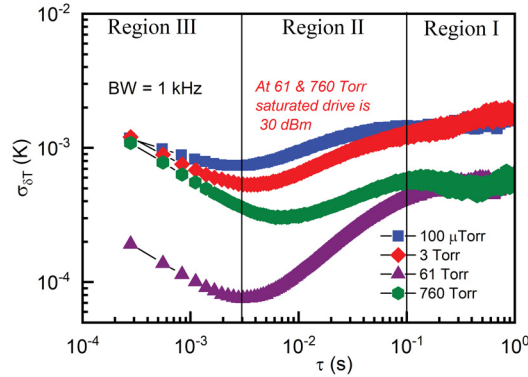


Figure 6.9: **Measured temperature resolutions at different pressures after nanoscale heat transfer correction:** Figure represents equation (6.17) for temperature stability during temperature measurements. Short-term stability here is enhanced (lowered) due to PLL gain with increasing damping. Also, suppression in the long term-stability with damping is evident. Results presented here are discussed in Chapter 5 in similar PLL experiments.

data of temporal frequency fluctuations before turning on the heater. From these data, corresponding Allan deviation plots are created for different Q s and measured temperature resolutions (equation 6.17) are presented in Figure 6.9.

Recall that our PLL transfer functions suppress noise (as well as signal) at shorter sample times. In the present case, region I (no suppression) is for 0.1 s and longer, region II (1st PLL rolloff) is for 3 to 100 ms, and region III (PLL plateau) for shorter than 3 ms. A 6 dB better resolution is observed in region I at 61 and 760 Torr in comparison to vacuum and 3 Torr. We attribute this to a reduction in f^{-1} frequency fluctuation noise from temperature fluctuations. Temperature fluctuation noise should

be reduced by the extra conductance channel at higher pressures due to the nanoscale heat transfer effect. It is tempting to attribute the reduction to the ability of the NEMS to read the surface temperature changes at higher pressure. However, that c_h factor is only 4 dB. Also, we assert the NEMS correctly reads its own temperature, so these Allan deviations are a real reduction in noise level for NEMS temperature readings.

6.4.5.1 Limit of detection (LOD)

Generally, the limit of detection of any sensor is considered as thrice of the sensor resolution. So, we may define LOD for temperature sensing as, $LOD = 3 \times \sigma_{\delta T}$. Consider the sample time of 3 ms (region III) in Figure 6.9: the LOD is 2.2, 1.6, 0.2 and 1 mK for 100 μ , 3, 61 and 760 Torr, respectively. The LOD in region I at 0.33 seconds is approximately 4.5, 4.5, 1.4 and 1.4 mK for at 100 μ , 3, 61 and 760 Torr, respectively. In both regions, higher pressure LOD is better. Below, we confirm that only the region I LOD is practically accessible.

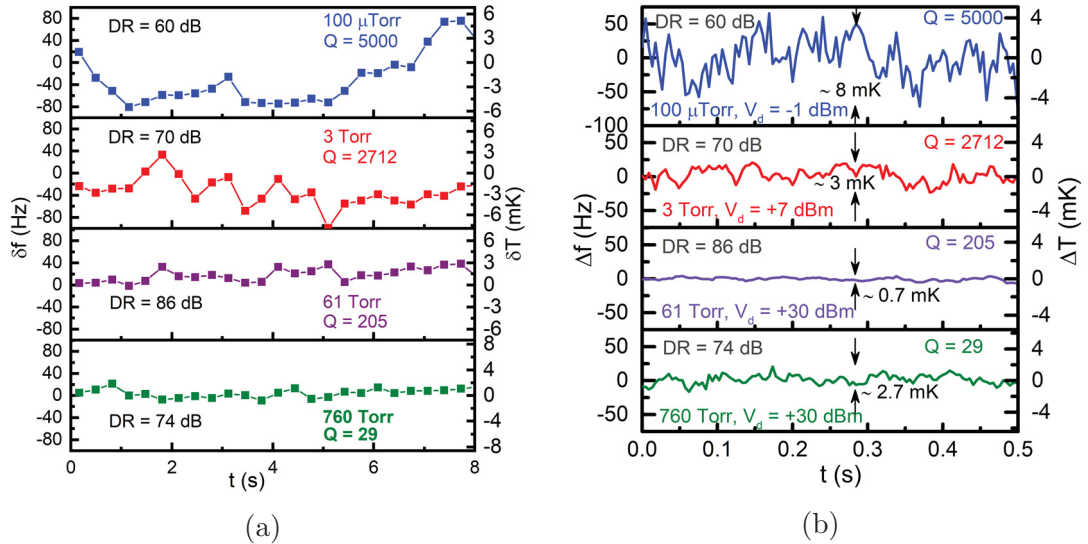


Figure 6.10: **NEMS Thermometry:** Measured frequency (temperature) fluctuations in an 8-s (a) and a 0.5-s (b) window for different pressures and Q . PLL BW is 1 kHz for each case and sampling frequency is 3.6 kHz. In both cases, higher DR correlates with improved stability. **a)** Data are shown for 3 Hz ($\tau \sim 330$ ms) sampling interval before the integration roll-off in PLL transfer function (region I). **b)** Plots represents data in the constant gain region of PLL transfer function (region III) and are shown at a 225 Hz ($\tau \sim 3$ ms) sampling interval. Arrows indicate the maximum fluctuations over the full half-second. From [16]. Reprinted with permission from AAAS.

6.4.6 Application of damping improved stability: temperature sensing

Figure 6.10 illustrates that temperature fluctuations improve with increasing pressure. Figure 6.10 (a) is a zoom-in of the 8 seconds window prior to heater turn on for the data of Figure 6.4. Data has been averaged into 330 ms sampling interval to ensure PLL were in region I. The reduction of fluctuations at higher pressures is evident, and temperature fluctuations are essentially consistent with the LOD identified above. Figure 6.10 (b) shows the same data zoomed into a 0.5 second window and averaged into 3 ms sampling intervals (PLL region III). This was the data presented in ref. [16]. Its temperature fluctuations are consistent with the LOD at 3 ms as well, though this temperature resolution is not experimentally accessible since any signal change of interest is also suppressed at this sampling interval and speed. To clarify the point,

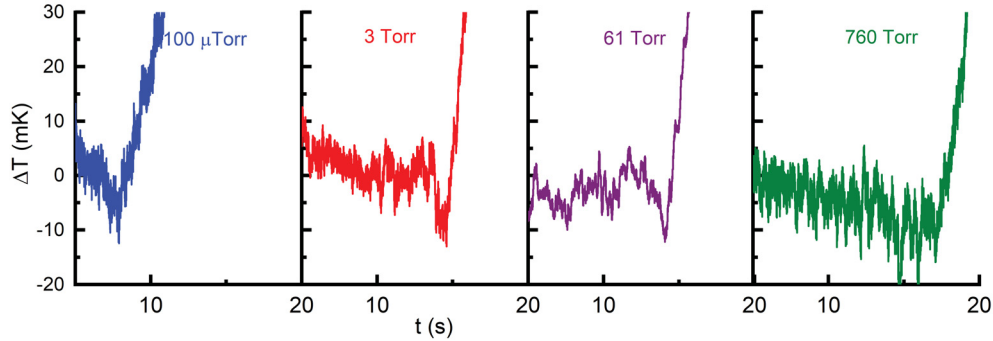


Figure 6.11: **Observed limit of temperature change detection at different damping:** The zoomed-in plot of temperature rise measured at different pressures shown in Figure 6.4 after correcting nanoscale heat transfer issue. The time axis is arbitrary. An improvement in $LOD = 3 \times \sigma$ is visible with increasing damping according to long-time averaging shown in Figure 6.10 (a). From measured Allan deviations from PLL at 3-ms, a 5mK LOD for 100 μ Torr and 3 Torr is expected which is not resolved in this experiments. Similarly, short-term resolutions from Allan deviation at 61 and 760 Torr corresponds to 1 and 0.2 mK LOD , which are impossible to observe in these experiments. So, PLL artifacts cannot improve the LOD despite displays better frequency stability. Here, we achieved better sensor performance in ambient by reduced temperature fluctuations through nanoscale heat transfer. 760 Torr data is averaged, so it is not showing actual fluctuations in experiments.

Figure 6.11 shows the frequency vs. time during onset of temperature change in the same data set, using the 3 ms sampling interval. The practical LOD for detecting these jumps, at the speed at which they occur, is on the order of 10 mK in all cases. The 0.2 mK LOD for 61 Torr is clearly a poor estimate. This confirms that PLL data beyond region I is not useful for actual measurement. LOD estimates from region I are

a bit low as well, but Figure 6.11 does confirm that atmospheric pressure sensing of temperature changes is at least as good as vacuum in this device. This is an important finding for temperature sensing as well as gas sensing at atmospheric pressure.

6.5 Conclusions

This chapter successfully develops the fundamentals of nano-optomechanical thermometry, where two thermometers, optical microring, and NEMS resonator can be calibrated against each other. Such orthogonal temperature sensing capability of two inherent thermometers in a NOMS make NOMS thermometry promising for relative temperature change on a smaller scale. NOMS thermometry can be a useful tool for the reliability of temperature measurements and remove the need for another kind of thermometer in experiments. The developed thermometry enables to test the reliability of PLL frequency tracking of mechanical resonators by loading a known amount of temperature. The experimental findings are consistent with a model for enhanced nanoscale heat conduction through air. The knowledge of nanoscale heat dissipation is found significantly helpful for extracting exact temperature change in chip surface with potential applications in IR detection. Moreover, temperature sensing experiments by HF2 built-in PLL architecture is found precise in tracking nanomechanical frequency shift by a known temperature loading irrespective of measurement bandwidth and driving power for slowly changing temperatures. Principally, results of this chapter verify that resolutions of any measurand of interest by the mechanical resonant sensor can improve with damping (lower Q), which is hypothesized in the introduction and developed from Chapter 2 to Chapter 5. In another way, it confirms that ambient condition mass sensitivity of DCB resonator can be equivalent to or better than that of high vacuum. In the next chapter, we will attempt to verify this hypothesis by ambient condition gas sensing through designing an integrated GC-NOMS gas sensor in ambient.

Chapter 7

Nanomechanical gas sensing in ambient by integrating NOMS with gas-chromatography

7.1 Introduction

Gas chromatography (GC) is a standard separation technique that determines the number of components and their proportionality within a mixture and is frequently used in analytical chemistry. For identification and quantification of these separated chemicals, mass spectrometry (MS) is widely accepted as a GC detector. Now, GC-MS is a mature technology and routinely used across the world. In a GC-MS, separated substances emerge from the GC column according to their characteristic retention time and flow into the electron ionization chamber of the MS. The chamber then generates multiple ions of each substance eluting from the GC and the MS analyzes them according to their specific mass-to-charge ratio allowing the identification of each species of molecule. In a full scan GC-MS analysis, the data acquisition is non-targeted. That is, any compound entering the MS will come out with a response that falls within the selected mass range. As a consequence, an analyst can detect things from mass spectrometry which are not known. Thus, a combination of these two techniques is precisely specific both for qualitative and quantitative evaluation of a solution containing several chemicals. Field use of GC-MS is limited due to the requirement for high vacuum, cryogenics, and a functioning ionization chamber for the MS. Moreover, GC-MS analysis also requires an expert analyst. The recent commercialization of micro-GC needs some viable mass spectrometers in developing a portable GC-MS, an inexpensive sensing system should be operated in ambient conditions, to eliminate the cost and complexity of vacuum tubing.

NEMS, by its unparalleled mass sensitivity down to proton limit [3], is a suitable

candidate to replace MS from the GC end. It becomes a more realistic alternative to conventional bench-top MS after demonstrating single molecule mass spectrometry [9] and applications as a gas detector at the GC end [5, 6, 43, 44]. Limited examples of GC-NEMS as GC-MS are probably due to lower mass sensitivity in ambient operations stemming from the lower quality factor that discourages the research community. In this thesis, we have already established that using the state-of-the-art of optomechanics a DCB NEMS driven to the intrinsic dynamic range can show better sensitivity at larger damping or at least a high-vacuum level sensitivity can be achieved at lower- Q conditions without reaching the intrinsic DR . Such vacuum level stability in ambient has potential in gas sensing experiments. Here, we want to establish this concept of improved nanomechanical sensitivity by using a NOMS device for detecting gaseous components of a mixture separated by a commercial GC. Using superior mass sensing capability of a nanomechanical resonator at the GC end can open a viable route of portable GC-MS that can fulfill the growing need of portable gas sensors. With this perspective, this chapter will demonstrate a comprehensive technique in integrating centimeter scaled NOMS chip with commercial gas chromatography (Agilent 5890) to quantify the mass of GC separated gas molecules from a mixture. The assembly and initial testing of a nanomechanical mass sensor integrated at a commercial GC end are described through VOC (volatile organic compound) detection. The same assembly GC-NOMS gas sensor has been used later for detecting more VOCs and metabolites by co-workers [5]. The research described herein focuses on improving the mechanical performance of a NOMS sensor by enhancing pressure in order to move toward a deployment of GC-MS in ambient conditions at atmospheric pressure.

7.2 Gas chromatography

Gas chromatographs are frequently used instruments in analytical chemistry that separate and measure volatile components from a mixture. The mixture is separated inside a tube, known as a column, and a detector identifies and quantifies the components that exit the column by comparing with the previously measured standard sample. The analysis made by a gas chromatograph is known as gas chromatography (GC). A gas chromatograph essentially consists of the following components for chromatography:

1. Gas supply: Carrier gas (often helium) carries the samples through the instrument by a controlled flow. If necessary gas needs to be supplied for the detector, for example, an FID (flame ionization detector) requires air and hydrogen for its functioning.

2. Sample injection port: Through the injector samples to be analyzed are loaded into the column via a hypodermic syringe. Often, the volume of the injected sample is further reduced for the column by what is called a split injection. The remaining samples leave the injector via a split vent. A split injector composed of a glass tube creates an inert environment inside the injector where the sample is vaporized to mix with a carrier gas and to transport inside the column. The injector temperature must be high enough to ensure instant vaporization without degrading the sample quality.
3. Capillary column: It is the heart of GC. The separation takes place inside the column through the physicochemical interaction of the sample with the stationary and the mobile phase (carrier gas). The column holds the stationary phase, which is a polymer coating inside the column with a small diameter. The high boiling point of polymer coating prevents it from evaporating off the column.
4. Detector: With properly chosen column conditions, the separated components in the sample flow past the detector one at a time which generates electric signals for each component. Among several types of detector FID (flame ionization detector) is widely used to analyze volatile organic compounds (VOC) or others with C-H bonding. FID uses air/hydrogen flame to pyrolyze the effluent. The pyrolyzation produces CH species proportional to the number of Carbon atoms. These fragmented CH species are ionized by reacting with Oxygen in the flame.



These electrons alter the current within the detector, which is to be detected. The resulted number of ions proportional to measured current depends on flame conditions and identity of each molecule in question. Roughly the current is proportional to the number of reduced Carbons in the molecules. Hence, the detector shows a different response to each compound, due to which separate calibration needs to be performed for each compound to be analyzed. Often, standard solution (known concentration) is used to make a calibration curve.

5. Temperature controlled oven: It accommodates all separation components for gas chromatography. Also allows controls of eluants interactions with the stationary phase.
6. Integrating recorder and data station: The output of the detector is sent to an integrating recorder. The recorder plots, and analyzes and stores data in a

computer.

7.2.1 Principle of GC

Following Figure 7.1 (a) shows inside view of the oven of a commercial GC Agilent 5890 used in this dissertation for gas chromatography. Schematic Figure 7.1 (b) explains the principle of gas chromatography.

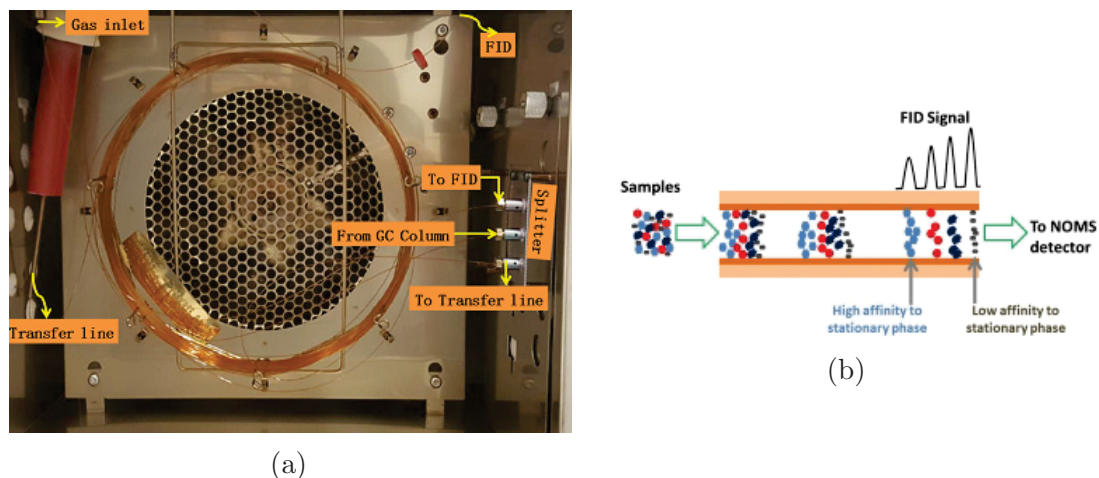


Figure 7.1: **Basic features and principle of gas chromatography.** a) Details of column connections inside GC oven. Length of fused silica capillary (ID= 0.32 mm) GC oven column for separation is 30m. A 50:50 splitter is added to the original commercial design to split the injected samples inside the capillary equally among the FID detector and NOMS mass detector through the transfer line (will be described later). b) Separation techniques: Injected analytes in the mixture to be separated show different affinities to the stationary phase. While moving through the capillary column, carried along by the mobile phase (helium gas), analytes with low affinity for the stationary phase move faster towards the detector, while those with a higher affinity will tend to lag behind. Thus, a GC separates analytes depending on the differential affinity of the analyte for the stationary phase. Depending on retention time detector output recorded by the recorder displays gaussian peaks of individual gas against the time axis.

Samples are loaded through an injection port which vaporizes the mixture before sending to the GC column via the inlet. A regulated flow of carrier gases (helium) makes it possible to carry the sample throughout the instruments. The carrier gas is chosen as inert so that it cannot interact with samples, and thus selectivity of GC separation can be attributed to the stationary phase alone. GC capillary column is the heart of any GC, as it separates the mixture into its constituents depending on their differential migration time through the column, as shown in Figure 7.1 (b). A programmable heater controls the temperature of the injection port, column, and detector of the

GC. The fused capillary column is composed of a thin layer inside it called stationary phase and an outer surface of polyamide film, which provides its flexibility. Another phase inside the column is known as the moving phase, which is a combination of carrier gas and sample gases. When boiling point of components approaches by an appropriate ramp of temperature, they will re-vaporized to enter the detector; here we are using a flame ionization detector (FID). In this way, a chromatograph can be obtained by a computer in the time axis for different composition depending on the boiling point. The area under the peak of each component gives a quantitative concentration of the gas.

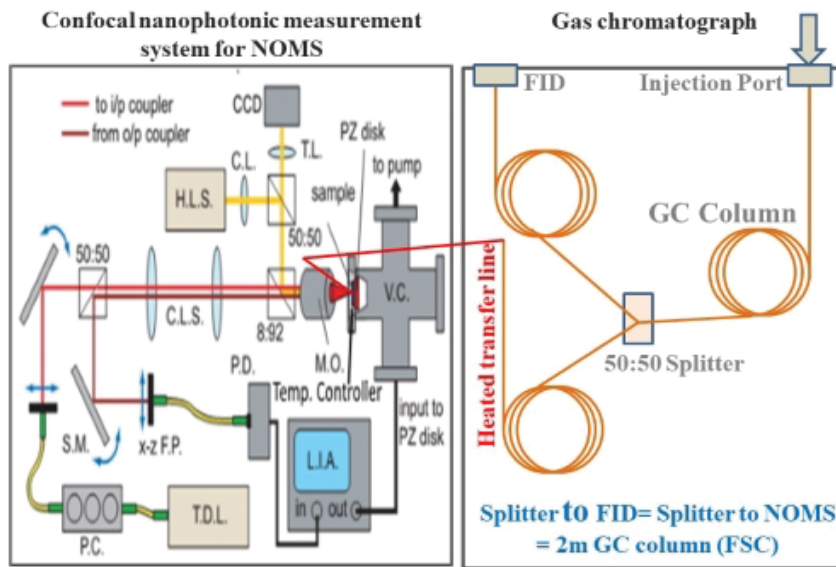


Figure 7.2: **Schematic of designed integrated GC-NOMS gas sensor for the ambient condition.** **Left:** The box shows the diagram of the confocal laser scanner-based NOMS measurement setup (described in [48]): C.L.: collector lens, C.L.S. confocal lens system, H.L.S.: halogen light source, M.O.: Microscopic objective, P.C.: polarization controller, T.D.L.: tunable diode laser, T.L.: tube lens, S.M.: steering mirror, V.C.: pressure controllable vacuum chamber, LIA: lock-in amplifier, P.D: Photodetector, x-z F.P.:x-z fibre positioner. **Right:** The box is a schematic of Gas chromatography. An Agilent 6890N gas chromatograph is used in the current work to integrate with the NOMS measurement systems in the left. Inside the oven, GC column is made of 0.32 diameter fused silica capillary (FSC) tube. The same of FSC of 2 m length is used to connect FID and NOMS from the 50:50 splitter. FSC from splitter to NOMS is brought out outside the GC oven by a temperature controlled transfer line (red line in the schematic). The temperature controller ensures that the transfer line is always at GC-oven temperature to prevent any condensation of analytes at the wall of the capillary tube. Left box of confocal measurement set up is adopted from reference [48]. Copyright 2013 The Japan Society of Applied Physics.

7.3 GC-NOMS integration

Our goal is to use NOMS as a mass sensor for detection and quantification of GC eluted peaks. We want to split the gas in the column before entering the FID in such a way so that an equal amount of analyte-laded carrier gas can flow past the FID and the NOMS sensor at the same time. This should allow us to compare and calibrate the NOMS with the FID. Hence the combination of GC-NOMS serves the purpose of gas separation and selection through GC and quantification of the mass of GC effluents by NOMS, which is analogous to the well-known GC-MS system. Since all the operations in our proposed design are in ambient condition, a successful demonstration of proposed GC-NOMS integration can be a baby step toward the future generation ambient condition GC-MS system.

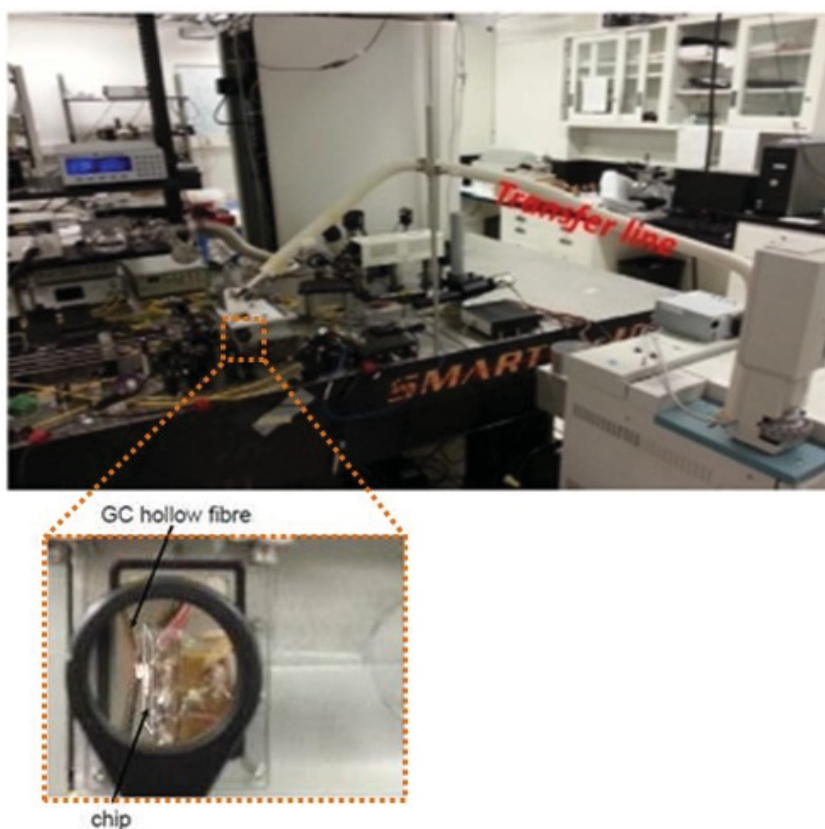


Figure 7.3: **Snapshot of the experimental setup.** The L-shaped white tube from the outside of the GC towards the specially designed aluminium chamber (where the NOMS chip is staged to the nanophotonic measurement system) contains the temperature controlled transfer line. White outside of the transfer line is insulated to prevent heat dissipations from the hot transfer line. The inset shows the magnified views of FSC close to device under test on the chip surface.

To do this, we have introduced a 50:50 splitter inside the GC oven (see Figure

7.2). From the splitter, we have used the same GC Fused Silica capillary (FSC) of 2 m length for both FID and NOMS housed in a specially designed aluminum chamber (see in the snapshot of actual lab arrangements in Figure 7.3). For bringing out the FSC towards NOMS chamber, we have incorporated a transfer line which can be heated at any desired temperature by a PID temperature controller, and always it has been kept at GC oven temperature. FSC position relative to the device has been controlled by a three-axis Newport 461 series microcontroller mounted on the top of the chamber (not shown in the figure). As in previous chapters, other arrangements of sample stage with Cu-base, piezo shaker, PID temperature controller along with the provision for connecting the vacuum pump remains the same.

7.4 Experiments

Before starting gas sensing experiments, NEMS characterizations were started from the high vacuum ($\leq 100 \mu\text{Torr}$) at 298 K)) by measuring the TM noise spectra, which gave the resonance frequency and quality factor as described in previous chapters. TM noise measurements were continued with slowly increased pressure to get the fundamental resonance frequency (10.9983 MHz) and quality factor (around 29) at atmospheric pressure. Then the device was driven at maximum available driving power (36 dBm) to attain the largest *SNR* which is slightly below the intrinsic critical amplitude (see Chapter 3) and thus ensured the linearity of the nanomechanical DCB resonator as a mass sensor. Sitting on this maximum drive, the built-in phase locked loop of Zurich instrument HF2 lock-in amplifier was established for the measured resonance frequency and quality factor to track the resonance frequency with time. In all experiments in the current dissertation, resonance frequency tracked by PLL were found stable with time. For re-confirming the PLL stability, GC operation of each sample was started after several minutes (at least 10-15 mins) of PLL establishment.

To test the nanomechanical device as a real-time mass detector at the gas chromatography end, we used VOC samples containing only toluene and xylene with hexane as the solvent. Five samples differing in concentrations of analytes (toluene and xylene) were chosen and tabulated below.

For all samples, injection volume was $1 \mu\text{L}$ which was further reduced through splitter with a split ratio, 10 : 1. Thus one-tenth of the injected solution was mixed with the carrier gas to flow through the fused silica capillary tube towards the 50 : 50 splitter inside the oven. The 50 : 50 splitter slices the incoming gas equally, one-half flow to the FID detector and the other half flow to the NOMS chamber through 2 m long heated transfer line. Thus both halves traverse the same distance with the same

Table 7.1: Concentrations of VOC analytes in each samples.

Sample No.	Toluene (mg/mL) in Hexane	Xylene (mg/mL) in Hexane
1	3.89	3.91
2	6.58	7.05
3	8.32	7.8
4	9.99	10.76
5	13.16	13.01

velocity of $v_{cg} = 19 \text{ cms}^{-1}$. Hence the volume of mobile phase towards the FID and NOMS after the splitter is $0.05 \mu\text{L}$.

7.5 Results and discussion

Injection of toluene and xylene mixtures in hexane into the integrated GC-NOMS system provides simultaneous responses of FID detector and NOMS detector with the same sequence. Figure 7.4 shows a representative GC-NOMS response after injecting sample 1 (see table 7.1). Pyrolyzation process in FID results in eluted peaks with corresponding retention time. Phase locked NOMS detector detects the eluted peaks with the same retention time by showing a negative frequency shift which is a signature of nanomechanical mass loading. The other four samples with higher concentrations also showed similar responses with larger frequency shift according to concentrations. Results are not displayed in Figure 7.4 for simplicity. The response of the optical ring due to gas exposure for different samples separated with the same retention time are excluded from this discussion since it will not give us information on nanomechanical mass sensing. The detail on the optical ring response of this NOMS system has been discussed in our Nano letter paper [5].

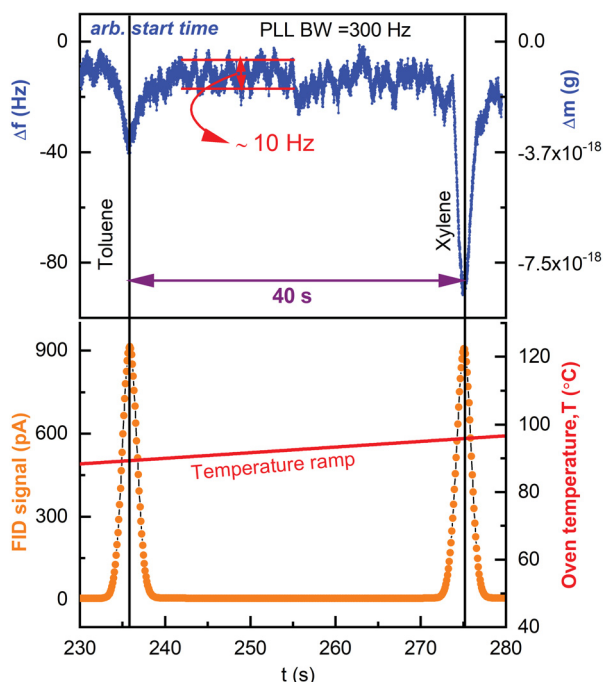


Figure 7.4: **An exemplary real-time ambient condition gas chromatogram from integrated GC-NOMS gas detector after injecting Sample 1 into the injection port of gas chromatography. Bottom)** The orange plot at the bottom shows FID detector peaks for toluene (left) and xylene (right) separated by GC column. The red line is the temperature ramp of the GC column. All three gases (toluene, xylene and the solvent hexane, which is not shown here) are separated according to their respective boiling points and result in their characteristic retention time of the GC conditions. For all samples, a linear relationship between the retention time and boiling point of individual components is consistent. **Top)** The response of nanomechanical DCB resonator's frequency in a phase locked condition for GC separated toluene and xylene. Gas adsorptions via native silicon oxides provoke an increase in device mass that results in a negative frequency shift which accounts the accreted mass by $\Delta m = 2M_{\text{eff}} \times \frac{\Delta f}{f_0}$. From the frequency shift, the loaded mass of toluene and xylene are in the right axis as $\approx 3 \times 10^{-18}$ and $\approx 8 \times 10^{-18}$ g respectively. Initial frequency drop to a minimum is characteristic of net gas adsorption on the bare silicon surface, and subsequent frequency increase up to the equilibrium (so-called zero level where there is no gas to adsorb) is featuring net desorption process. Larger shift by heavier xylene than toluene is attributed to its higher boiling point and surface chemistry. Same retention time difference of 40 s from both systems confirms that NOMS device is coupled with the GC as a real-time mass detector for GC separated gaseous analytes. A ~ 10 Hz frequency fluctuations within parallel red lines can be assumed to be the average drift in the gas sensing experiments which equivalent to the NEMS frequency resolution around $\sim 9 \times 10^{-7}$ and corresponding mass resolution (LOD) is $\sim 3 \times 10^{-18}$ g.

In our integrated GC-NOMS operations, two exit ports of the GC column are coupled to an FID and NOMS chamber for gas detection using a similar column of 2 m length from the 50:50 splitter. Hence identical retention time measured by both FID and NEMS is ascribed to the successful integration of the NOMS system to the gas chromatography.

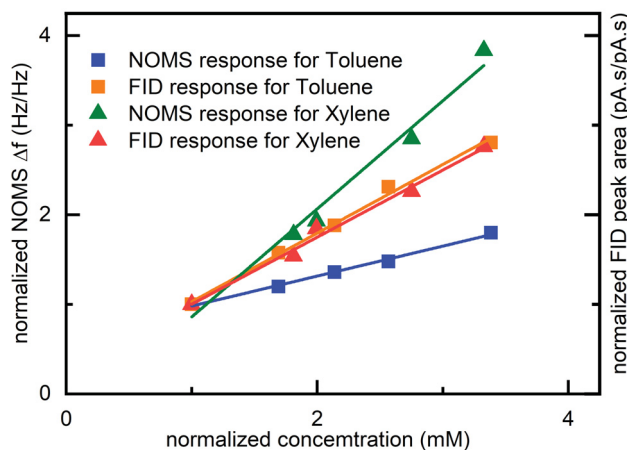


Figure 7.5: **Normalized response of FID and nanomechanical gas sensor in the integrated GC-NOMS system in ambient.** All data points, similar to Figure 7.4 for different samples are normalized by Sample 1 results. Normalized FID response has almost same slope both for toluene and xylene since the sensing mechanism for both VOC is same. On the other hand, NEMS responses to xylene is higher than toluene which is due to the underlying surface chemistry between gas phase the device surface. Higher slope of xylene indicates its better sticking affinity to the bare device surface. Native oxide on the surface mainly facilitates the sorption mechanisms which can be understood via kinetic theory of gases. However, linear response of both detector to gas concentration is a proof of NOMS compatibility with a commercial gas chromatography in developing future generation GC-NOMS instead of bench top GC-MS.

As in table 7.1, concentrations of both VOCs in the solvent are almost the same for each sample. The height of the FID peaks appears almost identical both for toluene and xylene and is consistent with the fact that an additional CH_3 in xylene is not taking part in ionization. The number of heavier xylene molecules flows past to the FID is assumed to be less ($\approx 13\%$) than toluene, but has a negligible effect in height as well as the peak areas (about 1%) calculated by Agilent GC software CHEMISTATION. By principle, FID response is proportional to the amount of column eluted compound passing through it. Usually, a GC analyst compared the measured peak area of the unknown compound to that of a standard solution measured previously. In the current work, we have used known compounds for GC analysis, and we expect a proportional increment of FID peak area with increasing concentrations of each species. The same

should be valid for the nanomechanical mass sensor in simultaneous measurements described here. Figure 7.5 compares performance between FID and nanomechanical resonators with concentrations of measured five samples. From the figure, it is evident that like FID the nanomechanical mass sensor response (resonance frequency shift due to gas loading) also grows linearly with concentration, but slopes are different.

Such discrepancy between FID and NOMS response to analytes is due to different gas detection principles of these two detectors. The normalized responses of FID and NEMS to GC separated VOCs distinguish gas detection mechanisms of these. The similar slope of FID is attributed to its same pyrolyzation principle for toluene and xylene. In contrast to FID, NEMS's response to xylene is steeper than toluene suggesting better sticking affinity of xylene to device surface governed by surface chemistry [45].

For practical realization of a nanomechanical gas sensor, it is essential to understand the surface chemistry of the device surface to landed gaseous molecules which require statistical interpretations [196] both for quantitative and qualitative point of views. Kinetic studies of the surface transport process of aromatic molecules explored that adsorption heat on SiO₂ increases by $\sim 20 \text{ kJ mol}^{-1}$ per $-\text{CH}_3$ group [197] with better sticking capability. Hence, a larger frequency shift by nanometric DCB resonator for xylene is not surprising; rather, it is due to the inherent surface properties of native oxide to aromatics with higher molar mass or boiling point. On the other hand, quantitatively limit of detection (LOD) of a nanomechanical resonator is another significant figure of merit to be addressed.

7.5.1 Limit of detection (LOD) of nanomechanical gas detector at the GC end

In this chapter, we demonstrated a novel gas sensor by integrating the NOMS chip with gas chromatography. It is of practical interest to check the LOD of the mechanical sensor in the integrated GC-NOMS. In section 2.2.6, we showed how a small mass loading alters the resonance frequency of any mechanical resonator, and the minimum detectable mass is merely the product of device effective mass (M_{eff}) and Allan deviation (σ_A). The minimum detectable mass is often referred to as mass resolution or mass sensitivity and expressed as

$$\delta m = 2M_{\text{eff}} \times \frac{\delta f}{f_0} = M_{\text{eff}} \times \sigma_A. \quad (7.2)$$

The mass resolution, δm can be minimized when the frequency noise, δf in equation 7.2 is thermomechanical noise limited. In this case, the LOD for mass sensing will be

$$LOD = 3 \times \delta m = 2M_{\text{eff}} \times 3\sigma_A. \quad (7.3)$$

For comparing measured LOD with that of vacuum, we recall open-loop Allan deviation presented in Figure 5.10 for 1 kHz bandwidth. From Figure 5.10, estimated frequency stability for 0.5 seconds averaging time are, $\sigma_{\text{vac}} \sim 2 \times 10^{-6}$ at 100 μTorr and $\sigma_{\text{atm}} \sim 4 \times 10^{-6}$ at 760 Torr (30 dBm drive power). For 36 dBm driving power (as in gas sensing experiments Figure 7.4) σ_{atm} can be assumed to have a 6 dB reduction than from Figure 5.10 i.e., $\sigma_{\text{atm}} \sim 2 \times 10^{-6}$. So expected ambient condition LOD for 1 KHz bandwidth has the similar value as in vacuum, and it is $\sim 2.3 \times 10^{-18}$ g. This is consistent with the noise level in Figure 7.4. Thus, despite a $300\times$ reduction in Q factor from vacuum to atmospheric pressure, we are able to achieve a vacuum like mass resolution. So, at atmospheric pressure and room temperature, the experimental LOD is $LOD = 3 \times \delta m = 2M_{\text{eff}} \times 3\sigma_A = 2 \times 5.9 \times 10^{-13} \text{ g} \times 9 \times 10^{-7} \simeq 3 \times 10^{-18} \text{ g}$. A conversion of the gas phase analytes from grams to ppm is shown in the co-authored journal [5].

Ambient condition gas sensing report in 2007 [28], used a cantilever of 100 fg effective mass. The resonance frequency and quality factor of the cantilever in air were 127 MHz and 400 respectively with 80 dB DR (they did not specify DR in vacuum, but vacuum of Q of the cantilever was only $2\times$ higher). According to Robins' approach the expected resolutions of that work was ~ 25 zg, but they got ~ 100 zg and detected ~ 1 ag. Compared to Ref. [28], ~ 3 ag LOD , in this dissertation (with order of magnitude larger mass device and order of magnitude smaller Q) is impressive for future gas sensing applications.

7.6 Conclusion

This chapter demonstrates that NOMS based gas sensor can be used at the gas chromatography end to precisely measure the mass of GC separated individual gas molecules in ambient condition. The nanomechanical mass sensor in the NOMS has a high vacuum mass resolutions (δm_R) close to 1 ag and thus an LOD of 3 ag. The ambient condition gas sensing experiments echo again that it is possible to attain a vacuum level mass sensitivity. Although experimental mass resolutions in ambient is not limited by short-term stability provided by the phase-locked loop, the integrated GC-NOMS achieved an experimental result of $\delta m_R \approx 1$ ag with a clearly defined LOD around 3 ag and agrees well with analytical interpretations. This important result

is a possible milestone in nanomechanical mass sensing and thus open an enormous possibility to design future generation GC-MS in ambient condition.

Chapter 8

Conclusions and Remarks

8.1 Summary

Dissipation studies [24, 198] on mechanical resonators established that enhanced damping with sub-micron devices is harmful for nanoscale sensing though it provides coupling of mechanical resonators to the surrounding environment. Such coupling, the presence of damping, in practice, enables the birth of mechanical sensors. Hence, it is fitting and fundamentally significant to use damping to achieve better mechanical sensor performance, which has been the approach of the current thesis. Any improvement of nanomechanical sensor performance at larger damping can significantly boost up their limited applications at atmospheric pressure and room temperature. Our group has a long-term goal to attain 1 Da (10^{-24} g) level nanomechanical sensitivity at atmospheric pressure so that NEMS can replace conventional MS from GC-MS system.

In quest of improved nanomechanical sensor performance at larger damping, we characterized a DCB resonator next to an optical ring resonator in the framework of Robins' theory. Robins' theory provides the frequency stability ($\sigma_A = 1/(4Q \times SNR)$) of NEMS in terms of damping (i.e., Q) and SNR (i.e., maximum linear DR) which at first glance implies that a mechanical resonator must have better frequency resolution (mass sensitivity) for higher Q compared to a lower Q device. Rather than considering high Q devices, this thesis has particularly focused on the interplay of Q and SNR of a device at different damping conditions, which was missing in NEMS research before the current dissertation.

Taking advantages of optomechanics, we showed that TM noise of the DCB were resolved from vacuum to atmosphere with proportion to loaded $Q^{+1/2}$ and forms the bottom end of the DR at each pressure. Within Duffing limited pressure regime, the top end of the DR enhances with $Q^{-1/2}$ that results in SNR improvement with proportion to damping, i.e., Q^{-1} . Thus, SNR was found to negate poorer Q effect on

frequency stability, which was experimentally verified in this thesis. Such success of reaching vacuum level mechanical sensor performance at larger damping is significant for using nanomechanical sensors in ambient conditions such as for gas sensing. In addition, experimental results showed that stability even can be better at atmospheric pressure than in vacuum.

To unveil the mystery of improved stability at larger damping, it is essential to sketch a comprehensive picture of Robins' phase noise in experiments. We have prudently reviewed this both for open loop and phase locked loop experiments. We have revealed the role of phase noise, and frequency noise spectral density stems from thermomechanical noise in a mechanical resonator. For a single Duffing oscillator, a DCB in the present case, experimental phase noise agrees with theory and, improves with damping, but that does not mean improved frequency noise at more substantial damping and better frequency resolution at low- Q operations. Devices intrinsic ring down time multiplies improved phase noise with damping to validate Robins' picture both in open and closed loop analysis. This finding was reflected in experiments by attaining similar Allan deviation at different Q operated at the maximum linear dynamic range.

We have thoroughly examined PLL transfer functions through experimental parameters from experiments at different Q to explore how PLL gain (bandwidth) can artificially reduce frequency noise to suggest better stability than predicted by Robins' formula. Understanding how PLL architectures can shape noise, particularly when advisor functions do not always accurately predict the transfer function shape, is fundamentally important for deploying NEMS in sensing by the widely accepted phase-locked loop method. Despite the artifact, the PLL was found to precisely track for slow (longer τ) changes, verified by measuring frequency shift due to known temperature change and modeling and measuring tracking speed.

Open loop measurements of the frequency noise imply presence of excess noise at high- Q , which was attributed to high- Q being more susceptible to frequency flicker fluctuation. With decreasing Q excess noise progressively weakened to demonstrate pure thermal noise limited characteristics at atmospheric pressure. The end result was, not only was stability conserved with more damping; there was a slight improvement in stability with damping as flicker noise was suppressed.

Although thermal limited mechanical sensor performance must be similar in Robins' picture with air damping, damping induces an additional pathway through thermal stabilization of the device to suppress excess noise at atmospheric pressure. This observation is a forerunner in NEMS domain to improve mechanical sensor performance through larger damping.

To see improved resolutions with damping, we have taken advantage of the inherent thermometry of a NOMS system by temperature sensing. NOMS thermometry not only has proved that measured temperature resolution is better at larger damping but also demystifies a fundamental issue in nanoscale thermometry called nanoscale heat transfer. This helped confirm that the air conduction provided the mitigation path for reducing the effect of frequency fluctuation noise in air. Adopted analytical model and simulations are also fundamentally important for future nanomechanical thermometry, which is another potential application of the nanomechanical resonator. Results from thermometry can be a significant step for remote temperature sensing by NOMS rather than any other thermometry. It can be a vital tool where a nanoscale thermometer is required, such as cancer study or chemical reactions. Also, phase-locked temperature sensing experiments agreements with the simulated PLL time constant removes the ambiguity on PLL operations at atmospheric pressure. With full confidence on (slow) PLL tracking, we have moved to design integrated GC-NOMS gas sensor in ambient.

Designing an integrated GC-NOMS system is not only the experimental goal of the current thesis but also it aims to achieve a vacuum level mass resolution at atmospheric pressure and room temperature. We showed the design and operation of the first GC-NOMS apparatus where the advantage is taken of optomechanical readout of the NEMS device. Further, we found that the mass resolution at atmospheric pressure was comparable to that in vacuum. To the best of our knowledge, the demonstration of a high vacuum level measured mass resolution in the atmosphere by a single NEMS is the first demonstration of this kind. Attogram ($1 \text{ ag} = 1 \cdot 10^{-18} \text{ g} = 6 \text{ MDa}$, and $1 \text{ Da} = 1 \cdot 10^{-24} \text{ g}$) level mass resolutions attained in ambient, combined with knowledge of $Q \times SNR$ conservation and flicker noise mitigation, light the path forward toward ultimate limit mass sensitivity at atmospheric pressure. This vision sees unique potentials to replace conventional mass spectrometer (MS) and GC-MS with GC-NOMS.

8.2 Original contributions of this thesis

The contributions of this thesis are not only important for applications but also for fundamental aspects. The DR concept was well known to M/NEMS researchers but was not demonstrated experimentally at different damping conditions as per existing literature. This thesis articulates that intrinsic SNR negates Q (and its repercussions for damping independent frequency stability) with sufficient experimental evidence. Frequency shift measurements of mechanical resonator due to known temperature change confirm these findings. Experimental evidence of better stability with higher

damping through the thermal channel by air molecules (which also induce nanoscale heat transfer) can open new horizons in NEMS applications at atmospheric pressure, at the same time it provides another insight on frequency fluctuation noise source in nanomechanical resonators.

Experimental study of nanoscale heat transfer is found more accessible by developed NOMS thermometry by recording temperature difference between optical and nanomechanical thermometers in the nano-optomechanical system (NOMS). Such observations on enhanced heat transfer at nanoscale by a single device are unprecedented.

Vacuum level mass resolution in ambient by bare silicon device of the integrated GC-NOMS is a consequence of the theorized DR concept. The integration and demonstration of GC-NOMS is a stepping-stone to develop GC-NOMS-MS in ambient condition for GC-MS purposes. In addition to gas sensing experiments, estimation of ambient humidity from TM noise spectra measurements asserts NOMS (used in this thesis) as a humidity detector. Quantification of adsorbed gas molecules via native oxide on silicon made NEMS opens the possibility of universal chemical sensors.

Finally, our review works on the theory of frequency stability also cleaned up confusions in NEMS community about phase noise to frequency noise conversion of mechanical resonators. Detailed analysis of PLL transfer functions on noise shaping with low gain to explain how noise suppression can happen in our data can be a useful reference for phase-locked operations of NEMS.

8.3 Conclusions

In this thesis, we have characterized a doubly clamped beam resonator coupled to an optical cavity. Nanomechanical characterizations by changing room temperature air pressure from high vacuum to atmosphere show that a linear resonator operated at its intrinsic dynamic range can mitigate poorer Q issue on device sensitivity. Also, the presence of air molecules improves the thermal stabilization of the device to attain frequency stability down to the thermal limit for a wide range of averaging time. Frequency resolutions at larger damping (low- Q) condition is found better than high vacuum (high- Q condition) because improved thermal stability at higher pressures reduces omnipresent frequency-fluctuation noise in resonance. Such improved frequency stability in ambient has a tremendous effect on NEMS application. We have shown applications with temperature sensing, developed thermometry for measuring temperature accurately by a nanomechanical resonator, and established the utility of NOMS thermometry in applications. For taking advantage of unprecedented nanomechanical mass sensitivity, we designed an integrated GC-NOMS as a proof

of concept for future generation GC-MS. An ag level mass resolution was attained in ambient condition gas sensing, which is equivalent to high-vacuum level mass resolution of the device; this is a significant step for utilizing NEMS sensor in ambient mass sensing experiments. Indeed, this thesis has solved the years-long problem with NEMS sensors for deploying them in the atmosphere.

Bibliography

- [1] H. Baltes, O. Brand, G. K. Fedder, C. Hierold, J. G. Korvink, and O. Tabata. *CMOS-MEMS: Advanced Micro and Nanosystems*. John Wiley & Sons, 2008.
- [2] N. Yazdi, F. Ayazi, and K. Najafi. Micromachined inertial sensors. *Proceedings of the IEEE*, 86(8):1640–1659, 1998.
- [3] J. Chaste, A. Eichler, J. Moser, G. Ceballos, R. Rurali, and A. Bachtold. A nanomechanical mass sensor with yoctogram resolution. *Nature Nanotechnology*, 7(5):301, 2012.
- [4] W. K. Hiebert. Mass sensing: Devices reach single-proton limit. *Nature Nanotechnology*, (5):278–280, 2012.
- [5] A. Venkatasubramanian, V. T. K. Sauer, S. K. Roy, M. Xia, D. S. Wishart, and W. K. Hiebert. Nano-Optomechanical Systems for Gas Chromatography. *Nano Letters*, 16(11):6975–6981, 2016.
- [6] I. Bargatin, E. B. Myers, J. S. Aldridge, C. Marcoux, P. Brianceau, L. Duraffourg, E. Colinet, S. Hentz, P. Andreucci, and M. L. Roukes. Large-scale integration of nanoelectromechanical systems for gas sensing applications. *Nano Letters*, 12(3):1269–1274, 2012.
- [7] M. S. Hanay, S. I. Kelber, C. D. O’Connell, P. Mulvaney, J. E. Sader, and M. L. Roukes. Inertial imaging with nanomechanical systems. *Nature Nanotechnology*, 10(4):339, 2015.
- [8] E. Sage, A. Brenac, T. Alava, R. Morel, C. Dupré, M. S. Hanay, L. Duraffourg, C. Masselon, and S. Hentz. Neutral particle mass spectrometry with nanomechanical systems. *Nature Communications*, 6:6482, 2015.
- [9] A. K. Naik, M. S. Hanay, W. K. Hiebert, X. L. Feng, and M. L. Roukes. Towards single-molecule nanomechanical mass spectrometry. *Nature Nanotechnology*, 4(7):445, 2009.
- [10] C. L. Degen, M. Poggio, H. J. Mamin, C. T. Rettner, and D. Rugar. Nanoscale magnetic resonance imaging. *Proceedings of the National Academy of Sciences*, 106(5):1313–1317, 2009.
- [11] J. E. Losby, F. Fani Sani, D. T. Grandmont, Z. Diao, M. Belov, J. A. J. Burgess, S. R. Compton, W. K. Hiebert, D. Vick, K. Mohammad, E. Salimi, G. E. Bridges, D. J. Thomson, and M. R. Freeman. Torque-mixing magnetic resonance spectroscopy. *Science*, 350(6262):798–801, 2015.

- [12] J. D. Teufel, T. Donner, D. Li, J. W. Harlow, M. S. Allman, K. Cicak, A. J. Sirois, J. D. Whittaker, K. W. Lehnert, and R. W. Simmonds. Sideband cooling of micromechanical motion to the quantum ground state. *Nature*, 475(7356):359–363, 2011.
- [13] J. Chan, T. P. M. Alegre, A. H. Safavi-Naeini, J. T. Hill, A. Krause, S. Gröblacher, M. Aspelmeyer, and O. Painter. Laser cooling of a nanomechanical oscillator into its quantum ground state. *Nature*, 478:89–92, 2011.
- [14] A. D. O’Connell, M. Hofheinz, M. Ansmann, R. C. Bialczak, M. Lenander, E. Lucero, M. Neeley, D. Sank, H. Wang, M. Weides, J. Wenner, J. M. Martinis, and A. N. Cleland. Quantum ground state and single-phonon control of a mechanical resonator. *Nature*, 464(7289):697, 2010.
- [15] T. P. Purdy, K. E. Grutter, K. Srinivasan, and J. M. Taylor. Quantum correlations from a room-temperature optomechanical cavity. *Science*, 356(6344):1265–1268, 2017.
- [16] S. K. Roy, V. T. K. Sauer, J. N. Westwood-Bachman, A. Venkatasubramanian, and W. K. Hiebert. Improving mechanical sensor performance through larger damping. *Science*, 360(6394):eaar5220, 2018.
- [17] D. W. Allan. Statistics of atomic frequency standards. *Proceedings of the IEEE*, 54(2):221–230, 1966.
- [18] W. P. Robins. *Phase noise in signal sources: theory and applications*, volume 9. IET, 1984.
- [19] T. R. Albrecht, P. Grütter, D. Horne, and D. Rugar. Frequency modulation detection using high-Q cantilevers for enhanced force microscope sensitivity. *Journal of Applied Physics*, 69(2):668–673, 1991.
- [20] A. N. Cleland and M. L. Roukes. Noise processes in nanomechanical resonators. *Journal of Applied Physics*, 92(5):2758–2769, 2002.
- [21] K. L. Ekinci, Y. T. Yang, and M. L. Roukes. Ultimate limits to inertial mass sensing based upon nanoelectromechanical systems. *Journal of Applied Physics*, 95(5):2682–2689, 2004.
- [22] M. Sansa, E. Sage, E. C. Bullard, M. Gély, T. Alava, E. Colinet, A. K. Naik, L. G. Villanueva, L. Duraffourg, M. L. Roukes, G. Jourdan, and S. Hentz. Frequency fluctuations in silicon nanoresonators. *Nature Nanotechnology*, 11(6):552–558, 2016.
- [23] Y. Tsaturyan, A. Barg, E. S. Polzik, and A. Schliesser. Ultracoherent nanomechanical resonators via soft clamping and dissipation dilution. *Nature Nanotechnology*, 12(8):776, 2017.
- [24] J. Moser, A. Eichler, J. Güttinger, M. I. Dykman, and A. Bachtold. Nanotube mechanical resonators with quality factors of up to 5 million. *Nature Nanotechnology*, 9(12):1007, 2014.
- [25] K. Y. Fong, W. H. P. Pernice, and H. X. Tang. Frequency and phase noise of ultrahigh Q silicon nitride nanomechanical resonators. *Physical Review B - Condensed Matter and Materials Physics*, 85(16):161410, 2012.

- [26] K. L. Ekinici, X. M. H. Huang, and M. L. Roukes. Ultrasensitive nanoelectromechanical mass detection. *Applied Physics Letters*, 84(22):4469–4471, 2004.
- [27] Y. T. Yang, C. Callegari, X. L. Feng, K. L. Ekinici, and M. L. Roukes. Zeptogram-scale nanomechanical mass sensing. *Nano Letters*, 6(4):583–586, 2006.
- [28] M. Li, H. X. Tang, and M. L. Roukes. Ultra-sensitive nems-based cantilevers for sensing, scanned probe and very high-frequency applications. *Nature Nanotechnology*, 2(2):114–120, 2007.
- [29] X. L. Feng, C. J. White, A. Hajimiri, and M. L. Roukes. A self-sustaining ultrahigh-frequency nanoelectromechanical oscillator. *Nature Nanotechnology*, 3(6):342, 2008.
- [30] K. Jensen, K. Kim, and A. Zettl. An atomic-resolution nanomechanical mass sensor. *Nature Nanotechnology*, 3(9):533, 2008.
- [31] S. Olcum, N. Cermak, S. C. Wasserman, and S. R. Manalis. High-speed multiple-mode mass-sensing resolves dynamic nanoscale mass distributions. *Nature Communications*, 6(May):7070, 2015.
- [32] E. Sage, M. Sansa, S. Fostner, M. Defoort, M. Gély, A. K. Naik, R. Morel, L. Durruffourg, M. L. Roukes, T. Alava, G. Jourdan, E. Colinet, C. Masselon, A. Brenac, and S. Hentz. Single-particle mass spectrometry with arrays of frequency-addressed nanomechanical resonators. *Nature Communications*, 9(1):3283, 2018.
- [33] S. Dominguez-Medina, S. Fostner, M. Defoort, M. Sansa, A. K. Stark, M. A. Halim, E. Vernhes, M. Gely, G. Jourdan, T. Alava, P. Boulanger, C. Masselon, and S. Hentz. Neutral mass spectrometry of virus capsids above 100 megadaltons with nanomechanical resonators. *Science*, 362(6417):918–922, 2018.
- [34] G. Muralidharan, A. Wig, L. A. Pinnaduwege, D. Hedden, T. Thundat, and R. T. Lareau. Adsorption–desorption characteristics of explosive vapors investigated with microcantilevers. *Ultramicroscopy*, 97(1):433–439, 2003.
- [35] L. A. Pinnaduwege, T. Thundat, A. Gehl, S. D. Wilson, D. L. Hedden, and R. T. Lareau. Desorption characteristics of uncoated silicon microcantilever surfaces for explosive and common nonexplosive vapors. *Ultramicroscopy*, 100(3):211–216, 2004.
- [36] T. Thundat, G. Y. Chen, R. J. Warmack, D. P. Allison, and E. A. Wachter. Vapor detection using resonating microcantilevers. *Analytical Chemistry*, 67(3):519–521, 1995.
- [37] D. W. Chun, K. S. Hwang, K. Eom, J. H. Lee, B. H. Cha, Woo Y. Lee, D. S. Yoon, and T. S. Kim. Detection of the Au thin-layer in the Hz per picogram regime based on the microcantilevers. *Sensors and Actuators A: Physical*, 135(2):857–862, 2007.
- [38] L. A. Pinnaduwege, A. Gehl, D. L. Hedden, G. Muralidharan, T. Thundat, R. T. Lareau, T. Sulchek, L. Manning, B. Rogers, M. Jones, and J. D. Adams. Explosives: A microsensor for trinitrotoluene vapour. *Nature*, 425(6957):474, 2003.
- [39] F. L. Dorman, J. J. Whiting, J. W. Cochran, and J. Gardea-Torresdey. Gas chromatography. *Analytical Chemistry*, 82(12):4775–4785, 2010.

- [40] C. J. Lu, W. H. Steinecker, W. C. Tian, M. C. Oborny, J. M. Nichols, M. Agah, J. A. Potkay, H. K. L. Chan, J. Driscoll, R. D. Sacks, K. D. Wise, S. W. Pang, and E. T. Zellers. First-generation hybrid mems gas chromatograph. *Lab on a Chip*, 5(10):1123–1131, 2005.
- [41] I. Azzouz, F. Marty, and T. Bourouina. Recent advances in micro-gas chromatography—the opportunities and the challenges. In *2017 Symposium on Design, Test, Integration and Packaging of MEMS/MOEMS (DTIP)*, pages 1–5. IEEE, 2017.
- [42] J. A. Contreras, J. A. Murray, S. E. Tolley, J. L. Oliphant, H. D. Tolley, S. A. Lammert, E. D. Lee, D. W. Later, and M. L. Lee. Hand-portable gas chromatograph-toroidal ion trap mass spectrometer (GC-TMS) for detection of hazardous compounds. *Journal of the American Society for Mass Spectrometry*, 19(10):1425–1434, 2008.
- [43] M. Li, E. B. Myers, H. X. Tang, S. J. Aldridge, H. C. McCaig, J. J. Whiting, R. J. Simonson, N. S. Lewis, and M. L. Roukes. Nanoelectromechanical resonator arrays for ultrafast, gas-phase chromatographic chemical analysis. *Nano Letters*, 10(10):3899–3903, 2010.
- [44] J. Arcamone, A. Niel, V. Gouttenoire, M. Petitjean, N. David, R. Barattin, M. Matheron, F. Ricoul, T. Bordy, H. Blanc, J. Ruellan, D. Mercier, N. Pereira-Rodrigues, G. Costa, V. Agache, S. Hentz, JC Gabriel, F. Baleras, C. Marcoux, T. Ernst, L. Duraffourg, E. Colinet, E. B. Myers, M. L. Roukes, P. Andreucci, E. Ollier, and P. Puget. VLSI silicon multi-gas analyzer coupling gas chromatography and NEMS detectors. pages 29–3. IEEE, 2006.
- [45] S. Tlili, and Gligorovski S. Alvarez, E. G., and H. Wortham. Adsorption behavior of two model airborne organic contaminants on wafer surfaces. *Chemical Engineering Journal*, 187:239–247, 2012.
- [46] S. J. Reitmeier, R. R. Mukti, A. Jentys, and J. A. Lercher. Surface transport processes and sticking probability of aromatic molecules in hzsm-5. *The Journal of Physical Chemistry C*, 112(7):2538–2544, 2008.
- [47] T. Kouh, M. S. Hanay, and K. L. Ekinici. Nanomechanical motion transducers for miniaturized mechanical systems. *Micromachines*, 8(4):108, 2017.
- [48] Z. Diao, J. E. Losby, V. T. K. Sauer, J. N. Westwood, M. R. Freeman, and W. K. Hiebert. Confocal scanner for highly sensitive photonic transduction of nanomechanical resonators. *Applied Physics Express*, 6(6):065202, 2013.
- [49] V. T. K. Sauer, Z. Diao, M. R. Freeman, and W. K. Hiebert. Nanophotonic detection of side-coupled nanomechanical cantilevers. *Applied Physics Letters*, 100(26):261102, 2012.
- [50] V. T. K. Sauer, Z. Diao, M. R. Freeman, and W. K. Hiebert. Optical race-track resonator transduction of nanomechanical cantilevers. *Nanotechnology*, 25(5):055202, 2014.
- [51] V. T. K. Sauer, Z. Diao, M. R. Freeman, and W. K. Hiebert. Wavelength-division multiplexing of nano-optomechanical doubly clamped beam systems. *Optics Letters*, 40(9):1948–1951, 2015.

- [52] J. N. Westwood-Bachman, Z. Diao, V. T. K. Sauer, D. Bachman, and W. K. Hiebert. Even nanomechanical modes transduced by integrated photonics. *Applied Physics Letters*, 108(6):061103, 2016.
- [53] V. T. K. Sauer, Z. Diao, J. N. Westwood-Bachman, M. R. Freeman, and W. K. Hiebert. Single laser modulated drive and detection of a nano-optomechanical cantilever. *AIP Advances*, 7:015115, 2017.
- [54] Z. Diao, V. T. K. Sauer, and W. K. Hiebert. Integrated on-chip nano-optomechanical systems. In *Scaling And Integration Of High-speed Electronics And Optomechanical Systems*, pages 119–140. World Scientific, 2017.
- [55] W. K. Hiebert, S. K. Roy, and V. T. K. Sauer. Poorer Q gives better mass sensitivity: reconsidering dynamic range in optomechanically transduced nems devices. In *2014 Solid-State Sensors, Actuators and Microsystems Workshop, Hilton Head Island, South Carolina*, pages 423–426, June 2014.
- [56] Z. Wang and P. X. L. Feng. Dynamic range of atomically thin vibrating nanomechanical resonators. *Applied Physics Letters*, 104(10):103109, 2014.
- [57] P. Taheri-Tehrani, M. Defoort, and D. A. Horsley. Operation of a high quality-factor gyroscope in electromechanical nonlinearities regime. *Journal of Micromechanics and Microengineering*, 27(7):075015, 2017.
- [58] J. Bernstein, R. Miller, W. Kelley, and P. Ward. Low-noise mems vibration sensor for geophysical applications. *Journal of Microelectromechanical Systems*, 8(4):433–438, 1999.
- [59] R. K. Karlquist, L. S. Cutler, E. M. Ingman, J. L. Johnson, and T. Parisek. A low-profile high-performance crystal oscillator for timekeeping applications. In *Proceedings of International Frequency Control Symposium*, pages 873–884. IEEE, 1997.
- [60] F. R. Blom, S. Bouwstra, M. Elwenspoek, and J. H. J. Fluitman. Dependence of the quality factor of micromachined silicon beam resonators on pressure and geometry. *Journal of Vacuum Science and Technology B: Microelectronics and Nanometer Structures Processing, Measurement, and Phenomena*, 10(1):19–26, 1992.
- [61] O. Svitelskiy, V. Sauer, N. Liu, K. M. Cheng, E. Finley, M. R. Freeman, and W. K. Hiebert. Pressurized fluid damping of nanoelectromechanical systems. *Physical Review Letters*, 103(24):244501, 2009.
- [62] A. K. Pandey, R. Pratap, and F. S. Chau. Effect of pressure on fluid damping in mems torsional resonators with flow ranging from continuum to molecular regime. *Experimental Mechanics*, 48(1):91–106, 2008.
- [63] J. F. Vignola, J. A. Judge, J. Jarzynski, M. Zalalutdinov, B. H. Houston, and J. W. Baldwin. Effect of viscous loss on mechanical resonators designed for mass detection. *Applied Physics Letters*, 88(4):041921, 2006.
- [64] D. M. Karabacak, V. Yakhot, and K. L. Ekinici. High-frequency nanofluidics: An experimental study using nanomechanical resonators. *Physical Review Letters*, 98(25):254505, 2007.

- [65] K. B. Gavan, J. Van Der Heijden, E. W. J. M. Van Der Drift, and H. S. J. Van Der Zant. Effect of pressure on the q factor and the resonance frequency of sin microcantilevers. In *Nano/Micro Engineered and Molecular Systems, 2009. NEMS 2009. 4th IEEE International Conference on*, pages 380–384. IEEE, 2009.
- [66] D. B. Asay and S. H. Kim. Evolution of the adsorbed water layer structure on silicon oxide at room temperature. *The Journal of Physical Chemistry B*, 109(35):16760–16763, 2005.
- [67] X. Wang, M. Zhao, and D. D. Nolte. Ambient molecular water accumulation on silica surfaces detected by a reflectance interference optical balance. *Applied Physics Letters*, 97(18):183702, 2010.
- [68] Y. Xu, J. T. Lin, B. W. Alphenaar, and R. S. Keynton. Viscous damping of microresonators for gas composition analysis. *Applied Physics Letters*, 88(14):143513, 2006.
- [69] T. Thundat, R. J. Warmack, G. Y. Chen, and D. P. Allison. Thermal and ambient-induced deflections of scanning force microscope cantilevers. *Applied Physics Letters*, 64(21):2894–2896, 1994.
- [70] J. Verd, M. Sansa, A. Uranga, F. Perez-Murano, J. Segura, and N. Barniol. Metal microelectromechanical oscillator exhibiting ultra-high water vapor resolution. *Lab on a Chip*, 11(16):2670–2672, 2011.
- [71] D. M. Karabacak, S. H. Brongersma, and M. Crego-Calama. Enhanced sensitivity volatile detection with low power integrated micromechanical resonators. *Lab on a Chip*, 10(15):1976–1982, 2010.
- [72] M. W. Pruessner, T. H. Stievater, M. S. Ferraro, W. S. Rabinovich, J. L. Stepnowski, and R. A. McGill. Waveguide micro-opto-electro-mechanical resonant chemical sensors. *Lab on a chip*, 10(6):762–768, 2010.
- [73] S. Schmid, S. Kühne, and C. Hierold. Influence of air humidity on polymeric microresonators. *Journal of Micromechanics and Microengineering*, 19(6):065018, 2009.
- [74] O. Boytsova, A. Klimenko, V. Lebedev, A. Lukashin, and A. Eliseev. Nanomechanical humidity detection through porous alumina cantilevers. *Beilstein Journal of Nanotechnology*, 6:1332, 2015.
- [75] H. Sadeghian, C. K. Yang, K. B. Gavan, H. Goosen, E. van der Drift, H. van der Zant, P. J. French, A. Bossche, and F. van Keulen. Surface contamination-induced resonance frequency shift of cantilevers. In *2009 4th IEEE International Conference on Nano/Micro Engineered and Molecular Systems*, pages 400–403. IEEE, 2009.
- [76] K. D. Sattler. *Handbook of nanophysics: clusters and fullerenes*. CRC press, 2010.
- [77] K. L. Ekinici. Electromechanical transducers at the nanoscale: actuation and sensing of motion in nanoelectromechanical systems (nems). *Small*, 1(8-9):786–797, 2005.
- [78] P. A. Truitt, J. B. Hertzberg, C. C. Huang, K. L. Ekinici, and K. C. Schwab. Efficient and sensitive capacitive readout of nanomechanical resonator arrays. *Nano Letters*, 7(1):120–126, 2007.

- [79] J. Sulkko, M. A. Sillanpaa, P. Hakkinen, L. Lechner, M. Helle, A. Fefferman, J. Parpia, and P. J. Hakonen. Strong gate coupling of high-q nanomechanical resonators. *Nano Letters*, 10(12):4884–4889, 2010.
- [80] J. R. Montague, K. A. Bertness, N. A. Sanford, V. M. Bright, and C. T. Rogers. Temperature-dependent mechanical-resonance frequencies and damping in ensembles of gallium nitride nanowires. *Applied Physics Letters*, 101(17):173101, 2012.
- [81] R.G. Beck, M. A. Eriksson, R. M. Westervelt, K. L. Campman, and A.C. Gossard. Strain-sensing cryogenic field-effect transistor for integrated strain detection in GaAs/AlGaAs microelectromechanical systems. *Applied Physics Letters*, 68(26):3763–3765, 1996.
- [82] R. B. Karabalin, M. H. Matheny, X. L. Feng, E. Defay, G. Le Rhun, C. Marcoux, S. Hentz, P. Andreucci, and M. L. Roukes. Piezoelectric nanoelectromechanical resonators based on aluminum nitride thin films. *Applied Physics Letters*, 95(10):103111, 2009.
- [83] H. Rongrui, X. L. Feng, M. L. Roukes, and Y. Peidong. Self-transducing silicon nanowire electromechanical systems at room temperature. *Nano Letters*, 8(6):1756–1761, 2008.
- [84] A. Koumela, S. Hentz, D. Mercier, C. Dupré, E. Ollier, P. X. L. Feng, S. T. Purcell, and L. Duraffourg. High frequency top-down junction-less silicon nanowire resonators. *Nanotechnology*, 24(43):435203, 2013.
- [85] I. Bargatin, I. Kozinsky, and M. L. Roukes. Efficient electrothermal actuation of multiple modes of high-frequency nanoelectromechanical resonators. *Applied Physics Letters*, 90(9):093116, 2007.
- [86] B. Ilic, S. Krylov, K. Aubin, R. Reichenbach, and H. G. Craighead. Optical excitation of nanoelectromechanical oscillators. *Applied Physics Letters*, 86(19):193114, 2005.
- [87] W. K. Hiebert, D. Vick, V. Sauer, and M. R. Freeman. Optical interferometric displacement calibration and thermomechanical noise detection in bulk focused ion beam-fabricated nanoelectromechanical systems. *Journal of Micromechanics and Microengineering*, 20(11):115038, 2010.
- [88] A. Sampathkumar, K. L. Ekinici, and T. W. Murray. Multiplexed optical operation of distributed nanoelectromechanical systems arrays. *Nano Letters*, 11(3):1014–1019, 2011.
- [89] I. D. Vlaminc, J. Roels, D. Taillaert, D. Van Thourhout, R. Baets, L. Lagae, and G. Borghs. Detection of nanomechanical motion by evanescent light wave coupling. *Applied Physics Letters*, 90(23):233116, 2007.
- [90] G. Anetsberger, O. Arcizet, E. Gavartin, Q. P. Unterreithmeier, E. M. Weig, J. P. Kotthaus, and T. J. Kippenberg. Near-field cavity optomechanics with nanomechanical oscillators. In *Quantum Electronics and Laser Science Conference*, page JMB2. Optical Society of America, 2010.
- [91] M. Li, W. H. P. Pernice, and H. X. Tang. Reactive cavity optical force on microdisk-coupled nanomechanical beam waveguides. *Physical Review Letters*, 103(22):223901, 2009.

- [92] W. H. P. Pernice, C. Xiong, C. Schuck, and H. X. Tang. High-Q aluminum nitride photonic crystal nanobeam cavities. *Applied Physics Letters*, 100(9):091105, 2012.
- [93] M. Aspelmeyer, T. J. Kippenberg, and F. Marquardt. Cavity optomechanics. *Reviews of Modern Physics*, 86(4):1391, 2014.
- [94] T. Kouh, D. Karabacak, D. H. Kim, and K. L. Ekinci. Diffraction effects in optical interferometric displacement detection in nanoelectromechanical systems. *Applied Physics Letters*, 86(1):013106, 2005.
- [95] D. Karabacak, T. Kouh, and K. L. Ekinci. Analysis of optical interferometric displacement detection in nanoelectromechanical systems. *Journal of Applied Physics*, 98(12):124309, 2005.
- [96] K. L. Ekinci and M. L. Roukes. Nanoelectromechanical systems. *Review of Scientific Instruments*, 76(6):061101, 2005.
- [97] M. Li, W. H. P. Pernice, C. Xiong, T. Baehr-Jones, M. Hochberg, and H. X. Tang. Harnessing optical forces in integrated photonic circuits. *Nature*, 456(7221):480, 2008.
- [98] G. Anetsberger, O. Arcizet, Q. P. Unterreithmeier, R. Rivière, A. Schliesser, E. M. Weig, J. P. Kotthaus, and T. J. Kippenberg. Near-field cavity optomechanics with nanomechanical oscillators. *Nature Physics*, 5(12):909, 2009.
- [99] B. Willke, P. Aufmuth, C. Aulbert, S. Babak, R. Balasubramanian, B. W. Barr, S. Berukoff, S. Bose, G. Cagnoli, M. M. Casey, et al. The geo 600 gravitational wave detector. *Classical and Quantum Gravity*, 19(7):1377, 2002.
- [100] B. P. Abbott, R. Abbott, F. Acernese, R. Adhikari, P. Ajith, B. Allen, G. Allen, M. Alshourbagy, R. S. Amin, S. B. Anderson, et al. An upper limit on the stochastic gravitational-wave background of cosmological origin. *Nature*, 460(7258):990, 2009.
- [101] D. Kleckner and D. Bouwmeester. Sub-kelvin optical cooling of a micromechanical resonator. *Nature*, 444(7115):75, 2006.
- [102] S. Gröblacher, J. B. Hertzberg, M. R. Vanner, G. D. Cole, S. Gigan, K. C. Schwab, and M. Aspelmeyer. Demonstration of an ultracold micro-optomechanical oscillator in a cryogenic cavity. *Nature Physics*, 5(7):485, 2009.
- [103] O. Arcizet, P. F. Cohadon, T. Briant, M. Pinard, A. Heidmann, J. M. Mackowski, C. Michel, L. Pinard, O. François, and L. Rousseau. High-sensitivity optical monitoring of a micromechanical resonator with a quantum-limited optomechanical sensor. *Physical Review Letters*, 97(13):133601, 2006.
- [104] O. Arcizet, P. F. Cohadon, T. Briant, M. Pinard, and A. Heidmann. Radiation-pressure cooling and optomechanical instability of a micromirror. *Nature*, 444(7115):71, 2006.
- [105] E. Verhagen, S. Deléglise, S. Weis, A. Schliesser, and T. J. Kippenberg. Quantum-coherent coupling of a mechanical oscillator to an optical cavity mode. *Nature*, 482(7383):63, 2012.

- [106] Y. S. Park and H. Wang. Resolved-sideband and cryogenic cooling of an optomechanical resonator. *Nature Physics*, 5(7):489, 2009.
- [107] M. Eichenfield, R. Camacho, J. Chan, K. J. Vahala, and O. Painter. A picogram- and nanometre-scale photonic-crystal optomechanical cavity. *Nature*, 459(7246):550–5, may 2009.
- [108] C. A. Regal, J. D. Teufel, and K. W. Lehnert. Measuring nanomechanical motion with a microwave cavity interferometer. *Nature Physics*, 4(7):555, 2008.
- [109] V. T. K. Sauer. *Nanophotonic detection of nanomechanical structures for use toward mass sensing applications*. PhD thesis, University of Alberta (Canada), 2014.
- [110] J. S. Bunch, A. M. Van Der Zande, S. S. Verbridge, I. W. Frank, D. M. Tanenbaum, J. M. Parpia, H. G. Craighead, and P. L. McEuen. Electromechanical resonators from graphene sheets. *Science*, 315(5811):490–493, 2007.
- [111] M. Li, W. H. P. Pernice, C. Xiong, T. Baehr-Jones, M. Hochberg, and H. X. Tang. Harnessing optical forces in integrated photonic circuits. *Nature*, 456(7221):480–484, 2008.
- [112] B. D. Hauer, C. Doolin, K. S. D. Beach, and J. P. Davis. A general procedure for thermomechanical calibration of nano/micro-mechanical resonators. *Annals of Physics*, 339:181–207, 2013.
- [113] A. N. Cleland. *Foundation of nanomechanics: From solid-state theory to device applications*. *Spring-Verlag, Berlin*, 2003.
- [114] T. Veijola, A. Pursula, and P. Råback. Extending the validity of squeezed-film damper models with elongations of surface dimensions. *Journal of Micromechanics and Microengineering*, 15(9):1624, 2005.
- [115] K. Kokubun, M. Hirata, H. Murakami, Y. Toda, and M. Ono. A bending and stretching mode crystal oscillator as a friction vacuum gauge. *Vacuum*, 34(8-9):731–735, 1984.
- [116] G. Duffing. Erzwungene schwingungen bei vernderlicher eigenfrequenz (forced vibration with variable natural frequency). *F. Vieweg, Braunschweig*, 41/42, 1918.
- [117] S. Schmid, L. G. Villanueva, and M. L. Roukes. *Fundamentals of nanomechanical resonators*. Number EPFL-BOOK-220923. Springer, 2016.
- [118] R. Lifshitz and M. C. Cross. Nonlinear dynamics of nanomechanical and micromechanical resonators. *Review of Nonlinear Dynamics and Complexity*, 1:1–52, 2008.
- [119] N. Kacem, S. Hentz, D. Pinto, B. Reig, and V. Nguyen. Nonlinear dynamics of nanomechanical beam resonators: improving the performance of NEMS-based sensors. *Nanotechnology*, 20(27):275501, 2009.
- [120] H. W. Ch. Postma, I. Kozinsky, A. Husain, and M. L. Roukes. Dynamic range of nanotube-and nanowire-based electromechanical systems. *Applied Physics Letters*, 86(22):223105, 2005.

- [121] I. Kovacic and M. J. Brennan. *The Duffing Equation: Nonlinear Oscillators and Their Behaviour*. Wiley, New York, 2011.
- [122] M. V. Andres, K. W. H. Foulds, and M. J. Tudor. Nonlinear vibrations and hysteresis of micromachined silicon resonators designed as frequency-out sensors. *Electronics Letters*, 18(23):952–954, 1987.
- [123] A. H. Nayfeh and D. T. Mook. *Nonlinear oscillations*. John Wiley & Sons, 2008.
- [124] N. Kacem, S. Baguet, L. Duraffourg, G. Jourdan, R. Dufour, and S. Hentz. Overcoming limitations of nanomechanical resonators with simultaneous resonances. *Applied Physics Letters*, 107(7):073105, 2015.
- [125] N. Kacem, J. Arcamone, F. Perez-Murano, and S. Hentz. Dynamic range enhancement of nonlinear nanomechanical resonant cantilevers for highly sensitive NEMS gas/mass sensor applications. *Journal of Micromechanics and Microengineering*, 20(4):045023, 2010.
- [126] I. Kozinsky, H. W. Ch. Postma, I. Bargatin, and M. L. Roukes. Tuning nonlinearity, dynamic range, and frequency of nanomechanical resonators. *Applied Physics Letters*, 88(25):253101, 2006.
- [127] E. Gavartin, P. Verlot, and T. J. Kippenberg. Stabilization of a linear nanomechanical oscillator to its thermodynamic limit. *Nature Communications*, 4:2860, 2013.
- [128] S. K. Roy, V. T. K Sauer, A. Venkatasubraminam, and W. K. Hiebert. Poor Q-factor? no problem: nano-optomechanical mass sensing in ambient conditions. In *American Vacuum Society, 62nd International Symposium and Exhibition. San Jose, California, USA, Oral No. 1465*, October 18-23 2015.
- [129] W. K. Hiebert, S. K. Roy, V. T. K. Sauer, and A. Venkatasubraminam. Applying nanooptomechanical systems to mass sensing. In *Proceedings of the 13th International Workshop on Nanomechanical Sensing, Delft, Netherlands.*, pages 70–71, Jun 22 2016.
- [130] G. Villanueva. Nonlinearity and phase noise. In *14th International Workshop on Nanomechanical Sensing, Kona Hawaii.*, 4-7 April 2017.
- [131] V. T. K. Sauer, Z. Diao, M. R. Freeman, and W. K. Hiebert. Single laser modulated drive and detection of nano-optomechanical cantilever nanomechanical cantilever sensors. In *Nanomechanical cantilever sensors, Madrid, Spain*, 1 May 2014.
- [132] S. K. Roy, V. T. K. Sauer, and W. K. Hiebert. Dynamic range effect on the mass sensitivity of optomechanically transduced nems devices with a poorer Q value. In *American Vacuum Society, 61st International Symposium and Exhibition. San Jose, California, USA, Oral No. 5356*, 12 Nov 2014.
- [133] A. Venkatasubramanian, S K. Roy, V. T. K Sauer, and Hiebert W. K. GC-MS to GC-NOMS: A step towards portable analysis. In *Canadian Association of Physicists Annual Congress, Edmonton, AB, Canada, Poster.*, 12 Nov 2015.
- [134] S K. Roy, V. T. K. Sauer, A. Venkatasubramanian, and Hiebert W. K. Poor Q-factor? No problem: nano-optomechanical mass sensing in ambient conditions. In *Canadian Association of Physicists Annual Congress, Edmonton, AB, Canada, Poster.*, 12 Nov 2015.

- [135] W. K. Hiebert. Nano-optomechanical systems (NOMS) for mass sensing. In *Nanotech Week Brazil ,Sao Paulo, Brazil, Oral*, 2015.
- [136] W. K. Hiebert, A. Venkatasubramanian, S. K. Roy, V. T. K. Sauer, J. Westwood-Bachman, M. Xia, K. Almutairi, and H. Qadi. Nano-optomechanical systems for gas chromatography and sensing in ambient conditions. In *Frontiers of Nanomechanical Systems, La Thuile, Italy, Oral*, 5-10 Feb 2017.
- [137] W. K. Hiebert, S. K. Roy, V. T. K. Sauer, A. Venkatasubramanian, J. N. Westwood-Bachman, and H. Qadi. Baby steps towards NEMS GC-MS: do we really need vacuum. In *14th International Workshop on Nanomechanical Cantilever Sensing, Kona, Hawaii. Oral*, 4-7 April 2017.
- [138] W. K. Hiebert. Optomechanics and the coming nanosensor revolution. In *NanoTech 2017 Conference and Expo (part of TechConnect World Innovation Conference and Expo, Washington, DC. Invited talk*, 14-17 May, 2017.
- [139] Igor Bargatin. *High-frequency nanomechanical resonators for sensor applications*. PhD thesis, California Institute of Technology, 2008.
- [140] E. Gavartin, P. Verlot, and T. J. Kippenberg. A hybrid on-chip optomechanical transducer for ultrasensitive force measurements. *Nature Nanotechnology*, 7(June):509–514, 2012.
- [141] J. R. Vig and Y. Kim. Noise in microelectromechanical system resonators. *IEEE transactions on ultrasonics, ferroelectrics, and frequency control*, 46(6):1558–1565, 1999.
- [142] A. Demir and M. S. Hanay. Phase-locked loop based resonant sensors: A rigorous theory and general analysis framework for deciphering fundamental sensitivity limitations due to noise. *arXiv preprint arXiv:1903.06497*, 2019.
- [143] P. P. Bohn. The relationship between phase stability and frequency stability and a method of converting between them. *Technical Report, NASA; United States, NASA-TM-X-65766, X-752-71-448*, 1971.
- [144] D. Halford, J. H. Shoaf, and A. S. Risley. Spectral density analysis: Frequency domain specification and measurement of signal stability. In *27th Annual Symposium on Frequency Control*, pages 421–431. IEEE, 1973.
- [145] E. S. Ferre-Pikal, J. R. Vig, J. C. Camparo, L. S. Cutler, L. Maleki, W. J. Riley, S. R. Stein, C. Thomas, F. L. Walls, and J. D. White. Draft revision of ieee std 1139-1988 standard definitions of physical quantities for fundamental, frequency and time metrology-random instabilities. In *Proceedings of International Frequency Control Symposium*, pages 338–357. IEEE, 1997.
- [146] E. Rubiola. *Phase noise and frequency stability in oscillators*. Cambridge University Press, 2009.
- [147] J. A. Barnes, A. R. Chi, L. S. Cutler, D. J. Healey, D. B. Leeson, T. E. McGunigal, J. A. Mullen, W. L. Smith, R. L. Sydnor, R. F. C. Vessot, et al. Characterization of frequency stability. *IEEE transactions on instrumentation and measurement*, (2):105–120, 1971.
- [148] F. J. Giessibl. Advances in atomic force microscopy. *Reviews of Modern Physics*, 75(3):949, 2003.

- [149] F. Sun, X. Dong, J. Zou, M. I. Dykman, and H. B. Chan. Correlated anomalous phase diffusion of coupled phononic modes in a side-band driven resonator. *Nature Publishing Group*, 7:12694, 2016.
- [150] O. Maillet, F. Vavrek, A. D. Fefferman, O. Bourgeois, and E. Collin. Classical decoherence in a nanomechanical resonator. *New Journal of Physics*, 18(7):073022, 2016.
- [151] S. Shen, A. Narayanaswamy, and G. Chen. Surface phonon polaritons mediated energy transfer between nanoscale gaps. *Nano Letters*, 9(8):2909–2913, 2009.
- [152] J. Varesi, J. Lai, T. Perazzo, Z. Shi, and A. Majumdar. Photothermal measurements at picowatt resolution using uncooled micro-optomechanical sensors. *Applied Physics Letters*, 71(3):306–308, 1997.
- [153] E. T. Arakawa, N. V. Lavrik, S. Rajic, and P. G. Datskos. Detection and differentiation of biological species using microcalorimetric spectroscopy. *Ultra-microscopy*, 97(1-4):459–465, 2003.
- [154] S. C. Jun, X. M. H. Huang, M. Manolidis, C. A. Zorman, M. Mehregany, and J. Hone. Electrothermal tuning of Al–SiC nanomechanical resonators. *Nanotechnology*, 17(5):1506, 2006.
- [155] X. C. Zhang, E. B. Myers, J. E. Sader, and M. L. Roukes. Nanomechanical torsional resonators for frequency-shift infrared thermal sensing. *Nano Letters*, 13(4):1528–1534, 2013.
- [156] N. Inomata, M. Toda, and T. Ono. Highly sensitive thermometer using a vacuum-packed Si resonator in a microfluidic chip for the thermal measurement of single cells. *Lab on a Chip*, 16(18):3597–3603, 2016.
- [157] M. H. Chien, M. Brameshuber, B. K. Rossboth, G. J. Schütz, and S. Schmid. Single-molecule optical absorption imaging by nanomechanical photothermal sensing. *Proceedings of the National Academy of Sciences*, 115(44):11150–11155, 2018.
- [158] Y. Hui, J. S. Gomez-Diaz, Z. Qian, A. Alù, and M. Rinaldi. Plasmonic piezoelectric nanomechanical resonator for spectrally selective infrared sensing. *Nature Communications*, 7:11249, 2016.
- [159] Y. Hui and M. Rinaldi. Fast and high resolution thermal detector based on an aluminum nitride piezoelectric microelectromechanical resonator with an integrated suspended heat absorbing element. *Applied Physics Letters*, 102(9):093501, 2013.
- [160] A. Jain, K. Ness, A. McConnell, and Goodson K. Jiang, L. Design, fabrication and thermal characterization of a mems device for control of nerve cell growth. In *ASME 2003 International Mechanical Engineering Congress and Exposition*, pages 251–257. American Society of Mechanical Engineers, 2003.
- [161] T. Larsen and L. G. Villanueva. Temperature fluctuation noise in mechanical resonators. In *Frontiers of Nanomechanical Systems (FNS2019) Abstract Book*, page 56. FNS, 2019.
- [162] N. Klimov, B. Michaela, and Z. Ahmed. Characterization of ring resonator structures for applications in photonic thermometry. In *Optical Sensors*, pages SeT4C–6. Optical Society of America, 2015.

- [163] H. Xu, M. Hafezi, J. Fan, J. M. Taylor, G. F. Strouse, and Z. Ahmed. Ultra-sensitive chip-based photonic temperature sensor using ring resonator structures. *Optics Express*, 22(3):3098–3104.
- [164] A. J. R. MacDonald, B. D. Hauer, X. Rojas, P. H. Kim, G. G. Popowich, and J. P. Davis. Optomechanics and thermometry of cryogenic silica microresonators. *Physical Review A*, 93(1):013836, 2016.
- [165] N. Rouger, L. Chrostowski, and R. Vafaei. Temperature Effects on Silicon-on-Insulator (SOI) Racetrack Resonators: A Coupled Analytic and 2-D Finite Difference Approach. *Journal of Lightwave Technology*, 28(9):1380–1391, 2010.
- [166] R. Melamud, B. Kim, S. A. Chandorkar, M. A. Hopcroft, M. Agarwal, C. M. Jha, and T. W. Kenny. Temperature-compensated high-stability silicon resonators. *Applied Physics Letters*, 90(24):244107, 2007.
- [167] P. Kolodner and J. A. Tyson. Remote thermal imaging with 0.7- μm spatial resolution using temperature-dependent fluorescent thin films. *Applied Physics Letters*, 42(1):117–119, 1983.
- [168] W. Liu and B. Yang. Thermography techniques for integrated circuits and semiconductor devices. *Sensor Review*, 27(4):298–309, 2007.
- [169] E. M. Graham, K. Iwai, S. Uchiyama, A. P. de Silva, S. W. Magennis, and A. C. Jones. Quantitative mapping of aqueous microfluidic temperature with sub-degree resolution using fluorescence lifetime imaging microscopy. *Lab on a Chip*, 10(10):1267–1273, 2010.
- [170] C. Gosse, C. Bergaud, and P. Löw. Molecular probes for thermometry in microfluidic devices. In *Thermal Nanosystems and Nanomaterials*, pages 301–341. Springer, 2009.
- [171] H. Huang, S. Delikanli, H. Zeng, D. M. Ferkey, and A. Pralle. Remote control of ion channels and neurons through magnetic-field heating of nanoparticles. *Nature Nanotechnology*, 5(8):602, 2010.
- [172] K. Okabe, N. Inada, C. Gota, Y. Harada, T. Funatsu, and S. Uchiyama. Intracellular temperature mapping with a fluorescent polymeric thermometer and fluorescence lifetime imaging microscopy. *Nature Communications*, 3:705, 2012.
- [173] J. B. Weaver. Bioimaging: Hot nanoparticles light up cancer. *Nature Nanotechnology*, 5(9):630, 2010.
- [174] O. Zohar, M. Ikeda, H. Shinagawa, H. Inoue, H. Nakamura, D. Elbaum, D. L. Alkon, and T. Yoshioka. Thermal imaging of receptor-activated heat production in single cells. *Biophysical Journal*, 74(1):82–89, 1998.
- [175] J. R. Barnes, R. J. Stephenson, M. E. Welland, Ch. Gerber, and J. K. Gimzewski. Photothermal spectroscopy with femtojoule sensitivity using a micromechanical device. *Nature*, 372(6501):79, 1994.
- [176] J. K. Gimzewski, Ch. Gerber, E. Meyer, and R. R. Schlittler. Observation of a chemical reaction using a micromechanical sensor. *Chemical Physics Letters*, 217(5-6):589–594, 1994.

- [177] D. G. Cahill, W. K. Ford, K. E. Goodson, G. D. Mahan, A. Majumdar, H. J. Maris, R. Merlin, and S. R. Phillpot. Nanoscale thermal transport. *Journal of Applied Physics*, 93(2):793–818, 2003.
- [178] D. G. Cahill, P. V. Braun, G. Chen, D. R. Clarke, S. Fan, K. E. Goodson, P. Keblinski, W. P. King, G. D. Mahan, A. Majumdar, H. J. Maris, S. R. Phillpot, E. Pop, and L. Shi. Nanoscale thermal transport. ii. 2003–2012. *Applied Physics Reviews*, 1(1):011305, 2014.
- [179] T. Luo and G. Chen. Nanoscale heat transfer—from computation to experiment. *Physical Chemistry Chemical Physics*, 15(10):3389–3412, 2013.
- [180] J. Peirs, D. Reynaerts, and H. Van Brussel. Scale effects and thermal considerations for micro-actuators. In *Proceedings. 1998 IEEE International Conference on Robotics and Automation (Cat. No. 98CH36146)*, volume 2, pages 1516–1521. IEEE, 1998.
- [181] C. Cheng, W. Fan, J. Cao, S. G. Ryu, J. Ji, C. P. Grigoropoulos, and J. Wu. Heat transfer across the interface between nanoscale solids and gas. *ACS Nano*, 5(12):10102–10107, 2011.
- [182] M. J. Shin, Y. Ban, B. M. Yu, J. Rhim, L. Zimmermann, and W. Y. Choi. Parametric characterization of self-heating in depletion-type si micro-ring modulators. *IEEE Journal of Selected Topics in Quantum Electronics*, 22(6):116–122, 2016.
- [183] M. J. Tudor, M. V. Andres, K. W. H. Foulds, and J. M. Naden. Silicon resonator sensors: interrogation techniques and characteristics. In *IEE Proceedings D-Control Theory and Applications*, volume 135, pages 364–368. IET, 1988.
- [184] A. Cagliani, V. Pini, J. Tamayo, M. Calleja, and Z. J. Davis. Ultrasensitive thermometer for atmospheric pressure operation based on a micromechanical resonator. *Sensors and Actuators B: Chemical*, 202:339–345, 2014.
- [185] University of Alberta Department of Physics. *Physics laboratory manual*. University of Alberta, 2012-13.
- [186] S. Berber, Y. K. Kwon, and D. Tománek. Unusually high thermal conductivity of carbon nanotubes. *Physical Review Letters*, 84(20):4613, 2000.
- [187] A. I. Hochbaum, R. Chen, R. D. Delgado, W. Liang, E. C. Garnett, M. Najarian, A. Majumdar, and P. Yang. Enhanced thermoelectric performance of rough silicon nanowires. *Nature*, 451(7175):163, 2008.
- [188] S. Neogi, J. S. Reparaz, L. F. C. Pereira, B. Graczykowski, M. R. Wagner, M. Sledzinska, A. Shchepetov, M. Prunnila, J. Ahopelto, C. M. Sotomayor-Torres, and D. Donadio. Tuning thermal transport in ultrathin silicon membranes by surface nanoscale engineering. *ACS Nano*, 9(4):3820–3828, 2015.
- [189] J. Strnad and A. Vengar. Stefan’s measurement of the thermal conductivity of air. *European Journal of Physics*, 5(1):9, 1984.
- [190] Z. Y. Guo and Z. X. Li. Size effect on microscale single-phase flow and heat transfer. *International Journal of Heat and Mass Transfer*, 46(1):149–159, 2003.

- [191] X. J. Hu, A. Jain, and K. E. Goodson. Investigation of the natural convection boundary condition in microfabricated structures. *International Journal of Thermal Sciences*, 47(7):820–824, 2008.
- [192] M. T. Alam, A. P. Raghunath, M. A. Haque, C. Muratore, and A. A. Voevodin. Structural size and temperature dependence of solid to air heat transfer. *International Journal of Thermal Sciences*, 73:1–7, 2013.
- [193] S. Narayanan, A. G. Fedorov, and Y. K. Joshi. Experimental characterization of a micro-scale thin film evaporative cooling device. In *Thermal and Thermomechanical Phenomena in Electronic Systems (ITherm), 2010 12th IEEE Intersociety Conference on*, pages 1–10. IEEE, 2010.
- [194] M. Hu, S. Shenogin, P. Keblinski, and N. Raravikar. Thermal energy exchange between carbon nanotube and air. *Applied Physics Letters*, 90(23):231905, 2007.
- [195] B. G. Dickins. The effect of accommodation on heat conduction through gases. *Proc. R. Soc. Lond. A*, 143(850):517–540, 1934.
- [196] Z. Djurić, O. Jakšić, and D. Randjelović. Adsorption–desorption noise in micromechanical resonant structures. *Sensors and Actuators A: Physical*, 96(2):244–251, 2002.
- [197] R. R. Mukti, A. Jentys, and J. A. Lercher. Orientation of alkyl-substituted aromatic molecules during sorption in the pores of H/ZSM-5 zeolites. *The Journal of Physical Chemistry C*, 111(10):3973–3980, 2007.
- [198] William E Newell. Miniaturization of tuning forks. *Science*, 161(3848):1320–1326, 1968.
- [199] W. Weaver Jr, S. P. Timoshenko, and H. Young, D. *Vibration problems in engineering*. John Wiley & Sons, 1990.
- [200] HF2 User Manual. Zurich instruments, 2014.
- [201] A. A. Clerk, M. H. Devoret, S. M. Girvin, F. Marquardt, and R. J. Schoelkopf. Introduction to quantum noise, measurement, and amplification. *Reviews of Modern Physics*, 82(2):1155, 2010.
- [202] M. V. Salapaka, H. S. Bergh, J. Lai, A. Majumdar, and E. McFarland. Multi-mode noise analysis of cantilevers for scanning probe microscopy. *Journal of Applied Physics*, 81(6):2480–2487, 1997.
- [203] G. Em. Karniadakis, A. Beskok, and M. Gad-el Hak. Micro flows: fundamentals and simulation. *Applied Mechanics Reviews*, 55:B76, 2002.
- [204] M. Bao and H. Yang. Squeeze film air damping in MEMS. *Sensors and Actuators, A: Physical*, 136(1):3–27, 2007.
- [205] J. J. Blech. On Isothermal Squeeze Films. *Journal of Lubrication Technology*, 105(4):615–620, 1983.
- [206] R. Thijssen, E. Verhagen, T. J. Kippenberg, and A. Polman. *Plasmon nanomechanical coupling for nanoscale transduction*, volume 13. ACS Publications, 2013.

- [207] X. Song, M. Oksanen, and Hakonen P. J. Li, J., and M. A. Sillanp. Graphene optomechanics realized at microwave frequencies. *Physical Review Letters*, 113(2):027404, 2014.
- [208] S. M. Meenehan, J. D. Cohen, S. Gröblacher, J. T. Hill, A. H. Safavi-Naeini, M. Aspelmeyer, and O. Painter. Silicon optomechanical crystal resonator at millikelvin temperatures. *Physical Review A*, 90(1):011803, 2014.
- [209] H. Li, Y. Chen, and Tadesse S. Noh, J., and M. Li. Multichannel cavity optomechanics for all-optical amplification of radio frequency signals. *Nature Communications*, 3:1091, 2012.
- [210] U. Dürig, H. R. Steinauer, and N. Blanc. Dynamic force microscopy by means of the phase-controlled oscillator method. *Journal of Applied Physics*, 82(8):3641–3651, 1997.

Appendix A

Chapter 2

A.1 Mechanical body model

In engineering mechanics, the term, "beam" has a particular meaning. Any component or structure which is designed only to support transverse load can be considered as a beam. Hence distributed loads are supposed to act perpendicularly to the longitudinal axis of the beam through bending only. Depending on various types of supports beams are classified mainly into five types: simply supported beam, cantilever beam (CB), doubly clamped beam (DCB), overhanging beam, and continuous beam. Several beam theories have been proposed based on different assumptions and conclude with a different level of accuracy. In this report, our study will focus only on CB and DCB in the light of Euler Bernoulli theory[113, 117]. For a straight, homogenous and untwisted beam of equal cross-section, this theory assumes that the width, w and thickness, t of the beam have to be small compared to its length, l , thus reduces the problem to a one-dimensional problem along the length of the beam (X - axis in Figure A.1 (a)). This theory is valid for undamped free vibration. The amplitude of the oscillation $a(x, t)$ is small compared to beam dimensions. The problem becomes simpler if all shear and rotational forces are negligible.

Downward transverse loads, as in Figure A.1 (a), can cause bending of the beam. The section near the top will contract while the bottom will expand. The neutral axis of the beam in this figure is along the X -axis, and this section of the neutral surface will not be affected by bending. The balance between acting forces and moments is shown at the bottom of Figure A.1 (a), by a free body diagram for a small section, $PQRS$ of dx thickness. The internal shear force applied upward on the PQ side of the

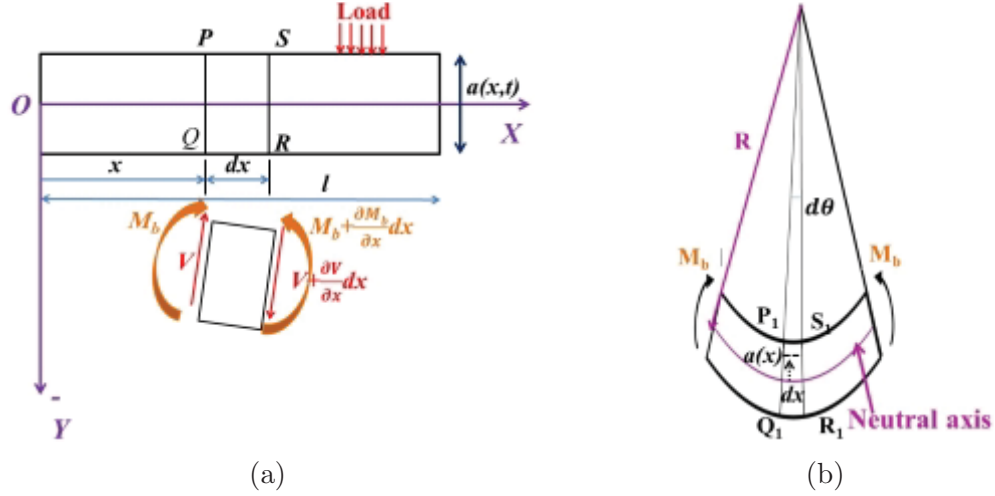


Figure A.1: **a)** Schematic representation of a beam under transverse load. The lower inset shows the forces and moments acting on an infinitesimal cross-section, $PQRS$, of the beam due to transverse vibration of small amplitude $a(x, t)$. **b)** Schematic of the deformed structure of the element due to pure bending.

section, and that applied downward on the SR side are V and $V + \frac{\partial V}{\partial x} dx$ respectively. This distribution of shear forces results in a moment M_b acting on the surface as depicted in the free-body diagram. Applied bending moment on the left-hand side, and right-hand side of the beam is M_b and $M_b + \frac{\partial M}{\partial x} dx$ respectively. Since any rotational motion is ignored the total moment acting on $PQRS$ must be zero, i.e., the sum of moments due to bending and due to shear force will be zero.

$$0 = M_b - (M_b + \frac{\partial M_b}{\partial x} dx) + V dx. \quad (\text{A.1})$$

This gives the shear force as below

$$V = \frac{\partial M_b}{\partial x}. \quad (\text{A.2})$$

Now by considering the geometry of Figure A.1 (b) the beam equation for pure bending can be expressed as follows:

$$\frac{M_b}{I} = \frac{E}{R}, \quad (\text{A.3})$$

where, R is the radius of curvature, E is the modulus of elasticity, M_b is the bending moment, and I is the second of moment of inertia of the beam. From elementary calculus by accounting for the slope at the point P_1 and S_1 the radius of curvature can be found as

$$\frac{1}{R} = -\frac{\partial^2 a(x, t)}{\partial x^2}. \quad (\text{A.4})$$

Now plugging equation A.4 into equation A.3 we have

$$M_b = -EI \frac{\partial^2 a(x, t)}{\partial x^2}. \quad (\text{A.5})$$

Therefore, equation A.2 yields

$$V = -EI \frac{\partial^3 a(x, t)}{\partial x^3}. \quad (\text{A.6})$$

Now, if the area of the section is A and the density of the material is ρ then the mass of the section will be $\rho A dx$. For a displacement $a(x, t)$ the acceleration will be $\partial^2 a(x, t)/\partial t^2$. The total force acting on the section can be found as $(\partial V/\partial x)dx$. Hence, the equation of motion of the beam due to bending will be

$$\rho A \frac{\partial^2 a(x, t)}{\partial t^2} + EI \frac{\partial^4 a(x, t)}{\partial x^4} = 0. \quad (\text{A.7})$$

Equation A.7 is a 4th order differential equation which is harmonic and linear. The harmonic solution of this equation can be found by assuming

$$a(x, t) = X(x) \cos(\Omega t). \quad (\text{A.8})$$

The spatial component, $X(x)$ in above describes the relative displacements along the beam axis and known as the mode shape. The equation A.7 can be simplified for the spatial solution by using A.8

$$\frac{d^4 X(x)}{dx^4} = \beta^4 X(x), \quad (\text{A.9})$$

where,

$$\beta^4 = \frac{\Omega^2 \rho A}{EI}. \quad (\text{A.10})$$

Here, β is a characteristic parameter of the system and Ω is the angular resonance frequency. The general solution of equation A.9 is given by

$$X(x) = c_1 \cosh(\beta x) + c_2 \sinh(\beta x) + c_3 \cos(\beta x) + c_4 \sin(\beta x), \quad (\text{A.11})$$

where c_1, c_2, c_3, c_4 , are real constants. To evaluate these constant the boundary conditions for cantilevers are: $X(0) = dX(0)/dx = 0$, since at the fixed end the displacement is zero with a zero slope. On the other hand at the free end when $x = l$ there is no bending moment or shear force, therefore, $d^2 X(l)/dx^2 = d^3 X(l)/dx^3 = 0$.

A nontrivial solution of equation A.11 for these constants gives the characteristic equation for a cantilever

$$\cosh(\beta_n l) \cos(\beta_n l) + 1 = 0, \quad (\text{A.12})$$

in which n is the order of mode. There is no analytical solution for equation A.12. All zeros of this equations can be found numerically for $\lambda_n = \beta_n l = 0, 1.876, 4.694, 7.855$ for $n = 0, 1, 2, 3$ and $\beta_n l \cong (2n - 1)\pi/2$ for $n \geq 4$ [113]. The solution for $\beta_n l = 0$ is trivial and is disregarded. Thus from equation A.10 resonance frequency of different modes will be,

$$\Omega_n = \beta_n^2 \sqrt{\frac{EI}{\rho A}} = \lambda_n^2 \frac{t}{l^2} \sqrt{\frac{E}{\rho}}, \quad (\text{A.13})$$

after substituting $I = wt^3/12$ and $A = wt$. Thus for the first mode, the resonance frequency of a cantilever is $\Omega_0 = 1.876^2(t/l^2)\sqrt{\frac{E}{\rho}}$. Hence, by tuning the thickness and length of NEMS devices it is possible to attain a desired higher frequency for suitable applications.

For a DCB the displacement and it's derivative is zero at both end. Hence, boundary conditions for DCB are: $X(0) = X(l) = dX(0)/dx = dX(l)/dx = 0$. After solving equation A.11 for DCB we can get

$$\cosh(\beta_n l) \cos(\beta_n l) - 1 = 0, \quad (\text{A.14})$$

and $\beta_n l = 0, 4.733, 7.853, 10.996$ for $n = 0, 1, 2, 3$ and $\beta_n l \cong (2n + 1)\pi/2$ for $n \geq 3$ and resonance frequencies follow the similar scaling law with device dimensions as described in equation 2.1. It differs by the value of $\beta_n l$ only. It is worth mention that the frequency equation is derived by considering the undamped free vibration. That is why often it is named as eigenfrequency or natural frequency of the beam. In the presence of light damping, it is close to the resonance frequency of a damped driven resonator discussed in the next section.

According to Hooke's law, an extension of linear elastic material is directly proportional to the applied load. Thus the spring constant, k is defined as $k = -F/a(x)$. Let a mass m is attached at the free end of the cantilever in A.1(a), i.e., at $x = l$. Then the moment will be Fl for corresponding load $F = mg$. Therefore, at a distance, x from the clamped end the bending moment on the right-hand side will be $-F(l - x)$

which can be equated with equation A.5 as follows

$$-EI \frac{\partial^2 a(x)}{\partial x^2} = -F(l-x). \quad (\text{A.15})$$

The boundary conditions for the problems are, $a(0) = da(0)/dx = d^2X(l)/dx^2 = 0$ and the solution of equation A.15 can be found as

$$a(x) = \frac{F(3l-x)x^2}{6EI} = \frac{2mg(3l-x)x^2}{Ewt^3}. \quad (\text{A.16})$$

Hence, the maximum displacement can be found at $x = l$

$$a_{\max} = u(l) = \frac{4Fl^3}{Ewt^3}. \quad (\text{A.17})$$

The scaling law for spring constant can be found simply as below

$$k = \frac{F}{u_{\max}} = \frac{Ewt^3}{4l^3}. \quad (\text{A.18})$$

According to equation A.18 if we want to double the thickness then we need $8(= 2^3)$ times higher tip force to provide the same deflection. Hence it is advantageous to scale a cantilever down to obtain higher force sensitivity.

In case of a double clamped beam the deflection can be found as

$$a(x) = \frac{F(l-x)^2x^2}{24EI} = \frac{mg(l-x)^2x^2}{2Ewt^3}. \quad (\text{A.19})$$

Since the maximum displacement occurs at the center of the beam hence

$$a_{\max} = a\left(\frac{l}{2}\right) = \frac{Fl^3}{32Ewt^3}. \quad (\text{A.20})$$

Therefore, the spring constant of a DCB can be found to follow the similar scaling law as cantilever

$$k = \frac{F}{u_{\max}} = \frac{32Ewt^3}{l^3}. \quad (\text{A.21})$$

Under the action of this external force F some work must be done to produce the deflection. Due to the elastic nature of the material, the beam tends to recover its unstrained state slowly, i.e., it can give back the amount of work done by the force F . Therefore, the work done in straining the beam can be considered as the energy stored in the beam which is known as the strain energy. Again by considering the beam of Figure A.1(a), the strain energy, E_{strain} for the entire beam can be found regarding

the acting moment due to the end load F along with the elastic modulus and moment of inertia as below

$$E_{\text{strain}} = \int_0^l \frac{M_b^2}{2EI} dx. \quad (\text{A.22})$$

At a distance x the balance of moment can be written as $-M_b - Fx = 0$. After plugging this into equation A.20 we can get maximum strain energy at $x = l$

$$E_{\text{strain}} = \int_0^l \frac{(-Fx)^2}{2EI} dx = \frac{F^2 l^3}{6EI}. \quad (\text{A.23})$$

Now by using the relation deflection = $2(E_{\text{strain}}/F)$ we can easily get back the deflection as described by equation A.17. Thus, the integration of the strain energy is effectively a measure of spring constant.

A.2 Simple damped harmonic model

In the earlier section, the elastic theory of bending is described for the free vibrations of a nanomechanical beam which is an ideal lossless continuum structure. It is seen that a beam by its elastic properties can store potential energy as deformation energy. If the structure comes out from its position of rest, then eventually a restoring force will act to accelerate the system mass towards the equilibrium and generate kinetic energy. Because of the generated kinetic energy, the mechanical system passes through the equilibrium, thereby generating new deflection energy, i.e., potential energy. Thus, a periodic energy conversion would continue forever and oscillates the body until dissipative forces resist the existing mechanical energy. It is interesting to note that without dissipations systems will go for an infinite oscillation (*cf.* section A.2.1) which results in a noninteracting mechanical body with its surroundings. In this scenario, there would be no nanomechanical sensor in practice. Elastic theory of bending neglects dissipative forces and consider conservation of total energy for any instant. However, in a mechanical structure, periodic energy conversion cannot continue endlessly. Dissipated forces cause a loss of finite energy; collectively this phenomenon is termed as damping. Therefore, an undriven mechanical body can oscillate for a finite time only before all the energy is lost. Hence, in order to keep the body oscillating, energy must be supplied from an external source, and the resonator can be called a driven damped oscillator.

In this section, we will begin by studying nanomechanical motion in the linear regime and will not consider the dynamics in the non-linear regime. This is because, at the end of the day, we will perform experiments for a linear resonant sensor. In this context, the term linear implies that the displacement of nanomechanical motion is proportional to the applied driving force, $F(t) = g(x)F_0e^{i\Omega t}$, where, $g(x)$ is the position dependent force per unit length, F_0 is the strength of driving force and Ω is its' frequency. This driving force will balance the energy dissipation to sustain the motion. Then after adding the damping term proportional to velocity equation A.7 can be written as [199]

$$EI\frac{\partial^4 a(x,t)}{\partial x^4} + \rho A\frac{\partial^2 a(x,t)}{\partial t^2} + \gamma\frac{\partial a(x,t)}{\partial t} = g(x)F(t), \quad (\text{A.24})$$

where, γ is the damping coefficient. Equation A.24 can be projected for fundamental mode as below

$$EI\frac{\partial^4 a(x,t)}{\partial x^4}\beta^4 l + \rho AL\frac{\partial^2 a(x,t)}{\partial t^2} + \gamma l\frac{\partial a(x,t)}{\partial t} = g(x)\int_0^l g(x)X(x)dx. \quad (\text{A.25})$$

In the above equation, $\rho AL = M$. A. N. Cleland [76] showed that if the force distribution $g(x)$ is proportional to the eigenfunction $X(x)$, the integral above becomes unity. Moreover, the equation can be identified as a lumped-spring mass model. The system is now comparable to driven damped harmonic oscillator whose equation of motion is described by the well-known second-order differential equation of the form

$$M\frac{d^2 a(t)}{dt^2} + b\frac{da(t)}{dt} + ka(t) = F_0e^{i\Omega t}, \quad (\text{A.26})$$

where, M is the mass of the system

$a(t)$ is the time dependent displacement function

$b = \frac{M\Omega_0}{Q} = M\Gamma$ is the damping constant at resonance frequency. $Q = \frac{\Omega_0}{\Gamma}$ is the quality factor which quantifies the damping.

$k = M\Omega_0^2$ is the spring constant and,

The resonance frequency is given by

$$\Omega_0 = \sqrt{\frac{k}{M}}. \quad (\text{A.27})$$

Rewriting equation A.26 we have

$$\frac{d^2 a(t)}{dt^2} + \Gamma\frac{da(t)}{dt} + \Omega_0^2 a(t) = \frac{F_0}{M}e^{i\Omega t}. \quad (\text{A.28})$$

Now, for steady state solution let us consider

$$a(t) = a_0 e^{\lambda t}, \quad (\text{A.29})$$

$$\frac{da(t)}{dt} = \lambda a_0 e^{\lambda t}, \quad (\text{A.30})$$

$$\frac{d^2 a(t)}{dt^2} = \lambda^2 a_0 e^{\lambda t}. \quad (\text{A.31})$$

Substitution of $a(t)$ in equation A.28 yields

$$(\lambda^2 + \Gamma\lambda + \Omega_0^2) a_0 e^{\lambda t} = \frac{F_0}{M} e^{i\Omega t}. \quad (\text{A.32})$$

To equalize both sides of the above equation at all times, we must have, $e^{\lambda t} = e^{i\Omega t}$ or $\lambda = i\Omega$. Therefore, the time dependence of mechanical displacement $a(t)$ must be a complex exponential with the same frequency as the driving force, i.e., $a(t)$ will also vary with Ω . After replacing $\lambda = i\Omega$, the complete solution of the displacement function can be found as

$$a(t) = a_0 e^{i\Omega t} = \frac{F_0}{M} \frac{e^{i\Omega t}}{\Omega_0^2 - \Omega^2 + i\Gamma\Omega}, \quad (\text{A.33})$$

where, the complex transfer function has its form as below

$$\chi(\Omega) = \frac{1}{M(\Omega_0^2 - \Omega^2 + i\Gamma\Omega)}. \quad (\text{A.34})$$

The complex function $a(t,)$ can be solved by separating real and imaginary parts in polar form

$$\frac{F_0}{M} \cos\phi = a_0(\Omega_0^2 - \Omega^2), \quad (\text{A.35})$$

$$\frac{F_0}{M} \sin\phi = a_0\Gamma\Omega. \quad (\text{A.36})$$

By solving equation A.35 and A.36 one can get the amplitude of the oscillation in response to the applied force at frequency Ω

$$a_0 = \frac{F_0}{M \sqrt{(\Omega_0^2 - \Omega^2)^2 + (\Gamma\Omega)^2}}, \quad (\text{A.37})$$

and the phase

$$\phi = \tan^{-1}\left(\frac{\Gamma\Omega}{(\Omega_0^2 - \Omega^2)}\right). \quad (\text{A.38})$$

Using the trigonometric identity, $\tan^{-1}(x) = \pm \frac{\pi}{2} - \frac{1}{x} + \frac{1}{3x^2} - \dots$ one may find equation 2.4 as below

$$\phi = \tan^{-1}\left(\frac{\Gamma\Omega}{(\Omega_0^2 - \Omega^2)}\right) \approx -\frac{\pi}{2} - \frac{\Omega_0^2 - \Omega^2}{\Gamma\Omega}. \quad (\text{A.39})$$

Equation A.39 tells us that at resonance frequency i.e., at $\Omega = \Omega_0$ the phase angle will be $-\pi/2$.

A.2.1 Frequency response

The effect of frequency response on the steady state displacement and phase of a nanomechanical resonator can be studied directly from equation 2.3 and 2.4. In Fourier transformation notation equation 2.3 can be re-written as

$$a(\Omega) = H(\Omega)F(\Omega), \quad (\text{A.40})$$

where, $H(\Omega)$ is the magnification factor which relates the magnitude of the displacement with the magnitude of the driving force and is given by

$$H(\Omega) = \frac{a_0}{F_0} = \frac{1}{M\sqrt{(\Omega_0^2 - \Omega^2)^2 + (\Gamma\Omega)^2}}. \quad (\text{A.41})$$

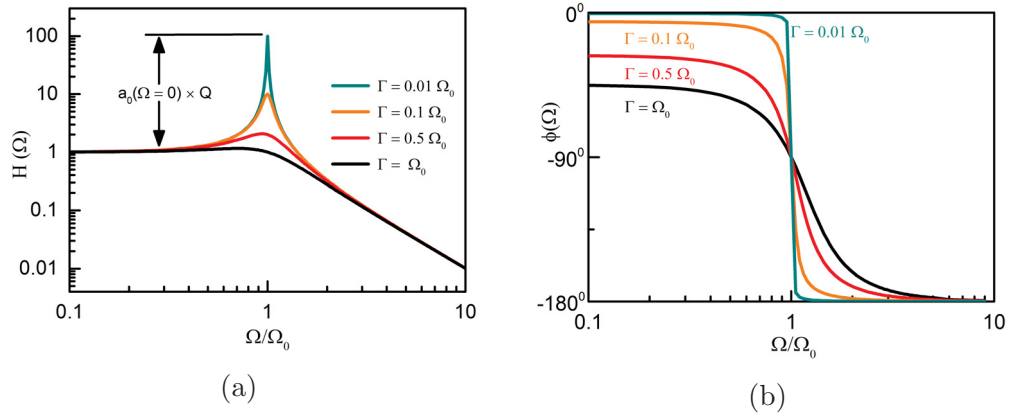


Figure A.2: **Transfer function of a damped mechanical resonator:** Comparing amplitude gain ($H(\Omega)$) and phase (ϕ) of a driven damped nanomechanical resonator as a function of the driving frequency(Ω). With unit mass of the system, $\Omega_0 = 1$ is used for calculation.

It is evident from the above equation that amplitude is proportional to the strength of the applied force F_0 , which means that the whole system is linear. It follows from the

fact that the differential equation is linear. The modulus of complex transfer function described in the equation A.41 is sketched in Figure A.2a. Here, one can look at some simple limit to reveal the fact of how it should behave. At zero frequency equation becomes, $H(0) = 1/M\Omega_0^2 = 1/k$. Since at zero frequency, the applied force is constant and change in mass or drag is irrelevant $H(\Omega)$ determines how much displacement can be expected for a fixed force. As seen from the Figure A.2a $H(\Omega)$ is almost constant for low frequency, $\Omega \ll \Omega_0$ and dramatically increases when approaching Ω_0 provided that $\Gamma < \Omega_0$. We observe that at $\Omega = \Omega_0$ the dominator of the equation attains its minimum value for a maximum displacement,

$$a_0(\Omega_0) = \frac{F_0}{k} \times Q = a_0(0) \times Q. \quad (\text{A.42})$$

Consequently, the lower the damping (Q^{-1}), the higher the displacement. As seen from the sketch, the amplitude at the resonance is Q times higher than the zero-frequency displacement. This is one reason why we want a high Q nanomechanical resonator: the higher the Q the sharper the peak. After passing the maximum at Ω_0 , $H(\Omega)$ falls off quickly and for $\Omega \gg \Omega_0$ it drops proportionally to Ω^{-2} .

The phase response schematic in Figure A.2b shows that the resonance frequency phase changes from 0° to -180° and at the resonance it is -90° whatever the damping (*cf.* equation A.39). Also, the slope of the phase-frequency curve becomes steeper with lower damping. Such rapid phase variations in the vicinity of the resonance frequency can be used to maintain the oscillation frequency close to the resonance by prohibiting any shift of phase from -90° . It is the principle of any frequency tracking experiments by a resonator and is the key of phase locked loop measurements [200]. Thus, it is interesting to investigate the phase variations close to the resonance frequency, in more detail. Differentiation of equation at $\Omega = \Omega_0$ gives us

$$\frac{d\phi}{d\Omega} = -\frac{2}{\Gamma} = -\frac{2Q}{\Omega_0}, \quad (\text{A.43})$$

i.e., the lower the damping the steeper the slope. According to the fluctuation-dissipation theorem, any damped system is a source of different noises that induce fluctuations in phase and frequency of a lightly damped resonator. Gradually in this dissertation impact of noises on nanomechanical resonator will be discussed in detail.

For now, let us express the phase and frequency fluctuations as $\partial\phi$ and ∂f respectively and rewrite equation A.43 as below

$$\left| \frac{\partial f}{f_0} \right| = \left| \frac{\partial\phi}{2Q} \right|. \quad (\text{A.44})$$

Where, the angular frequency is changed to linear frequency by $\Omega = 2\pi f$. According to the equation A.44, frequency fluctuations of a resonator can be minimized with the higher Q device.

The normalized frequency, $\partial f/f_0$ is the key FOM of a nanomechanical sensor and known as frequency stability which determines sensor performance. In Chapter 4 there will be detailed discussions on frequency stability characterizations. Later in this Chapter, I will show how this quantity, $\partial f/f_0$ plays the crucial role for better mass sensitivity. However, from the above discussions on the frequency response of a mechanical resonator, it can be inferred that any measurement near the peak, (i.e., close to the resonance frequency) provides useful information on nanomechanical vibrations. The remainder holds little information on the mechanical response.

A.2.2 Effective parameters

So far above, we have associated flexural beam mechanics with a lumped spring-mass model. The simple harmonic model assumes the beam as a point mass, and the entire mass of the beam participates uniformly in the vibration displacement with a punctual (i.e., structural mass) kinetic energy. Whereas, in Euler-Bernoulli theory, not only the mass but also the displacement is distributed along the length of the beam. Thus, the beam does not carry the same kinetic energy along its length. The kinetic energy is almost null to the anchors and approaches to a maximum at the point of maximum deflection. The maximum deflection occurs at the end of a cantilever beam and, at the midpoint of a doubly clamped beam. In other word, the effect of kinetic energy distribution implies that structures with low velocity appear to have reduced mass compared to those moving with high velocities. While calculating NEMS resonance frequency, effective mass, M_{eff} must be taken into account instead of the total mass. Galerkins method derives not only the mass but also other effective parameters for an undamped one-dimensional beam structure with the differential equation of motion described by the equation, where mode shape is accounted. Another approach

compares the maximum kinetic energy of the continuum structures to that of the lumped model system where $\Phi_n(x) = 1$. In the current work, only the fundamental mode is used. So, the detailed calculation of effective mass parameters is skipped here. We are following the approach of K. L. Ekinici, and M. L. Roukes [96] where effective spring constant is considered from the continuum model and effective mass is used as $M_{\text{eff}} = 0.73M$ for DCB and $0.24M$ for CB. From now for the sake of simplicity, throughout the dissertation at each place where the mass of the nanomechanical doubly clamped beam M will appear it will mean M_{eff} with a value of $0.73M$.

A.3 Thermal noise driven motion

In the treatment of nanomechanical motion made so far, we have discussed only the effect of the externally applied sinusoidal driving force. Apart from drive forces, nanomechanical resonators continuously interact with the environments through a mutual transfer of energy. In other words, these interactions make the resonator lossy and are collectively known as noise. There are several noise sources, for example, surface contaminations due to surroundings, surface defects of the resonator, phonon coupling between the resonator and the substrate, random collisions of the resonator with surrounding molecules etc.[20]. These are irreversible and random. Among different noise sources, thermomechanical noise is a consequence of mechanical resonator being in thermal equilibrium with the environment; random thermal motions of the mechanical beam results in measurable noise in the resonator's displacement signal. Moreover, the force term in the driven damped resonator will have an additional term $F_{\text{th}}(t)$, which constitutes the random thermal noise. Now the equation of motion, A.28 can be rewritten as

$$\frac{d^2a(t)}{dt^2} + \Gamma \frac{da(t)}{dt} + \Omega_0^2 a(t) = \frac{F_0}{M} e^{i\Omega t} + \frac{F_{\text{th}}(t)}{M}. \quad (\text{A.45})$$

In the absence of driving force, it will be

$$\frac{d^2a(t)}{dt^2} + \Gamma \frac{da(t)}{dt} + \Omega_0^2 a(t) = \frac{F_{\text{th}}(t)}{M}. \quad (\text{A.46})$$

In the current section, we will explicitly derive the frequency response due to random thermal noise. Unlike the deterministic signal (i.e., externally applied sinusoidal drive

signal), the frequency response due to a random process must be determined based on the stochastic nature of the random process or its statistical properties. Observed values of many practical systems under the influence of random effects change at each instant of time, and generally, observations are made over a period which shows a normal distribution. Thus random processes are Gaussian. A linear system under Gaussian force shows a Gaussian response. Here we will study the displacement response under white noise excitation. White noise by nature is Gaussian since its statistical properties can be found by averaging over a period as a constant. It is defined for a constant power spectral density (with a unit of Power per root Hz) independent of measurement bandwidth and thus named as white.

A noisy time-dependent quantity is expressed in terms of its spectral density (or power spectrum), $S(\Omega)$, often known as power spectral density (PSD). PSD expresses the intensity of the noise of interest at a given frequency [112, 201]. To derive PSD of nanomechanical displacement $a(t)$ let us first define the Fourier transform over a finite window as follows

$$a_\tau(\Omega) \equiv \frac{1}{\sqrt{\tau}} \int_{-\frac{\tau}{2}}^{\frac{\tau}{2}} a(t) e^{i\Omega t} dt, \quad (\text{A.47})$$

where, τ is the sampling time. The definition of displacement spectral density is then

$$S_a(\Omega) \equiv \lim_{\tau \rightarrow \infty} \langle |a_\tau(\Omega)|^2 \rangle. \quad (\text{A.48})$$

Now, in order to relate the mean square displacement with the power spectral density, we need to introduce the autocorrelation function, $R(\tau)$ between two sample $a(t)$ and $a(t + \tau)$ separated by a time interval τ as below

$$R(\tau) = \lim_{T \rightarrow \infty} \frac{1}{T} \int_0^T a(t) a(t + \tau) dt. \quad (\text{A.49})$$

At, $\tau = 0$, the autocorrelation function is reduced to mean square value of the displacement, $a(t)$

$$R(0) = \langle a^2(t) \rangle. \quad (\text{A.50})$$

The spectral density is related to the autocorrelation function through its Fourier transform

$$S_a(\Omega) = \int_{-\infty}^{\infty} R(\tau) e^{i\Omega\tau} d\tau. \quad (\text{A.51})$$

The spectral density, $S_a(\Omega)$ in A.48 or A.51 spans both positive and negative frequencies. $S_a(\Omega)$ is an even function for real-valued signals, as it is the case in real situations. Hence for single-sided spectral density, we may adopt the following convention [112] which still allows the conservation of total power in the signal integrated over positive frequencies.

$$S_a(\Omega) \equiv S_a(\Omega) + S_a(-\Omega). \quad (\text{A.52})$$

The inverse Fourier transform of the equation A.51 gives the autocorrelation function

$$R(\tau) = \frac{1}{2\pi} \int_{-\infty}^{\infty} S_a(\Omega) e^{i\Omega\tau} d\Omega. \quad (\text{A.53})$$

Now, using the equation A.50, we have a direct connection between the mean-squared thermal motion and its spectral density

$$\langle a^2(t) \rangle = \frac{1}{2\pi} \int_0^{\infty} S_a(\Omega) d\Omega. \quad (\text{A.54})$$

The square root of above expression is the rms amplitude due to thermal noise.

Following the procedure of driven damped harmonic oscillator, Fourier transform of the equation A.46 due to thermal noise force gives

$$a(\Omega) = \frac{F_{th}(\Omega)}{M} \frac{1}{\Omega_0^2 - \Omega^2 + i\Gamma\Omega}. \quad (\text{A.55})$$

or,

$$|a(\Omega)|^2 \equiv |F_{th}^2| \left(\frac{1}{M^2(\Omega_0^2 - \Omega^2)^2 + (\Gamma\Omega)^2} \right). \quad (\text{A.56})$$

Now, spectral density definition of the equation A.48 allows us to define the spectral density of thermal force noise, $S_F^{th}(\Omega)$ which determines the displacement spectral density as follows

$$S_a^{th}(\Omega) = \frac{S_F^{th}(\Omega)}{M^2[(\Omega_0^2 - \Omega^2)^2 + (\Gamma\Omega)^2]}. \quad (\text{A.57})$$

Referring to the relation A.54, we are now able to connect the fluctuations of thermal displacement with its force noise spectral density as below

$$\langle a^2(t) \rangle = \frac{S_F^{th}(\Omega)}{2\pi M^2} \int_0^{\infty} \frac{1}{(\Omega_0^2 - \Omega^2)^2 + (\Gamma\Omega)^2} d\Omega. \quad (\text{A.58})$$

Using the results of above integral evaluation by M. V. Salapaka *etal*[202] above equation gives us

$$\langle a^2(t) \rangle = \frac{S_F^{th}(\Omega)}{2\pi M^2} \times \frac{\pi}{2} \frac{1}{\Gamma\Omega_0^2} = \frac{S_F^{th}(\Omega)Q}{4M^2\Omega_0^3}. \quad (\text{A.59})$$

In thermal equilibrium, the temperature, T , of the nanomechanical resonator is equal to that of the surrounding environment. Now by applying the equipartition theorem [19], we can write the relationship between the kinetic energy (i.e., the variance of displacement) and potential energy as below ¹.

$$\frac{1}{2}k \langle a^2(t) \rangle = \frac{1}{2}k_B T. \quad (\text{A.60})$$

Solving equation A.59 and A.60 we are then able to get the thermal force spectral density as below

$$S_F^{\text{th}}(\Omega) = \frac{4k_B T \Omega_0 M}{Q} = 4k_B T M \Gamma. \quad (\text{A.61})$$

Such a result is known as *fluctuations-dissipation theorem* and has validity for any driven damped oscillator described so far governed by a *Langevin equation* [113]. From the above equation, it can be inferred that the spectral density of thermal force depends only on the environment temperature and intrinsic properties of the nanomechanical resonator irrespective of its microscopic origin. Furthermore, it indicates that the force noise density determines the dissipation (conversely the quality factor) of a resonator. Now plugging A.61 into A.57 we can have the well known expressions for the PSD of nanomechanical displacement noise

$$S_a^{\text{th}}(\Omega) = \frac{4k_B T \Omega_0}{MQ[(\Omega_0^2 - \Omega^2)^2 + (\frac{\Omega_0}{Q}\Omega)^2]}. \quad (\text{A.62})$$

A closer look at the displacement noise spectral density of nanomechanical motion above provides exactly similar transfer function as an externally driven resonator in the equation 2.3 and describes in the Figure A.2a. A sharp peak appears around the resonance frequency, Ω_0 , with an FWHM, Γ . The peak amplitude due to the transfer function in 2.6 can be found for $\Omega = \Omega_0$ as

$$S_a^{\text{th}}(\Omega_0) = \frac{4k_B T Q}{M \Omega_0^3} \text{ m}^2 \text{ Hz}^{-1}. \quad (\text{A.63})$$

The equation A.63 tells us that thermal noise detection becomes favorable by a high Q mechanical resonator, which drives NEMS researchers to develop high Q devices. It should be worth mentioning that conventionally displacement is expressed in terms of

¹The equipartition theorem is a principle of statistical mechanics which does not apply to quantum scale. It tells that potential energy stored in a mechanical structure is equal to the kinetic energy of the specific mechanical vibration.

x rather than a . To maintain the similarity with conventional notations, I will use in the rest of thesis displacement noise density as $S_x^{\text{th}}(\Omega_0)$. i.e.,

$$S_a^{\text{th}}(\Omega_0) = S_x^{\text{th}}(\Omega_0). \quad (\text{A.64})$$

The equation A.63 describes the evolution of thermal noise peak with damping (Γ). Later in the results discussion section, we will compare this equation with our experimental results which suggest we need to detect displacement noise density with $\sim fm/\sqrt{Hz}$ precision whereas the noise amplitude at resonance is around $\sim pm/\sqrt{Hz}$.

A.4 Quality factor

From the simple harmonic model of a mechanical resonator, we have seen that the quality factor (Q) of a resonator describes the sharpness of resonance peak. In other words, Q defines the energy dissipation rate by a mechanical resonator. The inverse of the quality factor, Q^{-1} quantifies the damping. Hence, the precise measurement of Q is fundamentally essential for identifying the dominant damping mechanism of the system of interest. There are several definitions of Q , which are equivalent to slight damping. Physically, the Q-factor of a damped system is the ratio of the energy stored (W) to the energy lost during (ΔW) one cycle at resonance

$$Q = 2\pi \frac{W}{\Delta W} = \frac{M\Omega_0}{b}. \quad (\text{A.65})$$

Direct measurement of dissipation is a daunting task; instead, we can measure damping by monitoring the dynamics of the resonator. Following experimental techniques are commonly used to extract the Q of a resonator:

- i) By fitting the measured linear response with a Lorentzian function.
- ii) From a driven linear amplitude response, Q is determined by -3 dB bandwidth method as follows $Q = \Omega_0/\Delta\Omega_{-3\text{dB}} = \Omega_0/\Gamma$, where, $\Delta\Omega_{-3\text{dB}} = \Gamma$ is the difference between two frequencies at which amplitude response has the half of the maximum power.
- iii) From the phase response, Q is extracted by the equation A.44.

- iv) For high Q devices ring down approach permits the mechanical body to oscillate freely after an initial excitation and measure the logarithmic decrement from the decaying amplitude.

All of the above procedures require external actuation of the device and is valid for small damping with linear response and need extra care to avoid any undesirable nonlinearities. To extract purely mechanical Q , Lorentzian fit of measured TM noise spectra is probably the best method. Since the motion is undriven, there is no possibility of any effect of driving techniques on the measured Q , i.e., the measured Q accounts different damping effect on the mechanical resonator only. Also, estimated damping from TM noise does not rely on knowledge of the device geometry, material properties, or structural stiffness. Fundamental links between thermomechanical noise and damping through the fluctuation-dissipation theorem is discussed in section A.3. Qualitatively, dissipation is the energy transfer from mechanical structure to the heat bath and from the heat bath to the structure. A heat bath with many macroscopic degrees-of-freedom is the surrounding environment of the mechanical resonator. At each cycle of vibration of a driven oscillator, the stored mechanical energy leaks away in the form of heat due to damping. By this way, the mechanical body can maintain the thermal equilibrium to its surroundings.

Conversely, the absence of any external force causes spontaneous random displacement of the structure around its equilibrium position because of energy injection from the heat bath, which is the thermal displacement noise. By combining the fluctuation-dissipation and equipartition theory, equation A.63 expresses TM noise density measurements as a function of damping. Stronger coupling between the resonator and the heat bath causes a faster decay of nanomechanical motions towards the thermal equilibrium and thus lower the mechanical Q . At the same time, the stronger coupling of the mechanical beam to its surroundings enhances the force noise density. Consequently, the presence of air is not desirable for high- Q operations of nanomechanical sensors. On the other side, a high vacuum is not possible for applications like gas sensing. Hence, understanding air damping effect on the quality factor and the resonance frequency is vital for ambient condition gas sensing.

A.5 NEMS damping in air

Airflow variations with pressure cause a wide range of dissipations on the nanomechanical vibrations ranging from continuum region to molecular free region. Studying the damping mechanism for nanomechanical resonators is a mature area with some controversial arguments in the transition regime [61, 60, 62, 63, 64, 65]. The goal of this thesis is not to explore the origin of different damping sources. Instead, we will look into dominant damping mechanisms which change the quality factor and resonance frequency of the device. There are many physical mechanisms responsible for the energy dissipation in nanomechanical resonators. Different authors are working on this area for years, ref. [61] - [65] are only a few of those studies. In a typical damping study, the range of pressure from vacuum to atmosphere can be divided into four regimes based on the Knudsen number. These regions are named after the dominant damping mechanisms which cause the change in the quality factor and the resonance frequency of the device, *viz.* the intrinsic, the molecular, the transition and the slip regime (often referred as a viscous regime) and the continuum flow regime. Knudsen number, K_n , which depends on device geometry and ambient pressure, distinguishes pressure dependence of damping mechanisms with a power law, $Q \propto P^{-r}$. It is the ratio of the mean free path of the gas molecules (λ) to the characteristic length of the flow (h),

$$K_n = \frac{\lambda}{h} = \frac{k_B T}{\sqrt{2\pi} d^2 h P}, \quad (\text{A.66})$$

where k_B is the Boltzmann constant, T is the temperature, d is the collision diameter, for air $d = 3.7 \times 10^{-10} \text{ m}$ and P is the pressure. h is taken as the thickness of vibrating body.

In the following table, different flow regimes with the power law of Q are tabulated based on Knudsen number [62]. In the intrinsic regime, air pressure is too low so that $K_n \rightarrow \infty$. So, air damping is negligible compared to different intrinsic dampings. F. R. Blom *et al.* [60] concluded that in the intrinsic regime both Q and Ω_0 are independent of pressure, i.e., in the power law $r = 0$. A quantitative determination of all contributions is out of the scope of this thesis.

With increasing pressure when $K_n \approx 10$ free molecular region starts where surrounding air molecules collide with the mechanical resonator and Q drops inversely

Table A.1: Power law of quality factor as a function of air pressure.

Range of K_n	Flow regime	Power law
$K_n \gg 10$	Intrinsic regime	$Q \propto P^0$
$K_n > 10$	Molecular flow regime	$Q \propto P^{-1}$
$0.1 < K_n < 10$	Transition flow regime	$Q \propto P^{-0.5}$
$0.01 < K_n < 0.1$	Slip flow regime	$Q \propto P^{-0.5}$
$K_n < 0.01$	Continuum or viscous flow regime	$Q \propto P^0$

with the pressure. Momentum exchange between individual molecules and the resonator is considered as the damping source. Next, after the FMF region, the transition regime starts. In this regime, the mean free path of the air molecules λ and the characteristic flow length h are of the same order. Intermolecular collisions occur along with the collisions of the molecules with the resonator and make the analysis complicated [203]. With decreasing K_n , next region is the slip flow regime where velocity slip and temperature jump is expected, but these are different from those in the continuum flow (ref.[62]). In the continuum flow regime mean free path of air molecules becomes comparable to the flow length. Consequently, the number density of air molecules is too large to influence the average gas property, so that, a strong coupling between the resonator and its surrounding establishes which results in an invariant lower quality factor with further increase in pressure. After considering all damping effect on a mechanical resonator, the effective damping is defined as follows

$$\frac{1}{Q_{\text{eff}}} = \frac{1}{Q_{\text{intrinsic}}} + \frac{1}{Q_{\text{air}}} + \frac{1}{Q_{\text{others}}}. \quad (\text{A.67})$$

A.6 Background noise floor

The possible sources of background noise in our nanophotonic detection system are the Johnson noise of electronic measurement instruments e.g. HF2 lock-in or spectrum analyzer ($5 \text{ nVHz}^{-\frac{1}{2}}$ from instrument manual), shot noise, S_V^{shot} from laser source and dark current S_V^{dark} of the photodetector. The total background is the sum of these $S_V^{\text{white}} = S_V^{\text{elec}} + S_V^{\text{shot}} + S_V^{\text{dark}}$. Measured optical power to voltage conversion factor for a 50Ω termination is [48], $\mathfrak{D} = 15 \text{ VmW}^{-1} = 15000 \text{ VW}^{-1}$. The free space optical beam shot noise is defined as

$$S_{\text{opt}}^{\text{shot}} = 2h\nu \langle P \rangle, \quad (\text{A.68})$$

where the Planck's constant $h = 6.64 \times 10^{-34} \text{ m}^2\text{kgs}^{-1}$; the laser frequency, $\nu = c\lambda^{-1} = 1.93 \times 10^{14} \text{ Hz}$ for 1550 nm wavelength; from the DC transmission data the average power, $\langle P \rangle = \frac{T_{\lambda\text{probe}}}{\mathfrak{D}} \frac{\text{V}}{\text{VmW}^{-1}} \approx \frac{0.08}{15} = 0.0053 \text{ mW}$.

With the detector quantum efficiency, η the power spectral density at the photodetector can be found as follows

$$S_W^{\text{shot}} = \frac{2h\nu \langle P \rangle}{\eta} \text{W}^2\text{Hz}^{-1}, \quad (\text{A.69})$$

where, $\eta = \frac{R\lambda}{\lambda} \times \frac{hc}{e} = \frac{1 \text{ AW}^{-1}}{1550 \text{ nm}} \times 1240 \frac{\text{Wnm}}{\text{A}} = 0.8$. Now plugging all values in equation A.69 we have, $\sqrt{S_W^{\text{shot}}} = 1.3 \text{ pWHz}^{-1}$ which gives the power spectral density of shot noise in voltage by $\sqrt{S_V^{\text{shot}}} = \sqrt{S_W^{\text{shot}}} \times \mathfrak{D} = 19.5 \text{ nVHz}^{-\frac{1}{2}}$

After blocking all input light, the measured dark current, $\sqrt{S_V^{\text{dark}}}$ of photodetector around the resonance frequency from Zurich lock in amplifier is found as $196 \text{ nVHz}^{-\frac{1}{2}}$ and from spectrum analyzer as $126 \text{ nVHz}^{-\frac{1}{2}}$. This results in $(S_V^{\text{white}})^{1/2}$ of $197 \text{ nVHz}^{-\frac{1}{2}}$ and $128 \text{ nVHz}^{-\frac{1}{2}}$ for vacuum and atmospheric pressure, respectively. Expressed in displacement noise (converted using responsivity (equation 2.21)) $(S_x^{\text{white}})^{1/2}$ is ≈ 20.3 for lock-in and ≈ 13.1 for spectrum analyzer in $\text{fmHz}^{-\frac{1}{2}}$.

A.7 Squeeze film effects

There is a small gap (140 nm) between our nanomechanical devices and the waveguides in the optical ring resonator. This geometry could indicate squeeze film effects, wherein the air in the gap can act to increase the effective stiffness of the nanomechanical

beam and hence affect its dynamic behavior. Using the dimensionless squeeze number [204, 205] for strip plates we can determine whether viscous or spring effects are dominant. The squeeze number is defined as below

$$\sigma = (12\mu L^2\omega)/(P_a h_a^2), \quad (\text{A.70})$$

where σ is the dimensionless squeeze number, μ is the dynamic viscosity (Nsm^{-2}) of the medium, L is the characteristic length scale (here it is the width of the nanomechanical beam, 220 nm), ω is the angular frequency of the nanomechanical beam, P_a is the pressure of the medium, and h_a is the gap between the beam and the photonic waveguide. In practice, $\sigma < 1$ signifies a regime when squeeze film spring effects are not important and that viscous damping effects are dominant. Using the values for our primary device, we calculate a squeeze number of 0.4, which implies viscous damping is the dominant effect. It is not important to our general analysis what precisely causes the damping at higher pressures (whether it be pure viscous air damping or squeeze film air pot damping), therefore, we conclude that further squeeze film analysis is unnecessary.

A.8 Fundamentals of optomechanical interaction in a Fabry-perot cavity

A generic example of an optomechanical cavity system is a Fabry-Perot cavity formed by two mirrors illustrated in Figure A.3. According to the Maxwell theory of electromagnetism, radiation/light pressure can induce optical force by transferring momentum to the mirrors of an optical cavity (Figure A.3 (a)) which can displace the free mirror [206].

The schematic of Figure A.3 (a) illustrates the most straightforward detection of motion due to the reflection of photons from a mechanical oscillator. If the oscillator moves by δx then the phase difference $\delta\varphi$ of the reflected beam will be

$$\delta\varphi = \kappa n_{\text{eff}}\delta x, \quad (\text{A.71})$$

where, $\kappa = \omega/c = 2\pi/\lambda$ is the wave vector of the incident light, ω , c and λ are the angular frequency, speed and wavelength of that light, $n_{\text{eff}}\delta x$ is the change

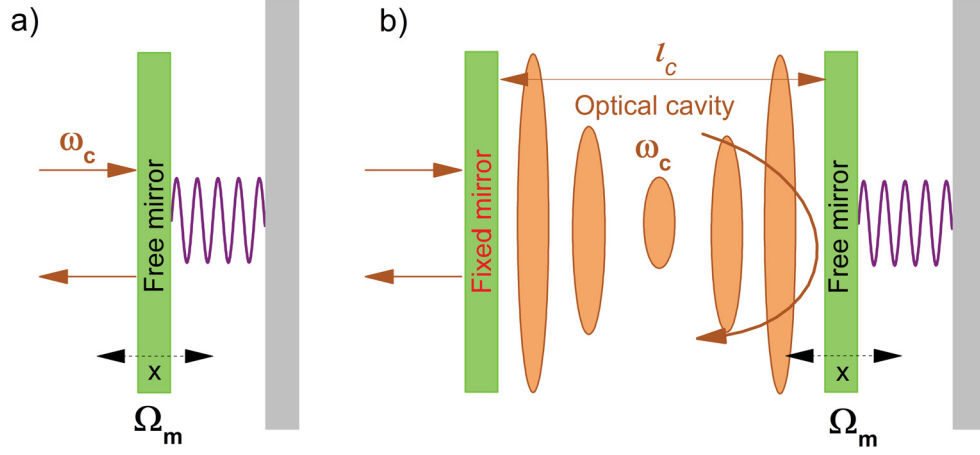


Figure A.3: **Schematic of typical optomechanical interaction.** a) Momentum transfer on light reflections, b) Fabry-Perot cavity as an example: The incoming light passes through the fixed mirror and resonant inside the cavity. The free mirror is the mechanical compliant. Position fluctuations, x of the free mirror causes fluctuations in optical path length which changes the optical resonance condition. The trapped light inside the cavity interacts many times with the mechanical element instead of just once and thus enhance the responsivity. In this way the mechanical motion becomes imprinted on the transmitted/reflected light signal.

in optical path length l and n_{eff} is the effective refractive index of the medium. If δx is small compared to the wavelength of light then $\delta\varphi$ is also small to detect. By using a reflecting mechanical oscillator as one of the mirrors in a Fabry-Perot cavity as depicted in Figure A.3 (b) $\delta\varphi$ can be boosted up for the same δx by accounting for the number of round trips of photons inside the cavity in a vacuum ($n_{\text{eff}} = 1$) as below

$$\delta\varphi = \frac{4\mathbb{F}}{\pi} \kappa \delta x. \quad (\text{A.72})$$

where the number of round trips of photons inside the cavity is expressed as cavity finesse, $\mathbb{F} \equiv \Delta\omega_{FSR}/\alpha$, here $\Delta\omega_{FSR} = \pi c/L$, is the free spectral range of a cavity of length L and α is the loss rate. So, the above equation tells that it is possible to have an enhanced phase change for a smaller displacement of the mechanical element by trapping the light inside an optical cavity. The rate of change of the optical resonance frequency, ω_c , with respect to the mechanical displacement define the optomechanical coupling constant, $G_0 \equiv \delta\omega_c/\delta x$. For a Fabry-Perot cavity $G_0 \equiv -\omega_c/l$. Thus equation A.72 can be written as

$$\delta\varphi = \frac{4G_0}{\alpha} \delta x. \quad (\text{A.73})$$

The equation above gives the phase change as a function of cavity resonance frequency/wavelength for a displacement δx . The light confined in the cavity reflects multiple times and thus produces standing waves for specific resonance frequencies that satisfy the condition of constructive interference. Almost all optomechanical systems follow the same principle stated above for a Fabry-Perot cavity.

Appendix B

Chapter 3

B.1 Notes on dynamic ranges measurements

B.1.1 Acoustic interference during piezoactuation

Large driving power and small quality factor, as we have in case of atmospheric pressure in our NOMS devices, can lead to bulk acoustic related complications in device piezoactuation. This issue has been well summarized in the thesis of Igor Bargatin [139] and is discussed in this section.

In our nano-phonic measurement system we can actuate NOMS either optically or piezoelectrically [53]. With our moderate values for optomechanical constants in these devices, we have found that optical forces are insufficient to drive up to the onset of Duffing non-linearity. Piezoshaker actuation with the aid of an rf-amplifier can provide enough driving power to test the Duffing behavior of our devices up to ≈ 30 Torr.

We follow the usual practice in piezodrive in which the chip containing vibrating elements like NEMS (see Figure 2.1) is glued to the top of a piezoshaker. When the piezoshaker is subjected to driving voltage it physically shakes the chip containing NEMS devices. The amplitude of the chip surface motion, a_s , applies a center of mass force to the NEMS of $F_{in} = M_{eff}\Omega_0^2 a_s^2$, where M_{eff} and $\Omega_0/2\pi$ are the effective mass and resonance frequency of the device in vibration. In the ideal scenario a_s , is assumed frequency independent (i.e. uniform within the frequency sweep range). For a high Q device (which has a "narrow" frequency span) amplitude of this surface motion is negligible compared to the resonator's amplitude a_{NEMS} . If $Q \gg 1$, the amplitude

of the NEMS can be written as

$$a_{NEMS} = Q \times a_s. \quad (\text{B.1})$$

For frequencies over 1 MHz, a_s is not uniform across the surface and varies by frequency for a given applied RF driving voltage. Propagation of ultrasonic waves inside the piezoshaker and NEMS substrate, including interface reflections, can result in complicated interference patterns of these waves. A complex spatial and frequency dependent motion of the chip surface due to such bulk acoustic interference results in frequency dependent drive strength (i.e. a_s). This results in a forest of weak, bulk-acoustic related resonance peaks when a large frequency is spanned. Depending on the size of the piezoshaker and the chip mounted on it, there is a characteristic span of driving frequency, Δf , within each acoustic resonance where the surface motion may be considered quasi-uniform. This Δf can vary at different frequencies. If a high Q NEMS is driven within any of the Δf , the NEMS resonance can be described by equation B.1 because of negligible and quasi-uniform magnitude of a_s compared to a_{NEMS} . In larger damping, when $\Gamma \gg \Delta f$, then resonance shape of the NEMS can be severely distorted (*cf.* Figure 3.3 for 40 and 760 Torr).

Figure B.1 (a) shows amplitude and phase response of a single NEMS device where the frequency span crosses 8 or 9 bulk acoustic peaks. The driving power is kept constant at 0 dBm as scans are taken at differing pressures (and damping conditions). Up to about 50 Torr, the background region outside of the span Δf_s is almost identical. The pressure changes have essentially no effect on bulk acoustic resonances, as would be expected. The signal to background ratio of the NEMS resonance peaks (against this bulk acoustic background) range from about 60x to 3x and the NEMS peaks are easily identifiable. For 85 and 760 Torr responses, the NEMS resonance widths are wider than Δf_s , and the NEMS amplitude contribution to the signals is comparable to the bulk acoustic resonance contributions. Thus, extra care needs to be taken when identifying NEMS resonance peaks at highest damping, for example, by tracking the peak from vacuum to atmosphere, to properly identify the appropriate locking frequency range (in this case, within the Δf_s span).

To fully confirm the nature of the acoustic wave interference during piezodrive, we measured the same device with optomechanical drive and the comparison is shown in

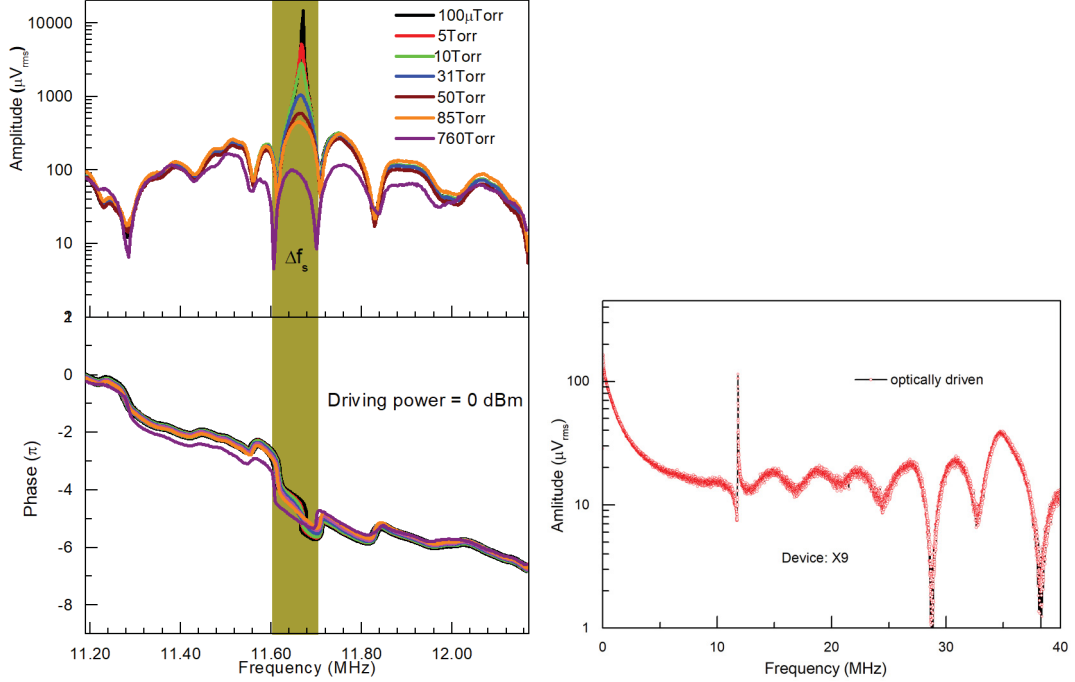


Figure B.1: **a) Evolution of mechanical resonance shape of the device by piezoactuation from high vacuum to atmospheric pressure.** A forest of acoustic peaks (Δf_s s) can be seen either side of the resonance peak at all pressures. The shaded area is the characteristic frequency span, Δf_s due to acoustic wave interference within which mechanical resonance can be seen. Mechanical resonance is showing a strong dependence on damping in contrast to surface motion. Phase evolutions of same experiments are shown at the bottom. **b) Measurements of optomechanically driven responses at 15 Torr.** Surface acoustic wave interference is absent. From [16]. Reprinted with permission from AAAS.

Figure B.1 (b) for a wide span. The optical drive response does not see the forest of bulk acoustic resonances, as expected. The optical drive has its own background due to imperfect filter extinction of the drive laser at the photoreceiver [53], with its own 4 MHz interference pattern, but this is irrelevant for the present work.

B.1.2 Non-linearity onset: modification at high pressure

It is evident from equation 3.6 that for a given device (geometry is constant) with increasing damping (i.e., decreasing Q) a_c increases. At the same time, decreasing Q requires large chip surface motion to achieve the same amplitude, since $a_{\text{NEMS}} \approx Q a_{\text{surface}}$. This combination necessitates quickly ramping up the drive power at high damping. Higher driving power by piezo-actuation generally causes on-chip heat

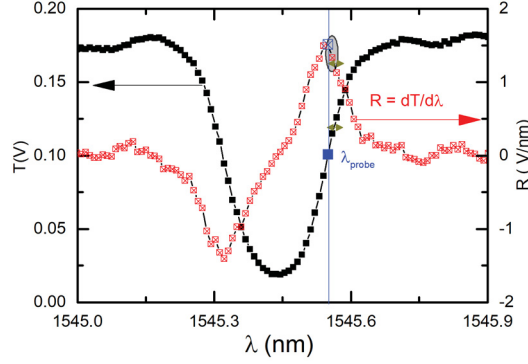


Figure B.2: **Optical resonance at 26 Torr.** Left axis is the measured transmission in Volts and the right axis is the corresponding slope. Blue data point at 1545.549 nm has the maximum slope, and probe wavelength is set at this wavelength for a transmission power around 0.1 Volts. By sitting on probe wavelength we are able to collect any transient change in probe power (transmission) by a home-built lab-view program. Dark yellow arrow symbol at 1545.569 nm, 0.12 Volts is the observed experimental shift due to piezo-heating effect during the 26 Torr power sweep shown in the next figure. From material properties it is discussed that optical ring resonance shifts by 80 pm for 1 K temperature change. Hence, this 20 pm shift corresponds to about 0.25 K temperature rise. The red squares are the change in slope of the optical resonance. The small gray circle shows the change in slope within the piezo-heating regime. From [16]. Reprinted with permission from AAAS.

generation as more power is dumped into the piezoelectric. Induced heating from actuation and detection is a familiar phenomenon in NEMS. It can happen either by the heating effect of driving or by optical adsorption and is common to optomechanical devices [207, 208]. Temperature induced changes to both the resonance frequency and the ring responsivity can complicate the nonlinearity measurement when there is significant heating during the ramp in power.

The changing responsivity is the dominant effect of the two. Figure B.2 shows the photodetector transmission in vicinity of the ring resonance and the slope $\frac{dT}{d\lambda}$ which is proportional to the transduction responsivity. During temperature changes, the curves shift causing transmission and responsivity changes. It is straightforward to track these values during a power sweep, which allows correcting 1 dB compression point values. Figure B.3 (a) shows photoreceiver transmission captured during vacuum, 5, 10, and 26 Torr power sweeps. Transmission (and implied responsivity) are constant for vacuum, 5, and 10 Torr. These sweeps max out below +30 dBm power. For 26 Torr the power sweep goes up to +38 dBm and is accompanied by significant heating. The

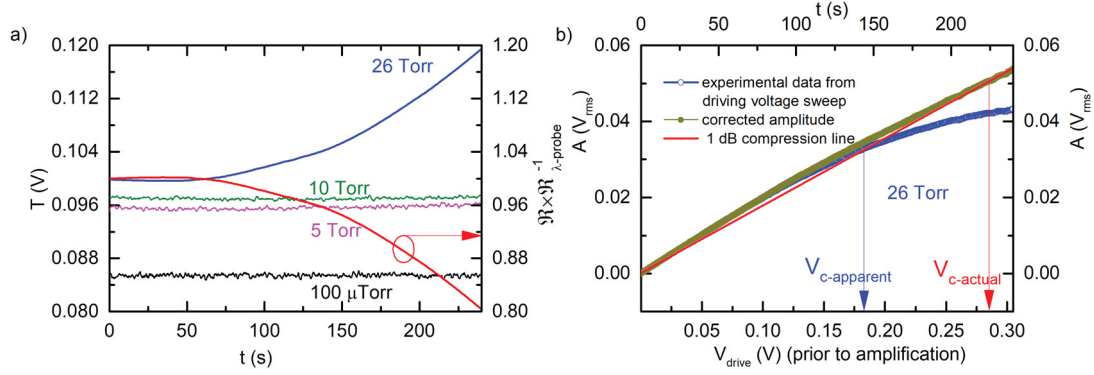


Figure B.3: **left: Left axis represents the temporal change of detected probe power at different pressures during voltage sweep shown in the right plot.** At low pressures flat optical transmission plots indicate absence of appreciable piezo-heating. 26 Torr data (blue) shows a significant change due to piezo-heating with a $0.25\ C$ temperature change. Corresponding slope change (due to tuning of the optical cavity with temperature) is normalized along the right axis. The slope change can be used to re-normalize data in the right panel. **Right : Amplitude sweep and corrected amplitude sweep with increasing driving voltage.** The corrected amplitude is obtained by dividing the experimental data by the red plot in the left panel ($\frac{R}{R_{\lambda\text{-probe}}}$). The blue line is the original data, the brown line is the corrected amplitude, and the red line is the 1 dB compression linear line. The red line crosses the blue data at the blue arrow and the brown data at the red arrow. The blue arrow indicates the early nonlinearity (for 1 dB compression) at 0.132 rms Volts or -4.7 dBm prior to amplifier. The effective gain of the rf-amplifier with a 6 dB attenuator is 38.3 dBm. Thus the apparent critical drive power from experimental data is 33.6 dBm. From the corrected amplitude response the actual critical drive is around 0.202 rms Volts or 37.42 dBm as shown by red arrow. From [16]. Reprinted with permission from AAAS.

experiment is conducted a few degrees above room temperature with the chip holder temperature locked by PID control. The placement of the Pt RTD sensor directly on the piezo produces a counter intuitive effect of actually lowering the chip surface temperature as the piezo dissipates more power (this is because the PID) heater shuts off to compensate). Thus the piezo heating blue shifts the optical ring resonance causing an increase in transmission, and a corresponding decrease in responsivity.

Figure B.3 (b) shows the 26 Torr power sweep plotted as response *vs.* V_{drive} . The original response voltage, and the corrected response voltage (the latter divided by normalized responsivity $\mathcal{R}/\mathcal{R}_{\lambda\text{-probe}}$) give apparent and corrected critical drive values, respectively.

B.1.3 A note on high drive powers

It should be remembered that these tiny mechanical resonators require only miniscule amounts of stored energy to be driven to their nonlinearity limits. Even at largest damping reported here, required mechanical powers are only in the pW range. The high piezodrive powers we used (e.g. 4 W) are thus a bit misleading. Piezo drive is inherently inefficient since power is applied to the whole chip. Transfer from electrical to mechanical also becomes extremely inefficient above 1 MHz frequency. Our experiments were conducted with piezodrive since that is what we were configured for. There are alternatives to provide drive power more efficiently (both more localized and suffering less high frequency loss) to MEMS and NEMS devices such as capacitive drive, and more recently optomechanical drive. These techniques are several orders of magnitude more efficient. (Our initial tests indicate reaching mechanical nonlinearity with sub-mW optical power modulations.) In particular, optomechanical driving force is an avenue where increasingly efficient driving can be pursued by increasing optomechanical coupling.

The limitation for optomechanical drive will tend not to be from inability to provide enough drive power. Rather, the exponential nature of the evanescent electromagnetic fields that provide the coupling can cause drive power nonlinearity and displacement readout nonlinearity. These nonlinearities can limit access to the full upper end of the intrinsic dynamic range (as mentioned in the discussion). This is a topic our group is actively studying [J. N. Westwood-Bachman, W. K. Hiebert, unpublished]. This problem can be somewhat mitigated by the freedom to choose a precise amount of optomechanical coupling for the mechanical dynamic range of interest.

B.1.4 A note on comparing different drive levels

The question can be asked, "is it fair to compare different drive levels for different Q conditions" (that is, loading up a lower Q device with more energy by driving it with higher power). After all, if the devices were provided with the same driving force, the high- Q device would exhibit better stability performance. This question is, perhaps, at the heart of why the fascinating flat-band regime has not yet been discovered and explored (see the next chapter). We point out in the introduction

(Figure 1.4), that the traditional view assumes that one leaves the drive power or drive force untouched when Q falls off. Doing so quickly reduces the DR . When people talk about high- Q devices having more stability, we assert that what they partly mean is that high- SNR or high- DR devices have more stability. To date, high- DR and high- Q have been assumed to be synonymous. There is no fundamental reason for this to be so, particularly when NEMS are inherently ultralow power devices, and the intrinsic DR scales with the damping, as we have established.

We assert that it is fair to provide higher drive power to the lower- Q device. In our demonstration, both the high- Q and the low- Q (at least down to Q of a few hundred) device are operating at their fundamental limits (i.e. taking advantage of the full intrinsic dynamic range). They are both holding the maximum amount of energy that they can store without injecting excess phase noise from nonlinear amplitude-to-phase conversion. The lower- Q device's capability to store more (linear) energy is an inherent fundamental advantage that it has.

B.1.5 Notes on optomechanics

B.1.5.1 Optomechanical coupling coefficient calibration

The device under test is a doubly clamped beam (DCB) approximately $9.75\ \mu\text{m}$ long and $160\ \text{nm}$ thick in the direction of oscillation. It is fabricated on a standard nanophotonic silicon on insulator wafer with a $220\ \text{nm}$ thick device layer. The DCB oscillates in the plane of the wafer towards and away from a racetrack resonator optical cavity, in an all-pass configuration, which is fabricated $120\ \text{nm}$ away. The waveguide which creates the racetrack resonator is $430\ \text{nm}$ wide. The racetrack resonator has an optical Q of ~ 8400 , a linewidth of $0.18\ \text{nm}$, a free spectral range of $\sim 13.1\ \text{nm}$, and a finesse of ~ 70 .

To calculate the optomechanical coupling coefficient ($g_{\text{om}} = \partial\omega/\partial x$) from simulation, we can use the change in effective index over distance to calculate the optomechanical coupling [50, 111]. This calculation results in an optomechanical coupling coefficient $g_{\text{om}} \sim 2.86\ \text{rad GHz nm}^{-1}$.

The measured optomechanical devices are designed to operate deep in the Doppler regime where the overall optical cavity intensity decay rate (κ) is much, much greater

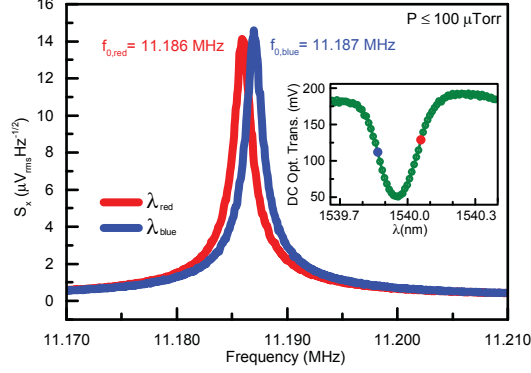


Figure B.4: **Optomechanical spring effect in the device.** Blue and red detuning amounts are shown on the inset. They are approximately at $\pm \kappa/2$, respectively, which is where maximum frequency detuning would occur. From [16]. Reprinted with permission from AAAS.

than the mechanical frequency of the device (Ω_0) [93]. In this way, gains are made with mechanical transduction sensitivity while minimizing optomechanical effects such as optical damping or amplification. This maintains a more simple system for a more robust sensor. The κ of our optical racetrack is approximately $1.5 \times 10^5 \text{ MHz} \cdot \text{rad}$ compared to $\Omega_0 = 70.3 \text{ MHz} \cdot \text{rad}$, which satisfies the $\kappa \gg \Omega_0$ criterion.

To confirm that the optical damping effects are negligible compared to the mechanical damping in the system, the optical spring effect is used to extract the light enhanced optomechanical coupling strength, g , of the system using the equation[93]

$$\delta\Omega_0(\Delta)|_{\kappa \gg \Omega_0} = g^2 \frac{2\Delta}{\kappa^2/4 + \Delta^2}. \quad (\text{B.2})$$

Above, Δ is the wavelength detuning of the probe in relation to the optical cavity centre (red-detuned: $\Delta < 0$, blue-detuned: $\Delta > 0$). The measurement is taken at the greatest slope of the DC optical transmission curve on the blue and red side of the optical cavity (inset Figure B.4) which is approximately equal to a detuning of $\pm \kappa/2$, respectively. Assuming the optical spring effects are equal and opposite for the blue and red measurement, $\delta\Omega_0 \approx 3.2 \text{ kHz} \cdot \text{rad}$ as shown in Figure B.4. This gives a value of $g \approx 16 \text{ MHz} \cdot \text{rad}$. To convert this to the optomechanical coupling coefficient for comparison to simulated values, we can use the following equation:

$$g_{\text{om}} = \frac{g}{n_{\text{cav}}^{1/2} x_{\text{ZPF}}}. \quad (\text{B.3})$$

In the above equation, n_{cav} is the number of photons in the optical cavity and

x_{ZPF} is the zero point fluctuations of the DCB. This results in an experimental $g_{\text{om}} \sim 2.83 \text{ rad GHz nm}^{-1}$.

Maximum cooling/heating for the Doppler regime will occur with the detuning used in this measurement, and the maximum optical damping/amplification is calculated using[93]

$$\Gamma_{\text{opt}} \left(\Delta = -\frac{\kappa}{2} \right) = 8 \left(\frac{g}{\kappa} \right)^2 \Omega_0. \quad (\text{B.4})$$

This gives a value of $6 \text{ Hz} \cdot \text{rad}$ which is much less than the mechanical damping of $\sim 2 \text{ kHz}$. This confirms that the total damping will be dominated by the mechanical element, and optomechanical damping effects can be considered negligible.

B.1.5.2 Optomechanical Nonlinearity

One potential source of nonlinearity in optomechanical systems is a readout nonlinearity. This is caused by the Lorentzian lineshape of the optical cavity. If the amplitude of the mechanical device is sufficiently large to shift the cavity out of the linear section on the side of the Lorentzian optical resonance, nonlinearities in the transduction can occur. Briefly, the nonlinearity coefficient can be calculated using the optical cavity properties and the optomechanical coupling coefficient. By starting from the expression for the dispersive optical force,

$$F = \frac{-2P_{\text{in}}\gamma_{\text{ex}}G}{\omega(\Delta + \gamma)}, \quad (\text{B.5})$$

and expanding about the static position x_0 of the mechanical resonator, we can extract the cubic spring constant k_3 . This can be used to derive the nonlinearity coefficient α and therefore the critical amplitude. This calculation is explored more thoroughly in[209] and work ongoing in our group [J. N. Westwood-Bachman, W. K. Hiebert, unpublished].The minimum critical amplitude calculated given our optical cavity parameters is 28 nm , significantly above the nonlinear amplitude observed in experiment. For this reason, we are confident that the nonlinearity is not a result of a transduction nonlinearity.

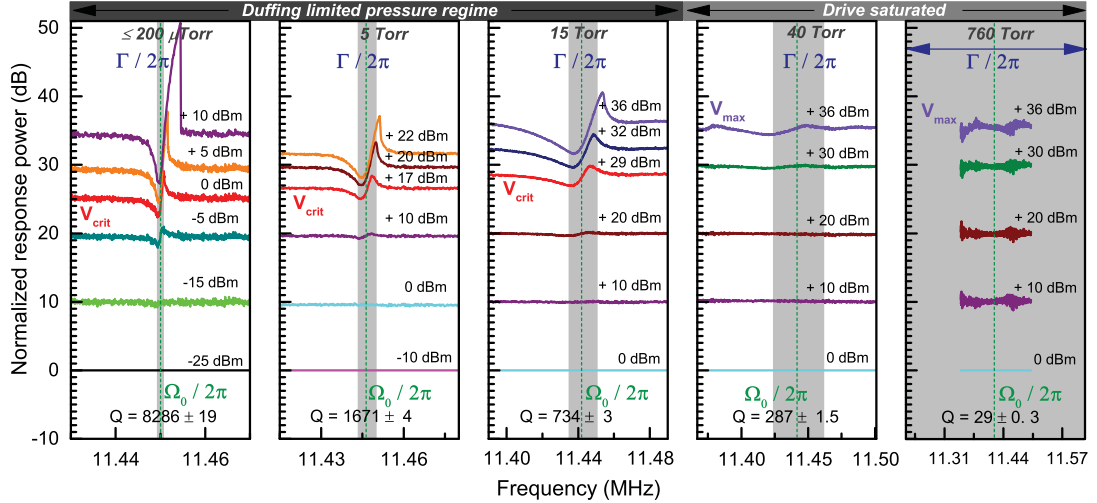


Figure B.5: **Evolution of nonlinearity with increasing drive power.** Figure 3.3 driven response data is replotted here with normalization by the lowest driven response curve. Each lowest curve, normalized by itself, produces a completely flat line. Normalization is listed in power decibels rather than amplitude decibels for quicker comparison to the drive power. Green vertical dashed lines are the resonance frequency $\Omega_0/2\pi$ and gray vertical bands represent the linewidth $\Gamma/2\pi$. Red curves labeled V_{crit} are the critical amplitude curves and inspection confirms 1 dB compression on resonance. High pressures (40 and 760 Torr) remain almost flat with increasing drive, showing only slight nonlinearity. The shape of the +36 dBm curve for 40 Torr implies that it is within a few dB of reaching critical amplitude. From [16]. Reprinted with permission from AAAS.

B.1.6 Acoustic interference, nonlinearity, and revisiting Figure 3.3

The distortion caused by acoustic interference has the unfortunate side effect of masking the nonlinearity onset at higher pressures in Figure 3.3. To circumvent this problem, we replot the driven responses from Figure 3.3 with normalization by their lowest driving power at each pressure displayed below.

This representation quickly reveals the deviation from linear behavior. In spite of their distorted shapes from acoustic interference in Figure 3.3, the drive saturated responses (40 and 760 Torr) in Figure B.5 are quite flat looking, indicating linear response. The first three pressures have obvious deviations that indicate the drive power is enough to push them nonlinear; their three critical drive curves should have roughly the same shape, with excursions away from a flat line by a few dB. The vacuum case has a slightly higher excursion at critical voltage although close inspection shows

that these red curves do all have a 1 dB compression on resonance. The discrepancy perhaps calls for a new definition of end of linear range other than 1 dB compression, but this discussion is beyond the scope of the present work.

For 40 and 760 Torr, a hint of nonlinearity is evident at higher driving powers (+30 and +36 dBm for 40 Torr and +36 dBm for 760 Torr). For example, compare +36 dBm at 40 Torr to +10 dBm at 5 Torr. The 40 Torr case looks to be only about 5 dB more drive power or so shy of the Duffing limit. This is consistent with a driven amplitude that is comparable to the 15 Torr case while their Q 's differ by a factor of 2.6. The available intrinsic linear driven amplitude for 40 Torr should be $2.6^{1/2}$ or about 2 dB higher which would be provided by about 5 dB more drive power, taking into account there should be about 1 dB compression in the driven amplitude. Altogether, this representation of the data helps support the analysis in the main text that the nonlinearity limit scales with $Q^{-1/2}$.

Appendix C

Chapter 5

C.1 Allan deviation due to readout imprecisions

Before discussing experimental frequency stability by thermomechanical noise, it is essential to quantify background noise contributions stems from measurement systems. The thermal noise spectral density, S_x^{th} described in section A.6 of Chapter 2 and in the current section is regarded as frequency distributed displacement noise. As discussed in Robins' phase noise analysis we have seen that only half of the total noise power contributes to the phase modulation and another half contributes to the amplitude modulation. A phase-locked loop operation is inherently insensitive to noise due to amplitude modulation [210]. Hence, any external interactions or noise which may translate into phase modulation can result in excess fluctuations in the oscillation frequency (set at the resonance frequency of the resonators) of the PLL. In conventional NEMS transduction additional noise from readout instruments often referred as background noise dominates over mechanical motion as illustrated in the Figure 1.4 of the Chapter 1. To achieve a fundamental limit of frequency stability of nanomechanical resonator down to its thermal limit it is necessary to attain off resonance impressions in mechanical vibration due to background significantly lower than thermal displacement noise, and it is accomplished in the current work as described in the Figure 2.6 for our optomechanical system. In ref. [210] authors discussed the effect of incoherently $\delta f_{total} = \sqrt{\delta f_{th} + \delta f_{background}}$ added background noise on the thermal motion limited frequency noise which scales with $\tau^{-3/2}$ which is in contrast to thermal noise. Ref. [210] gives the total frequency noise due to

background noise as

$$\delta f_{\text{background}} = \frac{(S_x^{\text{white}})^{1/2}}{\pi x_d} \tau^{-3/2}.. \quad (\text{C.1})$$

In section A.6 we have shown that in the current work the background noise S_x^{white} is dominated by the photodetector dark noise and is around $20 \text{ fmHz}^{-1/2}$ for lock-in used to measure the frequency noise. In the above equation, x_d is the driven amplitude of measurement. Within the Duffing limited region, it is the critical amplitude, a_c . Averaging time is related with bandwidth by $\tau = 1/f$. For background contributions equation C.1 is widely accepted by other groups also like Kippenberg [127]. Now corresponding Allan deviation due to background induced frequency noise can be written regarding equation C.1 as below

$$\sigma_{\text{background}} = \frac{\delta f_{\text{background}}}{f_0} = \frac{(S_x^{\text{white}})^{1/2}}{\pi f_0 x_d} \tau^{-3/2}.. \quad (\text{C.2})$$

In Figure 5.3, Allan deviations due to the background are shown by orange shaded region at the bottom of the plot which results from equation C.2 and is well below the thermal limit at each pressure.

C.2 Phase noise behavior with damping in *Science* is equivalent to open loop behavior

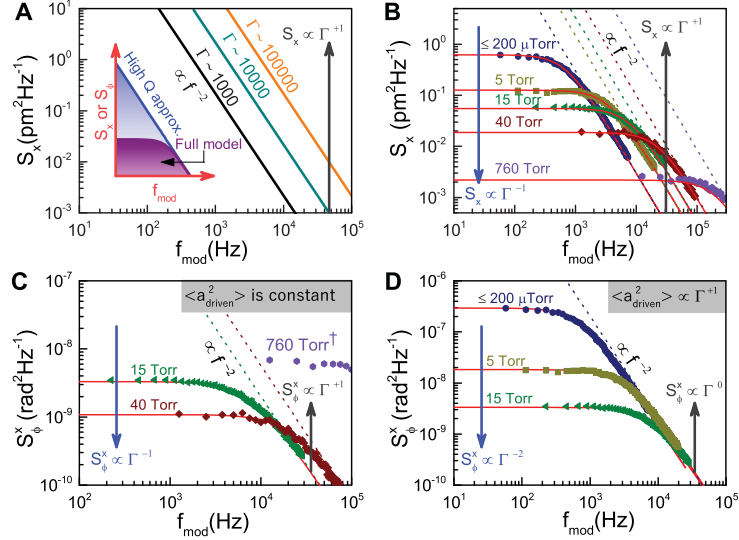


Figure C.1: Noise power behaviour with respect to damping can be proportional, constant, inversely proportional, and inversely quadratic. (A) Concept of thermomechanical displacement noise being proportional to damping for pure rolloff. **Inset.** Pure rolloff (high- Q approximation) over-estimates integration in comparison to low-pass full model. (B) Measured thermomechanical noise fit to equation 8; noise is proportional to damping above the rolloff, inversely proportional below. (C) Measured displacement noise converted to phase noise (Eqn. 9) with constant driven amplitude; noise is proportional to damping above the rolloff and inversely proportional below. †760 Torr is at a lower driven amplitude than 40 and 15 Torr and is included here for completeness. (D) Measured displacement noise converted to phase noise with squared driven amplitude proportional to damping; noise is independent of damping above the rolloff and inversely quadratic below. From [16]. Reprinted with permission from AAAS.

C.3 Further verification of open loop frequency fluctuations

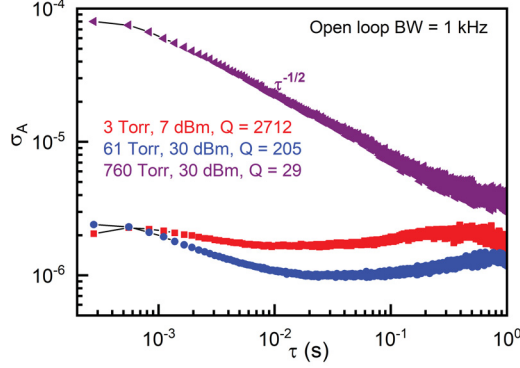


Figure C.2: Measured Allan deviations at different pressure regimes and various driving powers with 1 KHz demodulation bandwidth in another series of experiments. Similar to the main text results, this plot also shows a gradual weakening f^{-1} noise with increasing air pressure.

C.4 Notes on PLL measurements

For resonance frequency shift measurements phase-locked loop is advantageous over open-loop measurements because of HF2 PLL's ability to produce frequency as the output of the sensor. It is seen that a lower PLL bandwidth yields higher noise rejection to get lower frequency stability than theoretical predictions, but it also lessens NEMS resonators agility (slower frequency sweep rate) and reduces measurement accuracy. PLL transfer function depicted in Figure 5.5 shows that it is the low-pass integration (K_i parameter) that reduces the effective bandwidth for lower Q transfer function because of particular placing of zero and pole. So while the low-pass filter mitigates some problems through a cleaner frequency output, it also creates some problems by slowing the loop response. As a consequence, PLL operation with lower bandwidth can also attenuate resultant frequency shift because of an event of interest such as sudden temperature change or mass addition. Rewriting equation 5.2 for a frequency deviation $\Delta\Omega(s)$ at NCO output we have,

$$\chi_{\Delta\omega, \text{PLL}}^{\text{th}}(s) = \frac{\Delta\Omega(s)}{\Theta_n(s)} = \frac{1}{\tau_r} \frac{(sK_p + K_i)\chi_L(s)}{s^2 + \frac{s}{\tau_r} + (sK_p + K_i)\chi_L(s)}, \quad (\text{C.3})$$

where, $\Theta_n(s)$ is the input phase noise from the NEMS, $\tau_r = \frac{2Q}{\Omega_0}$, $K_p = P$ in rad/s/rad, and $K_i = \frac{K_p}{I}$, and $\chi_L(s) = \left(\frac{\Omega_0}{s+\Omega_0}\right)^4$ for applied low-pass filter or 1.

If we introduce a phase step

$$\Theta_n(s) = \frac{\Delta\Phi}{s},$$

then

$$\Delta\Omega(s) = \frac{\Delta\Phi}{s} \frac{1}{\tau_r} \frac{(sK_p + K_i)\chi_L(s)}{s^2 + \frac{s}{\tau_r} + (sK_p + K_i)\chi_L(s)}. \quad (\text{C.4})$$

Plugging $\Delta\phi = \frac{2Q}{\Omega_0}\Delta\omega = \tau_r\Delta\omega$ into above

$$\Delta\Omega(s) = \frac{\Delta\omega}{s} \frac{(sK_p + K_i)\chi_L(s)}{s^2 + \frac{s}{\tau_r} + (sK_p + K_i)\chi_L(s)}. \quad (\text{C.5})$$

If we assume $\chi_L(s) = 1$ and take the inverse Laplace transform (using the symbolic

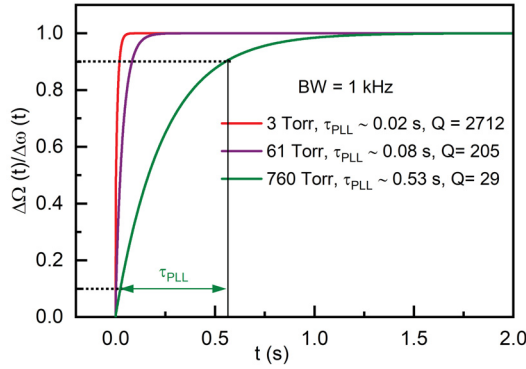


Figure C.3: **Normalized Frequency response due to a phase step in Phase locked transient frequency output at different damping.** The plot demonstrates MATLAB simulated results for equation C.7 to follow the transient frequency change for a phase change by any event at different damping in PLL operations. Measured values at each pressure with PLL advised PI parameters for a PLLBW of 1 kHz have been used in the simulation. It is evident that PLL response becomes slower at a lower Q by integration gain effect at a lower frequency in the PLL transfer function than that of a higher Q . We define PLL time constant, τ_{PLL} as the time taken to frequency rise from 10% to 90% of the total frequency shift.

toolbox in MATLAB), we obtain the time-response of the frequency fluctuations $\Delta\Omega(t)$:

$$\Delta\Omega(t) = \Delta\omega \left(1 - e^{-\left(\frac{K_p\tau_r+1}{2\tau_r}\right)t} \left[\cosh\left(\frac{a}{2\tau_r}\right)t - \frac{K_p\tau_r-1}{a} \sinh\left(\frac{a}{2\tau_r}\right)t \right] \right), \quad (\text{C.6})$$

where, $a = \sqrt{K_p^2\tau_r^2 + 2K_p\tau_r - 4K_i\tau_r^2 + 1}$ is a placeholder variable,

We then plot normalized frequency fluctuations, i.e.,

$$\frac{\Delta\Omega(t)}{\Delta\omega} = (1 - e^{-\left(\frac{K_p\tau_r+1}{2\tau_r}\right)t}) \left[\cosh\left(\frac{a}{2\tau_r}\right)t - \frac{K_p\tau_r - 1}{a} \sinh\left(\frac{a}{2\tau_r}\right)t \right]. \quad (\text{C.7})$$

Using measured parameters, e.g., Q , Ω_0 at given pressure and PI controller parameters for a chosen bandwidth in equation C.7 one can quickly get transient step response of PLL at different damping conditions to get the desired PLL time constant for respective bandwidth. Figure C.3 shows representative plots for three different pressures. Simulated results in Figure C.3 verifies that for $\omega \ll \Gamma$ reduce the PLL ability to track any frequency shift event that happens faster than PLL time constant. In practice, many sensing experiments are implemented in seconds for which shorter PLL time constant may not be a problem to track resultant frequency shift measurement at longer scale.

Bringing temperature sensing experiment from the next chapter of this thesis, we are going to illustrate experimental PLL response here. By shining 1064 nm laser, we induced instant heat at different damping conditions to see the frequency jump for 1 kHz PLLBW as in Figure C.4. 3 Torr measurement shows a larger instantaneous jump due to frequency change by relative temperature modification. As mentioned, in the caption, these experiments are for proof of concept. We did not design experiments for any short-pulse measurement. Moreover, focusing the heating laser appropriately on the device with our current set-up is a tedious job and hard to compare the measured temperature gradient from one experiment to another. This is why we will move into resistive heating by PID controlled temperature controller that was used in all cases in this project.

The experimentally observed PLL response time reasonably agrees with that of simulated in Figure C.3. Also, from the PLL transfer function analysis, we have seen that mechanical sensor performance at a longer time scale accounts actual resonator contribution by region I. So, PLL artifacts will not affect any frequency shift measurements at longer time scale. As a conceptual illustration, Figure C.5 schematically describes that any missing event faster than τ_{PLL} cannot reduce the total frequency shift at a longer time. In gas sensing experiments we will show that a GC pulse equivalent to 5.1 s requires to track NEMS frequency for measuring gas adsorption and desorption. So we do not feel any further investigation on PLL

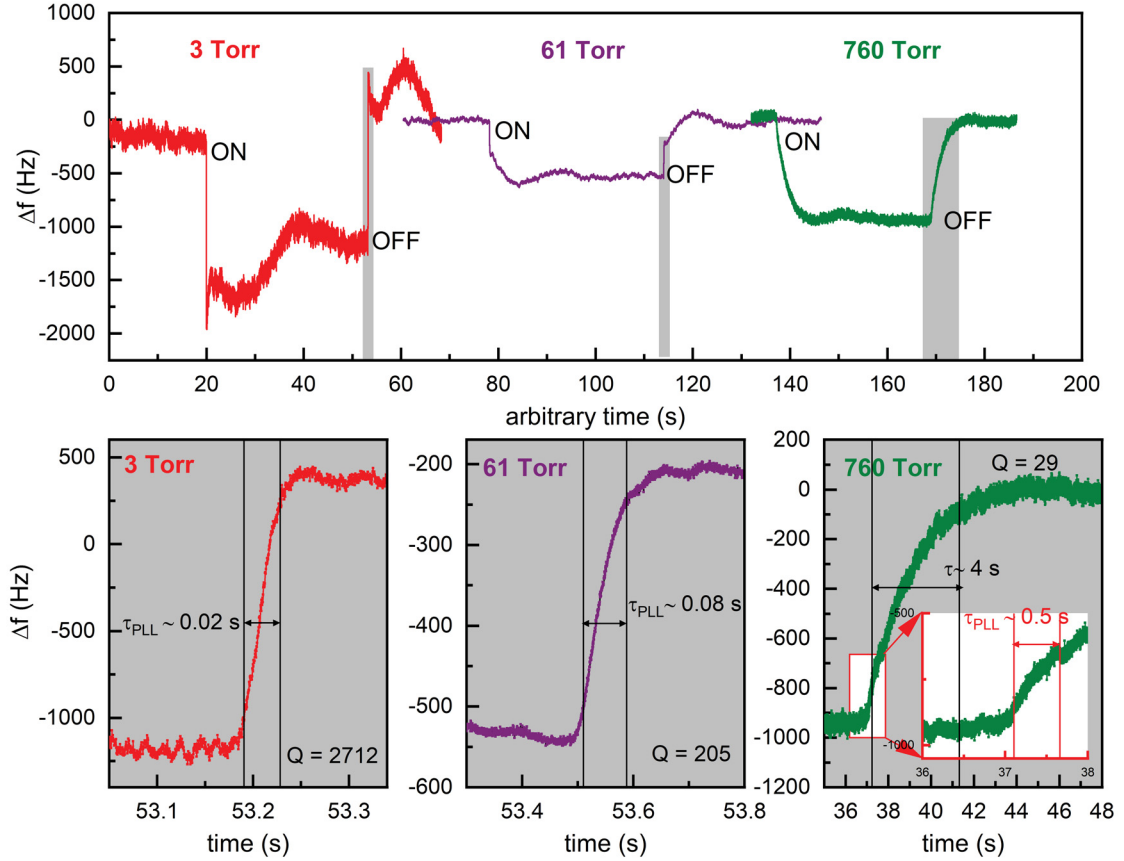


Figure C.4: **An instantaneous change in frequency of DCB nanomechanical resonator due to heat adsorption/desorption after irradiating 1064 nm laser at different pressures.** Top: Irradiated laser change relative temperature of the device surface, which results in a sudden frequency jump at ON state before attaining a steady-state of current temperature at a longer time. At OFF state reverse effect happens and highlighted in the shaded region. Bottom: zoom-in portion shaded region at each pressure. To see the frequency shift at 760 Torr inset is the zoom-in portion to get experimental time constant of PLL. The resultant time constants from these experiments agree well with those from the simulation in Figure C.3. The slow response ($\tau = 4$ s) at 760 Torr for total frequency shift could be due to temperature controller dynamics. We have some issues with appropriate laser focusing on the chip (see next chapter) to compare the relative temperature change by laser shining. As a proof of concept, these experiments clearly show that PLL response becomes slower with lower- Q . Slow response of PLL at 760 Torr masks the frequency jump at its output. However, in all cases, PLL response is reversible and measures the actual temperature change for a longer duration (details will be found in the next chapter).

short-term response.

We have derived the frequency stability equation based on Phase-locked loop theory and required simulation so well to explain the frequency output for sensing experiments.

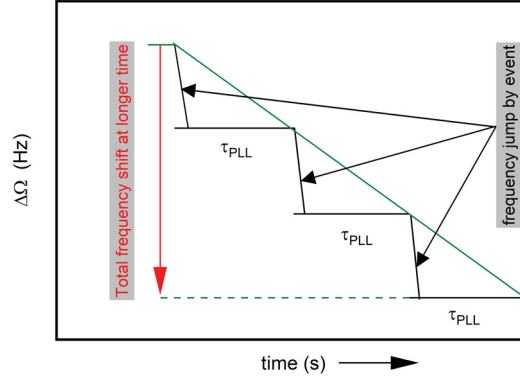


Figure C.5: **Schematic view of transient frequency shift measurement at low Q condition when an event occurs faster than PLL time constant, τ_{PLL} :** Although a slower PLL is missing the faster frequency shift at every event of interest, it can track the actual cumulative frequency shift for a time longer than the respective time constant of the PLL experiments. Hence, choosing a suitable bandwidth for sensing experiments is user-defined.

Since PLL frequency output is more consistent as well as directly measurable, we decide to test the NEMS sensor by PLL resonant frequency tracking. Also, to create a known event on PLL tracked resonance frequency, the resistive heater of the PID controlled temperature controller is suitable in the experiments instead of inconsistent 1064 nm laser focusing discussed earlier. In the next chapter, we will show improved performance of a mechanical sensor by developing Nano-optomechanical thermometry.

Appendix D

Chapter 6

D.1 Numerical evaluation of h and underlying thermal physics

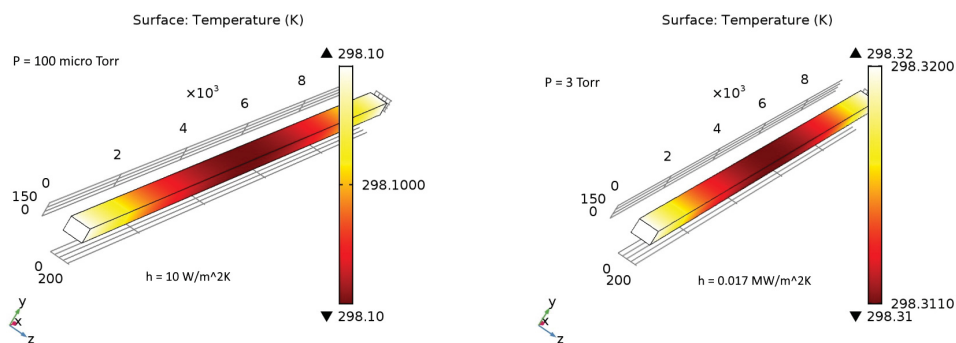


Figure D.1: **Heat transfer coefficients from COMSOL simulations at high and low vacuum.** Both ends of the DCB are at/around surface temperature measured by the optical ring at each pressure. The middle portion of the beam is stretched to a driven amplitude (at resonance) contains the resonance frequency. Thus, frequency shift measurements by a PLL can only see the temperature of the beam portion that contains the resonance. Here, the Up to 3 Torr, the resonance portion of beam feels the exact surface temperature like as the ring.

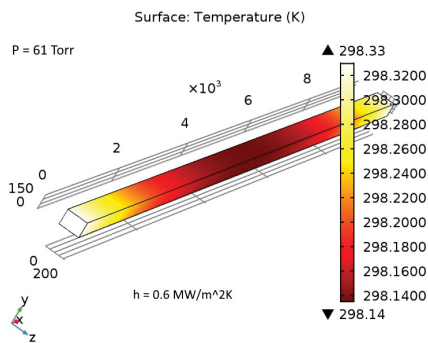


Figure D.2: **Heat transfer coefficients from COMSOL simulations at 61 Torr for dynamic temperature measurement conditions.** Due to heat dissipation, this portion feels a lower temperature than the surface at 61 Torr and 760 Torr (presented in the previous figure). 3 – 760 Torr h values are in good agreement with Dickins’ model illustrated in Figure 6.6. At 100 μ Torr, $h = 10 \text{ Wm}^{-2}\text{K}^{-1}$ is the value usually used for natural convection process in COMSOL. Too high heat transfer coefficients for higher pressure clearly demonstrate that underlying thermal physics is different for the NEMS and dominated by air conduction rather than convection.